Technology Survey and Performance Scaling for the Design of High Power Nuclear Electric Power and Propulsion Systems

by

Daniel B. White
B. S. 2003, Electrical Engineering, Texas A&M University
M. S. 2008, Aeronautics and Astronautics, MIT

Submitted to the Department of Aeronautics and Astronautics in partial fulfillment of the requirements for the degree of

Doctor of Philosophy in Aeronautics and Astronautics
in the field of
Space Propulsion

at the

MASSACHUSETTS INSTITUTE OF TECHNOLOGY

[June 2011]
May 2011

Author .....
Daniel B. White Jr.
Department of Aeronautics and Astronautics
May 13, 2011

Certified by.....
Manuel Martínez-Sánchez
Professor, Aeronautics and Astronautics
Thesis Supervisor

Certified by.....
Paulo Lozano
Associate Professor, Aeronautics and Astronautics

Certified by.....
Jeffrey Hoffman
Professor of the Practice, Aeronautics and Astronautics

Accepted by.....
Eytan Modiano
Chair, Committee on Graduate Students

TECHNOLOGY SURVEY AND PERFORMANCE SCALING FOR THE DESIGN OF HIGH POWER NUCLEAR ELECTRIC POWER AND PROPULSION SYSTEMS

by
Daniel B. White Jr.

Submitted to the Department of Aeronautics and Astronautics on May 21, 2011
in partial fulfillment of the requirements for the degree of
Doctor of Philosophy in Aeronautics and Astronautics

ABSTRACT

High power nuclear electric propulsion systems have the capability to enable many next-generation space exploration applications. To date, use of electric primary propulsion in flight systems has been limited to low-power, solar electric missions. There is a need for a large-scale research and development effort to field systems capable of meeting the demands of future high-power electric propulsion missions, especially missions utilizing nuclear power plants to power electric propulsion systems. In formulating such an effort, it is first important to identify the likely requirements around which such a system might be designed. These requirements can be effectively cast in terms of required thruster lifetime, thrust, specific impulse, output power, and power plant specific power. Projected requirements can be derived based on the mass characteristics of space-borne nuclear power plants, and the optimized trajectories of spacecraft missions enabled by the use of megawatt-level nuclear electric power systems. Detailed mass modeling of space-based Rankine cycle nuclear power plants is conducted to evaluate the achievable specific power of these systems. Based on the figures for specific power so obtained, mission modeling is next conducted using the Mission Analysis Low-Thrust Optimization software package. Optimized thrust, specific impulse and lifetime figures are derived for several missions of interest. A survey of available electric propulsion thrusters is conducted and thruster configurations presenting the lowest developmental risks in migrating to high thruster output power are identified. Design evolutions are presented for three thrusters that would enhance or enable operation at the megawatt level. First, evaluation of projected lifetime for dual-stage gridded ion thrusters is conducted using the CEX2D simulation tool to evaluate the utility of multi-stage gridded ion engines in obtaining the required thruster lifetime for operation at high specific impulse. Next, to evaluate the utility of Hall thrusters operating at high propellant mass flow rate, a numerical thruster model is developed that incorporates the effects of the neutral fluid in predicting thruster performance. Using this code, numerical simulations are conducted to investigate the effects of variations in propellant mass flow rate, magnetic field topology, and thruster channel geometry on achievable performance. Finally, the effects of variations in the channel contour of magnetoplasmadynamic thrusters on performance and efficiency are evaluated using the MACH2 software package. Incremental variations in thruster channel contour are implemented, and the effects of these variations on the performance onset condition, and electrode current distributions are observed. Conclusions regarding the utility of each of these three design evolutions in developing thrusters for multi-megawatt electric propulsion systems are discussed. Contributions stemming from this research include, first, the establishment of an appropriate requirements space for the design of advanced high-power electric power and propulsion systems. This design space is comprised of projected requirements for power plant specific power, derived from power plant mass modeling, and thruster output power, specific impulse and lifetime derived from mission modeling. Additionally, this work provides evaluation, using state-of-the-art simulation suites, of several electric thruster design evolutions of potential utility in developing electric propulsion systems designed to operate at the megawatt level.

Thesis Supervisor: Manuel Martínez-Sánchez
Title: Professor of Aeronautics and Astronautics

Acknowledgements

This work is the product of the insights, expertise and support of several individuals and groups provided over the last several years. The most visible of these has certainly been Professor Manuel Martinez-Sanchez who has served as my advisor in conducting this work. Like so many students before me, my experience these last several years has been overwhelmingly informed by your wisdom, your patience and your kindness. I hope that in the future I might continue to enjoy your friendship.

My gratitude is also owed to the other members of my committee, Professor Paulo Lozano and Professor Jeffery Hoffman. Your insights, kind words of encouragement and your patience have been invaluable in the conduct of this work. I am privileged to call you my friends.

I am indebted to Ira Katz, Dan Goebel, John Anderson and Yiangos Mikellides and the NASA Jet Propulsion Laboratory for their friendship and their kindness, as well as their guidance in learning to use the CEX2D code over the summer of 2010. I am also grateful to Yiangos Mikellides of NASA JPL and to Pavlos Mikellides of Arizona State University for many helpful correspondences in learning to use the MACH software. I would also thank my undergraduate research assistant, Dominic Gallegos, for hours spent at work performing mission analysis simulations.

In addition to these, I would also express my gratitude to those whose contributions have been less tangible, but no less real. The first of these is my wife, Brooke Anderson-White. I am enriched by your love and kindness. Your peaceful and quiet way is sustaining, and your light brightens everything in this life. I love you and I never want to be without you. Next are our friends and labmates at MIT and in the Boston College Biology Department. Your fellowship has been indispensible in coping with the rigors of these last several years, and your friendship is precious. Finally, I'm grateful to my parents, Brent and Mishelle White, for a childhood spent in peace and faith and love. I am happy and strong, and these are a testament to your good stewardship.

I am blessed by a loving God, in the Person of Jesus Christ, who is constantly mindful of me. He has placed me in the midst of all these wonderful people whose love and hope overwhelmingly influence my wellbeing. I have nothing more to offer than my love and the trust that wherever this life may lead, You are never far.

Table of Contents

List of Figures

List of Tables

Chapter 1

Introduction

Space propulsion refers to the variety of methods useful for effecting changes in the velocity of a vehicle in space. This is typically accomplished through the use of reaction engines. Space propulsion is important to the human exploration of the cosmos, as it provides the means to deliver scientific payloads to any number of targets for exploration in our celestial neighborhood. As the technology of space propulsion evolves, scientific forays to more remote destinations are enabled for a given mission time. Increasingly advanced missions are also possible, which may require much greater payload masses, ultimately including human missions to targets such as near-Earth bodies, Mars, and beyond.

A particular class of reaction engine that holds great promise for expanding the frontiers of space exploration is the electric thruster. Rather than relying on the conversion of energy contained within propellant chemical bonds to obtain jet kinetic power, as in a conventional chemical rocket, electric propulsion systems rely on the application of external electrical power to heat or ionize a propellant and accelerate it to high velocity. With the exception of electrothermal thruster concepts, the acceleration process is accomplished using electromagnetic body forces. A survey of common electric propulsion devices is undertaken in a subsequent chapter of this work.

Appreciation of the utility of charged particles for propulsion can trace its genesis to many of the fathers of modern rocketry, being at least marginally understood by Tsiolkovsky [1], Goddard and Oberth [2]. During the 1950s, Ernst Stuhlinger did much to develop the field of electric propulsion [3-5]. A thorough recounting of the history of electric propulsion is provided in [6].

1.1 Background

To better understand the physics underlying the operation of all reaction engines, it is useful to briefly develop the governing relations from first principles.

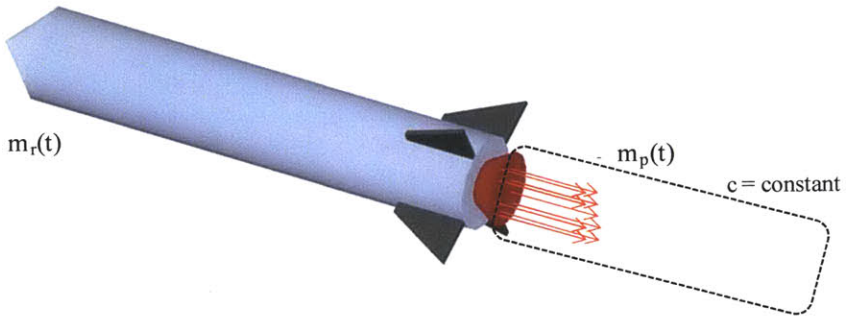

Figure 1.1. The ideal rocket equation can be derived from the conservation of linear momentum

Consider the simple illustration in Figure 1.1. The mass of the rocket and the total mass of propellant in the plume are given by $m_r(t)$ and $m_p(t)$ respectively, and c is the effective exhaust velocity of the propellant in the plume. For an observer in the rocket frame, the conservation of momentum can be written:

$$\frac{dp_r}{dt} = m_r(t)\frac{dv_r(t)}{dt} \qquad \text{(Eq. 1.1)}$$

Next, we can imagine a control volume that encloses the entire column of plume materials. If the effective exhaust velocity of the plume is taken to be constant in time, the time rate of change of momentum inside this control volume is known:

$$\frac{dp_p}{dt} = \frac{dm_p(t)}{dt}c \qquad \text{(Eq. 1.2)}$$

From the conservation of linear momentum for the entire system consisting of the rocket and the plume, it must be true that:

$$\frac{dp_p}{dt} + \frac{dp_r}{dt} = 0 \qquad \text{(Eq. 1.3)}$$

The conservation of mass requires that the mass lost by the rocket must be precisely equal to the mass gained by the plume:

$$\frac{dm_p(t)}{dt} = -\frac{dm_r(t)}{dt} = \dot{m} \qquad \text{(Eq. 1.4)}$$

This allows us to finally express:

$$\frac{dv_r(t)}{dt} = \frac{c}{m_r(t)}\frac{dm_r(t)}{dt} \quad \text{(Eq. 1.5)}$$

We can integrate this expression between an initial and final maneuver time to find:

$$\Delta V = v(t) - v_0 = c \ln\left(\frac{m_0}{m(t)}\right) \quad \text{(Eq. 1.6)}$$

This expression is known as the Tsiolkovsky rocket equation or ideal rocket equation. The exhaust velocity, u_e, is commonly expressed as the specific impulse:

$$I_{SP} = \frac{c}{g_0} \quad \text{(Eq. 1.7)}$$

Specific impulse represents the total impulse available from a unit weight of propellant. For the storable chemical propellants used on board spacecraft, the specific impulse typically lies in the range of 200 – 300 s. The combination of liquid oxygen and liquid hydrogen provides the highest specific impulse of any operational chemical system, with typical values of vacuum ISP between 430 – 460 s.

In practice the required velocity increment, or ΔV, is a function of the maneuver to be performed, with more distant targets or more time constrained missions requiring proportionally higher ΔV. Sample values for required ΔV of several missions of interest are presented in Table 1.1. Velocity increments are assumed to be applied impulsively.

Mission	ΔV [km/s]
Earth Surface to LEO	9.3
Earth Surface to C3	11.2
LEO to GEO	4.2
LEO to C3	3.2
LEO to LLO	3.9
LEO to Mercury Orbit & Return	31.0
LEO to Venus Orbit & Return	16.0
LEO to Mars Orbit	5.7
LEO to Mars Orbit & Return	14.0
LEO to Mars Surface and Return	34.0
LEO to Jupiter Orbit and Return	64.0
LEO to Saturn Orbit and Return	110.0
LEO to Solar Escape	8.7
LEO to 1000 AU (50 yr)	142.0

Table 1.1. Required velocity increments for several missions of interest [7,8]

Inspection of Eq. 1.6 indicates two approaches to increasing the ΔV capability of a spacecraft: increasing the specific impulse, or decreasing the dry mass fraction. Assuming current and near-term technologies, decreasing the dry mass fraction of spacecraft does not seem to offer a great deal of leverage for increasing achievable ΔV. As will be shown in the subsequent section, however, reducing the mass of the power system in an electric propulsion system is indeed a driving consideration. These observations highlight the importance of high propellant exhaust velocity and motivate an exploration of propulsion technologies capable of delivering high specific impulse.

A more general metric by which spacecraft propulsive requirements can be expressed is in terms of the required mission total impulse:

$$I_{TOT} = \int_{t_0}^{t_f} T dt \qquad \text{(Eq. 1.8)}$$

Where T is the possibly time-dependent thrust force acting on the spacecraft:

$$T = \dot{m}c \qquad \text{(Eq. 1.9)}$$

The thrust and specific impulse can be related to the propulsion system total input power:

$$\eta P_{in} = \frac{T^2}{2\dot{m}} = \frac{1}{2} T g I_{SP} = \frac{1}{2}\dot{m}c^2 \qquad \text{(Eq. 1.10)}$$

The thruster efficiency is denoted by η.

1.2 Electric Propulsion

Electric propulsion (EP) holds great promise for realizing the improvements in specific impulse that will be required for future space exploration applications. Electric propulsion relies on the application of external electrical power to accelerate a working fluid. In conventional chemical rockets, the source of energy to achieve this acceleration is contained within the chemical bonds of the working fluid—the fuel and oxidizer. The total energy available in such a system is strictly a function of the mass of fuel and oxidizer present. The instantaneous power delivery capability of these systems, however, is a function of mass flow rate and may in principle be increased to very large values. For this reason, chemical systems may be considered energy limited systems. Electric propulsion systems rely on an external source of electrical energy that is decoupled from the working fluid. Thus, while the rate of energy deposition to the working fluid in an EP system is limited, the total deposited energy is only a function of the operating time, and may in principle, increase to extremely high values, potentially much higher than those that can

be achieved in chemical systems. In real systems, engineering considerations tend to limit both the achievable power output of chemical systems and the achievable change in total energy of the propellant in electric systems. The sum of these effects implies that chemical propulsion systems are typically quite useful in producing very high values of thrust, with limited total impulse capability. This makes them suitable for missions like planetary launch. Electric propulsion systems produce a limited thrust, but large values of total impulse, making them more suitable for in-space propulsion applications.

Recently low-power solar electric propulsion systems have begun demonstrating their utility as primary propulsion in several small probes [9-14]. As confidence in the utility of this technology continues to grow with mission designers, migration to higher input powers is likely. Higher electrical input powers will allow missions to carry far greater payload masses or to achieve a given velocity increment in a shorter mission time compared to current electrically propelled spacecraft. In the medium- to far-term, coupling of high power electric thrusters to nuclear power systems will enable missions not energetically feasible using other more conventional propulsion systems. Based on this premise, an area of research that promises to provide future value is in the scaling behavior of nuclear electric power and propulsion systems to the multi-megawatt level, the requirements that these future systems will likely have to meet, and the implementations that will provide the lowest design and operational barriers to development.

An important consideration in the design of electric propulsion systems is the interplay of power plant specific power with specific impulse and the dry mass fraction of the spacecraft. The plant specific power is the ratio of the power plant output power to its total mass. This is illustrated in the analysis originally developed by Stuhlinger [15]. Consider a spacecraft whose total mass can be decomposed into components:

$$M_O = M_{PROP} + M_S + M_L + M_{PP} \qquad \text{(Eq. 1.11)}$$

These components are the propellant, M_{PROP}, the structural mass, M_S, the payload mass, M_L, and the power and propulsion system mass, M_{PP}. In this case, the final mass of the spacecraft is the initial mass, less the propellant consumed, so that we can use the rocket equation to express:

$$\frac{M_S + M_L + M_{PP}}{M_O} = e^{-\frac{\Delta V}{c}} \qquad \text{(Eq. 1.12)}$$

Next, we can define the specific power of the power and propulsion system, α, which has units of power per unit mass, to obtain:

$$\frac{M_S + M_L}{M_O} = e^{-\frac{\Delta V}{c}} - \frac{P_{in}}{\alpha M_O} \qquad \text{(Eq. 1.13)}$$

We can express the input power to the system in terms of the jet kinetic power and system efficiency:

$$\frac{M_S + M_L}{M_O} = e^{-\frac{\Delta V}{c}} - \frac{M_{PROP}c^2}{2\alpha\eta M_O \Delta t} = e^{-\frac{\Delta V}{c}} - \frac{c^2}{2\alpha\eta\Delta t}\left(1 - e^{-\frac{\Delta V}{c}}\right) \quad \text{(Eq. 1.14)}$$

Dimensionally, we can see that the group $2\alpha\eta\Delta t$ has units of L^2T^{-2}. Stuhlinger introduced the characteristic velocity:

$$v_{ch} = \sqrt{2\alpha\eta\Delta t} \quad \text{(Eq. 1.15)}$$

There is an optimum specific impulse, for which the dry mass fraction in Eq. 1.12 is a maximum. If we approximate the exponential function using the series expansion, we can evaluate this optimum specific impulse:

$$c_{Opt} \cong v_{ch} - \frac{1}{2}\Delta V - \frac{1}{24}\frac{\Delta V^2}{v_{ch}} \quad \text{(Eq. 1.16)}$$

The existence of this optimum can be understood qualitatively. Given a fixed time to complete a mission, with a given power plant specific power and system efficiency, there is one value of specific impulse for which the payload and structure mass fraction will be a maximum. At specific impulse values above this optimum, more input power will be required, increasing the required power supply mass and reducing the overall payload fraction. Below the optimum, more propellant will be required than in the optimum case, again reducing the fraction of the spacecraft that can be devoted to payload.

One should expect that the requirements of mission designers for propulsion system performance will be a function not only of the mission to be flown, which effectively sets ΔV, but also of the mass characteristics of the spacecraft power plant, which determine α. It is therefore essential that the mass characteristics of space-based nuclear power plants are evaluated carefully to inform the derivation of projected requirements for multi-megawatt nuclear electric propulsion systems. This analysis is undertaken in Chapter 2 of this work.

A second mission-level consideration that should be highlighted in the discussion of any low-thrust propulsion system is the impact of extended burn times and the concurrent ΔV losses that they yield. In order to understand these losses it is useful to evaluate the approximate ΔV for a low-thrust spiral climb from a gravity well and compare this with the ΔV that would be required for an impulsive Hohmann transfer.

For a spacecraft in an initially circular orbit at a radius r_0 we know that the velocity is given by:

$$v_{C0} = \sqrt{\frac{\mu}{r_0}} \qquad \text{(Eq. 1.17)}$$

Where μ is the standard gravitational parameter for the body:

$$\mu = GM_B \qquad \text{(Eq. 1.18)}$$

The gravitational constant, G, has a value of $6.673 \times 10^{-11} \frac{m^3}{kg \cdot s^2}$. The mass of the central body is denoted by M_B. If we assume that thrust is applied tangential to the orbit, and that the orbit remains nearly circular during the thrusting period, the conservation of energy requires:

$$\frac{d}{dt}\left(-\frac{1}{2}v^2\right) = \frac{d}{dt}\left(-\frac{\mu}{2r}\right) = a\sqrt{\frac{\mu}{r}} \qquad \text{(Eq. 1.19)}$$

Expanding gives:

$$\frac{\mu}{2r^2}\frac{dr}{dt} = a\sqrt{\frac{\mu}{r}} \qquad \text{(Eq. 1.20)}$$

We can separate and integrate this expression to find:

$$\Delta V = \int_{t_0}^{t_f} a dt = \frac{1}{2}\int_{r_0}^{r_f} \sqrt{\frac{\mu}{r^3}} dr \qquad \text{(Eq. 1.21)}$$

Evaluating the above expression finally gives:

$$\Delta V = \sqrt{\frac{\mu}{r_0}} - \sqrt{\frac{\mu}{r_f}} = v_{C0} - v_{Cf} \qquad \text{(Eq. 1.22)}$$

This result is well-known and indicates that the total required change in velocity for a low-thrust transfer between two coplanar circular orbits is approximately the difference in the circular velocities of the orbits corresponding to the initial and final orbital radii. We can compare this result to that of a general two-burn impulsive Hohmann transfer. The Hohmann transfer is an orbital transfer maneuver between two coplanar circular orbits. It requires two engine firings tangent to the initial and final circular orbits, respectively. The first velocity increment is given by:

$$\Delta V_1 = \sqrt{\frac{\mu}{r_0}}\left(\sqrt{\frac{2r_f}{r_0 + r_f}} - 1\right) \qquad \text{(Eq. 1.23)}$$

The second velocity increment:

$$\Delta V_2 = \sqrt{\frac{\mu}{r_f}}\left(1 - \sqrt{\frac{2r_0}{r_0 + r_f}}\right) \qquad \text{(Eq. 1.24)}$$

We can compare the total ΔV required by the low-thrust transfer to the Hohmann transfer given an initial orbital altitude. This comparison is shown in Figure 1.2.

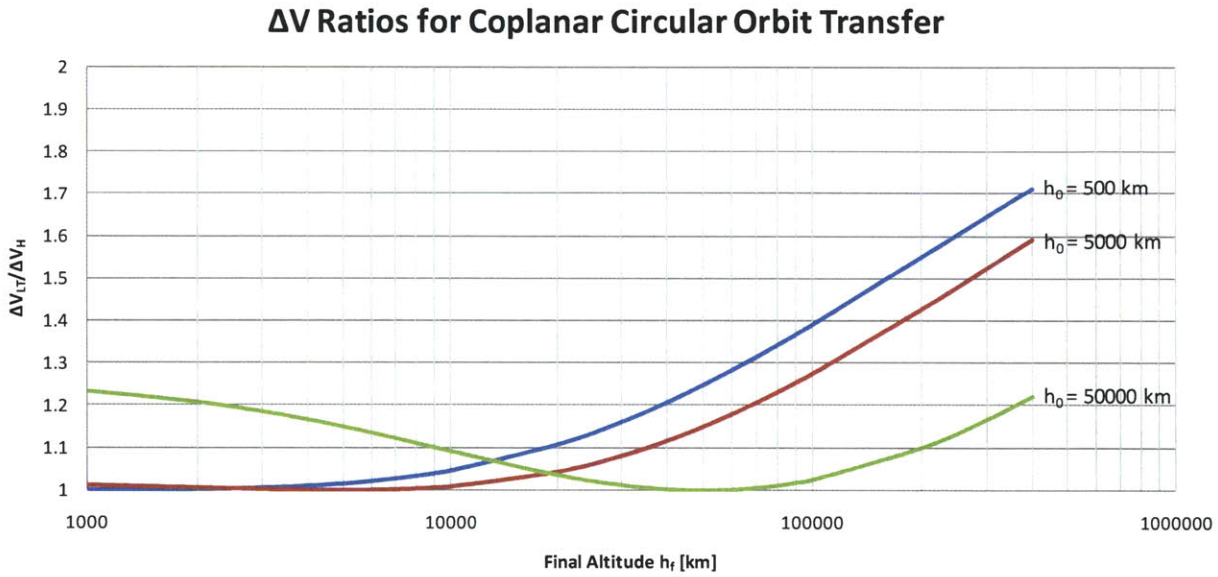

Figure 1.2. Comparison of the ΔV requirements for low-thrust spiral climb versus impulsive Hohmann transfer

While this comparison clearly demonstrates that a penalty in velocity increment is incurred in all cases for low-thrust spiral transfers, the propellant mass savings derived from the use of high I_{SP} of low-thrust electric propulsion systems is much greater than the incremental increase in propellant mass required to overcome these losses.

Given the enormous potential of electric propulsion to enable advanced space missions, it is the object of this work to explore the utility of electric propulsion systems deriving primary power from space-based nuclear power plants in advanced spaceflight applications.

1.3 Challenges of Migrating to High Thruster Output Power

There are two fundamental engineering challenges in driving current EP thrusters to higher levels of output power. First, the propellant ionization and plasma acceleration processes at work in an EP thruster, as well as the high energy of the particles comprising the plasma itself, work together to create a

destructive environment for material surfaces exposed to the plasma. These factors often impose severe lifetime limitations on thruster components and substantially reduce usable life and available total impulse. Increased current and plasma densities also give rise to a harsher thermal environment, further degrading material performance.

The second engineering challenge facing thruster designers is the greater mass of devices designed to operate at high output power. One necessary aspect of most high power electric propulsion devices is increased dimension. The effect of increased power handling on thruster specific power is unclear, and likely varies with particular thruster implementation. If the mass increase with dimension is greater than the concurrent power increase in dimension, the specific power of a given thruster may be a decreasing function of output power. However, if the specific power is an insensitive or increasing function of output power, the engineering challenge is precisely to maximize the slope of this relation. It is advantageous to identify particular thruster implementations whose mass-scaling behavior provides the greatest potential growth in specific power for a given increase in total jet power.

Apart from the engineering challenges associated with lifetime and thruster specific power, there are also operational regimes in which the governing physical processes driving thruster behavior are not well understood. For example, the physics of magnetic nozzles as applied to electric propulsion devices continues to present a rich opportunity for research [16-18], and offers the potential to increase the performance and lifetime of plasma-phase electrothermal devices [19], as well as applied field MPD thrusters [20].

1.4 Previous Work

The utility of nuclear power sources to power electric propulsion devices was first quantitatively explored in the literature in 1947 [21]. Early exploration of NEP systems tended to pre-suppose the use of electrostatic gridded ion thrusters [15, 21]. Some systematic consideration has been given to the utility of various thrusters at intermediate power levels, up to hundreds of kilowatts, in recent years [22].

Beginning early in the development of electric propulsion systems there have been any number of proposed spacecraft designs intended to serve a wide variety of functions or complete various missions, both manned and unmanned. There is a general tendency to point-design particular reactor types, thermal conversion cycles and electric propulsion thrusters in such spacecraft designs that utilize some form of NEP. A brief review of several of the more detailed NEP spacecraft designs found in the literature is given in Table 1.2.

Mission	Thruster Type	P_{OUT} [kW]	I_{SP} [s]	Reactor Power & Type	PCS	t_{LIFE} [h]	M_{PP} [kg]	P_{OUT}/M_{PP} [kW/kg]	Ref.
Geo. Comm. Satellite	Arcjet	12	1000	SNAP-8	Rankine	2160	960.1	0.0125	23
SP-100 Flight Ex. Vehicle (OTV)	Arcjet	38.64	1030	100 kW_e SP-100	Thermoelectric	4380	3540	0.0109	24-29
SP-100 Flight Ex. Vehicle (OTV)	Arcjet	36.7	960	100 kW_e SP-100	Thermoelectric	--------	4436	0.0083	30
SP-100 Flight Ex. Vehicle (OTV)	Arcjet	12.6	1030	30 kW_e SP-100-Type	Thermoelectric	6000	2370	0.0053	31
Outer Planet Explorer	MPD	1350	9000	LMFR OCT	Thermionic	30000	9840	0.1372	32,33
Neptune Orbiter Spacecraft	Pulsed MPD	12	5000	100 kW_e SP-100	Thermoelectric	52296	5204	0.0023	34
Manned Mars Vehicle	MPD	3000	5000	PBR-Type	Brayton	12240	34000	0.0882	35
Pegasus Manned Mars Mission	MPD	3000	5000	8.5 MW_e LMFR	Rankine	12240	34000	0.0882	36-38
Mars Cargo Ferry	MPD	2401	5000	10 MW_e LMFR	Rankine	2280	60700	0.0396	39
Mars Cargo Ferry	MPD	1999.2	3000	10 MW_e LMFR	Rankine	2280	60700	0.0329	39
Mars Cargo Mission	Li-Fed MPD	929	5000	1.5 MW_e SP-100-Type	Rankine	61320	42530	0.0218	40
OTV Transport	PIT	42	2000	100 kW_e	Thermoelectric	61320	3389	0.0124	41
Jupiter Spacecraft	Gridded Ion	700	8000	1.17 MW_e	-------	6600	10000	0.0700	42
Manned Mars Vehicle	Gridded Ion	2200	5828	3.3 MW_e UO_2 Fast RX	Thermionic	8760	52000	0.0423	43
Outer Planets Explorer (Jupiter)	Gridded Ion	311	9000	400 kW_e UO_2 LMFR	Thermionic	30000	10000	0.0311	44-46
Space-Based Radar OTV	Gridded Ion	57.82	2000	100 kW_e UO_2 Fast RX	Brayton	-------	3550	0.0163	47,48
Outer Planets Spacecraft	Gridded Ion	73.75	5300	100 kW_e UO_2 - Fueled	Thermoelectric	50,000	4367	0.0169	49-52
NEP OTV	Gridded Ion	185.25	3000	300 kW_e SP-100-Type	Thermoelectric	5000	9860	0.0188	53
Tau Spacecraft	Gridded Ion	406.7	12500	1 MW_e SP-100-Type	Thermoelectric	17500	16500	0.0246	54
NEP Space Test Program (NEPSTP)	Gr. Ion / Hall	4.507	1,600 - 3,000	5.75 kW_e TOPAZ-II	Thermoelectric	-------	3500	0.0013	55,56
Jupiter Icy Moons Orbiter	Gridded Ion	129.6	6,000 - 8,000	200 kW_e GCR	Brayton	61320	6472	0.0200	57
ISC-2000 Spacecraft	Gridded Ion	26.4	4000	TOPAZ-25 30 kW_e LMFR	Thermionic	15000	3120	0.0085	58
100 kW-Class Robotic Explorer	Gridded Ion	77	5,000 - 16,000	100 kW_e SAFE-300-Type	Brayton	30000	1658.1	0.0464	59
1 MW Gridded Ion NEP Spacecraft	Gridded Ion	739.2	5,000 - 16,000	1 MW_e SP-100-Type	-------	8778	3969.5	0.1862	59
NEPTranS Vehicle Baseline	Gridded Ion	70	5000	100 kWe Gas-Cooled	Brayton	27936	3582	0.0195	60

Table 1.2. Review of various NEP concept spacecraft from 1961 – 2005

A detailed summary of several other concepts developed prior to 1990 is provided in [61]. Parsing this dataset according to thruster type, and comparing the projected jet output power to the overall power and propulsion system specific power provides some insight to the anticipated effects of increased output power, as well as the supposed thruster implementations to effectively convert the output electrical power into jet power.

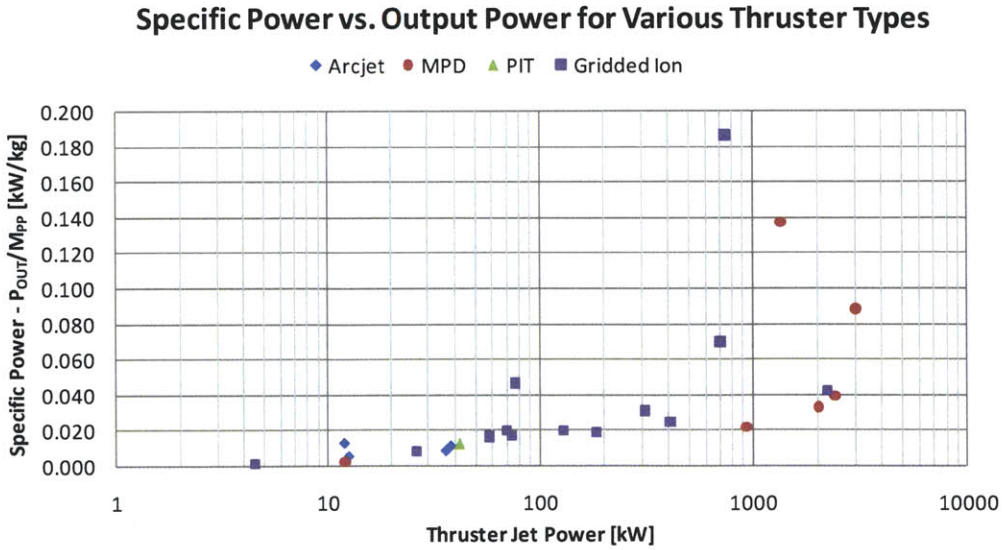

Figure 1.3. Estimates for the achievable output-rated specific power for megawatt-class nuclear electric propulsion systems vary over an order of magnitude. Gridded ion thrusters and MPD thrusters are almost universally proposed for use in high-power NEP missions.

One trend evident from the data in Table 1.2 is the use of static power conversion systems with low-power reactors, and the increasing use of dynamic systems, particularly the Rankine and Brayton power cycles, as the required output power increases. This kind of analysis highlights two factors motivating this avenue of research. First, there is a need for a systematic evaluation of EP technologies to identify implementations that offer the lowest barriers to development at megawatt output power levels. Second, there is a need for strict quantification of the power scaling trends of various configurations of reactor and power conversion systems for space nuclear power plants.

The design of space nuclear power plants has an enormous impact on the types of missions that can be efficiently conducted using this technology. For a given value of propulsive output power, allowable mission time, and spacecraft initial mass, a higher power plant specific power (kW/kg) will admit a higher allowable I_{SP}, and thus a higher overall mass fraction. There is a broad consensus expressed in the literature on the near-term optimality of the potassium-Rankine thermal conversion cycle in terms of maximizing specific power [62 - 66]. Because of the wealth of materials compatibility and operational testing of components and systems for potassium-Rankine power conversion systems, this type of system is thought to provide the fewest barriers to near-term employment in space nuclear power systems [63].

A review of national programmatic activity in the US and the former Soviet Union in developing nuclear power systems for deployment in space is included in Chapter 2.

1.5 Goals of this Work

The broad scope of the selected topic provides a rich opportunity to explore and develop fundamental insights on the application of various electric propulsion technologies to mission concepts in which the supply of electrical power is abundant. The expected contributions emerging from this work can be broadly cast in three categories: characterization of the solution space, identification of future needs for power and propulsion systems, and analysis of design evolutions to enable EP thruster operation at the megawatt level.

1.5.1 Characterizing the Solution Space

The first goal of this work is the development of a solution space for the problem of scaling electric propulsion thrusters to high power that is based on the current, and near-term projected state of the art. This involves the development of a set of representative performance requirements and performance trends based on analysis of mission studies. Based on the performance and lifetime of a given thruster, its ability to meet representative requirements can be assessed.

In order to realize this contribution, a detailed comparison of the needs developed by mission analysis to the performance capability of current electric propulsion technologies must be undertaken.

Quantitatively, these needs are represented by thruster specific impulse, power handling and lifetime capabilities.

1.5.2 Identifying Future Needs

A key strength of this analysis is that it offers the opportunity to explore not only appropriate technologies for a given region of the solution space, but also highlights regions in which technology has not matured sufficiently to provide a good match of mission needs and technological capability. These regions can be thought of as performance gaps, areas in the power-I_{SP}-I_{TOT} space in which a particular mission might fall, but which is not satisfactorily covered by any thruster. Highlighting these potential gaps provides an essential contribution to inform future development efforts to realize high-power electric propulsion systems.

1.5.3 Evaluating Design Evolutions

The final goal of this thesis is to characterize, by simulation, several design evolutions for various thrusters that will enable or enhance their operation at the megawatt level. Given a representative set of propulsive requirements, the EP thrusters representing the lowest technical risk for design at high power can be identified. Design evolutions that have the potential to enable or enhance the operation of the identified thrusters at high power can then be studied. Analysis of particular design evolutions may serve to guide subsequent numerical or experimental work in high power thruster design.

1.6 Organization

This work explores the problem of how to best utilize power-rich space platforms, particularly space-based nuclear electric power plants, with electric propulsion systems. As outlined in the preceding sections, developing an understanding of this issue requires an understanding of two related problems. First, the mass characteristics of the nuclear power plant must be well understood. Power plant specific power is a dominant driver of spacecraft mass and mission optimal exhaust velocity in platforms using space-based nuclear power plants. Second, the propulsive requirements for particular missions of interest must be developed. These missions must typify the required operating lifetime, output power and efficiency, as well as optimum specific impulse of missions that will utilize nuclear electric propulsion at the megawatt level. Only after characterizing these two key drivers can the problem of thruster design at high power be addressed.

The first important step in achieving the goals of this work is to characterize the mass properties of space-based nuclear power plants operating at the power levels of interest. Mass modeling of space-based nuclear power plants based on the potassium Rankine thermoelectric conversion cycle is conducted using

the ALKASYS-PC software developed by Oak Ridge National Labs. By incorporating two plant configurations representative of current technology, and medium-term technology goals, a range of power plant specific powers is obtained. Plant specific power is later used in the development of mission models to identify propulsive requirements. Mass modeling of space-based nuclear power systems is discussed in Chapter 2.

In an effort to appropriately gauge the propulsive needs of mission designers and systems engineers involved in the development of advanced missions using high power nuclear electric propulsion systems, several missions of interest are developed and modeled using the MALTO software package [67-69]. The optimized propulsion system performance metrics derived from this mission analysis can then be used to effectively inform the design of these future power and propulsion systems [70]. The results of this mission modeling work are presented in Chapter 3.

The set of commonly studied electric propulsion devices is introduced in Chapter 4, including a brief description of their operating principles. Typical performance characteristics and engineering challenges associated with scaling to high power are outlined. Based on this analysis, design evolutions for three types of thrusters are selected for detailed study in Chapters 5 – 7. In Chapter 5 the achievable lifetime of dual-stage gridded ion thrusters is evaluated to ascertain their utility in achieving the long operating lifetimes required for high-I_{SP} systems. In Chapter 6 a one-dimensional three-fluid model of the Hall thruster discharge is developed that includes the effects of the neutral particle fluid in predicting thruster performance. This allows for evaluation of Hall thruster operation at elevated mass flow rate. Studies are also conducted to evaluate variations in thruster magnetic field topology and channel geometry as a means of improving thruster performance. In Chapter 7 the effects of channel contouring on performance and efficiency of magnetoplasmadynamic thrusters are characterized using fluid model simulations. The work concludes with a summary of the findings developed herein, as well as suggestions for future directions.

Chapter 2

Nuclear Power in Space

2.1 Introduction

The widespread application of nuclear power to space exploration systems has the potential to dramatically enhance human efforts in the exploration of the solar system. Power plants based on nuclear fission reactors, in particular, offer mission designers compact, potentially lightweight, long-lifetime, high reliability power systems with values of specific power that are of interest for electric propulsion applications. To date, Russia has used over 30 fission reactors in space. The US, on the other hand, has flown only one - the SNAP-10A (System for Nuclear Auxiliary Power) in 1965 [71, 72]. In the sections that follow, three applications of nuclear power to spaceflight systems will be outlined, with specific attention to nuclear power plants to facilitate the use of high power electric propulsion systems.

2.1.1 Nuclear Thermal Rockets

Research into the use of nuclear thermal propulsion in the US began in 1953 under the auspices of Project Rover. As a joint effort between the US Atomic Energy Commission (AEC) and the US Air Force, the primary goal of Project Rover was to develop nuclear thermal rockets for intercontinental ballistic missiles (ICBMs). This research was largely performed in parallel with the research into developing suitable chemical rockets for the same purpose. At the time, it was uncertain whether chemical rocket systems could be developed with sufficient propulsive capability to meet the mission requirements of then-envisioned ICBMs. NASA later replaced the Air Force in partnering with the AEC on the program, and in the early 1960s the Rover program was integrated into the Nuclear Engine for

Rocket Vehicle Application (NERVA) program. Concentration in the Rover program was with the development of small, lightweight high power nuclear reactor cores, while NERVA was primarily concerned with the integration of these nuclear sources into rocket powered vehicles. Between 1955 and 1973, 20 rocket reactors were designed built and tested under these programs [71, 73]. The first of these systems, the KIWI-A, was tested in 1959, and achieved a power level of 70 MW.

Notably, in June of 1963 the Phoebus-2A reactor operated at an output power level of 4.1 GW for 12 minutes. This was the most powerful nuclear rocket core ever built. Also, in June of 1972, the nuclear furnace (NF-1) fuel demonstrated a power density of 4.5 GW/m^3, with a power output of 54 MW during a 109 minute operational test. This is the highest power density achieved in a nuclear rocket core [71, 74]. For comparison, the space shuttle main engine (SSME) produces 2.28 MN of thrust at a specific impulse of 453 seconds in vacuum. This corresponds to a jet output power of 5.06 GW.

In March of 1969 the first down-firing nuclear rocket prototype, the XE-prime was successfully test fired at 1.1 GW. The XE-prime configuration was similar to that of a flight engine. However, with the subsequent suspension of Saturn V launch vehicle development, the prime launch vehicle envisioned for the nuclear rocket engine, and because of changing national priorities of the 1970s, the Rover/NERVA project was cancelled in January of 1973 [74].

2.1.2 Radioisotope Thermal Generators

There is a great deal of heritage in using direct thermoelectric conversion of decay heat from radioisotopes to provide electrical power to deep space probes. These systems are typically quite robust, and have the potential to provide low to medium electrical and thermal power output for decades [75]. To date, twenty-five US missions have used these devices for onboard electrical power, shown in Table 2.1 below.

Power System	Spacecraft	Mission Type	Launch Date	Status
SNAP-3B	TRANSIT 4A	Navigational	29-Jun-61	Successfully achieved orbit
SNAP-3B	TRANSIT 4B	Navigational	15-Nov-61	Successfully achieved orbit
SNAP-9A	TRANSIT-5BN-1	Navigational	28-Sep-63	Successfully achieved orbit
SNAP-9A	TRANSIT-5BN-2	Navigational	5-Dec-63	Successfully achieved orbit
SNAP-9A	TRANSIT-5BN-3	Navigational	21-Apr-64	Mission aborted - burned up on reentry
SNAP-10A	SNAPSHOT	Experimental	3-Apr-65	Successfully achieved orbit
SNAP-19B2	NIMBUS-B-1	Meterological	18-May-68	Mission aborted - heat source retrieved
SNAP-19B3	NIMBUS III	Meterological	14-Apr-69	Successfully achieved orbit
SNAP-27	Apollo 12	Lunar	14-Nov-69	Successfully placed on lunar surface
SNAP-27	Apollo 13	Lunar	11-Apr-70	Aborted - heat source returned to south Pacific Ocean
SNAP-27	Apollo 14	Lunar	31-Jan-71	Successfully placed on lunar surface
SNAP-27	Apollo 15	Lunar	26-Jul-71	Successfully placed on lunar surface
SNAP-19	Pioneer 10	Planetary	2-Mar-72	Successfully operated to Jupiter and beyond
SNAP-27	Apollo 16	Lunar	16-Apr-72	Successfully placed on lunar surface
TRANSIT-RTG	TRIAD-01-1X	Navigational	2-Sep-72	Successfully achieved orbit
SNAP-27	Apollo 17	Lunar	7-Dec-72	Successfully placed on lunar surface
SNAP-19	Pioneer 11	Planetary	5-Apr-73	Successfully operated to Jupiter, Saturn and beyond
SNAP-19	Viking 1	Mars	20-Aug-75	Successfully landed on Mars
SNAP-19	Viking 2	Mars	9-Sep-75	Successfully landed on Mars
MHW	LES 8/9	Communication	14-Mar-76	Successfully achieved orbit
MHW	Voyager 2	Planetary	20-Aug-77	Successfully operated to Jupiter and Saturn
MHW	Voyager 1	Planetary	5-Sep-77	Successfully operated to Jupiter and Saturn
GPHS	Ulysses	Solar	6-Oct-90	Successfully operated in solar orbit
GPHS	Galileo	Planetary	18-Oct-89	Successfully operated in Jupiter orbit
GPHS	Cassini	Planetary	15-Oct-97	Successfully operated in Saturn orbit
GPHS	New Horizons	Kuiper Belt	19-Jan-06	Operational - will reach Pluto July 14, 2015

Table 2.1. US spacecraft utilizing radioisotope thermal generators for onboard power

Early RTG devices produced in the US for spaceflight were developed under the SNAP Program. Figure 2.1 illustrates the construction of the SNAP-19 RTG, which powered the Viking 1 and Viking 2 Martian Landers and the Pioneer 11 and Pioneer 12 deep space probes [71].

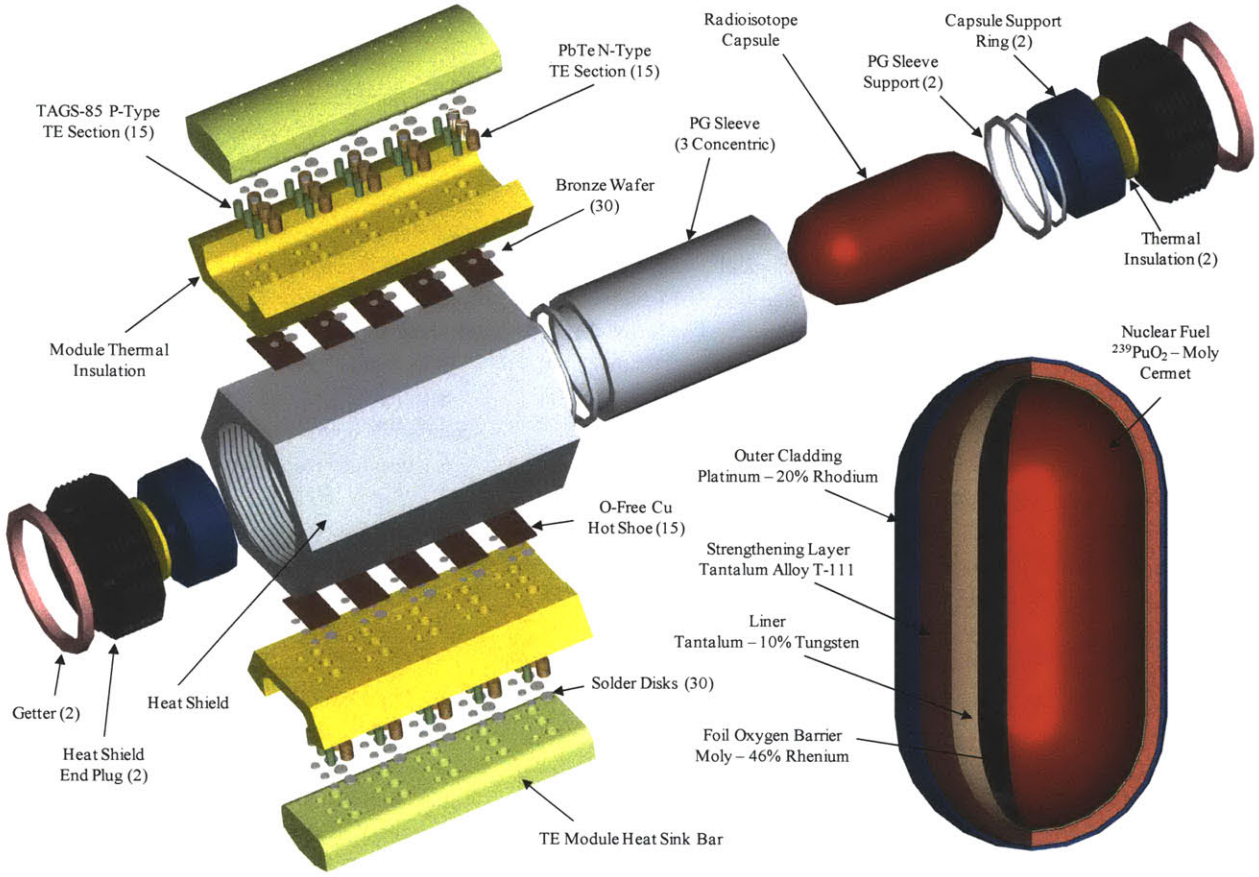

Figure 2.1. Composite construction of the SNAP-19 RTG and nuclear heat source; total mass of the SNAP-19 RTG was 14 kg; overall length is only 28 cm and diameter 51 cm.

In spite of their ruggedness and long lifetime, RTGs exhibit poor power scaling characteristics and are generally unsuitable for very high power electric propulsion applications. This is due in part to the relatively high mass of radioisotope contained in the heat source, somewhat lower operating temperatures than those typically encountered in a fission reactor, and the low conversion efficiency of thermoelectric sources in general. Recently, there has been renewed interest in the use of RTGs to power modest electric propulsion systems for small spacecraft with relatively long transit times [76, 77].

2.1.3 Space-Based Nuclear Power Plants

A nuclear reactor is a system that makes use of the thermal energy produced during controlled nuclear chain reactions in fissile material to produce electricity. In a fissile material, decay of the heavy nuclides results in the release of energy and additional neutrons following the absorption of a neutron by the nucleus. This sequence of events creates a potentially self-sustaining cycle called a chain reaction. The criticality of the process is a characterization of the neutron economy in such a system. In a sub-critical

reactor, less than one interacting neutron is produced in the fission process per neutron absorbed. In this case, the total number of available neutrons in the system will tend to decrease in each subsequent generation, eventually reaching zero. In a critical system, the number of interacting neutrons created is exactly equal to the number of neutrons absorbed, so that power is produced at a constant rate. Finally, in a super-critical system the total number of neutrons increases with each generation, so that the output power of the system increases exponentially with time [78]. A distinction should be drawn between super-critical and prompt-critical assemblies. In a super-critical system, reactor power may increase slowly with time, at a manageable rate. Periodic super-criticality is, in fact, required to increase the output power of a nuclear reactor at startup. In a prompt-critical system, on the other hand, the rate of increase in reactor activity is unmanageable, leading to core meltdown and a variety of catastrophic failure modes on very short timescales.

Historically the United States has trailed behind Russia in the application of nuclear fission reactors in spaceflight. The only US-built fission reactor to fly in space was the SNAP-10A, launched in 1965. After 43 days of operation, a spacecraft failure unrelated to the power plant forced an automatic shutdown of the reactor core and effectively terminated the mission. To date, the Russians have launched over thirty fission reactor systems, including the Romashka, Bouk, and TOPAZ reactor designs. All space nuclear power plants launched to date have used either thermoelectric or thermionic conversion to generate electrical power. While these direct energy conversion devices can be made very reliable because of their lack of moving parts, the efficiency and power output of such devices is somewhat limited. Since the 1970s, however, a great deal of progress has been made in improving thermionic converters in particular [79].

More recently in the US, programs like Project Prometheus have renewed interest in fission reactors for space application. Between March 2004 and March 2005, the US Department of Energy's Naval Reactors Division designed a gas-cooled Brayton cycle system to meet the Prometheus-1 Jupiter Icy Moons Orbiter (JIMO) mission requirements [80].

2.2 Impact on Mission Design

The design of space nuclear power plants has an enormous impact on the types of missions that can be efficiently conducted using this technology. For a given value of propulsive output power, allowable mission time, and spacecraft initial mass, a higher power plant specific power (kW/kg) will admit a higher allowable I_{SP}, and thus a higher overall mass fraction.

Returning to the data presented in Table 1.2 and Figure 1.3, we observe a general increase in the values of specific power obtainable as the reactor output power increases. As previously discussed, there is a broad consensus expressed in the literature on the near-term optimality of the potassium-Rankine

thermal conversion cycle in terms of maximizing specific power [62 - 66]. The ALKASYS program [81] developed at Oak Ridge National Laboratory provides a means for estimating the mass of potassium-Rankine power conversion systems used in conjunction with conventional pin-type fuel reactors. Use of this tool will provide a means of estimating the achievable specific power for a nuclear electric power and propulsion system.

2.3 ALKASYS-PC Software Package

The ALKASYS-PC software package is a tool designed to compute the performance and mass scaling of nuclear power plants using a potassium-Rankine thermal conversion cycle. In the sections that follow, a brief description of each of the five power plant design modules is given. The discussion in each section draws heavily from [81].

2.3.1 Reactor Model

The reactor assumed in the ALKASYS sizing is based on fast spectrum, conventional pin-type fuel assemblies using uranium nitride fuel pellets. Thermal transport from the reactor can be via direct boiling potassium or lithium primary circuit and secondary potassium boiler and is user selectable. The reactor design module of the ALKASYS software package requires the system lifetime, output power, turbine inlet and condensing temperature, and overall power conversion efficiency. The procedure used in defining the reactor configuration is illustrated in Figure 2.2 below.

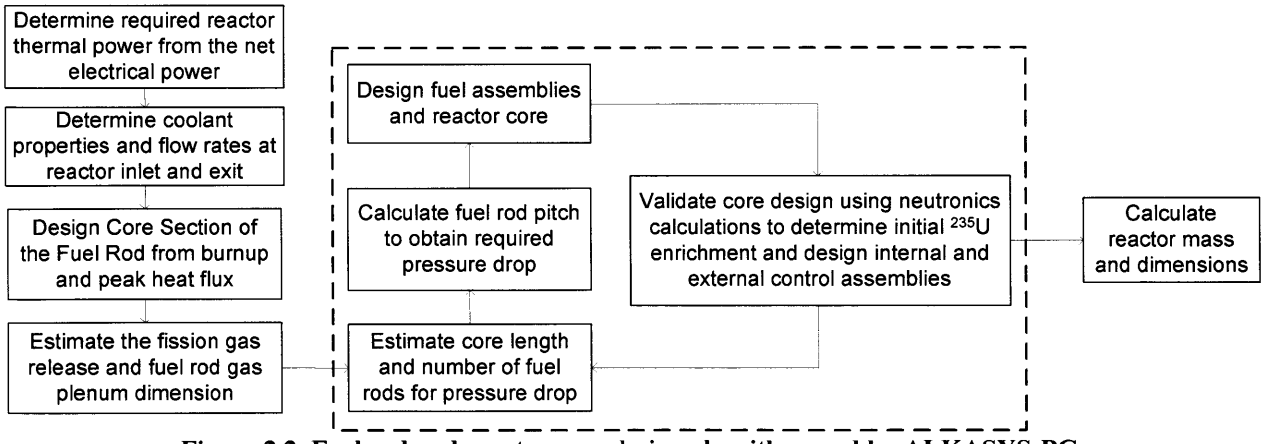

Figure 2.2. Fuel rod and reactor core design algorithm used by ALKASYS-PC

In the boiling potassium reactor, the required reactor thermal power can be computed from the thermal conversion efficiency:

$$P_t = P_e\left(\frac{1}{0.99}\right)\left(\frac{1}{\eta_r}\right) \quad \text{(Eq. 2.1)}$$

In this model it is assumed that 1% of the reactor thermal power is lost as heat. The thermal conversion efficiency accounts for the cycle and generator efficiencies:

$$\eta_r = \eta_c \eta_g \quad \text{(Eq. 2.2)}$$

In the second design step, the temperatures of the coolant entering and leaving the reactor can be determined from the turbine inlet temperature. For the boiling potassium reactor, the reactor inlet temperature is $T_{RX_i} = T_{BF}$, where T_{BF}, the boiler feed temperature, is known from the power conversion model. In a similar way, the temperature at the reactor outlet is $T_{RX_o} = T_{T_i}$, the turbine inlet temperature, an input parameter. These temperatures are used to compute the properties of the potassium working fluid, including pressure, density, viscosity, enthalpy and thermal conductivity. These properties are used to iteratively solve for the fuel rod pitch that gives a pressure drop across the reactor core which is equal to 3% of the saturation pressure corresponding to the turbine inlet temperature [82, 83].

In the next step, the section of the fuel rod containing the uranium nitride fuel pellets is evaluated. Peak pellet burn up is limited to 10%. The ratio of peak pellet burn up to average core burn up is denoted $\frac{pp}{a}$. For the relatively low powers of interest in this work, this ratio of pp/a is estimated using an empirical relation derived from SP-100 data [84]:

$$\frac{pp}{a} = \left(0.44356 - 1.612P_t \times 10^{-6} + \frac{85.83}{P_t}\right)^{-\frac{1}{2}} \quad \text{(Eq. 2.3)}$$

The ratio of peak rod burn up to average core burn up is estimated to be:

$$\frac{pr}{a} = \sqrt{\frac{pp}{a}} \quad \text{(Eq. 2.4)}$$

The peak pellet to average core burn up ratio is used to compute the maximum allowable rod diameter that will ensure the peak heat flux at the surface of the rod does not exceed 50 W/cm^2. The amount of heat flux at the surface of the rod can be expressed as:

$$\dot{q}'' = \frac{Q'''_{UN}\pi r_f^2 L}{L_{FP}\pi d_{pin} L} \quad \text{(Eq. 2.5)}$$

In this expression, $\dot{q}''$ is the surface heat flux, L_{FP} is the full power life time in seconds, r_f is the radius of the fuel pellet, L is the total fuel length, d_{pin} is the pin diameter, and Q'''_{UN} is the burn up limited energy

density of the UN fuel. This can be found from the fuel density, the burn up percentage, and the theoretical maximum energy density of UN fuel:

$$Q'''_{UN} = Q'''_{UN_{MAX}} \frac{\rho_f}{\rho_{f_{max}}} b \qquad \text{(Eq. 2.6)}$$

Here, the $Q'''_{UN_{MAX}} = 1.0963 \times 10^{12}$ J, the ratio of actual to maximum fuel density is taken to be 0.85, and b, the burnup fraction, is 10%. Rearranging Eq. 2.5, we find:

$$r_f^2 = \frac{\dot{q}'' L_{FP}}{Q'''_{UN}} d_{pin} \qquad \text{(Eq. 2.7)}$$

The pin diameter is given by:

$$d_{pin} = 2r_f + 2(t_C + t_W) \qquad \text{(Eq. 2.8)}$$

The clad and liner thicknesses given by t_C and t_W have values of 0.0635cm and 0.0127cm respectively. Finally, expanding Eq. 2.7, we obtain the quadratic equation:

$$r_f^2 - \frac{2\dot{q}'' L_{FP}}{Q'''_{UN}} r_f - \frac{2\dot{q}'' L_{FP}}{Q'''_{UN}} (t_C + t_W) = 0 \qquad \text{(Eq. 2.9)}$$

This can be solved to determine r_f and subsequently d_{pin}. The peak rod burn up is used to estimate the fission gas release and for fuel rod plenum sizing. Finally, the peak centerline temperature for the UN fuel is computed. The ALKASYS algorithm approximates the heat transfer as taking place through four media – conduction through the fuel, fuel-clad gap, clad-liner, and convection through the alkali metal coolant film to the fluid bulk. Conductivities and the heat transfer coefficient are assumed constant. Variations in the thermal profile of the fuel due to restructuring are neglected. Cast in terms of thermal resistances, then, the centerline temperature can be found:

$$T_{CL} = T_{BULK} + \dot{q}'' \left(\frac{r_f}{2k_f} + \frac{\ln\left(\frac{r_{pin} - t_C - t_W}{r_{pin} - t_C - t_W - t_g}\right)}{k_g} + \frac{\ln\left(\frac{r_{pin}}{r_{pin} - t_C - t_W}\right)}{k_C} + \frac{1}{h_K} \right) \qquad \text{(Eq. 2.10)}$$

Where k_f = 0.24 W/cm-K, k_g = 0.0047 W/cm-K, k_C = 0.57 W/cm-K, are the thermal conductivities of the fuel, gap and clad, and h_K = 5 W/cm^2-K, the heat transfer coefficient to the potassium coolant.

To determine the fission gas release and the required plenum volume, we must first determine the fractional fission gas release from the fuel rod with the highest burn up. This is accomplished using an empirical relation derived from data found in the literature [84, 85]:

$$FGR = 2.22 \times pr \left(\frac{T_{CL}}{1500}\right)^3 \quad \text{(Eq. 2.11)}$$

In this expression, T_{CL} is the peak fuel temperature. Statistically, 0.27 atoms of fission gas are produced per fission. Using this fact, coupled with the peak rod burn up, pr, the density of UN fuel, the coolant temperature at the reactor inlet, and fission gas release, we can apply the ideal gas law and allowable clad stress in the fuel rod to determine the amount of plenum volume required per unit volume of fuel in each rod.

In the final recursive step the core length-to-diameter ratio is estimated using an empirical function derived from literature data [84, 86]:

$$\frac{L}{D} = \begin{cases} 1 + \left(\frac{P_t}{30000}\right) \\ 2.5 \; Max \end{cases} \quad \text{(Eq. 2.12)}$$

Rod pitch is assumed to be 1.2 for the boiling potassium core. Next the preliminary core diameter and height are computed, along with the number of required fuel rods, and the lengths of the gas plenum, alumina reflectors and total rod length. Given these core parameters, the core physics is modeled to determine the required uranium enrichment. The details of the model used to compute the required enrichment are detailed in [55]. If the computed required uranium enrichment is greater than 99%, the burnup and full power life are adjusted, and the process iterates beginning with the computation of the fuel pin diameter. Finally, control drums and control fuel assemblies are designed, and the flux of fast neutrons (>1 MeV) to the walls of the pressure vessel is evaluated using empirical data [86].

The representative configuration for the fuel pins, fuel assemblies and reactor core design is given in Figure 2.3.

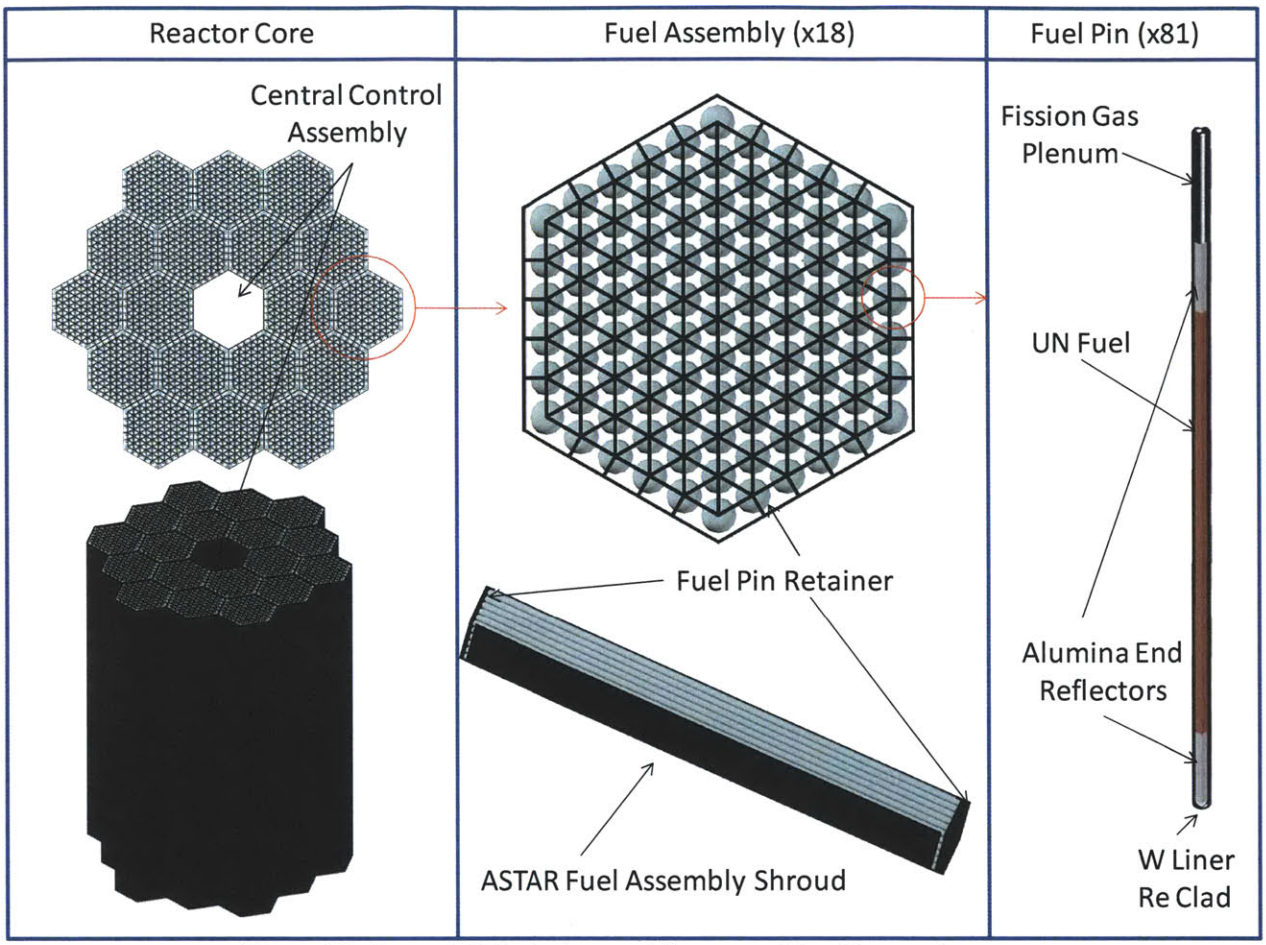

Figure 2.3. Layout of the fuel assemblies comprising the reactor core

2.3.2 Shield Model

The ALKASYS software package provides the user with the ability to select between two shield types in the design of a power plant. The first is a two-pi option in which the reactor assembly is encased in layers of lithium hydride and tungsten. The lithium hydride is cast in a honeycomb matrix of stainless steel. The shield is sized to provide a fast neutron fluence of 10^{13} n/cm^2 and a hard gamma dose of 10^6 rad at a plane located at a user-selectable distance from the reactor vessel.

The second shield option is a shadow shield. This option also provides for a layer of lithium hydride composite surrounding the reactor assembly, similar to the one found in the two-pi shield. In this case, however, the payload-facing radiation shield is designed to protect the payload from the effects of fast neutrons and gamma radiation. Gamma radiation shielding is provided by a layer of tungsten alloyed with molybdenum with a density of 18.6 kg/m^3. Shielding from fast neutron flux is provided by a layer of lithium hydride in a stainless steel honeycomb structure. The overall density of this layer is 1.024 kg/m^3. The shield is frustum-shaped, with the payload-facing surface the larger of the two bases. A simplified illustration of the shield configuration is shown in Figure 2.4 below.

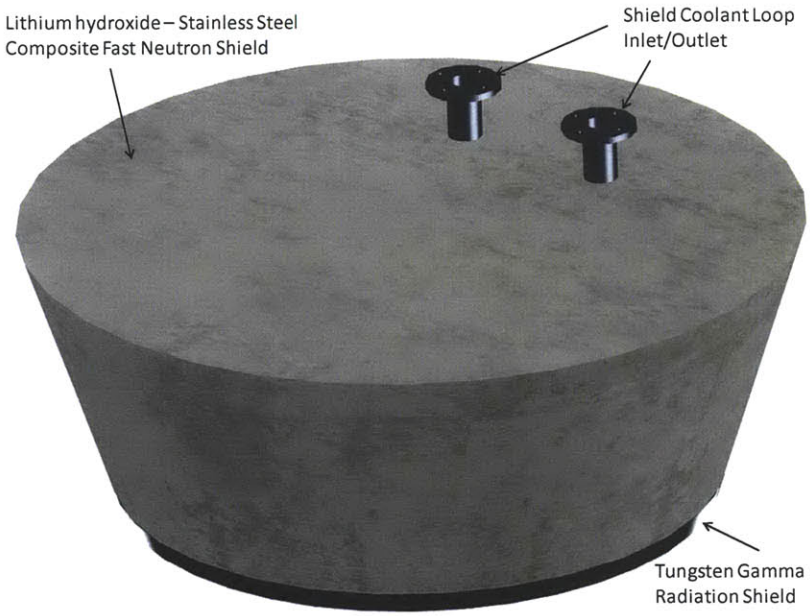

Figure 2.4. Fast neutron/gamma radiation shadow shield with integral cooling loop; reactor structural supports not shown.

One simple option for reducing the shield mass required to obtain the specified neutron fluence and gamma exposure is to provide a larger separation distance between the reactor and payload. To compute the required shield dimensions, the effects of fast neutron fluence, primary gamma dose and secondary gamma dose are incorporated. The expressions relating allowable radiation levels to required shield thickness are derived from correlations from the literature [87 - 89]. The thickness required to reduce the fast neutron fluence to the 10^{13} neutrons/m^2 over the lifetime of the power plant is given by:

$$t_W + t_L = 5.62 \ln\left(\frac{A_1 P_0 L_{FP} f_s}{4\pi r^2 n_v}\right) \quad \text{(Eq. 2.13)}$$

The expression restricting the limit on primary gamma dose is given by:

$$\rho_W t_W + \rho_L t_L = 25 \ln\left(\frac{A_2 P_0 L_{FP} f_s}{4\pi r^2 D_g}\right) \quad \text{(Eq. 2.14)}$$

Finally, accounting for secondary gamma dose gives:

$$\rho_W t_W + \rho_L t_L = 43.5 \ln\left(\frac{A_3 P_0 L_{FP} f_s}{4\pi r^2 D_g}\right) \quad \text{(Eq. 2.15)}$$

The factor f_s is the self-shielding factor. This describes the attenuation of radiation due to the structure of the reactor. The self-shielding factor is given by:

$$f_s = \frac{e^{(-0.02\rho_r t_r)} e^{-0.011\rho_V t_V}}{0.011\rho_C H_C} \qquad \text{(Eq. 2.16)}$$

The remaining factors used in modeling the shield are given in Table 2.2, below.

Constants			
ρ_W	Density of Tungsten Alloy	18.6	g/cm^3
ρ_L	Density of LiH-SS	1.024	g/cm^3
ρ_r	Density of Reflector Material	6.2	g/cm^3
ρ_V	Density of ASTAR-811C	16.84	g/cm^3
ρ_C	Average Core Density	8.2	g/cm^3
A_1	Fast Neutron Fitting Factor	2.41×10^{21}	neutrons/kW-yr
A_2	Prompt Gamma Fitting Factor	6.7×10^{12}	rads/kW-yr
A_3	Secondary Gamma Fitting Factor	1.0×10^{12}	rads/kW-yr
t_r	Thickness of Reflector	7.5	cm
Process Variables			
t_v	Thickness of Pressure Vessel		cm
H_C	Core Height		cm
Input Variables			
P_0	Reactor Thermal Power		kW
L_{FP}	Full Power Life		yr
r	Distance from Reactor to Dose Plane		cm
D_g	Gamma Dose at Dose Plane		rad
n_v	Fast Neutron Fluence at Dose Plane		$neutrons/cm^2$
Output Variables			
t_W	Thickness of Tungsten Alloy		cm
t_L	Thickness of LiH-SS		cm

Table 2.2. Constants and variables used in the ALKASYS shield modeling subroutine

Based on Eq. 2.13 - 2.15, at a given output power and full-power life the total shield thickness will decrease as the log of the inverse square of the shield-to-dose-plane separation distance. Shield masses for three values of output power at variable dose plane distances are plotted in Figure 2.5, below.

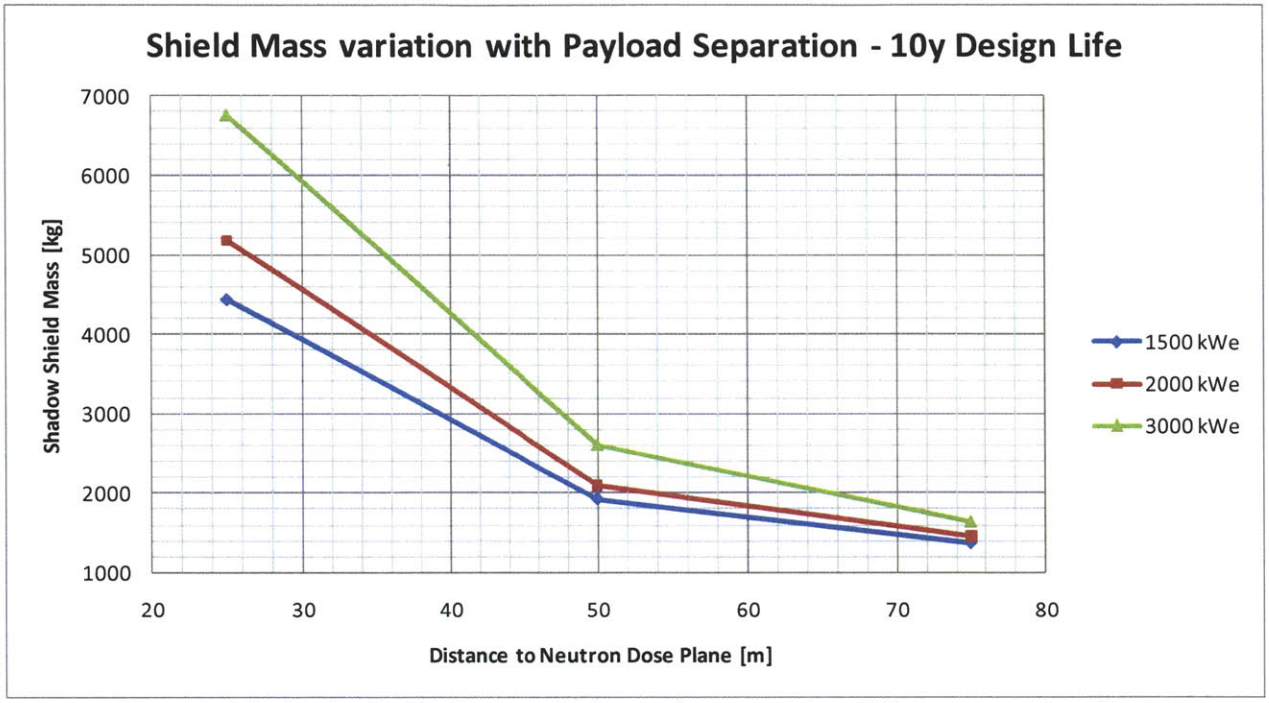

Figure 2.5. Reduction in shield mass with increasing separation of the reactor and payload

It is clear that one of the greatest barriers to development of nuclear power plants with very high specific power is launch vehicle packaging requirements. It may provide some insight, therefore, to develop two power plant mass models. The first is a baseline reactor configuration that is compatible with current launch vehicle packaging considerations. The second configuration assumes on-orbit construction, allowing for large double-sided radiator arrays and a much longer reactor separation boom.

2.3.3 Power Conversion Model

The power conversion system model is based on a Rankine cycle using potassium as the working fluid. The thermodynamic cycle analysis essentially consists of mass and energy balance around each of the components associated with the cycle. Condensed potassium is pressurized by a turbine driven fuel pump and driven into the reactor vessel. Heat addition takes place within the reactor, producing a mixture of saturated liquid and vapor at the reactor output with a nominal quality of 25%. Following a liquid-vapor separation stage, the primary vapor flow is expanded in a six-stage turbine assembly, which drives the system electric generator. Turbine modeling in ALKASYS is conducted largely in Imperial units and results are subsequently converted to metric. Required inputs to the turbine model are the turbine inlet temperature, the user-specified last stage tip velocity, and the isentropic efficiency of each turbine stage. Equal temperature drops across each turbine stage are imposed by the model, and a last-stage hub-to-tip ratio of 0.5 is assumed. Given the fluid properties at the last-stage exit, the resulting tip diameter is given by:

$$d_{TIP} = 25.95\sqrt{\frac{\dot{Q}_{LS}}{V_{TIP}}} \quad \text{(Eq. 2.17)}$$

This formulation is used by the algorithm and gives the tip diameter in inches provided the volumetric flow rate $\dot{Q}_{LS}$ has units of ft^3/s, and the tip velocity V_{TIP} has units of ft/s. The turboalternator rotational speed is:

$$\omega_T = 229.2\frac{V_{TIP}}{d_{TIP}} \quad \text{(Eq. 2.18)}$$

This rotational speed has units of revolutions/min. Next, using conceptual designs [64 - 66] of turbines for use with alkali metals, including potassium, the casing structure is taken to have a thickness of 2.5 inches. Given that the first stage rotor diameter is much smaller than the outlet rotor diameter, a conservative inlet rotor diameter allowance of $\frac{d_{TIP}}{2}$ is applied, so that the turbine inlet and outlet diameters are finally:

$$d_{T_{in}} = \frac{d_{TIP}}{2} + 5 \quad \text{(Eq. 2.19)}$$

$$d_{T_{out}} = d_{TIP} + 5 \quad \text{(Eq. 2.20)}$$

The overall length of the turbine is the sum of the length of each of the stages, L_{STG}, the bearing and end structure, L_{BRG}, the inlet and outlet passages, L_{IO}, and the external separator passages, L_{SEP}:

$$L_{TOT} = \sum_{i=1}^{6} L_{STG_i} + L_{BRG} + L_{IO} + L_{SEP} \quad \text{(Eq. 2.21)}$$

Again using a set of detailed conceptual designs [90 - 92], a model for each of these contributions is developed in [81]:

$$L_{STG} = 0.40 n_s P_{gen}^{0.25} \quad \text{(Eq. 2.22)}$$

$$L_{BRG} = 5 + 0.84 P_{gen}^{0.25} \quad \text{(Eq. 2.23)}$$

$$L_{IO} = 0.306\frac{\dot{Q}_{LS}}{d_{TIP}} \quad \text{(Eq. 2.24)}$$

$$L_{SEP} = 0.23\frac{\dot{Q}_{LS}}{d_{TIP}} \quad \text{(Eq. 2.25)}$$

In this model, n_s denotes the number of stages, and $P_{gen}^{0.25}$ is the power produced by the generator in kW. Given the machine inlet and exit diameters, and the total length, the mass model of the turbine is based on a superficial density applied to the resulting frustum volume. Based on the referenced turbine designs, the superficial density is taken to be 357 lb/ft^3 (5719 kg/m^3).

Next, the mass model of the alternator is developed. The alternator is assumed to be an induction-type. Its dimensions are estimated using an empirical database developed in a series of reports by Westinghouse under contract to NASA [93] for a large number of induction alternators. The allowable rotor diameter is found to be related to the maximum design stress of the rotor and the rotational speed:

$$V_R = \sqrt{\frac{\sigma_R}{0.356}} \qquad \text{(Eq. 2.26)}$$

In this empirical relation, the maximum design stress σ_r is taken as 32,000 psi, and V_R has units of m/s. Further, the rotor and stator outer diameters, respectively, are estimated as:

$$d_R = 32\frac{\sqrt{\sigma_R}}{\omega_T} \qquad \text{(Eq. 2.27)}$$

$$d_S = 39.4\frac{\sqrt{\sigma_R}}{\omega_T} \qquad \text{(Eq. 2.28)}$$

The generator output power is assumed to be proportional to the alternator volume and rotational speed:

$$P_{gen} = K d_S^2 L_S \omega_T \qquad \text{(Eq. 2.29)}$$

The length of the stator is given by L_S, with units of meters. The constant K is a constant of proportionality with units of kW-min/(m^3-rev). Typical values for this constant based on the previously referenced induction alternator dataset range from 0.53 – 1.26. In ALKASYS this value is taken as 1.0, and Eq. 3.29 can be used to solve for the stator length. The empirically determined superficial density is found to be ρ_{gen} = 3850 kg/m^3. Finally, adding an additional 20% to the mass implied by the dimensions above, we obtain the expression for the alternator mass in kg:

$$m_{alt} = 3628\frac{P_{gen}}{\omega_T} \qquad \text{(Eq. 2.30)}$$

The final major component mass estimated in the power conversion model is that of the centrifugal potassium feed pump and its associated drive turbine. A single empirically derived relation is used to model this component:

$$m_{FP} = 0.0953(\dot{m}_{FP}\Delta p)^{0.992} \qquad \text{(Eq. 2.31)}$$

In this relation, $\dot{m}_{FP}$ has units of lb/s, the pump head, Δp, has units of psi, and the resultant feed pump mass is given in pounds.

Additional masses, including those of the regenerative feed heaters, and piping runs are also computed in ALKASYS using simple geometric arguments, and, in the case of the piping runs, the maximum allowable liquid, vapor and mixture velocity inputs. In sum, these components constitute a relatively minor contribution to the overall plant mass, as can be seen in Tables 2.5 and 2.6 for the baseline and high-performance plant designs evaluated in this work.

2.3.4 Heat Rejection Subsystem Model

The baseline radiator design included in the ALKASYS software package assumes heat pipes constructed entirely of Nb-1% Zr with a user-defined thickness. Typical achievable areal mass densities for radiators using this construction are 15 – 18 kg/m^2. These very large areal densities are inconsistent with values typically found in flight articles such as the ISS HRS radiator system (13.4 kg/m^2) and the Swales Aerospace Alpha Radiator (5.6 kg/m^2) [94]. While the preceding examples operate at a much lower rejection temperature, detailed radiator modeling at the University of New Mexico for low power reactors (~100kW) indicates that single-sided areal mass densities of 6.8 – 7.1 kg/m^2 are achievable for high power applications [95]. Finally, researchers at NASA's Glenn Research Center have constructed and tested laboratory heat pipe articles with single-sided areal mass densities of 4.2 kg/m^2 [96-99]. Designs using high thermal conductivity, thermally annealed pyrolytic graphite appear to approach single-sided areal mass densities of 2.0 kg/m^2 [99]. These radiator concepts utilize potassium vapor as the heat pipe cooling medium, and operate at temperatures approaching 1000K, temperatures similar to those predicted for the cases under consideration in this work. In light of technological advances in the design and construction of these types of heat pipes, baseline radiator design will assume an areal mass density consistent with these values. Figure 2.6 illustrates the construction of an integrally woven heat pipe using a Nb-1% Zr liner and metal foil wick.

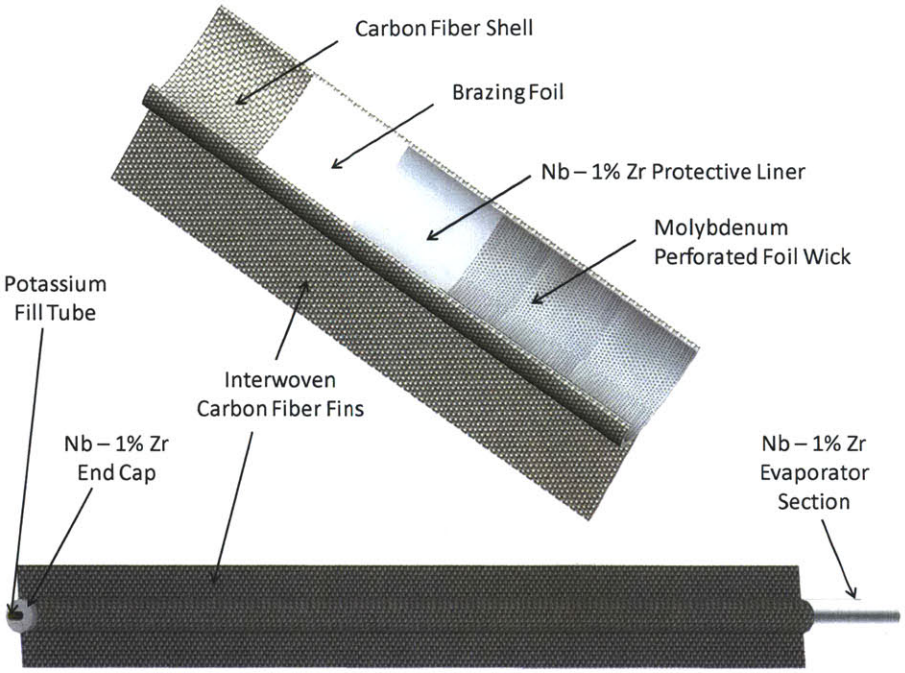

Figure 2.6. Configuration of a single heat pipe assembly assumed in the construction of lightweight radiators for use in high power nuclear electric power plants

Depending upon stowage requirements, packaging configurations, and method of deployment, a high power heat pipe radiator may be able to reject heat from one or both of its planar surfaces. Present launch systems preclude the design of large area radiators which reject heat from both surfaces due to limitations in payload volume. Systems developed to be compatible with present launch vehicle technology will necessarily utilize conical or conical-cylindrical radiator designs that may be considered to radiate from one surface only. However, future launch systems may allow for packaging large, two-sided radiator systems. Two-sided radiator systems have the advantage of effectively doubling the radiating area over single-sided systems, thereby reducing the required radiator mass by 50%. Figure 2.7 illustrates some single- and double-sided radiator systems in the deployed state.

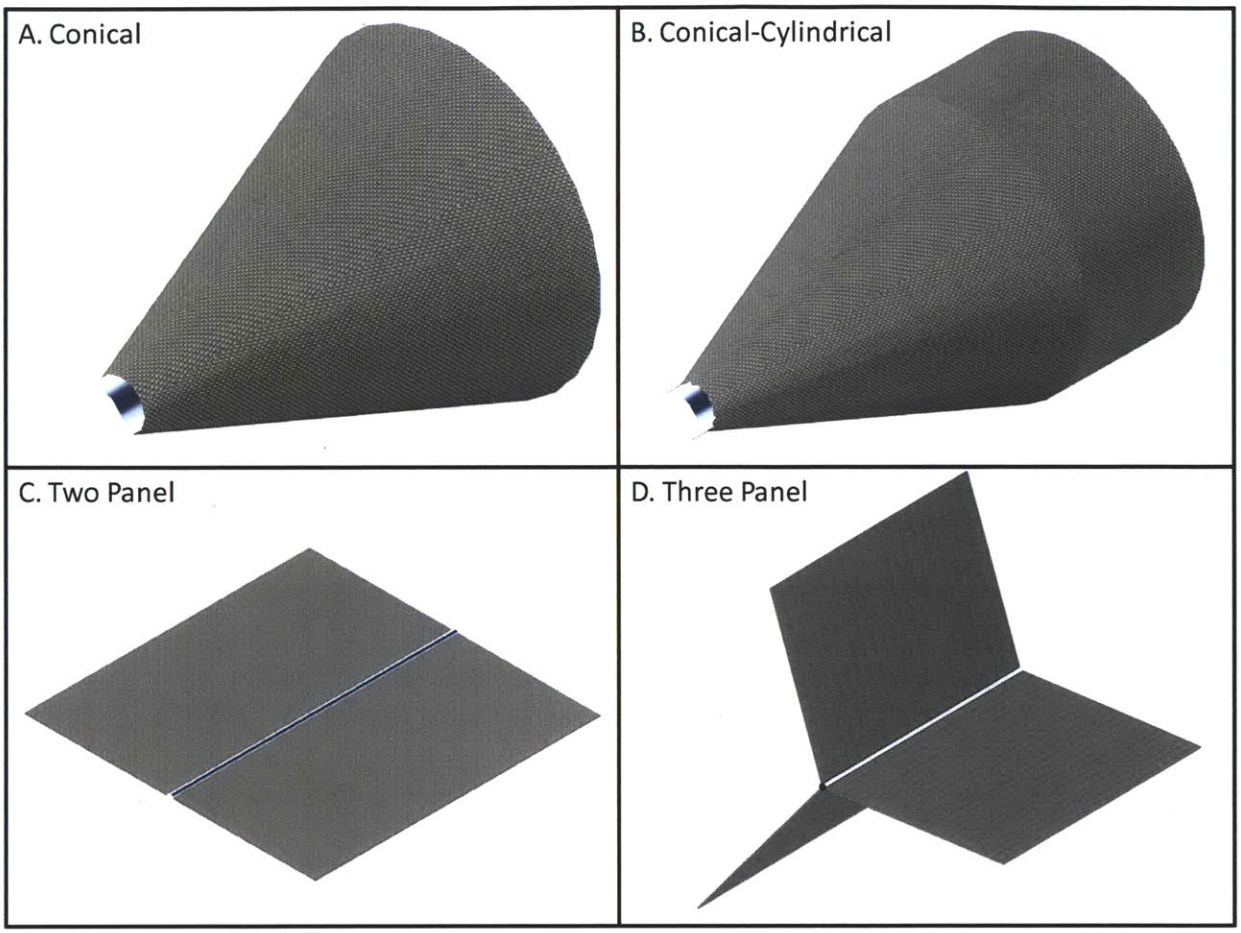

Figure 2.7. Deployed single- and double-sided radiator configurations

In the baseline design considered in this work, the radiator is assumed to radiate from one side only. The high-performance design incorporates a double sided radiator design.

2.3.5 Power Conditioning Model

In sizing the power conditioning equipment for the power plant, a simplified model is adopted in which PCU specific mass is assumed to be 4 kW_e/kg.

2.4 Near-Term Power Plant Design

The reactor component of the direct cycle potassium-Rankine cycle space-based power plant is designed to provide a potassium vapor quality of 25% at the output of the reactor vessel to provide some margin in preventing boiling crises and rod burn-up. Microgravity liquid-vapor separation hardware and a liquid recirculation jet pump are included in the reactor head. The reactor core is based on fast-

spectrum, metallic-clad fuel rod bundles comprised of UN pellets. Peak burn-up is constrained to be less than 10% and maximum heat flux is specified at less than 50 W/cm^2.

The baseline cycle design uses three recovery feed heater stages. Heater 1 exchanges heat between the reactor inlet stream and the feed pump drive turbine exit. Heater 2 extracts heat from either the primary vapor stream, or an early turbine stage in order to increase the feed stream temperature to satisfy the input value of boiler feed subcooling temperature. Finally, heater 3 uses vapor extracted from an intermediate turbine stage, as well as the drains from heater 1, and, in principle, fluid extracted from the turbine vapor separator to increase the feed stream temperature. Each of the heaters are modeled as simple tube-in-shell heat exchangers.

The power turbine uses both interstage and external separators to maintain a minimum vapor quality of 88% throughout the expansion in order to avoid excessive damage and erosion rates to turbine blades. In the baseline design, the turbine is comprised of six stages, with a maximum tip velocity of 304.8 m/s. Design decisions for turbine inlet conditions, and estimated dry stage efficiency are based on technological assumptions. In the baseline design, the turbine inlet temperature is specified at 1450 K, and the estimated dry stage efficiency is taken as 85%.

The primary feed from the condenser is provided by a turbine driven pump. The feed pump drive turbine tap from the main vapor feed is limited to a maximum of 12%. The exhaust from the feed pump drive turbine is then feed directly into the heater 1 heat exchanger, heating the primary feed. The flow diagram associated with this cycle description is given in Figure 2.8, below.

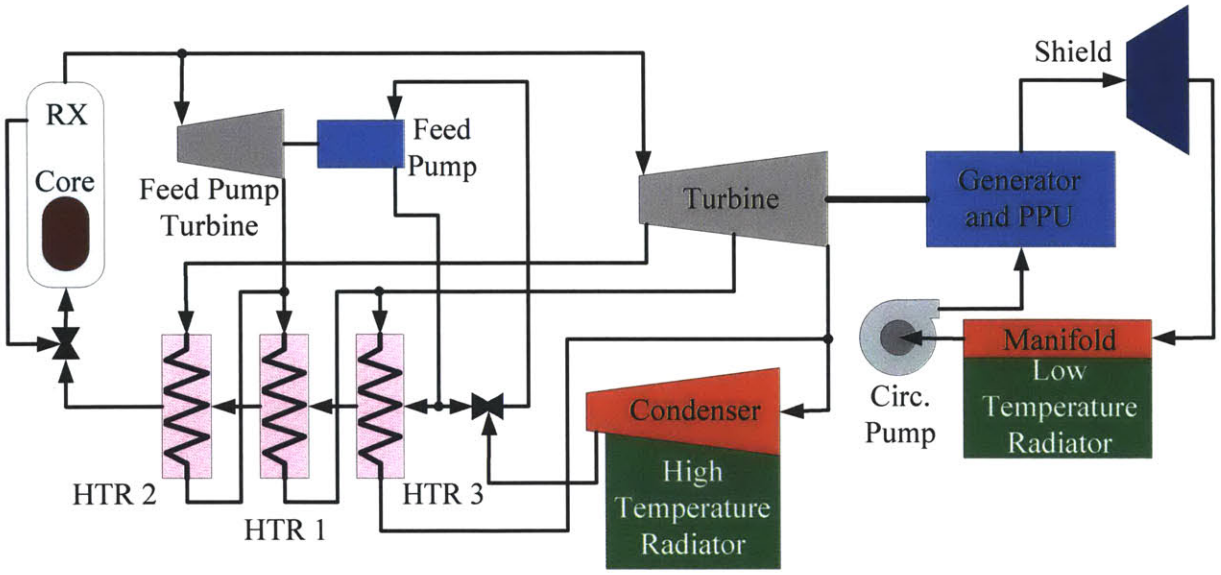

Figure 2.8. Simplified flow diagram for the baseline design of space power plant using a liquid metal-cooled direct Rankine cycle

The heat rejection subsystem is comprised of two radiators. The primary radiator is responsible for rejecting heat from the cycle, and operates at a higher temperature. The secondary, or low temperature radiator, is responsible for removing heat due to inefficiencies in the alternator and power processing unit. In the case of the baseline design, the high temperature radiator has a total heat load of 5565.5 kW_{th}, and a required rejection area of 154.8 m^2. The low temperature radiator has a total heat load of 151.1 kW_{th} at an average rejection temperature of 600 K, and corresponding required rejection area of 30.8 m^2. This baseline radiator is configured as a cylinder-cone, with a total conical length of 8.06 m, and a cylindrical length of 3.44 m.

Finally, the baseline power plant uses a shadow shield designed to reduce the lifetime fast neutral fluence and gamma radiation dose at a reactor-to-payload dose plane separation of 25 m, and a payload diameter of 15 m. This payload diameter corresponds to the diameter of the neutron shadow at the reactor-to-payload separation distance. The maximum allowable neutron fluence under these conditions is 10^{13} n/cm^2. The maximum allowable gamma radiation dose at the payload is 10^6 rad. The shield is comprised of layers of lithium hydroxide and tungsten. It has a maximum thickness of 0.55 m, a payload-facing diameter of 1.73 m, and a total mass of 3385 kg. Plant design data, output data and mass breakdown are provided in Tables 2.3-2.5, below.

System Level Inputs		
Reactor Type	Boiling Potassium	
Net System Electric Output	1500	kW_e
System Full Power Life	10	yr
Launch Bay Diameter	7.01 (23)	m (ft)
Launch Bay Length	22.01 (72.2)	m (ft)
Shield Design		
Shield Type	Shadow Shield	
Gamma Radiation Dose at Payload	10^6	rad
Fast Neutron Fluence at Payload	10^{13}	n/cm^2
Reactor-to-Dose Plane Distance	25 (82)	m (ft)
Diameter of Payload Dose Plane	15 (49.2)	m (ft)
Cycle Data		
Turbine Inlet Temperature	1450 (2610)	K (R)
Vapor Quality to Turbine	1.00	
Condensing Temperature	1025 (1845)	K (R)
Boiler Feed Subcooling	111.1 (200)	K (R)
Condenser Subcooling	5.55 (10)	K (R)
Feed Heater Terminal Temperature Difference	5.55 (10)	K (R)
Drain Cooler Terminal Temperature Difference	11.1 (20)	K (R)
Turbogenerator Design		
Number of Turbine-Generators in the System	1 + 1	
Turbine Dry Stage Efficiency	0.85	
Turbine Last-Stage Tip Velocity	304.8 (1000)	m/s (ft/s)
Generator Efficiency	0.95	
Turbine Exhaust Loss	11.6 (5)	kJ/kg (btu/lb)
PPU Specific Power	4 (2.42)	kW/kg (hp/lb)
Pump Design		
Fraction of Gross Electrical Output for Li EM Pump	Not Applicable	
Condenser Jet Pump Flow Ratio (Suction/Driving)	4.00	
Temperature Drop Through Pump Drive Turbine	194.4 (350)	K (R)
Feed Pump Drive Turbine Efficiency	0.70	
Feed Pump Efficiency	0.60	
Feed Heater Design		
Number of Stages of Regenerative Feed Heating	3	
Feed Heater Tube Outer Diameter	6.35 (0.25)	mm (in)
Feed Heater Tube Wall Thickness	0.508 (0.02)	mm (in)
Piping Design		
Flow Velocity in Vapor Lines	137.2 (450)	m/s (ft/s)
Flow Velocity in Wet Mixture Lines	30.5 (100)	m/s (ft/s)
Flow Velocity in Liquid Lines	3.1 (10)	m/s (ft/s)
Radiator Design		
Radiator Overall Areal Mass Density	4.00	kg/m^2 (lb/ft^2)
Low-Temperature Radiator Temperature	600 (1080)	K (R)

Table 2.3. Design data for potassium Rankine cycle space reactor power system

Cycle Data		
Thermal Input	7144.5	kW_{th}
Cycle Efficiency	0.221	
Plant Efficiency	0.210	
Main Vapor Flow	4.08 (8.97)	kg/s (lb/s)
Reactor		
Reactor Thermal Power	7216.6	kW_{th}
Core Inlet Pressure	1623.7 (235.5)	kPa (psia)
Core Outlet Pressure	1576.8 (228.7)	kPa (psia)
Core Inlet Temperature	1338.9 (2410)	K (R)
Peak Fuel Centerline Temperature	1549.2 (2788.6)	K (R)
Shield		
Shield Outside Diameter - Front	1.73 (5.68)	m (ft)
Shield Outside Diameter - Core	0.86 (2.82)	m (ft)
Maximum Shield Thickness	0.55 (1.8)	m (ft)
Turbogenerator		
Number of Turbine Stages	6	
Turbine Diameter at Inlet	0.234 (.768)	m (ft)
Turbine Diameter at Outlet	0.34 (1.12)	m (ft)
Turbine Length	0.726 (2.38)	m (ft)
Machine Speed	2861.6 (27326)	rad/s (rpm)
Generator Losses	78.95	kW_{th}
Feed Pump Power	31.22	kW_e
Feed Pump Flow	5.1 (11.21)	kg/s (lb/s)
Radiator		
High Temperature Radiator Load	5565.5	kW_{th}
Low Temperature Radiator Load	151.1	kW_{th}
High Temperature Radiator Area	154.8 (1666.3)	m^2 (ft^2)
Low Temperature Radiator Area	30.8 (331.5)	m^2 (ft^2)
Radiator Conical Length	8.06 (26.5)	m (ft)
Radiator Cylindrical Length	3.44 (11.28)	m (ft)
Maximum Radiator Diameter	7.01 (23)	m (ft)

Table 2.4. Plant output data

Reactor		
Core Hardware	1017.2	kg
Coolant in Reactor	76.4	kg
Pressure Vessel	681.3	kg
Drums and Radial Reflector	205.7	kg
Reactor Total Mass	1980.6	kg
Shield		
Shield Total Mass	3385	kg
Turbogenerator		
Turbine	544.5	kg
Generator	199.1	kg
Feed Pump and Turbine	161.7	kg
Feed Heater	14.2	kg
Piping	32.0	kg
Turbogenerator Subsystem Total Mass	951.6	kg
Radiator		
Vapor Header	11.6	kg
Liquid Header	2.5	kg
Nipple	90.8	kg
Heat Pipe	742.3	kg
Radiator Total Mass	847.2	kg
Power Processing Unit		
Power Processing Unit Total Mass	375.0	kg
Total Power Plant Mass	7539.3	kg
Power Plant Specific Power	0.199	kW/kg
Power Plant Specific Energy	1.990	kW-yr/kg

Table 2.5. Overall power plant mass mapping

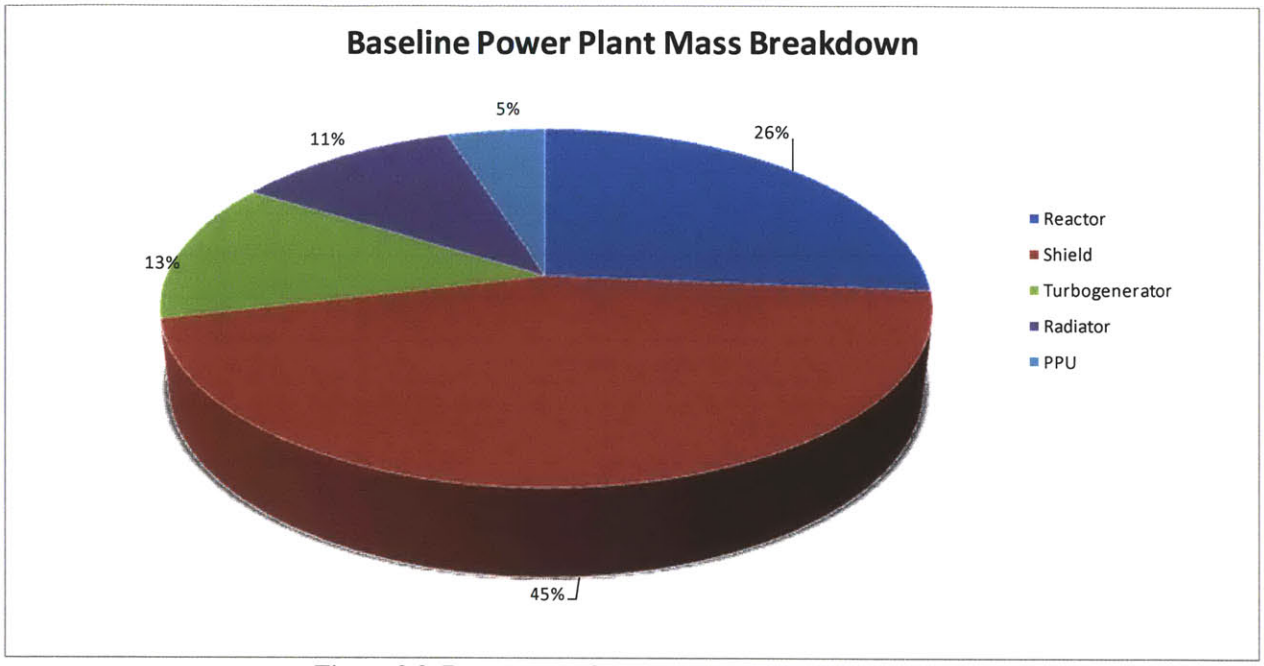

Figure 2.9. Percentage of total plant mass by subsystem

2.5 Advanced Power Plant Design

In modeling the design of the medium- to far-term advanced power plant configuration, three key modifications from the near-term configuration are assumed:

- Reactor-payload boom separation increased to 75 m
- Radiator areal mass density based on double-sided radiation (2 kg/m^2)
- High-reliability single turbogenerator system

These assumptions for advanced power plant construction have the advantages of requiring no new technological developments, with the possible exception of increased turbogenerator reliability. Additional advances in minimizing reactor mass, lightweight electronics for power processing, and dual-use of propellant tanks and spacecraft structures to further reduce neutron and gamma shielding requirements will almost certainly provide avenues for additional mass reductions. However, these improvements will likely require improvements in manufacturing and modeling prior to implementation.

The relevant changes in the design variables and resulting subsystem masses are given in Table 2.6 and Figure 2.10, below.

Reactor		
Core Hardware	1017.2	kg
Coolant in Reactor	76.4	kg
Pressure Vessel	681.3	kg
Drums and Radial Reflector	205.7	kg
Reactor Total Mass	1980.6	kg
Shield		
Reactor To Dose Plane Separation Distance	75	m
Shield Total Mass	1128	kg
Turbogenerator		
Number of Turbine-Generators in the System	1 + 0	
Turbine	272.3	kg
Generator	99.6	kg
Feed Pump and Turbine	161.7	kg
Feed Heater	14.2	kg
Piping	32.0	kg
Turbogenerator Subsystem Total Mass	579.8	kg
Radiator		
Vapor Header	11.6	kg
Liquid Header	2.5	kg
Nipple	90.8	kg
Heat Pipe	371.1	kg
Radiator Heat Pipe Areal Density	2.0	kg/m^2
Radiator Total Mass	476.0	kg
Power Processing Unit		
Power Processing Unit Total Mass	375.0	kg
Total Power Plant Mass	4539.5	kg
Power Plant Specific Power	0.330	kW/kg
Power Plant Specific Energy	3.304	kW-yr/kg

Table 2.6. Overall advanced power plant mass mapping; changes to baseline reactor technology assumptions highlighted

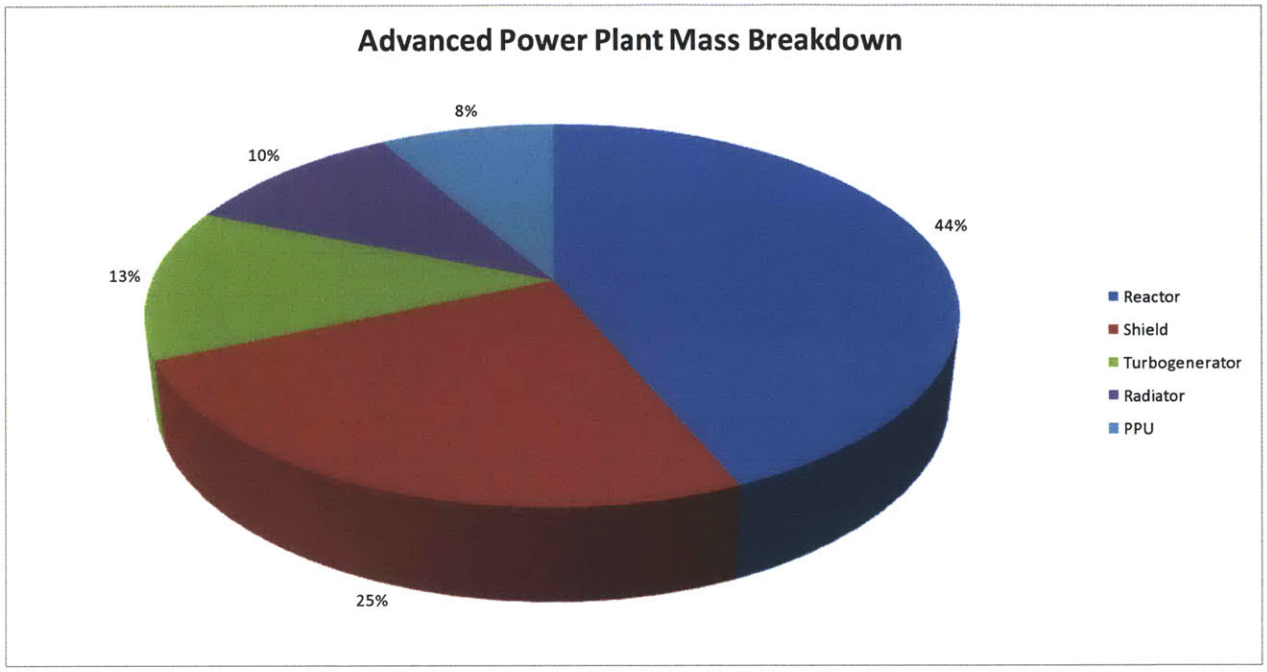

Figure 2.10. Percentage of advanced plant mass by subsystem

2.6 Conclusions

In conclusion, by drawing upon extant test and development data for power conversion systems based on alkali metal working fluids in conjunction with fast spectrum reactors, it appears possible to develop space-based nuclear power systems with specific powers between 0.2 – 0.3 kW_e/kg. The baseline system considered in this work was designed to produce an output power of 1.5 MW_e with a full-power lifetime of ten years. These capabilities are compatible with the mission-level needs derived for near-term missions enabled by the use of high power nuclear electric propulsion systems.

Chapter 3

Mission Analysis

3.1 Introduction

Having developed estimates for the achievable specific power of near- to medium-term space nuclear power plants, one can proceed to develop preliminary mission models that incorporate such power systems for use with electric propulsion systems. In an effort to appropriately gauge the propulsive needs of mission designers and systems engineers involved in the development of advanced missions using high power nuclear electric propulsion systems, several missions of interest are developed and modeled using the Mission Analysis Low Thrust Optimization (MALTO) software package developed by NASA JPL [67-69]. The optimized propulsion system performance metrics derived from this mission analysis can then be used to effectively inform the design of these future power and propulsion systems [70].

3.2 Approach

In developing power and propulsion systems to make use of abundant electrical power, a necessary first step is the development of representative requirements around which these systems should be designed. For the propulsion system, the relevant requirements are the total propulsive output power, thrust, specific impulse, and thruster lifetime. Similarly for the power system, the important parameters are the power system specific power, the total output power and the required lifetime.

Representative values for these performance metrics are fundamentally driven by the types of missions that will be enabled or enhanced by these systems. Using this rationale, several missions of interest were

modeled using MALTO. Each of these missions is derived from mission concepts previously studied by NASA or ESA [100-105], and each is sufficiently demanding in terms of propulsive requirements that nuclear electric propulsion would be either mission enhancing or mission enabling.

The MALTO software package is a medium-accuracy trajectory design tool used to perform initial evaluation of mission concepts. Low thrust trajectories are divided into a large number of finite segments, and the thrust profile is approximated by a series of impulsive maneuvers which occur at the midpoint of each segment. Additionally, in constructing trajectory solutions the only gravitational field modeled by MALTO is the field due to the central body. For example, in modeling the interplanetary trajectories considered in this work, which use spiral escapes and captures around departure and rendezvous targets, MALTO will neglect the gravitational effects these bodies except during the capture and escape maneuvers.

MALTO can perform several types of optimizations, and make use of several optimization variables. The following optimizations are available using MALTO:

- Maximize final spacecraft mass for a specified initial mass and constrained mission time
- Minimize initial spacecraft mass for a fixed final mass and constrained mission time
- Minimize total trip time based on constraints on initial and/or final mass
- Optimize a weighted combination of final mass and trip time
- Minimize total ΔV subject to constrained mission times and/or spacecraft initial/final mass

For all the cases considered in this work, the reactor power is constant during a particular run. In conducting these optimizations, MALTO is able to take advantage of several optimization variables:

- Encounter Time
- Spacecraft Mass at Encounter
- Stay Times at Rendezvous Body
- Arrival and Departure V_∞
- States at Non-Body Control Points
- Specific Impulse
- Thrust/ΔV Profile
- Reference Power

Finally, based on the needs of the mission designer, mission goals, and real world constraints, MALTO is able to incorporate several constraints into its mission models:

- Flight Times
- Propellant Mass
- Launch and Arrival V_∞
- Distance from the Central Body
- Initial Mass Dictated by Launch Vehicle Model
- Flyby Altitude, Angle

The optimization engine used by MALTO is the SNOPT optimization code [106]. The SNOPT code is a parametric optimization program based on a sequential quadratic programming algorithm.

A product of the mission models developed in this work is the optimum specific impulse at which the mission might be accomplished. This is one of the key requirements that must be developed to inform the design of future electric propulsion thrusters for high power. In each case, we can compare the numerically derived optimum specific impulse to that obtained using the approximate Stuhlinger optimization introduced in Chapter 1. Returning to Eq. 1.16, the mass fraction corresponding to the optimum case for a given mission ΔV can be found:

$$\left.\frac{M_f}{M_0}\right|_{OPT} = e^{-\frac{\Delta V}{c_{opt}}} \qquad \text{(Eq. 3.1)}$$

Expanding Eq. 1.10 to include optimum specific impulse and mass characteristics as well as the required thrusting time, we can express:

$$P_{in} = \frac{M_0\left(1 - e^{-\frac{\Delta V}{c_{opt}}}\right)}{2\eta t}\left(\sqrt{2\eta\alpha t} - \frac{1}{2}\Delta V - \frac{1}{24}\frac{\Delta V^2}{v_{ch}}\right)^2 \qquad \text{(Eq. 3.2)}$$

This can be equivalently expressed in terms of the spacecraft final mass:

$$P_{in} = \frac{M_f\left(e^{\frac{\Delta V}{c_{opt}}} - 1\right)}{2\eta t}\left(\sqrt{2\eta\alpha t} - \frac{1}{2}\Delta V - \frac{1}{24}\frac{\Delta V^2}{v_{ch}}\right)^2 \qquad \text{(Eq. 3.3)}$$

It is clear that if the required velocity increment for a given mission does not vary a great deal during optimization, and the input power is specified this analysis can provide a check on the propulsion system

Finally, based on the needs of the mission designer, mission goals, and real world constraints, MALTO is able to incorporate several constraints into its mission models:

- Flight Times
- Propellant Mass
- Launch and Arrival V_∞
- Distance from the Central Body
- Initial Mass Dictated by Launch Vehicle Model
- Flyby Altitude, Angle

The optimization engine used by MALTO is the SNOPT optimization code [106]. The SNOPT code is a parametric optimization program based on a sequential quadratic programming algorithm.

A product of the mission models developed in this work is the optimum specific impulse at which the mission might be accomplished. This is one of the key requirements that must be developed to inform the design of future electric propulsion thrusters for high power. In each case, we can compare the numerically derived optimum specific impulse to that obtained using the approximate Stuhlinger optimization introduced in Chapter 1. Returning to Eq. 1.16, the mass fraction corresponding to the optimum case for a given mission ΔV can be found:

$$\left.\frac{M_f}{M_O}\right|_{OPT} = e^{-\frac{\Delta V}{c_{opt}}} \qquad \text{(Eq. 3.1)}$$

Expanding Eq. 1.10 to include optimum specific impulse and mass characteristics as well as the required thrusting time, we can express:

$$P_{in} = \frac{M_0\left(1 - e^{-\frac{\Delta V}{c_{opt}}}\right)}{2\eta t}\left(\sqrt{2\eta\alpha t} - \frac{1}{2}\Delta V - \frac{1}{24}\frac{\Delta V^2}{v_{ch}}\right)^2 \qquad \text{(Eq. 3.2)}$$

This can be equivalently expressed in terms of the spacecraft final mass:

$$P_{in} = \frac{M_f\left(e^{\frac{\Delta V}{c_{opt}}} - 1\right)}{2\eta t}\left(\sqrt{2\eta\alpha t} - \frac{1}{2}\Delta V - \frac{1}{24}\frac{\Delta V^2}{v_{ch}}\right)^2 \qquad \text{(Eq. 3.3)}$$

It is clear that if the required velocity increment for a given mission does not vary a great deal during optimization, and the input power is specified this analysis can provide a check on the propulsion system

specific impulse and firing time metrics derived in the subsequent sections. A comparison of the optimum specific impulse figures obtained in this work with the Stuhlinger optimum is provided in Section 3.4. Additional discussion is also provided for the case of the Saturn Transit Stage, which attempts to explore the utility of NEP for enabling ambitious outer planets missions with relatively small launch vehicles.

Development of input files for MALTO is most easily accomplished using a Matlab-based graphical user interface (GUI). The main control panel of the GUI is shown in Figure 3.1, below.

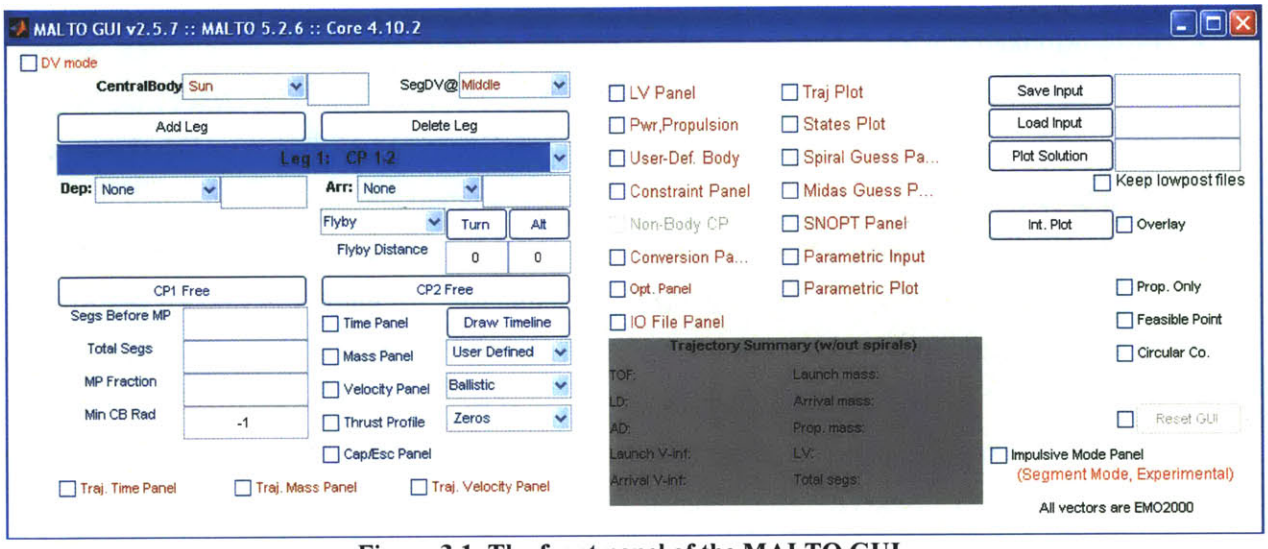

Figure 3.1. The front panel of the MALTO GUI

Missions may be developed in segments that occur between two user defined control points. Generally these control points will be various solar system bodies of interest, but non-body control points may also be defined. Leg-specific inputs and input panels in the GUI are represented in blue, and trajectory-specific inputs are shown in red. Input panels are accessed from the top-level GUI shown above by checking the boxes corresponding to the desired panel.

When constructing a mission for simulation, the user first specifies the desired mission central body. An important limitation to the version of MALTO used in this work is that the mission central body may not be changed for different legs of a given mission. This means that a mission beginning in Earth orbit, for example, to objects in orbit around solar system bodies other than the sun cannot be developed using a single MALTO input file. In this work these types of missions are explored using two or more input files. First, an optimized trajectory from Earth to a specified orbit around the target planet is generated. A new input file and new MALTO run is then generated in which the target planet is the specified central body. In this new case, the initial state of the spacecraft is specified at a non-body control point corresponding to the final state as set in the first case, the Earth-Target transfer trajectory.

The next step in mission construction is to specify the departure and arrival control points. Using ephemeris data for all cataloged objects, any numbered solar system body may be specified as a control point. Given a departure and arrival body, the user may then specify whether the spacecraft should perform a flyby or rendezvous at the destination. Inputs to the Cap/Esc panel are used to specify the initial and final orbits around the departure and arrival bodies respectively. The Cap/Esc input panel is shown in Figure 3.2.

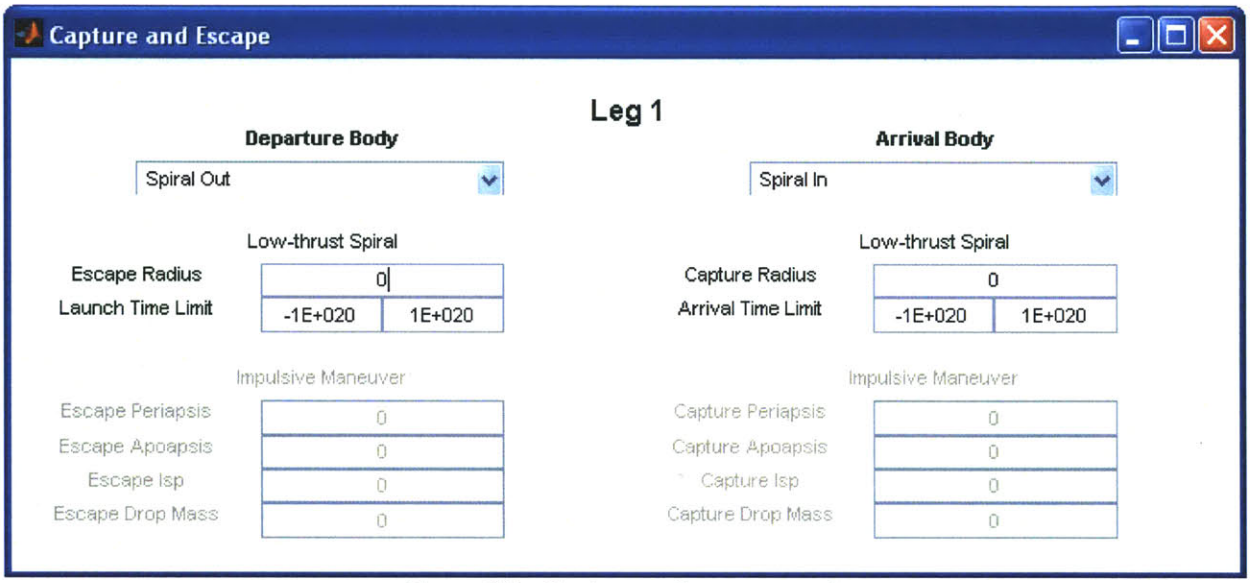

Figure 3.2. Capture and escape panel

The leg-specific time, mass, and velocity panels, shown in Figure 3.3 below, allow the user either to fix, or to place upper and lower constraining bounds on each of these variables in turn. With the exception of the interstellar precursor trajectory, the missions developed in this work assume low thrust spirals out from the Earth, and spirals into various orbits around the target body. In these cases the arrival and departure velocities are identically zero.

Figure 3.3. The leg-specific time, mass and velocity input panels

It is also possible to program the time, mass and velocity variables using the trajectory-specific time, mass and velocity panels, tagged in red at the bottom left of the main GUI panel. This is especially useful for trajectories consisting of several legs.

The user must specify the number and distribution of segments with which MALTO should approximate the low thrust trajectory using the three inputs near the bottom left of the main panel of the GUI. Because low thrust trajectories in MALTO are approximated by impulsive maneuvers on each segment, increasing the number of segments for a given trajectory will tend to increase the fidelity of the solution. However, for each additional segment on a given trajectory, MALTO must compute the three components of the spacecraft thrust vector on that segment. This means that increasing the number of segments in a simulation will tend to increase the simulation run time.

Finally, the two columns of trajectory specific input panels in the right central portion of the GUI offer additional control and simulation options for creating missions of interest. The LV panel allows the user to specify a particular launch vehicle for the spacecraft, effectively imposing constraints on the initial

mass in low-Earth orbit (IMLEO) and the hyperbolic excess velocity at departure. User defined bodies may be specified by entering the relevant ephemeris data in the User-Def. Body Panel. The Constraint panel offers a simple way of entering constraints on mission execution times and propellant mass. These three panels are shown in composite in Figure 3.4.

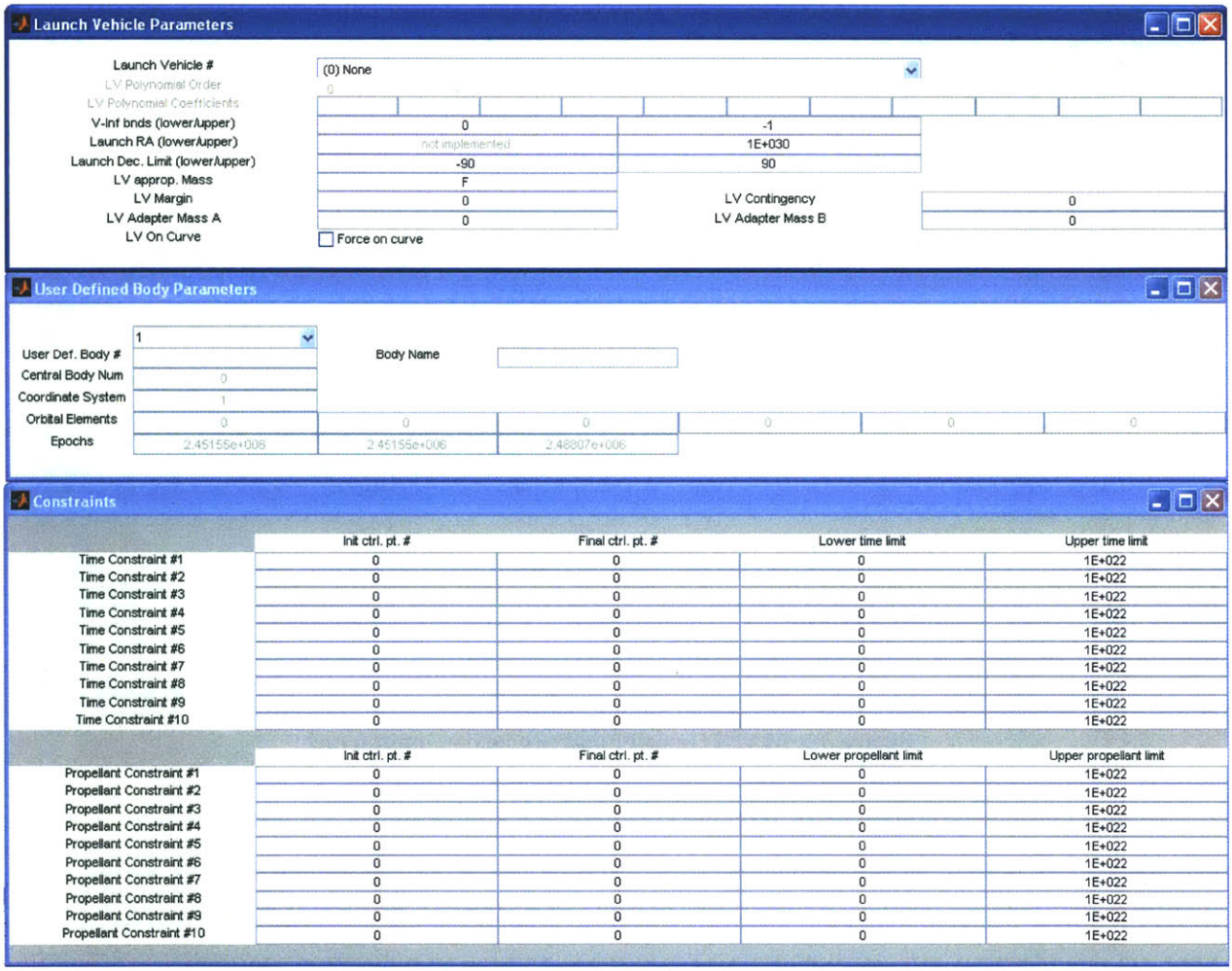

Figure 3.4. Launch vehicle, user-defined body and mission constraints panels

The Optimization panel allows the user to specify the type of optimization MALTO will perform. Options for the type of optimization are those included in the bulleted list above. The last panel of interest from this group is the SNOPT Panel. In order to run, the SNOPT engine requires an input file, SNOPTA_SPECS. This file provides the optimizer with important information including iterations limits, as well as feasibility and optimality tolerances. The SNOPT panel provides the user with a panel to create and modify the SNOPTA_SPECS file.

The PWR/Propulsion panel, shown in Figure 3.5, below is of particular interest for the application considered in this work.

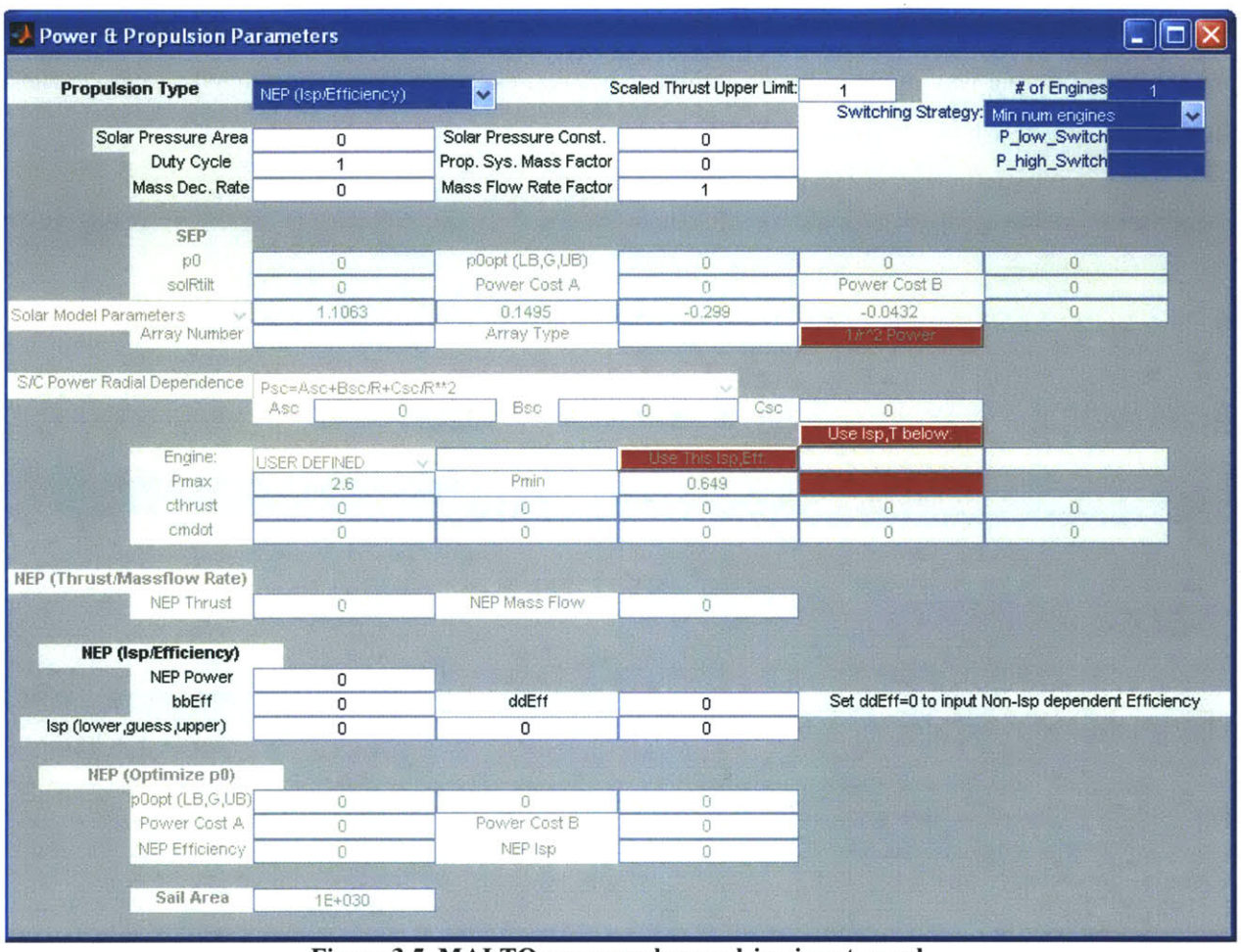

Figure 3.5. MALTO power and propulsion input panel

The user must specify the type of propulsion system that will be used for a given mission. Missions may use solar or nuclear electric propulsion (SEP or NEP), as well as solar sail propulsion. In the case of an SEP system, the user may opt to specify both the initial power and the specific impulse, or have MALTO compute an optimum initial power based on a power cost function. In the case of an NEP system, the user may opt to fix thrust and mass flow rate, and therefore output power and specific impulse. Alternatively, one may fix the output power and have MALTO compute a mission-optimal I_{SP}, or one may fix the I_{SP} and have MALTO compute a mission optimal output power level based on a power cost function. For the missions considered in this work, the NEP power and system efficiency were specified, allowing MALTO to compute the mission optimal I_{SP}. These optimal exhaust velocities are then included in the list of mission level requirements detailed in the concluding section of this chapter. In all cases the efficiency was specified as unity. This effectively fixes the system output power. The input power and the required mass of the nuclear power plant will depend on the propulsion system efficiency, which may be unknown. In establishing the mass budget for each of the missions outlined

below, a conservative margin is included to account for additional reactor mass required to produce the additional power to offset these inefficiencies.

There are several additional trajectory specific input panels in Figure 3.1, including the Conversion panel, IO panel, and various plotting and visualization tools. These are generally somewhat less useful in constructing the missions developed in this work.

In the sections that follow, this tool is used to generate models for several missions of interest. Each of these is discussed in detail below. Results of this analysis and a summary of derived requirements are then outlined.

3.3 Mission Models

Five mission models have been developed in this work. Each is based on studies by one or more national space agencies that would have used conventional chemical propulsion systems, or, in the case of the Galilean Satellites Orbiter and the Neptune Orbiter, Probe and Triton Lander, 100 kW-class nuclear propulsion.

3.3.1 Galilean Satellites Orbiter

The Galilean Satellites Orbiter mission architecture is similar to the proposed Jupiter Icy Moons Orbiter (JIMO) mission developed by NASA in 2003-2005 under Project Prometheus [100]. The conceptual mission would place a scientific payload into the orbit of each of the Galilean satellites in succession, for a stay time of approximately one year per satellite. This mission architecture is somewhat more ambitious than that proposed for the JIMO spacecraft, as a one year stay around the innermost satellite, Io, is also included. The trajectory and timeline for the mission are given in Figures 3.6 and 3.7, below.

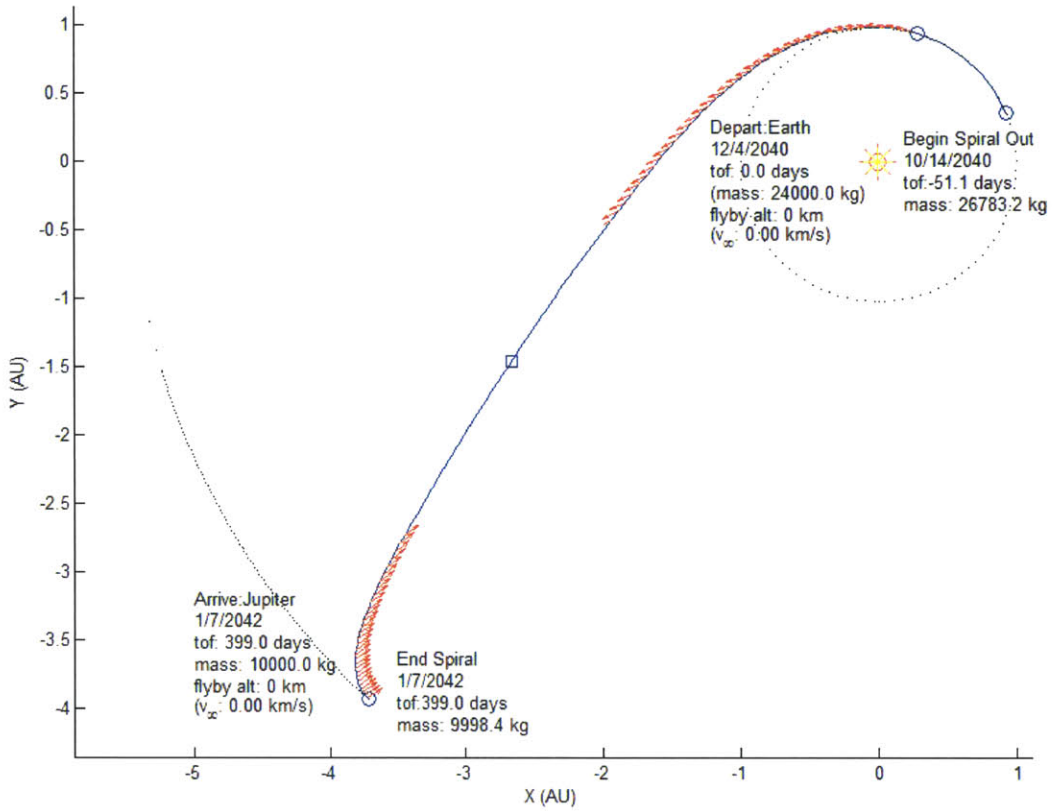

Figure 3.6. Earth-Jupiter transfer trajectory for the Galilean Satellites Orbiter mission

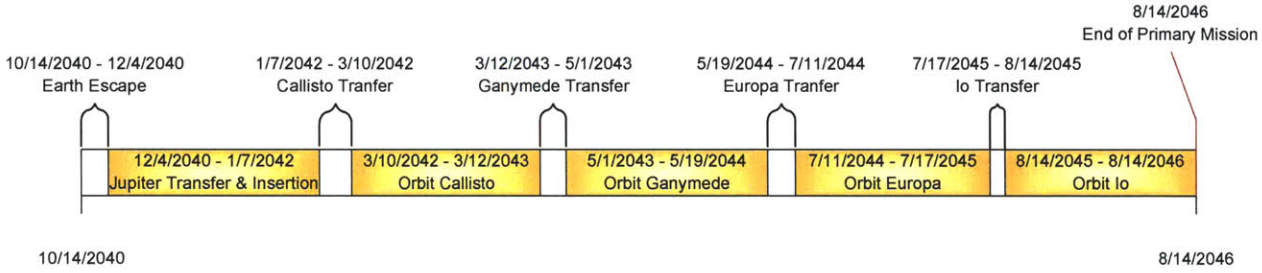

Figure 3.7. Timeline for the optimized Galilean Satellites Orbiter mission model

In addition to the specified stay times, the IMLEO is constrained to be less than 29 metric tons, and the spacecraft mass at Jupiter arrival is specified at 10 metric tones. Earth-Jupiter transit time is constrained to be less than 2 years. Total propulsive output power of the spacecraft is specified at 1 MW.

The burnout mass of the spacecraft must be comprised of the nuclear power plant, as well as scientific payload and other supporting systems. Assuming a power and propulsion system specific power of 0.2 kW/kg, achieving a positive payload and structure mass will require a thruster operating at $\eta \geq 0.67$. While this is a reasonable efficiency, realistic spacecraft designs will require additional mass, and this mass overhead will place a hard constraint on the minimum efficiency of the electric propulsion system.

3.3.2 Saturn Transit Stage

The Saturn Transit Stage mission architecture has been explored with the goal of delivering a relatively large payload to the Saturn system while minimizing IMLEO for a given allowable transit time. This mission could allow the delivery of surface assets to Titan and Enceladus, for example, for a minimum launch cost. The trajectory for this mission is shown in Figure 3.8, and the mission timeline is given in Figure 3.9.

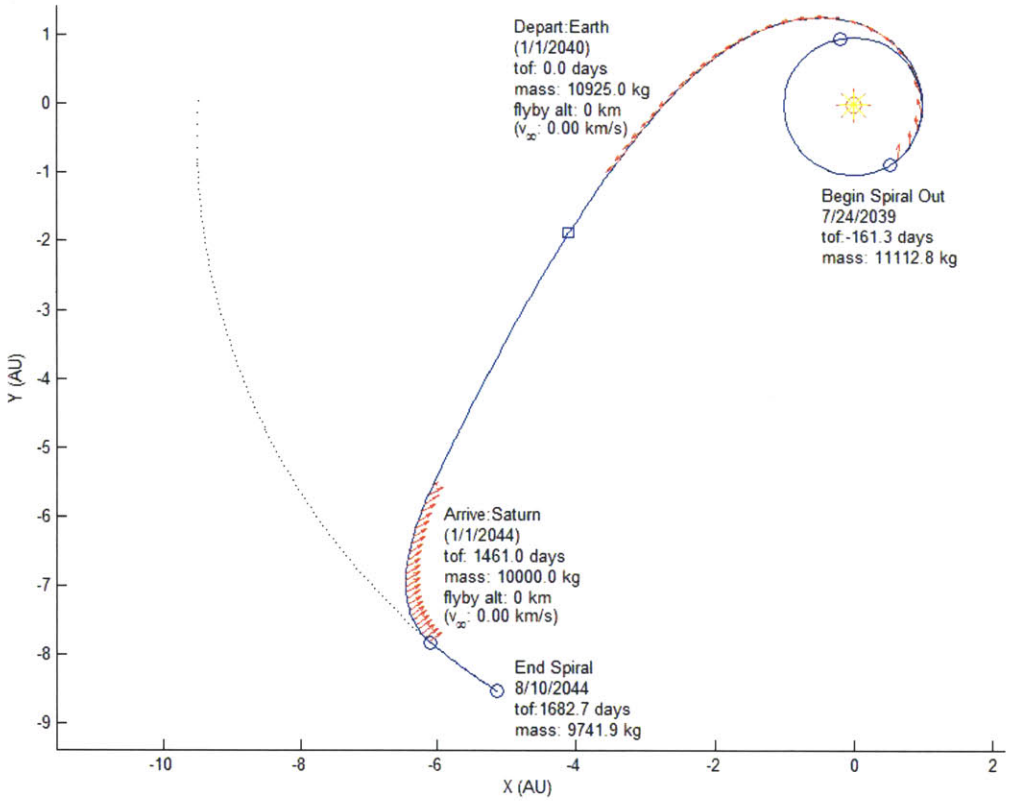

Figure 3.8. Earth-Saturn Transit Stage trajectory with transit time constrained to 4 years

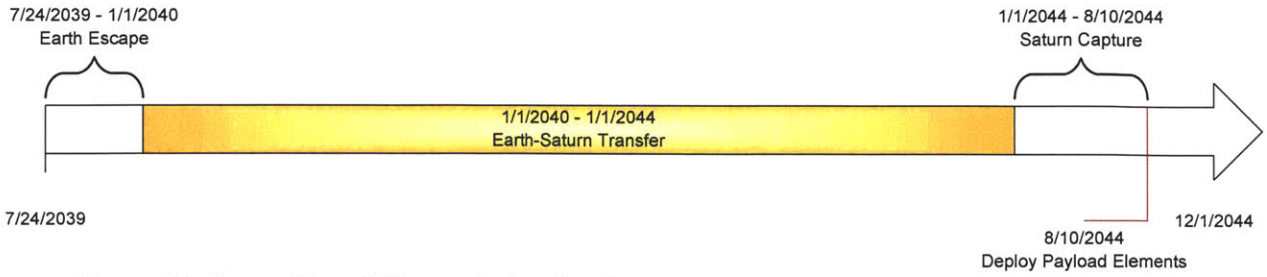

Figure 3.9. Saturn Transit Stage mission timeline with four-year Earth-Saturn transit constraint

The required value of IMLEO varies inversely with the allowed Earth-Saturn transit time. For a set total required mass at Saturn capture, in this case 10 metric tons, the IMLEO will decrease as propulsion system specific impulse increases. However, because the transit time is driven by system thrust-to-weight ratio, and since thrust must decrease with increasing specific impulse for a constant output power, lower values of IMLEO can be obtained for an increase in the allowable transit time. If the propulsion system power, the final mass at Saturn arrival and the maximum transfer time are specified, the optimum specific impulse will only be a function of the required mission ΔV, which itself is only weakly a function of the transfer trajectory. To see this, we begin with the Stuhlinger argument as presented in Eq. 1.14. Combining the structural mass in with the effective payload, we can recast this equation:

$$\frac{M_L}{M_0} = e^{-\frac{\Delta V}{c}} - \frac{c^2}{v_{ch}^2}\left(1 - e^{-\frac{\Delta V}{c}}\right) \qquad \text{(Eq. 3.4)}$$

For illustration, it is helpful to eliminate the characteristic velocity from this expression. The ratio of power to initial spacecraft mass is given by:

$$\frac{P}{M_0} = \left(\frac{M_{PROP}}{M_0}\right)\frac{c^2}{2\eta t} = \left(1 - e^{-\frac{\Delta V}{c}}\right)\frac{c^2}{2\eta t} \qquad \text{(Eq. 3.5)}$$

The ratio of the power to the initial spacecraft mass can then be expressed:

$$\frac{P}{M_L} = \frac{P}{M_0}\frac{M_0}{M_L} = \frac{\left(1 - e^{-\frac{\Delta V}{c}}\right)\frac{c^2}{2\eta t}}{e^{-\frac{\Delta V}{c}} - \frac{c^2}{v_{ch}^2}\left(1 - e^{-\frac{\Delta V}{c}}\right)} \qquad \text{(Eq. 3.6)}$$

Rearranging Eq. 3.6 yields:

$$\frac{P}{M_L}e^{-\frac{\Delta V}{c}} = \left(1 - e^{-\frac{\Delta V}{c}}\right)\frac{c^2}{2\eta t} + \left(1 - e^{-\frac{\Delta V}{c}}\right)\left(\frac{P}{\alpha M_L}\right)\frac{c^2}{2\eta t} \qquad \text{(Eq. 3.7)}$$

Further simplification of this expression gives:

$$\frac{c^2}{2\eta t} = \left(\frac{e^{-\frac{\Delta V}{c}}}{1 - e^{-\frac{\Delta V}{c}}}\right)\left(\frac{\frac{P}{M_L}}{1 + \frac{P}{\alpha M_L}}\right) \qquad \text{(Eq. 3.8)}$$

Incorporating the specific power, we can express this ratio in terms of the characteristic velocity:

$$\frac{c^2}{v_{ch}^2} = \left(\frac{e^{-\frac{\Delta V}{c}}}{1 - e^{-\frac{\Delta V}{c}}}\right)\left(\frac{\frac{P}{\alpha M_L}}{1 + \frac{P}{\alpha M_L}}\right) \quad \text{(Eq. 3.9)}$$

Returning to the ratio of the payload to initial spacecraft mass given in Eq. 3.4, we find:

$$\frac{M_L}{M_0} = e^{-\frac{\Delta V}{c}} - \left(\frac{e^{-\frac{\Delta V}{c}}}{1 - e^{-\frac{\Delta V}{c}}}\right)\left(\frac{\frac{P}{\alpha M_L}}{1 + \frac{P}{\alpha M_L}}\right)\left(1 - e^{-\frac{\Delta V}{c}}\right) \quad \text{(Eq. 3.10)}$$

Simplifying this expression finally gives:

$$\frac{M_L}{M_0} = \frac{e^{-\frac{\Delta V}{c}}}{1 + \frac{P}{\alpha M_L}} \quad \text{(Eq. 3.11)}$$

As previously outlined, for a fixed power, velocity increment and payload mass, there is no value of specific impulse for which the mass ratio in Eq. 3.11 will be maximized. In this case, the value of specific impulse will take on the largest value dictated by the allowable mission duration. In reality, the required velocity increment is not exactly constant for various trajectories, thus MALTO is useful in identifying the optimum specific impulse incorporating these relatively less important variations in ΔV.

In order to carry out the trade between increased transit time and decreased IMLEO, a parametric study was conducted in MALTO to evaluate the sensitivity of the IMLEO to allowable transit time. The results are given in Figure 3.10.

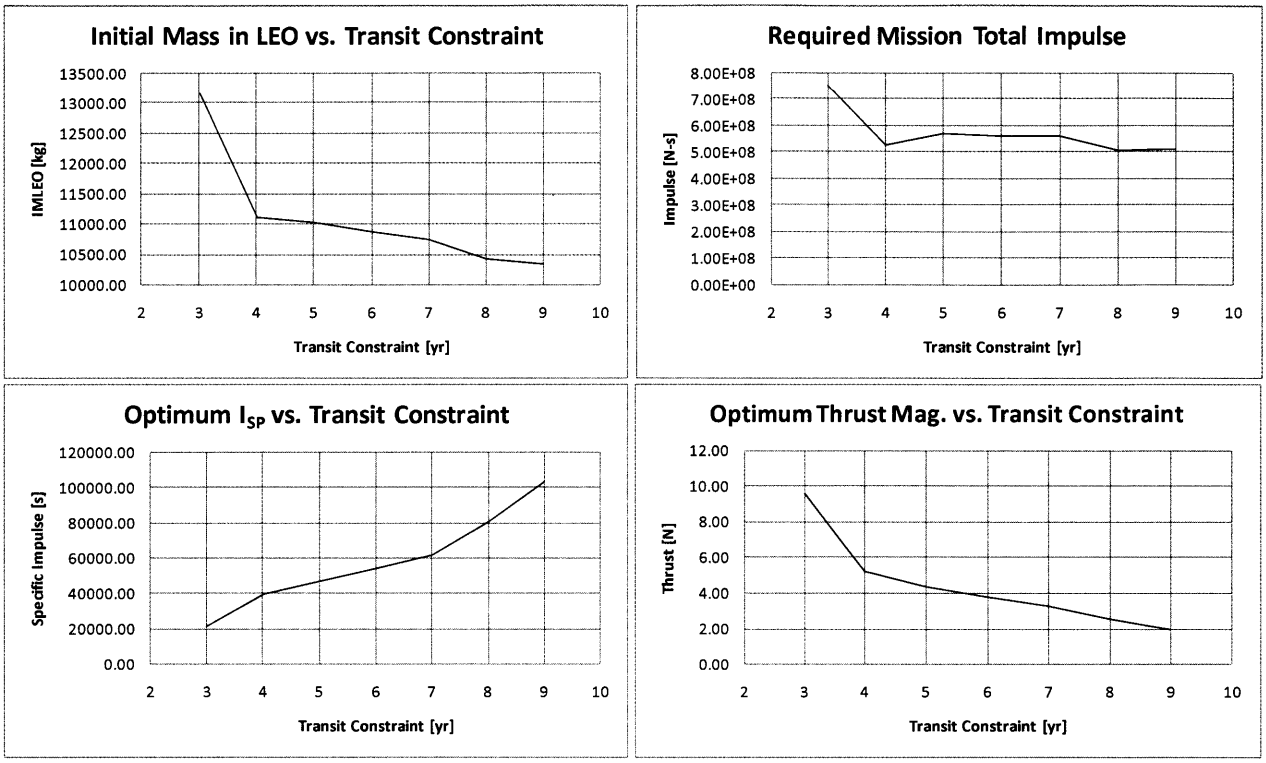

Figure 3.10 Parametric simulation demonstrating the effects of increased allowable transit time on the required IMLEO for a conceptual Saturn Transit Stage.

The first feature demonstrated in this parametric study was the decreased rate of return on IMLEO for allowable transit times greater than four years. A four-year transit results in an initial mass of just over 11 metric tons. Doubling the allowable transit time, from four to eight years, results in an initial mass savings of only 0.5 metric tons. A second noteworthy feature is the very high specific impulse required to realize the favorable mass fractions derived in this mission study. The four-year transit time yields a specific impulse of nearly 40,000 seconds at which the additional mass savings for IMLEO is a diminishing function of allowed transit time. Based on the results of this simulation, an allowable transit time of four years is selected for the Saturn Transit Stage mission architecture.

3.3.3 Interstellar Precursor

The objective of the Interstellar Precursor mission is to place a modest scientific payload at a distance of 250 AU, outside the bow shock of the solar system, to study the nature of the interstellar medium and the dynamics of the heliospheric boundary. The transit time is constrained to be less than 10 years, after which time the primary mission of the interstellar precursor is assumed to begin. The minimum burnout mass of the spacecraft is also constrained to be no less than 6.5 metric tons. Propulsion system output power is specified at 1 MW. The resulting trajectory and timeline for the Interstellar Precursor mission are shown in Figures 3.11 and 3.12.

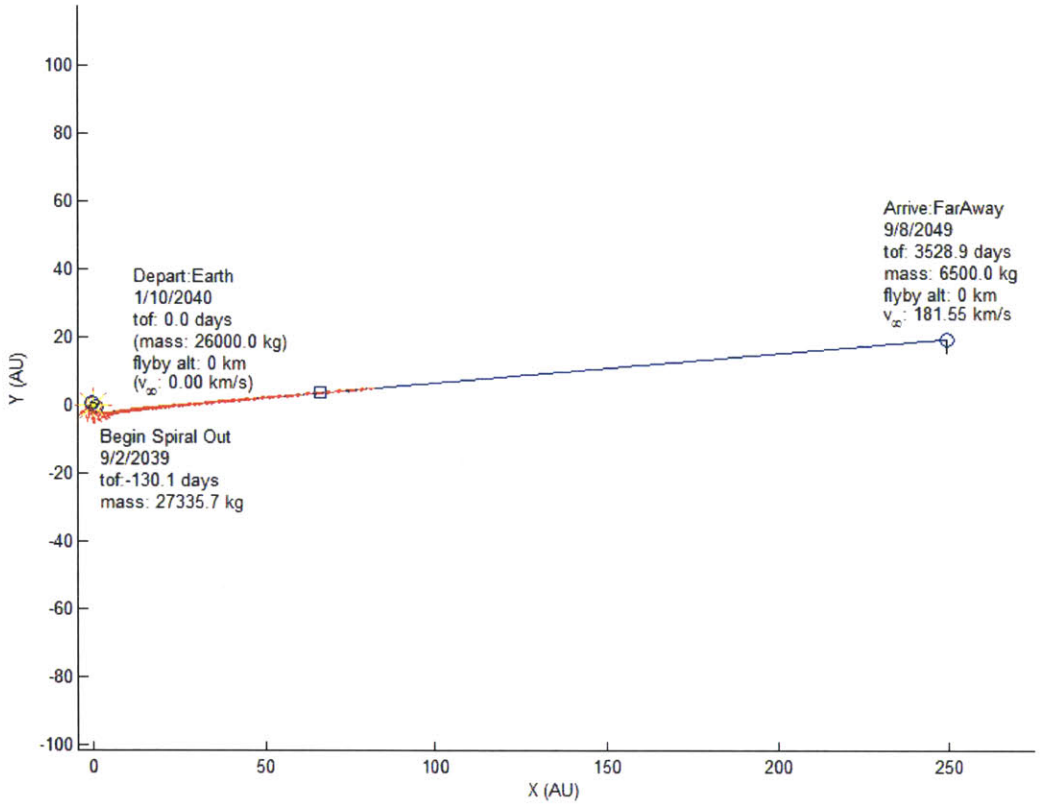

Figure 3.11. Interstellar Precursor Mission trajectory for a ten-year transit to 250 AU

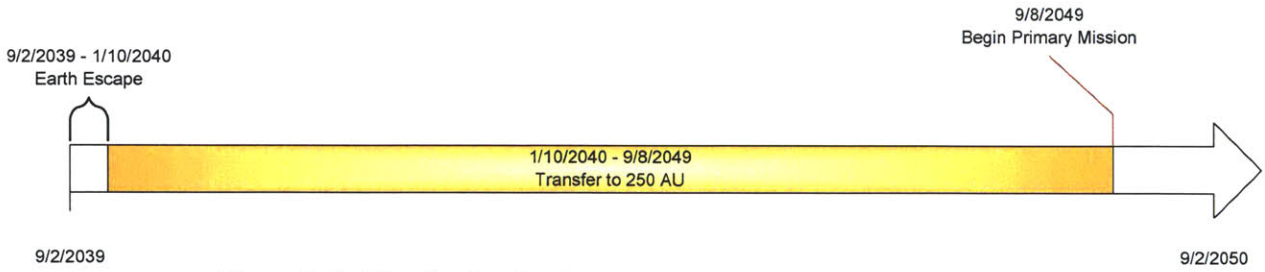

Figure 3.12. Timeline for the Interstellar Precursor mission architecture

One important result of the simulation for the Interstellar Precursor mission is the lack of time and mass margins. In fact, for constraints on burnout mass greater than approximately 6.5 metric tons, and time constraints on transit time of less than ten years, the system will not converge to a solution. If the power plant specific power is again estimated at $\alpha = 0.2$ kW/kg, in order to achieve a positive payload and structural mass, the required electric propulsion system efficiency must be $\eta \geq 0.77$. As with the Galilean Satellites Orbiter, the very tight mass budget associated with this mission means that the mass characteristics of the spacecraft will place a lower limit on the propulsion system efficiency. This mission may be regarded as the limit for what is achievable using the near-term power plant configuration as

described in Chapter 2. The optimized performance parameters for the Interstellar Precursor mission simulation are given in Table 3.2.

3.3.4 Neptune System Explorer

The Neptune orbiter, probe and Triton lander (NOPL) mission is a NASA space science vision mission which was initially envisioned using the Prometheus bus [105]. The mission consists of four components: the nuclear-powered orbital asset, two probes which would enter the Neptunian atmosphere, and a lander that would land on the surface of Triton. Allocated science payload for the mission, as originally envisioned, is 1500 kg.

In order to highlight the utility of megawatt level NEP in enhancing science and exploration returns for this type of mission, the payload mass simulated in this work is increased by 1000 kg to 2500 kg total. This allows the replacement of a Triton lander with a rover similar in mass to the Mars Science Laboratory. Further, the interplanetary cruise period is constrained to be less than 6.5 years, or half the required time for the baseline NOPL mission. The trajectory for this mission is shown in Figure 3.13, and the mission timeline is given in Figure 3.14.

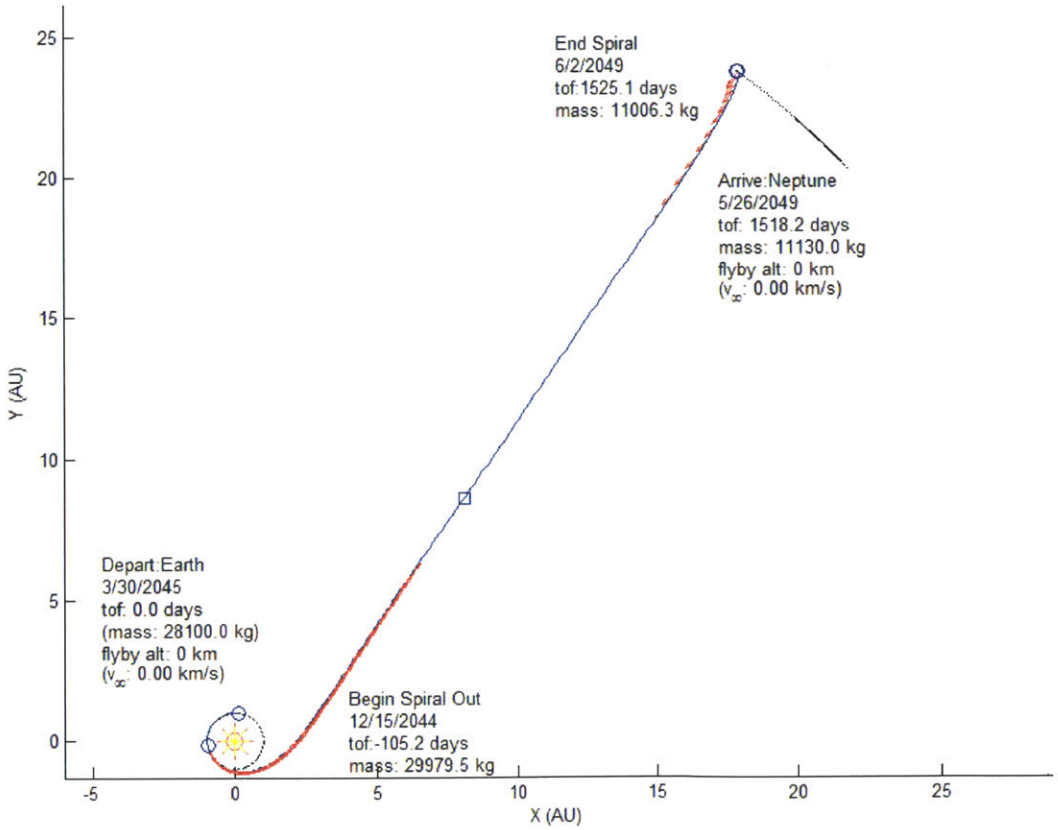

Figure 3.13. Advanced Neptune Orbiter, Probe and Triton Lander Mission to explore the Neptune System

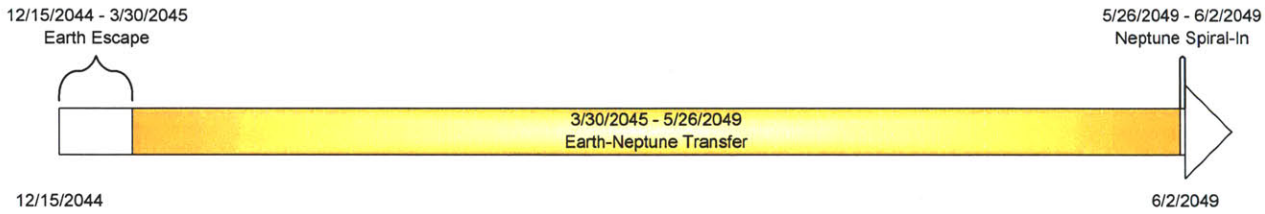

Figure 3.14. Timeline for the NOPL-Advanced mission architecture

3.3.5 Crewed Mars Mission

The final mission simulation conducted to evaluate the performance requirements of future nuclear electric propulsion systems is a crewed mission to Mars. Constraints and parameters imposed on this system are derived from the current version on NASA's Design Reference Mission Architecture [104]. The model concentrates on only the crewed component of the Constellation architecture, the Earth Departure Stage (EDS). To be consistent with this architecture, the IMLEO is constrained to be less than 188 metric tons, the projected launch capacity of the Ares V to LEO. While the Ares V launch vehicle is no longer a national priority for the United States, it can be reasonably assumed that the next heavy lift launch vehicle will possess comparable capability. The burnout mass of the EDS is constrained to be no less than 76.8 metric tons, providing 30 metric tons for the power and propulsion system, and the balance of the mass to the proposed inflatable TransHab module [107], and the entry vehicle that will ultimately deliver the astronauts back to Earth.

The optimization objective of the crewed Mars mission is the total transit time. Given a constant mass of the power and propulsion system, we can explore the effect that variations in propulsive output power will have on the transit time. The results of this parametric study are given in Figure 3.15.

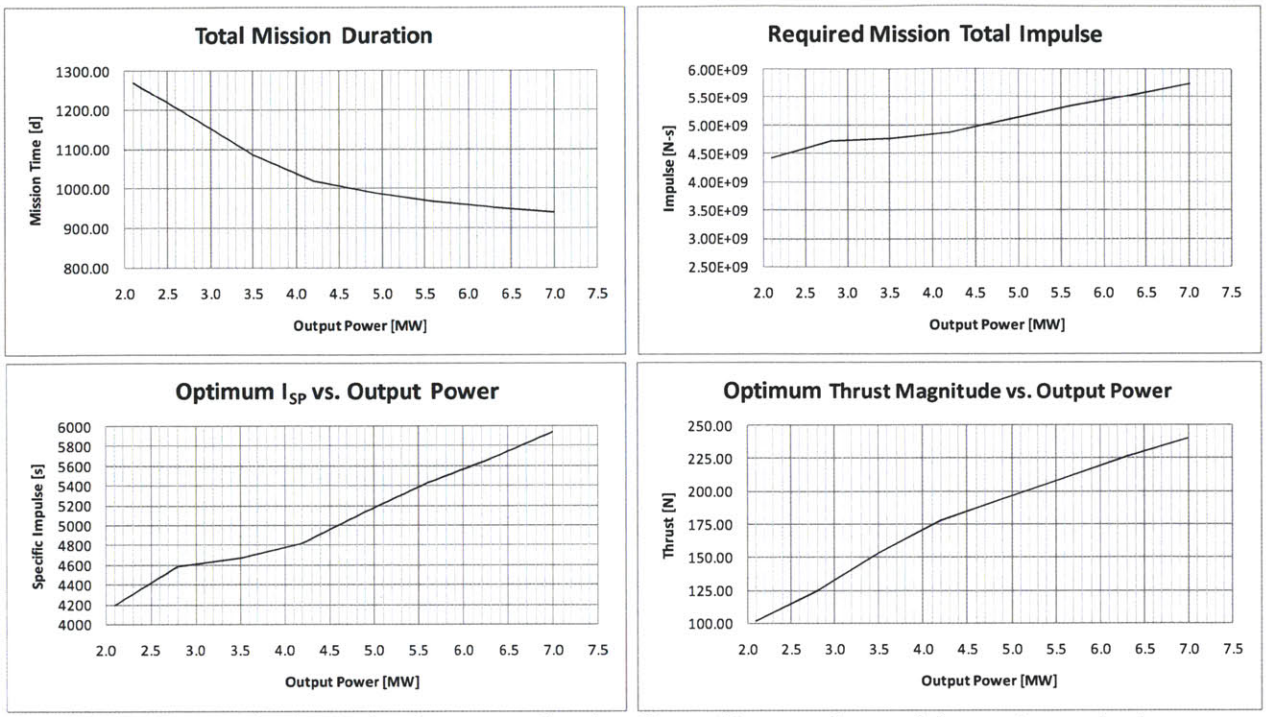

Figure 3.15. Parametric simulation demonstrating the effects of increased propulsion system output power on the required mission duration for a crewed Mars mission

The most important feature of this parametric study is the observed diminishing return on mission duration for power levels above about 4.2 MW. Thus, for the development of this mission model, the total output power is set at 4.2 MW. With a total propulsion mass of 30 metric tons, this corresponds to a power and propulsion system specific power of 0.14 kW/kg, easily within the range of specific powers outlined in Chapter 2 of this work.

In order to remain consistent with popular mission architectures, a surface stay time of 18 months is imposed in this model. Not including the extended escape times from Earth and Mars, the transit times to and from Mars are approximately 191 days and 186 days respectively. These transfer times are very competitive with those of other popular mission architectures [108]. The trajectory geometry for the crewed Mars mission is shown in Figure 3.16 below. The mission timeline is given in Figure 3.17.

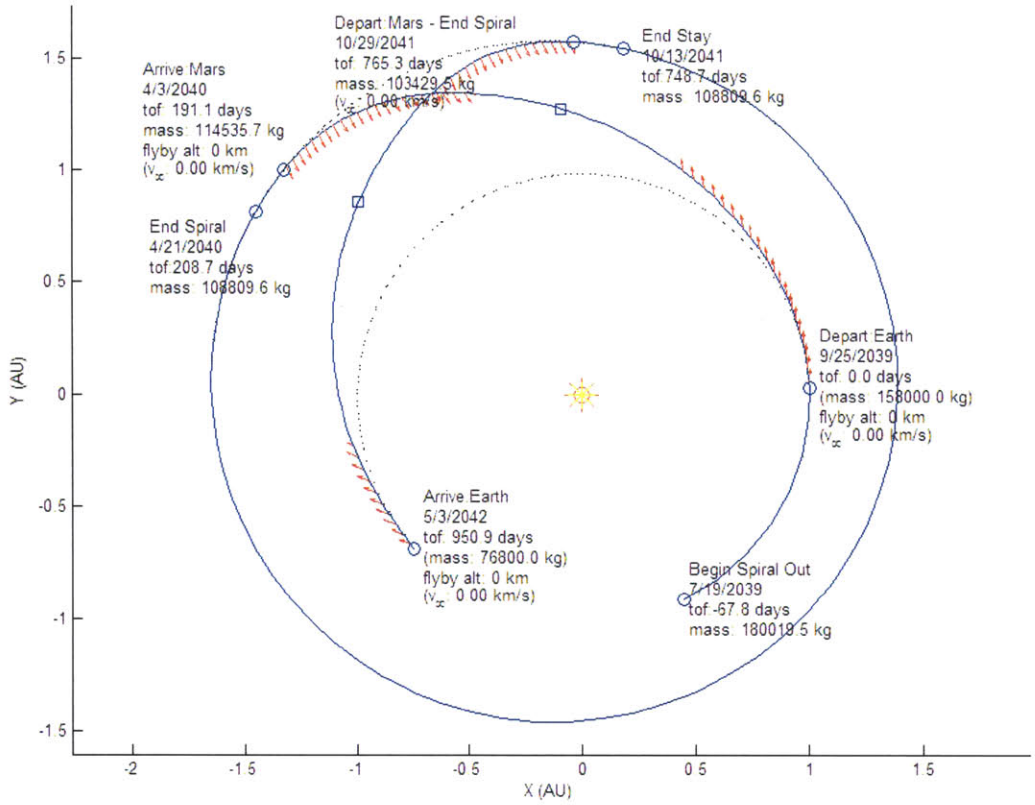

Figure 3.16. Crewed Mars Mission trajectory for 4.2MW propulsive output power

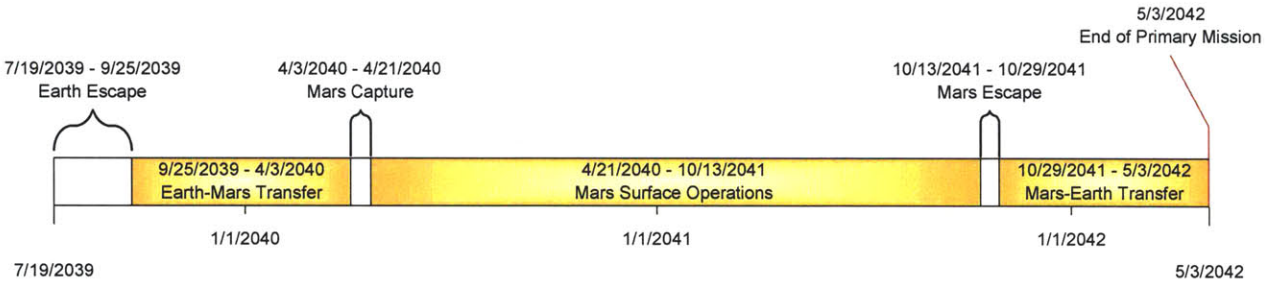

Figure 3.17. Timeline for the crewed Mars Mission architecture

3.4 Derived Propulsive Requirements

The goal of the mission analysis component of this work has been to derive a set of propulsion system requirements consistent with both the nuclear power plant technology level as characterized by the power and propulsion system specific power, as well as the likely applications for future NEP spacecraft. The MALTO software tool is able to calculate a mission-optimal specific impulse for the trajectories that meet the various imposed mission constraints. Output power in most cases was specified at 1 MW. The propulsion system lifetime can be evaluated by integrating the total thrusting times, including the spiral escape and capture times, which are also calculated by MALTO. This allows computation of the required

mission total impulse. The mission objectives and constraints, and the optimized propulsion system performance metrics are given in Tables 3.1 and 3.2 respectively.

	Galilean Satellites Orbiter	Saturn Transit Stage	Interstellar Precursor	Neptune Orbiter, Probes & Triton Lander	Crewed Mars Mission
Mission Duration [d]	2130	1844	3659	1630.00	1019
IMLEO [kg]	26783	11113	27336	29979	180020
MBO [kg]	7814	9742	6500	11006	76800
Total ΔV [km/s]	69.34	50.69	186.22	91.06	40.26
Objective	M_{BO}	IMLEO	M_{BO}, Trip Time	Trip Time	Trip Time
Parametric Variable	None	Transit Time	None	None	P_{OUT}
Constraints	IMLEO < 29,000 kg P_{OUT} = 1 MW	M_{SC} @ Saturn Arrival = 10,000 kg P_{OUT} = 1 MW	Transit Time < 10 y MBO ≥ 6,500 kg IMLEO < 29,000 kg P_{OUT} = 1 MW	M_{SC} @ Neptune Arrival = 11,000 kg P_{OUT} = 1 MW Transit Time < 6.5 y	IMLEO < 188,000 kg M_{BO} = 76,800 kg M_{PP} = 30,000 kg

Table 3.1. Mission model characteristics including the mission objective function, parametric variable and constraints

	P_{OUT} [MW]	Thrust [N]	I_{SP} [s]	Lifetime [h]	I_{TOT} [N-s]
Galilean Satellites Orbiter	1.00	35.50	5744	10306	1.317E+09
Saturn Transit Stage	1.00	5.19	39288	28262	5.281E+08
Interstellar Precursor Mission	1.00	15.42	13229	48906	2.715E+09
Neptune Orbiter Probe Lander	1.00	20.34	10027	25505	1.671E+09
Crewed Mars Mission	4.20	177.64	4822	7632	4.880E+09

Table 3.2. Derived propulsive requirements

As mentioned previously, it is useful to compare the derived values of specific impulse for each of these cases to the Stuhlinger optimal specific impulse to provide a check on the calculated performance requirements for these optimized mission models. This is provided in Table 3.3.

	I_{SP} (MALTO) [s]	I_{SP} (Ideal) [s]
Galilean Satellites Orbiter	5744	6662
Saturn Transit Stage	39288	NA
Interstellar Precursor Mission	13229	12491
Neptune Orbiter Probe Lander	10027	11496
Crewed Mars Mission	4822	6817

Table 3.3. Comparison on derived optimal specific impulse with the Stuhlinger optimum; $\eta_{REF} = 0.7$; $\alpha_{REF} = 0.2\ kW/kg$

With the exception of the Saturn Transit Stage, as previously outlined in Section 3.3.2, the derived values of specific impulse show good agreement with those obtained from the Stuhlinger treatment. This provides an analytic check on the performance estimates derived in this work. Reference efficiency is taken to be $\eta_{REF} = 0.7$ and the specific power $\alpha_{REF} = 0.2$ kW/kg.

3.5 Conclusions

The mission analysis conducted thus far yields some general conclusions regarding the likely propulsion system requirements for future high power nuclear electric missions. First, two ranges of specific impulse are needed to service the full spectrum of these types of missions. There is a need for relatively low specific impulse, approximately 5000s, with correspondingly high thrust, as well as high specific impulse, around 13,000s and up. It is interesting to note that at the power levels considered in this work very high values of specific impulse may provide more utility for mission planners than in the current state of the art. For favorable values of specific power, high-power, high I_{SP} systems are able to develop more useful accelerations than current systems will allow.

A second general observation is that, in spite of adopting a wide range of constraints and objective functions in optimizing these missions, the required total impulse in all cases falls into an envelope of less than one order of magnitude, from 0.5 – 5 GN-s.

Finally, it is worth noting that all the missions simulated in this work can be accomplished with 1-5 MW of propulsive output power. For propulsion system efficiencies $\eta \geq 0.70$, required reactor output powers will likely fall into a range of 1.5 – 7 MW.

In conclusion, the development of these four missions has allowed for the development of a coherent set of requirements to drive the investigation of future electric propulsion devices for use with high output nuclear electric power supplies. These requirements provide a general picture of the likely medium-term needs to facilitate missions in which government space agencies have previously expressed interest.

Chapter 4

Survey of Electric Propulsion Devices

4.1 Introduction

In the preceding chapters we have first outlined the utility of high power nuclear electric propulsion in ambitious, next-generation spaceflight applications. Missions using this technology are shown to provide increased scientific yields compared to missions conducted using conventional chemical propulsion. Next, by conducting detailed mass modeling simulations of space nuclear power plants based on a liquid metal Rankine thermoelectric conversion cycle, we have been able to determine the specific power and lifetime characteristics of these power systems. Finally, given an understanding of power plant mass scaling, we have been able to derive a range of propulsive requirements from detailed mission modeling that high power electric propulsion systems will likely encounter.

In the following section, a variety of electric propulsion thrusters are described. The physics of operation for each is described, limitations related to high power application are considered, and possible design evolutions that might enable high power operation are outlined. These thrusters are grouped according to the fundamental acceleration mechanism at work in each: electrothermal, electrostatic and electromagnetic. Conclusions from this survey are presented in the form of selected design evolutions that enable high power operation at a minimum of design risk. These provide the basis for the analysis and modeling undertaken in subsequent sections.

4.2 Electrothermal Thrusters

As in a chemical rocket, electrothermal thrusters rely on the direct conversion of propellant enthalpy to jet kinetic energy through the process of expansion in a nozzle. In a conventional chemical rocket, however, the chamber temperature is a function of the difference in the enthalpies of formation of the products and reactants. The energy used to develop high propellant temperatures in the rocket chamber is the chemical bond energy of the propellants. In an electrothermal device, however, the energy to heat the propellant must come from supplied electrical power. Three thruster types that rely on electrothermal conversion processes are presented below. These are the resistojet, the arcjet and plasma phase electrothermal concepts.

4.2.1 Resistojet

The resistojet is arguably the simplest electric propulsion device that might be implemented. This thruster makes use of thermal energy created in a resistive element to heat a propellant gas which is then exhausted in a conventional converging-diverging nozzle. A notional thruster using this type of acceleration mechanism is shown in Figure 4.1. Several resistive element configurations that have been used in past applications are given in Figure 4.2.

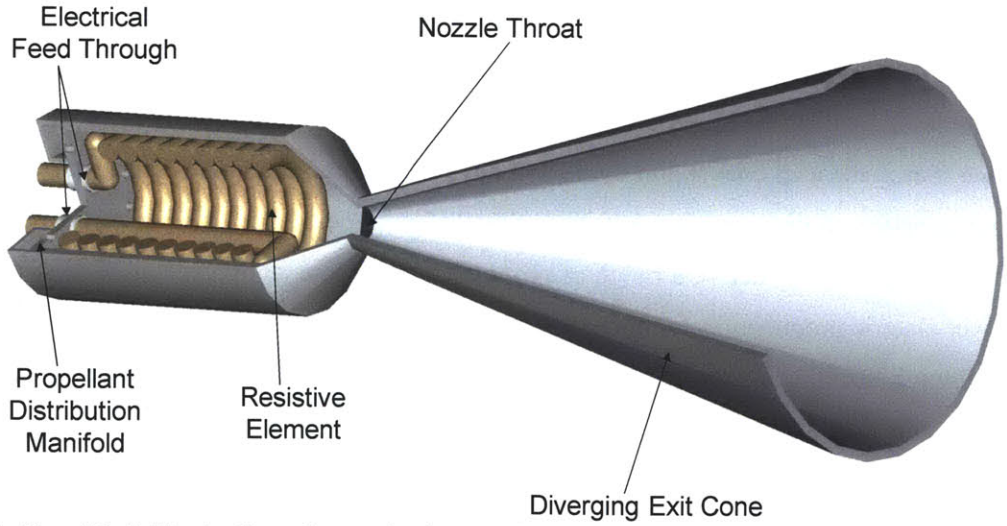

Figure 4.1. Simplified illustration of a resistojet employing a coiled resistive element. Propellant gas is injected into the chamber and convectively heated by passing over the resistive element, a coil in this illustration. Hot gas is exhausted through a converging-diverging nozzle.

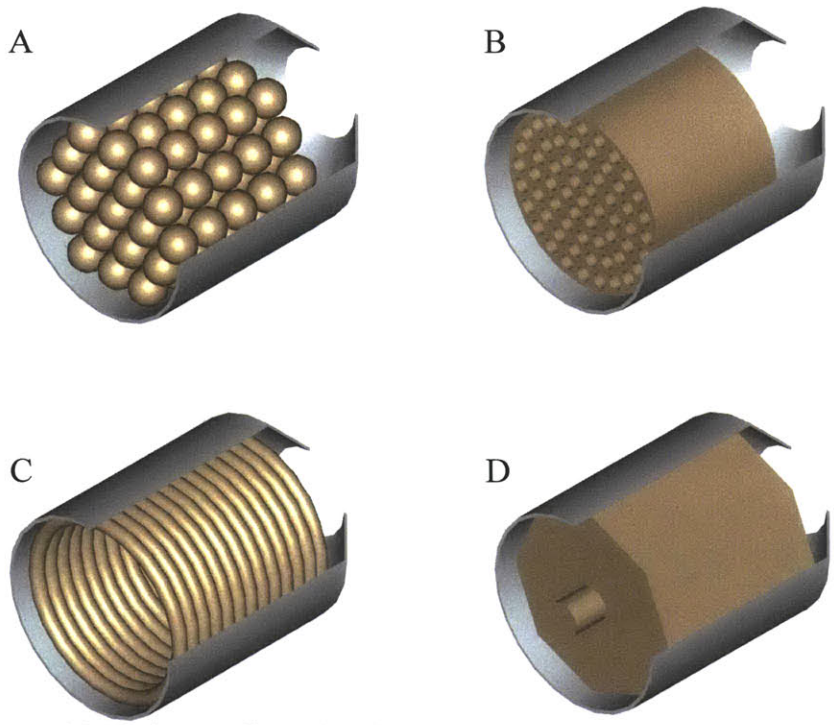

Figure 4.2. Various configurations for resistive elements in resistojet thrusters

The energy balance for one dimensional adiabatic expansion in a nozzle for a fluid with constant specific heat can be expressed simply:

$$\frac{1}{2}\dot{m}u_e^2 = \frac{1}{2}\dot{m}u_c^2 + \dot{m}c_p(T_c - T_e) \qquad \text{(Eq. 4.1)}$$

The propellant mass flow rate is given by $\dot{m}$ and propellant specific heat by c_p. The chamber temperature and exit temperatures are given by T_c and T_e and the chamber and exit velocities by u_c and u_e respectively. In the limit that the chamber inlet velocity is negligible and $T_e \ll T_c$, we can solve for the maximum exhaust velocity:

$$u_e = \sqrt{2c_pT_c} \qquad \text{(Eq. 4.2)}$$

To illustrate the performance that can be achieved by a resistojet thruster one can specify a liberal maximum allowable chamber temperature of $T_c = 3300\,K$, and compute the theoretical exhaust velocities assuming a constant value of specific heat for several common gases. This is shown in Table 4.1.

Propellant	c_p [J/kg-K]	I_{SP} [s]
H_2	16610	1068
He	5190	597
CH_4	4708	569
H_2O	2080	378
CO_2	1150	281
Air	1100	275
N_2	1040	267
Ar	520	189

Table 4.1. Achievable specific impulse for several common gases at $T_c = 3300\ K$

It is clear that, given the temperature limitations of common thruster construction materials, resistojet performance is incompatible with the propulsive requirements for specific impulse derived from mission modeling. Finally, it is worth observing that, for systems utilizing a heat source and electrothermal conversion cycle to produce electrical power it will always be more efficient to utilize the heat source directly to heat the propellant. By applying direct heating to the propellant gas, inefficiencies associated with energy conversion and power conditioning equipment may be avoided. Obviously, then, direct nuclear thermal rocket engines and solar thermal systems will always outperform resistojet systems for a fixed thermal input power.

Because of the performance limitations stemming from material constraints, as well as the fundamental limit on thermoelectric conversion efficiency, resistojet thrusters present little utility for high power primary electric propulsion.

4.2.2 Arcjet Thrusters

The arcjet circumvents some of the material thermal limitations inherent to the resistojet by utilizing an electric arc to heat propellant. While the resistive body associated with the resistojet can only reach 3300 K, an electrical arc may have a core temperature in excess of 20,000 K. A simplified cutaway diagram of the arcjet is shown in Figure 4.3, and an illustration of the constrictor region is given in Figure 4.4.

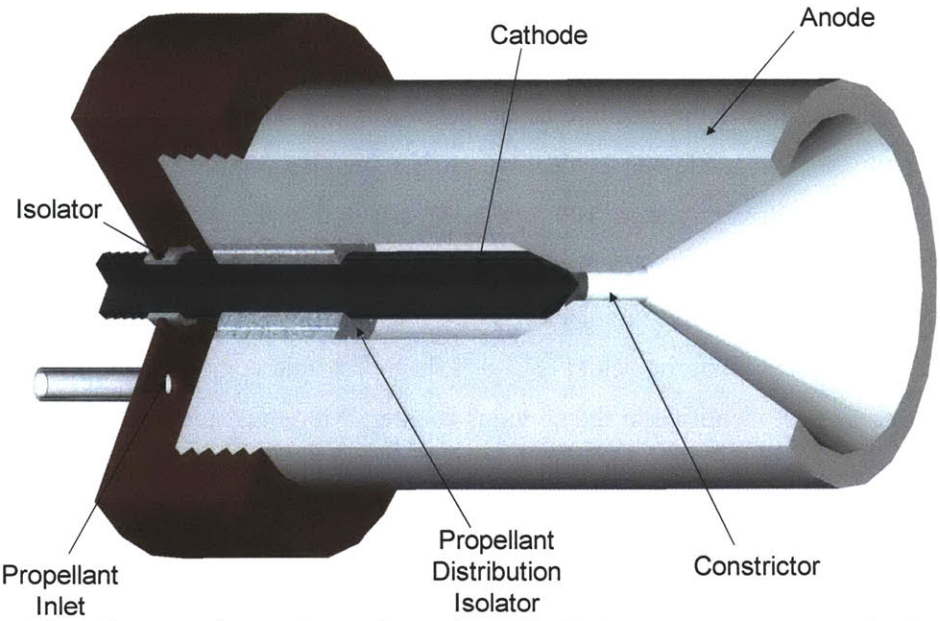

Figure 4.3. Simplified diagram of an arcjet configuration. The high temperature arc core in the constrictor passage heats propellant before it is exhausted through the anode nozzle.

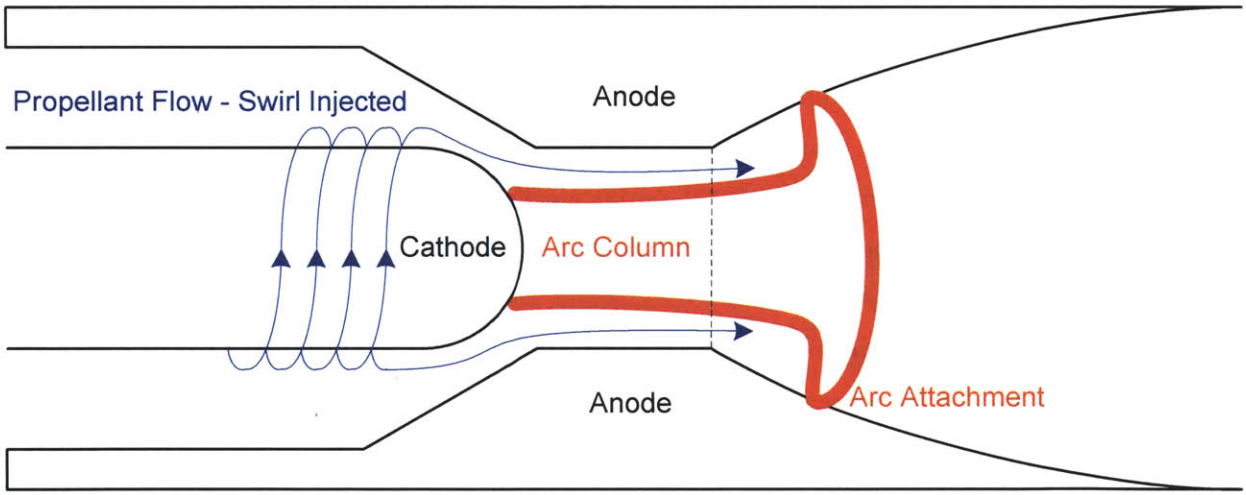

Figure 4.4. Illustration of arc growth through the constrictor passage and downstream attachment in the nozzle section of the anode; dotted line denotes propellant sonic surface

Arcjet models are generally developed with the goal of predicting three key operational characteristics of these thrusters [109]. These are, first, thruster performance in terms of thrust and specific impulse, second, thruster terminal voltage, and finally heat losses to the electrodes. These models are widely fit to empirical data for thrusters with known performance and operating characteristics.

A simplified model for predicting arcjet performance [110] can be developed based on a two fluid approximation. This model is based on the assumption that no flow occurs in the high temperature arc. All flow is in the outer stream, which is heated by radial heat conduction. Heating of this sheath flow also

results in radial arc growth down the length of the constrictor. The arc, in this case, can be thought of as a constrictor plug, reducing mass flow while leaving the integral of pressure at the constrictor exit intact.

Provided that engineering challenges like electrode erosion and thruster cooling can be overcome, the utility of arcjet thrusters in achieving projected specific impulse requirements remains questionable. Experimental work in Germany on a 100 kW-class arcjet thruster using hydrogen propellant has demonstrated an achievable I_{SP} of more than 2,000 s at a peak efficiency of 29% [111-113]. While some additional improvements in specific impulse might be achieved in a thruster designed to operate at the megawatt level, it is unlikely that the achievable performance would coincide with the anticipated needs for the missions of interest identified in the previous chapter. Moreover, provided that projected specific impulse requirements could be met with such a device, it is likely that other thrusters may provide the same capability at greater efficiency.

4.2.3 Plasma Phase Electrothermal Thrusters

In order to circumvent the material limitations associated with DC electrothermal devices in scaling to very high power levels, it may be desirable to use RF power to ionize and heat a propellant gas. Thrusters using RF power to ionize a propellant have the added benefit that they may be designed without electrodes immersed in the plasma flow. This feature may allow these thrusters to avoid life-limiting issues associated with electrode erosion. Additionally, unlike resistojet and arcjet systems, in an electrodeless discharge complete propellant ionization is feasible. This may provide options for magnetic conditioning of the flow, including magnetic confinement as well as the use of a magnetic nozzle. Admittedly, concepts like these are no longer strictly electrothermal in nature. However, as electromagnetic body forces are not used to accelerate the flow, these may be considered thermal. Simplified notional configurations for this type of thruster are shown in Figure 4.5 and Figure 4.6, below.

There are several concepts for generating and heating plasmas in an electrodeless discharge. Helicon wave [114, 115], and ion cyclotron resonance heating [116] have each been studied for their utility in generating and heating an electrodeless plasma discharge. It is also possible to implement plasma phase electrothermal systems in staged configurations that decouple the ionization and plasma heating processes, as is done in the VASIMR engine concept [117]. Recent testing of a 200kW staged configuration of this type has demonstrated a specific impulse of 5000s at an operating efficiency of 72% [118].

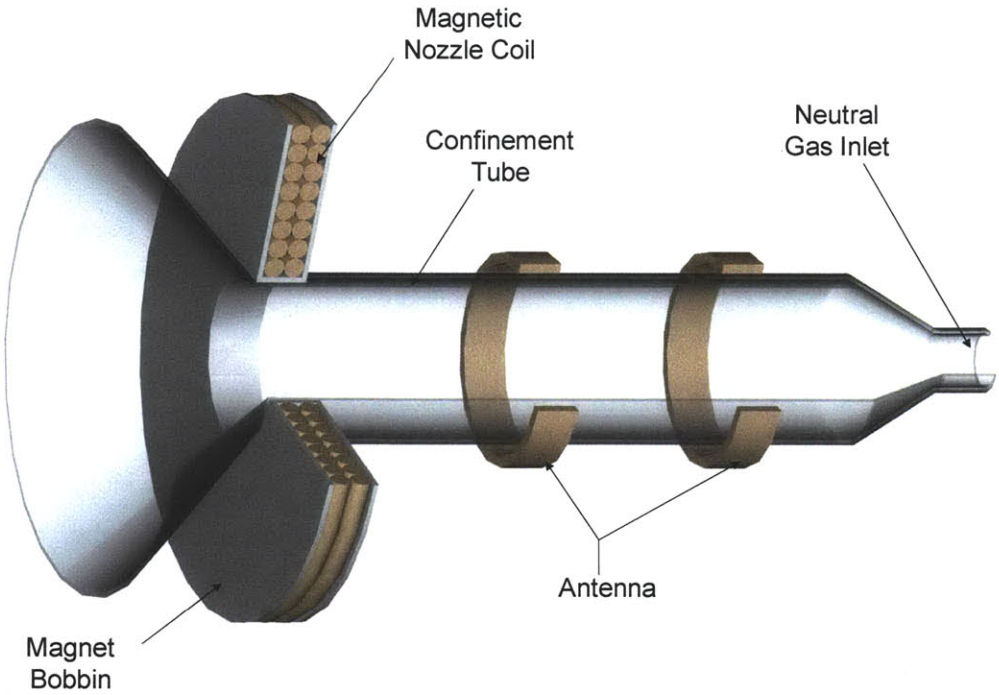

Figure 4.5. General configuration of an electrodeless discharge device. The device shown above is useful for exciting capacitively-coupled plasmas. By varying the antenna geometry and the magnetic field strength, this configuration can drive capacitively-coupled or helicon-type discharges.

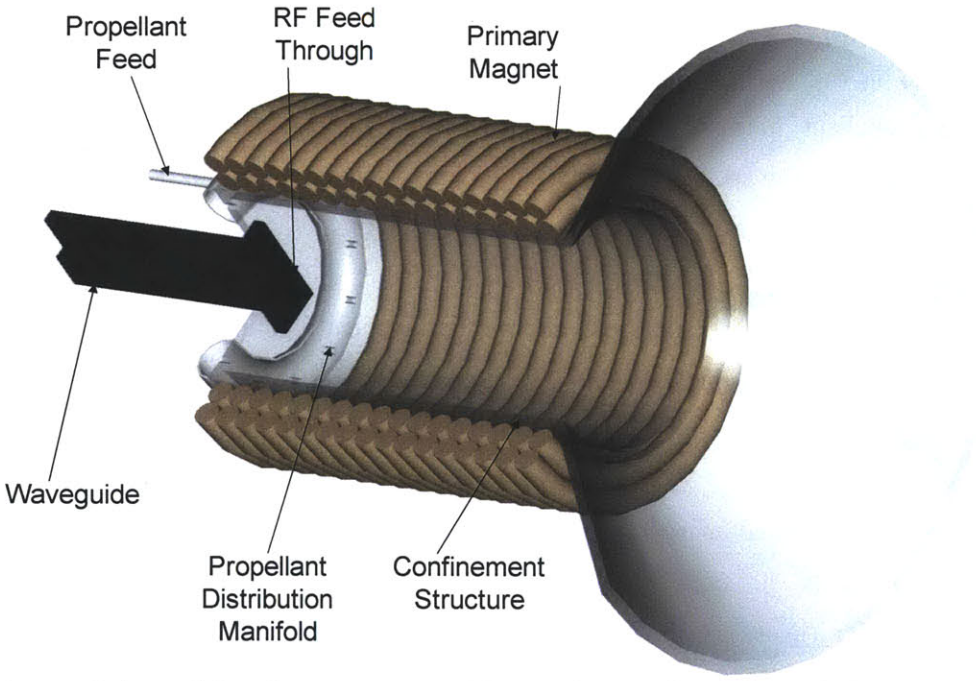

Figure 4.6. A second electrodeless thruster concept. The relatively uniform magnetic field inside the chamber is useful for exploiting ion cyclotron heating to increase the enthalpy of the propellant plasma.

While electrodeless plasma phase electrothermal discharges appear to offer a number of advantages for high power thruster implementation, a number of engineering challenges also exist. In the following

sections, the subsystems common to all PPET-type thrusters are outlined, and a brief discussion of the engineering and design considerations associated with each is presented.

4.2.3.1 Power Processing

PPET concepts are unique in that, of all frequently studied electric propulsion systems, these require the use of RF power. In order to efficiently convert low frequency AC power, as from a turbo-generator, or relatively low-voltage DC power from a solar array, to high frequency RF requires somewhat more substantial power conditioning equipment.

A critical advancement in the design of RF power processing units for use in multi-megawatt applications is the application of high temperature electronics. Research and development efforts have been underway for several years at NASA Glenn Research Center to develop silicon carbide for use in advanced spacecraft electronics applications [119,120]. Silicon carbide-based semiconductors are an exciting prospect for spacecraft applications in terms of both power processing and data handling tasks. They possess the unique potential to operate at high power and high temperature [121] and in high radiation environments [122].

4.2.3.2 Applied Magnetic Field

As discussed in the previous section, PPET devices rely on the deposition of RF power to increase the enthalpy of a propellant plasma. These devices also typically rely on the application of an electromagnetic nozzle to convert that enthalpy into jet kinetic energy. There is a fluid mechanical analog between convergent-divergent gasdynamic nozzles and electromagnetic nozzles, although the particulars differ. In a gasdynamic nozzle, the flow accelerates in the convergent region, becoming sonic at the throat before continuing to expand supersonically in the divergent region. In an electromagnetic nozzle the flow follows magnetic field lines, reaching the magnetosonic speed at the point in the nozzle where the field strength is maximum before expanding supersonically in the downstream section in which the field lines are divergent.

To minimize the additional mass required for the application of the magnetic field, the use of superconducting magnets is typically envisioned. Barring the advent of high temperature superconductors it will be necessary to provide cryogenic cooling of the superconducting electromagnet.

A final consideration related to the applied magnetic field is the generation of torques on the spacecraft due to induced magnetic dipole moment. To provide a null magnetic moment for operation inside of the interplanetary magnetic field, or a planetary magnetosphere, it may be necessary to provide two thrusters configured as a zero-torque magnetic quadrapole.

4.2.3.3 Cryogenic Magnet Cooling

The application of superconducting solenoids for magnetic nozzles in plasma-phase electrothermal devices will require cryogenic cooling at temperatures between 50K-100K. In a closed cycle system suitable for long mission duration there are two possibilities for providing the required cooling: passive radiators and closed-cycle cryocoolers.

Closed-cycle cryocoolers differ from passive radiators in that they used a closed thermodynamic cycle requiring work input in order to reject process heat at a higher temperature than would be possible in a passive radiator system. There are many types of closed-cycle cryocoolers that have been developed for a variety of spacecraft applications. An extensive review of the various types of coolers is provided in [123]. Those most readily applicable to high power at listed below:

- Stirling Cycle Cryocoolers
- Joule-Thompson Cryocooler
- Reverse Brayton Cycle Cryocooler
- Pulsed Tube Cryocooler

We can evaluate the utility of closed cycle cryocoolers and passive radiators for cryogenic cooling of superconducting magnets based on their achievable mass. Detailed mass models of single stage and multi-stage cryogenic coolers for spaceflight applications is developed in [124] based on fits to the existing data for cryocooler masses. Given the required thermal power rejection, we can estimate the efficiency of a cryocooler:

$$\eta\varepsilon_c = 10^{-0.92237+0.07763\log(1+Q_C)} \quad \text{(Eq. 4.3)}$$

In this expression ε_c is the Carnot efficiency:

$$\varepsilon_c = \frac{T_H}{T_C + T_H} \quad \text{(Eq. 4.4)}$$

The product $\eta\varepsilon_c$ is the fractional Carnot efficiency. Knowing this efficiency and the required thermal power rejection allows us to determine the input power to the cooler:

$$\eta\varepsilon_c = \frac{Q_C}{P_{in}} \quad \text{(Eq. 4.5)}$$

Finally, the first law of thermodynamic requires that:

$$Q_H = Q_C + P_{in} \quad \text{(Eq. 4.6)}$$

Once the total input power is known we can estimate the cooler mass. As discussed in [124], tabulation and fitting of empirical data indicates that for first-order estimation, the required cooler mass is only a function of the input power. Assuming a single-stage cooler operating above 65K, we apply the ter Brake [125] correlation to find:

$$m_C = 0.0711 P_{in}^{0.905} \quad \text{(Eq. 4.7)}$$

The ter Brake correlation in Eq. 4.7 incorporates design choices for the thermal rejection temperature around which the mass of flight articles have been optimized. The mass of closed-cycle cryocoolers may be compared to an ideal radiator operating as a blackbody. Two passive radiator cases are considered. Radiation temperature in the first case is taken at 77K, corresponding to the boiling point of liquid nitrogen. In the second case the radiation temperature is taken as 130K, implying an advanced high temperature superconductor. The areal density in both cases is assumed to be 2.0 kg/m^2. Results of this comparison are given in Figure 4.7.

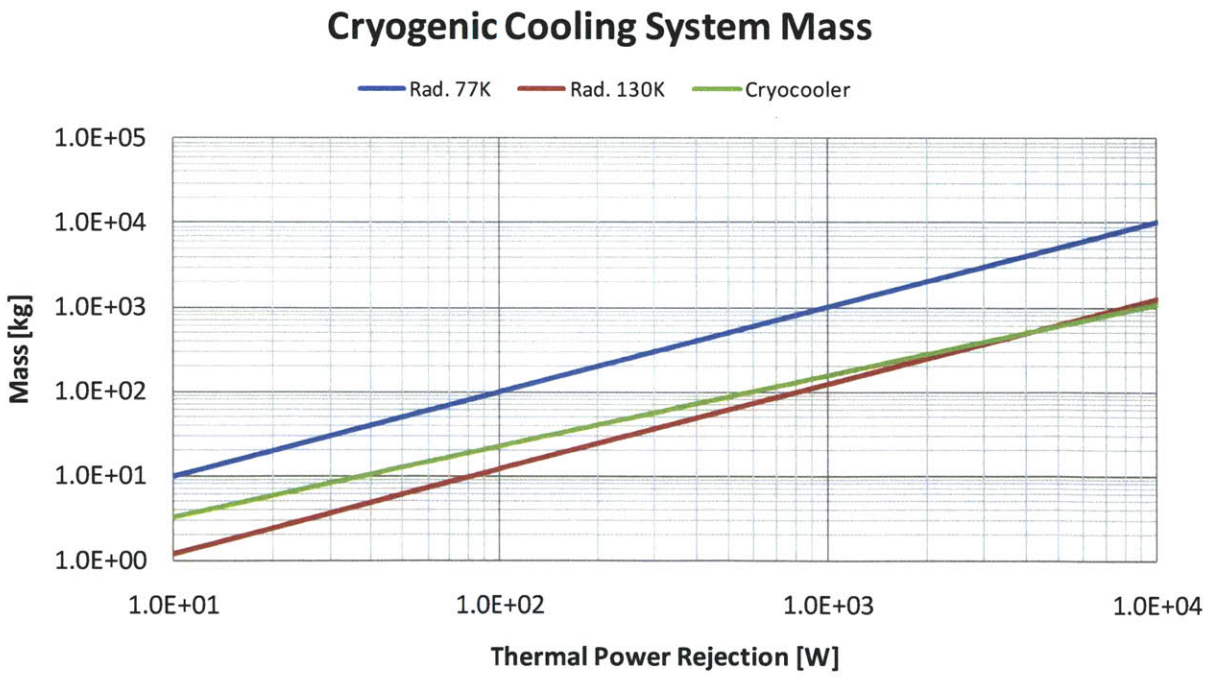

Figure 4.7. Comparison of cryogenic cooling system mass indicates that, for near-term superconductors operating near 77K closed cycle cryocoolers outperform passive radiators for a given required thermal power rejection.

The cooling requirement of superconducting magnets is assumed to be unique to the plasma-phase electrothermal concepts. It is likely that other electric propulsion thrusters can be cooled at high temperatures, where passive radiators are more mass efficient.

On the whole, including the support systems required for power conditioning, power conditioning cooling for conventional silicon semiconductor switches, superconducting electromagnets, and electromagnet cooling will tend to drive down the specific power for PPET propulsion systems. It is possible that competing EP thrusters discussed in subsequent sections of this chapter will achieve more favorable values of specific power at similar I_{SP} figures with somewhat less developmental risk.

4.3 Electrostatic Thrusters

Electrostatic thrusters make use of electric fields to accelerate ions to high exhaust velocities. Three types of electrostatic thruster are considered in the following sections. These are gridded ion engines, Hall effect thrusters, and electrospray thrusters.

All electrostatic thrusters share the common feature that the extracted propellant beam is not charge neutral, and these systems require beam neutralization to prevent spacecraft charging. In the gridded ion and Hall effect thrusters, beam neutralization is accomplished using an external cathode which injects electrons into the positively charged beam. In electrospray systems, charge neutralization can be achieved by extracting both positive and negative species from the propellant. A brief discussion of cathodes and the engineering challenges for high power is included following the discussion of the three electrostatic thruster types.

4.3.1 Gridded Ion Engines

Gridded ion thrusters represent the simplest conceptual application of electrostatic acceleration to produce thrust. Propellant is introduced in the chamber, where it is ionized. Two grids at the downstream face of the chamber are biased to produce a potential profile favorable for the extraction of positive ions through the grid apertures. Ions so extracted are accelerated through the potential drop between the grids producing an ion beamlet. In thrusters with many such aperture pairs, appreciable beam currents, and therefore thrusts, can be obtained. Because the plume in this case is positively charged, an external neutralizer cathode is used to prevent spacecraft charging. The major components associated with the gridded ion engine are shown in Figure 4.8. In some thrusters, a third, so-called deceleration grid is used. This grid is biased to some voltage slightly higher than that of the acceleration grid and this allows some modulation of the ion exit velocity. Deceleration grids may also be biased to electrostatically shield the acceleration grid from charge exchange ions created outside the thruster that might otherwise reverse flow and impinge the acceleration grid. These and other issues are discussed in greater detail in Chapter 5.

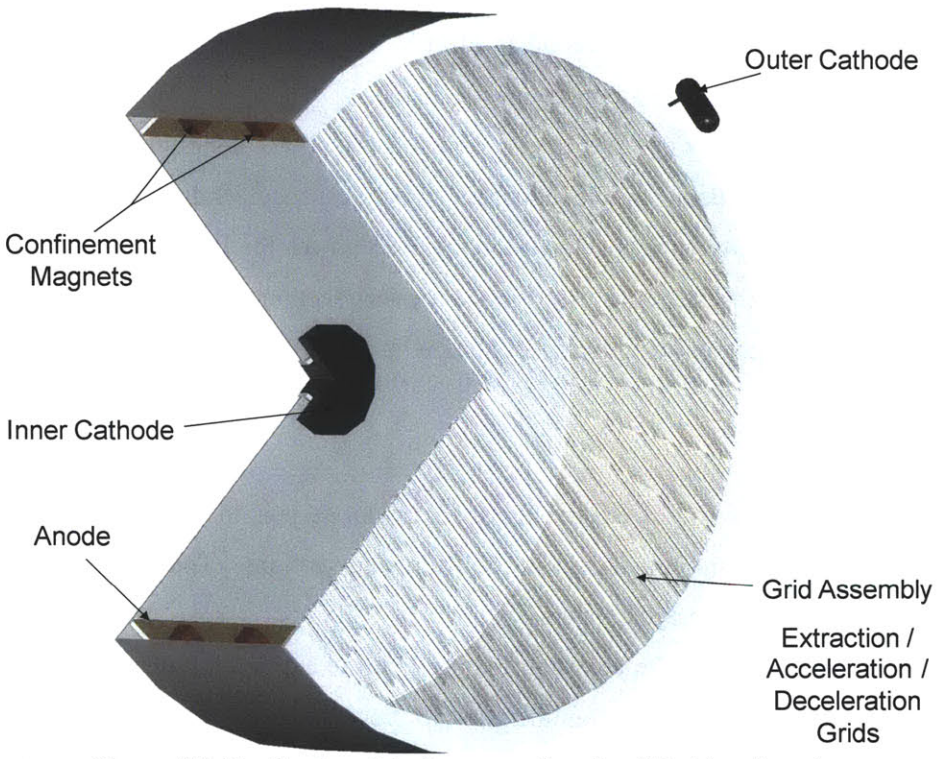

Figure 4.8. Idealized model of a conventional gridded ion thruster

The physics that govern extraction and acceleration of ion beams in a gridded ion thruster impose some limitations on the performance that can be achieved in conventional two- and three-grid thrusters. Considering a two-grid thruster for simplicity, the maximum current that may be extracted through an aperture pair occurs at the space charge limit. Conceptually, this is the limit at which the presence of the positive charges contained in the portion of the beam between the screen and acceleration grid perturbs the field to such a degree that the potential gradient at the screen grid tends to zero. The space-charge limited current density in a gridded ion device is given by the Child-Langmuir Law:

$$j = \frac{4\sqrt{2}}{9}\varepsilon_0\sqrt{\frac{e}{m_i}}\frac{V_a^{\frac{3}{2}}}{d^2} \qquad \text{(Eq. 4.8)}$$

In this expression the accelerating potential is given by V_a, and the separation distance between the screen and acceleration grids is given by d. The maximum achievable exhaust velocity is achieved by the conversion of electrostatic potential energy to ion kinetic energy so that:

$$u_e = \sqrt{\frac{2eV_a}{m_i}} \qquad \text{(Eq. 4.9)}$$

We next look for the limiting value of thrust per unit area. Noting that the mass flow rate is related to the extracted current density:

$$\frac{\dot{m}}{A} = j\frac{m_i}{e} \qquad \text{(Eq. 4.10)}$$

The thrust per unit area follows:

$$\frac{T}{A} = \frac{\dot{m}}{A}u_e = \frac{m_i}{e}j\sqrt{\frac{2eV_a}{m_i}} = \frac{8}{9}\varepsilon_0\frac{V_a^2}{d^2} \qquad \text{(Eq. 4.11)}$$

Finally, noting that the thruster power is simply half the product of thrust and exhaust velocity, we find that:

$$\frac{P}{A} = \frac{4}{9}\varepsilon_0\sqrt{\frac{2eV_a}{m_i}}\frac{V_a^2}{d^2} \qquad \text{(Eq. 4.12)}$$

We can see from this simple treatment the relationship between the inter-grid electric field, the thruster specific impulse and the area scaling characteristics of the thruster. In order to design a thruster for multi-megawatt output power, subject to a dimensional constraints typical of a launch vehicle it is necessary to increase the inter-grid field, $\frac{V_a}{d}$, or to increase the operating I_{SP}. In practice, the maximum electric field that can be sustained without excessive losses due to intermittent arcing between the grids is limited to 2.5 – 3.5 kV/mm. Increasing specific impulse with a fixed electric field by increasing the grid spacing is of little practical utility, however. Extracted ion beams should be well focused in order to provide a minimum of grid impingement and erosion. Tighter grid spacing will generally be more favorable for beam focusing.

These limitations of conventional gridded ion thrusters in migrating to higher thruster output powers may be offset through some recent developments in improved grid configurations [126]. A new dual-stage four-grid (DS4G) thruster configuration has been implemented and tested under contract to the ESA [127], and has been shown to provide a substantial improvement in performance over conventional designs. The essential strength of the staged configuration is that it effectively decouples the ion extraction and acceleration processes. This allows for both precise focusing of the extracted ion beam, while admitting the freedom to increase specific impulse, potentially to very high values. This circumvents the problem of creating thrusters of large diameter capable of utilizing megawatts of electrical power, while simultaneously providing a solution for missions that tend to optimize at extremely high values of specific impulse.

The large magnitude of the accelerator grid potential that is implied by this approach may pose additional problems for grid erosion. Charge exchange ions produced in the acceleration region may gain considerably more kinetic energy before impinging a grid in this case, thus undermining thruster lifetime. In order to evaluate the impact of these erosion processes, gridded ion thruster lifetime modeling is undertaken in this work for the dual-stage four grid thruster configuration. Simulations are completed using the JPL-developed CEX2D software package [128]. The approach and results of this study are detailed in Chapter 5.

4.3.2 Hall Thrusters

In a Hall-effect thruster, the accelerating potential that was provided by the extraction grids in the gridded ion thruster is replaced by a more extended zone between the anode, typically at the inlet of the thruster channel, and the external cathode located outside the channel. A conceptual schematic of a hall thruster is given in Figure 4.9, and an idealized solid model of an SPT-type thruster is shown in Figure 4.10.

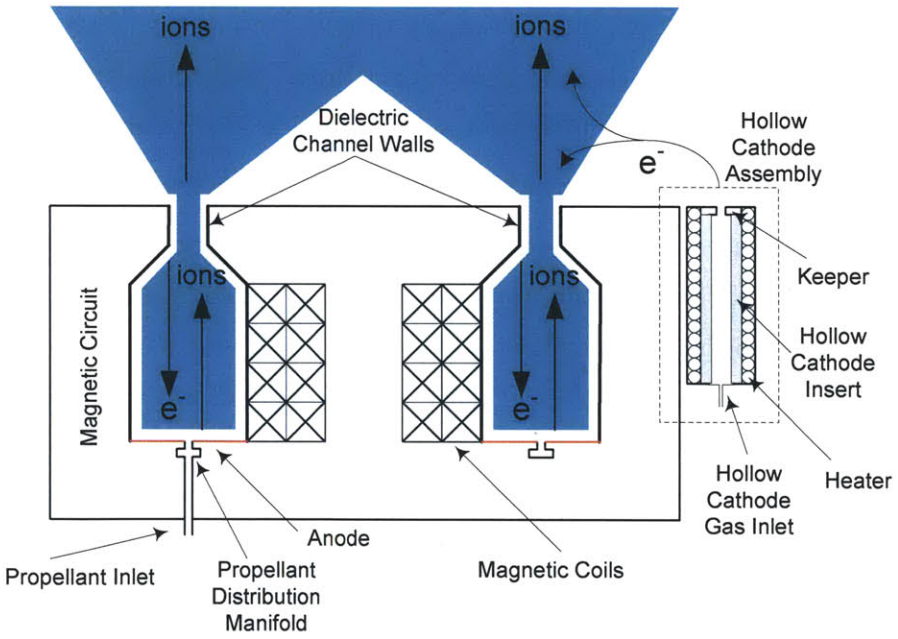

Figure 4.9. Conceptual schematic of an SPT-type Hall effect thruster

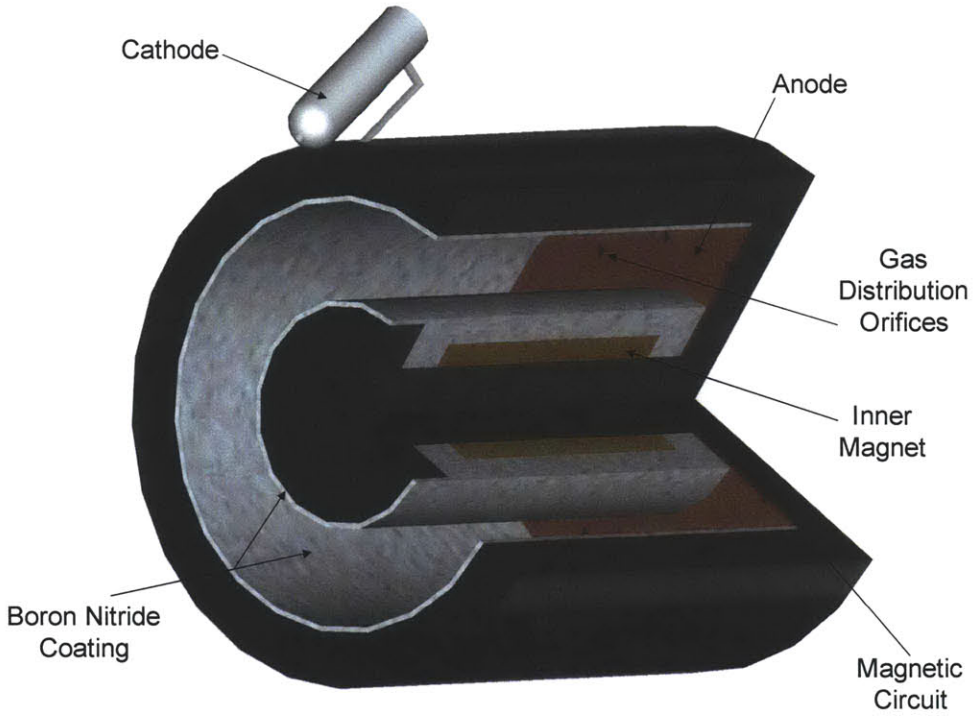

Figure 4.10. Idealized solid model of an SPT-type Hall effect thruster

The key advantage of the Hall thruster compared to the gridded ion thruster is the capability to extract more beam current. The presence of reverse electron flow in the channel means that the Hall thruster can circumvent the Child-Langmuir space charge limit, as the plasma flow remains quasi-neutral throughout the channel.

There are two configurations Hall thrusters generally assume. The first, the stationary plasma thruster or SPT-type has the configuration shown above. The second, called the Thruster with Anode Layer or TAL-type differs somewhat from the SPT-type in its configuration and construction, but both share common principles of operation. An excellent discussion of the similarities and differences in these two thrusters is provided in [129]. The fundamental difference between the SPT- and TAL-types of thrusters is the qualitatively different structure of the ion accelerating potential distribution. In the familiar SPT thruster, the thruster walls are comprised of an insulating material, and the accelerating potential is extended through the channel. In a TAL thruster the walls are metallic, and the accelerating potential is restricted to a thin layer in front of the anode.

The effect of the channel walls on the character of the accelerating potential can be understood in terms of the secondary electron emission from the walls. Qualitatively, for a given wall material (insulator or conductor) the wall potential is a function of the electron temperature, and may experience a change of sign above a critical electron temperature, Te*. Below this critical temperature, the walls are negatively biased and serve to repel electrons. Once the critical temperature is exceeded the number of secondary electrons becomes sufficiently great that the wall potential changes sign, absorbing a large

amount of energy and limiting further increase in electron temperature. This feedback effectively limits the electron temperature to Te*.

There has been some work in operating Hall-effect thrusters (HETs) at power levels of 50 – 100 kW, both in Russia and in the United States. In 2002 NASA's 457M SPT-type HET operated at 72 kW and achieved an overall I_{SP} of 2929s at a total efficiency of 58% [130]. Application of conventional scaling laws [131 – 138] to the design of a high power HET will result in a device whose dimension, and therefore mass, scales unfavorably in output power. There is, however, some evidence that an HET of fixed geometry can operate more efficiently at increased values of input power and mass flow rate [139]. One requisite for efficient operation of a Hall thruster is that the ratio of ionization region dimension, L, to the mean free path for ionization, λ_{ion}, must be large. A large number of ionizations must occur prior to electron diffusion through the ionization region. Because the mean free path for ionization is inversely proportional to the neutral density, which is itself proportional to the propellant mass flow rate for a constant channel area, it is, in principle, possible to drive the mean free path to very low values simply by increasing mass flow rate into the thruster.

In order to quantitatively analyze the effect that increased mass flow rate will have on HET performance and efficiency, a one-dimensional steady state model has been created to simulate thruster operation for a variable mass flow rate. This model and the results that have been obtained using it, are described in Chapter 6 of this work. The model is used not only to investigate performance variations for thrusters of fixed geometry and magnetic field configuration with increasing mass flow rate, but also to vary thruster dimensions and field topology to obtain optimum thruster performance. Based on these performance predictions, some general conclusions are drawn detailing potential improvements in the mass scaling of HETs for high power devices. Finally, the effect of this operational change on the achievable I_{SP} and efficiency can be quantitatively ascertained, and this analysis can inform the assessment of potential solutions for the projected needs of future high power missions.

4.3.3 Electrospray Thrusters

The final electrostatic thruster concept that will be surveyed in this work is the electrospray-type thruster. This concept may be thought of as representing a family of thrusters consisting of two variants. In the so-called droplet mode, relatively large masses of liquid with a bulk charge are extracted from the Taylor cone and accelerated through the potential drop between the cone tip and the extractor. The promise in this approach is improving the charge-to-mass ratio of the propellant quanta over those obtainable in atomic ions. In the ion mode, electrostatic fields become sufficiently intense to extract ions directly from the fluid bulk. Figure 4.11 provides an idealized model of a single-capillary emitter. The conducting fluid held in the capillary will be charged to a very high positive or negative value, and the

emitter grid will be biased to create an electrostatic field that will deform the fluid interface, eventually extracting charge from the fluid bulk.

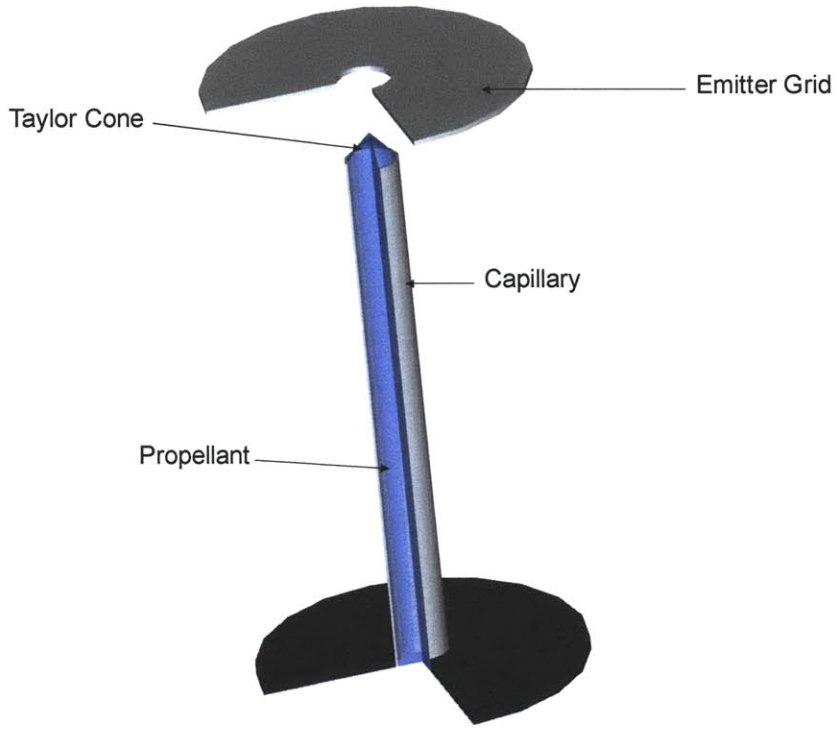

Figure 4.11. A single capillary colloid emitter. Deformation of the liquid surface occurs as a result of the potential difference between the conductive liquid and the emitter grid.

Electrospray thrusters have several unique properties that lend themselves to high power applications. First, electrospray thrusters avoid gas-phase ionization of propellant. Almost all other electric propulsion technologies rely on ionization of the propellant gas to allow electromagnetic conditioning of the flow. The process of ionization consumes a great deal of energy that is not recouped by the system. Second, because both positive and negative ions may be extracted, it is, in principle, possible to configure an electrospray system which does not require an external cathode to provide charge neutralization of the exhaust. As discussed in previous sections regarding electrostatic thrusters, the neutralizing cathode is a potentially lifetime-limiting component which requires additional input power to operate, and thus lowers the overall efficiency of an electrostatic system. Finally, electrospray hardware allows for some liberty in operating regime. Because electrospray hardware may be operated in the droplet or the ion regime by careful control of propellant flow rate and extraction voltage, this allows some tuning of the specific impulse, albeit at the expense of operating efficiency [140].

Some properties of electrospray thrusters present challenges to future high-power implementation. These devices historically provide very small values of thrust-per-emitter. However, recent research [141]

into new implementations and manufacturing methods for electrospray emitters offer some promise for very large arrays which might one day be useful in high-power applications. Finally, while considerations like grid impingement may not play a lifetime-limiting role in low-power implementations, at very high powers this phenomenon and its adverse impact on overall thruster efficiency may prove detrimental.

The challenges, then, associated with the development of electrospray thruster arrays are fundamentally problems of manufacturing and of scale. Limiting grid impingement to enhance thruster efficiency, manufacturing high density two-dimensional arrays of electrospray emitters and obtaining an automated, highly reproducible manufacturing process may allow for the development of very large thruster arrays consisting of many independent thruster modules. Coupled with the reduced propellant feed complexity of thruster emitters derived from porous substrates, the thin form factor of such arrays may allow the development of deployable thruster panels not unlike the folding deployable solar arrays frequently used for spacecraft power.

4.3.4 Cathodes for Electrostatic Thrusters

A complicating factor for scaling electrostatic ion devices to very high power levels is the need for very high performance neutralizing cathodes. In order to neutralize the thruster exhaust in a gridded ion engine, the cathode must produce an electron current equal to the beam current. In the case of the Hall thruster, the cathode must additionally provide a backstreaming electron population for propellant ionization.

In the case of the ion engine, we can express the propellant mass flow rate in terms of the beam current,

$$\frac{\dot{m}}{A} = \frac{J_B M_M}{e N_A} \qquad \text{(Eq. 4.13)}$$

The propellant molar mass is given by M_M, the elementary charge, e, and Avogadro's number, N_A. Substituting into the expression for beam kinetic power we obtain:

$$\frac{P_B}{A} = \frac{m}{2A} v_e^2 = \left(\frac{M_M}{2eN_A}\right) J_B v_e^2 \qquad \text{(Eq. 4.14)}$$

This allows us to finally express the total beam current in terms of the applied power and the specific impulse:

$$I_B = \frac{2P_B N_A e}{M_M g^2 I_{SP}^2} \qquad \text{(Eq. 4.15)}$$

For an ion engine operating with Xenon propellant at an I_{SP} of 3500 s and a beam power of 1 MW, for example, the required cathode current is I_B = 1.249 kA. Increasing the I_{SP} to 20,000 s, representative of DS4G capability, we find that the cathode current decreases to I_B = 38.2 A, a value typical for conventional thrusters. For Hall thrusters designed to operate at lower I_{SP} values and correspondingly higher currents, the development of cathodes to support the substantial discharge currents is a design need. Designs for hollow cathodes operating at up to 100 A have been tested at NASA Glenn [142], but additional development and testing will certainly be required to field cathode designs capable of meeting the needs for future low-I_{SP} high-power electrostatic thruster applications.

4.4 Electromagnetic Thrusters

Electromagnetic thrusters differ from the electrothermal and electrostatic thrusters discussed thus far in that they make use of electromagnetic body forces to accelerate fluid elements to very high velocity. In this section three thrusters will be discussed. The first, the magnetoplasmadynamic (MPD) thruster is a steady operating device, typically comprised of a coaxial channel in which current density is applied radially, resulting in azimuthal magnetic fields. Interaction of the radial current and azimuthal magnetic field accelerates the conducting medium. The other two devices considered in this section include the pulsed plasma thruster, which operates using principles similar to those of the MPD thruster, and the pulsed inductive thruster.

4.4.1 Magnetoplasmadynamic Thrusters

In a coaxial magnetoplasmadynamic thruster, body forces on the conductive plasma arise as the result of the interaction between a radially applied current and the resulting induced azimuthal magnetic field. The equation of motion for a particle with charge e in arbitrary electric and magnetic fields is given by:

$$\vec{F} = e\left(\vec{E} + \vec{v} \times \vec{B}\right) \qquad \text{(Eq. 4.16)}$$

Per unit volume of charge, this expression becomes:

$$\vec{f} = \sum_j n_j e_j \left(\vec{E} + \vec{v_j} \times \vec{B}\right) \qquad \text{(Eq. 4.17)}$$

In a quasi-neutral plasma it must be true that:

$$\sum_j n_j e_j \vec{E} = 0 \qquad \text{(Eq. 4.18)}$$

Finally, we know that the current can be written:

$$\vec{j} = \sum_j n_j e_j \vec{v_j} \qquad \text{(Eq. 4.19)}$$

This gives an applied body force per unit volume:

$$\vec{f} = \vec{j} \times \vec{B} \qquad \text{(Eq. 4.20)}$$

The thrust force associated with a simple coaxial MPD scales according to Maecker's law [7, 143]:

$$F = \frac{\mu_0 I^2}{4\pi} \ln \frac{R_A}{R_C} \qquad \text{(Eq. 4.21)}$$

In this formulation, R_A is the anode inner radius, and R_C is the cathode radius. It is important to note that the thrust force is relatively insensitive to thruster dimension, and has very favorable current scaling, as I^2. We can see the approximate exhaust velocity implied by this scaling:

$$u_e = \frac{\mu_0 I^2}{\dot{m} 4\pi} \ln \frac{R_A}{R_C} \qquad \text{(Eq. 4.22)}$$

The Mach number then will scale as the quantity $\frac{I^2}{\dot{m}\sqrt{M_M}}$. Operation of self-field MPD thrusters demonstrates that there is a critical value of this parameter above which thruster operation becomes unstable. The theoretical basis for this so-called "onset" phenomenon has been developed extensively in the literature [144-150]. The limiting value of the onset criterion is a function of the thruster geometry and configuration, and higher values of efficiency and exhaust velocity are obtained for configurations with higher critical values of the onset criterion. Onset effectively limits the amount of current that can be realized in MPD thrusters, thereby limiting achievable exhaust velocity and thruster efficiency. Current concentrations at the anode lip and cathode root also have deleterious effects on achievable lifetime. The problem of realizing thruster designs that overcome the lifetime and efficiency limitations typical of conventional MPD devices, then, reduces to designing thruster geometries that maximize the critical onset criterion.

In an idealized coaxial MPD thruster, as shown in Figure 4.12, the thrust force in Eq. 4.21 develops as a result of the radial current density. The azimuthal magnetic field required to produce axial acceleration is induced by this current density. It becomes apparent that high values of current density are required for optimum thruster operation, requiring very high power. There has been some success in operating MPD thrusters in which an applied axial magnetic field is used to stabilize the discharge, as shown in Figure 4.13. The best performance achieved by an AF-MPD thruster operating in the megawatt range to date is

the Osaka University MY-III [151-156]. Between 1987 and 1995, this thruster operated at powers ranging from 0.48 – 3.875 MW, and values of specific impulse between 1650-9415 s, using H_2, N_2 and Argon as propellants. The highest demonstrated performance of the MY-III thruster was achieved using H_2 propellant with an applied field of 0.2 T, and a total input power of 3.63 MW. Operating with these conditions, the device achieved a specific impulse of 9415 s at a total efficiency of 47%.

In Chapter 7 of this work, the viability of channel contouring will be examined as a means to delay the onset phenomenon in self-field MPD devices operating in the 1-10 MW power range. Several geometries will be developed and evaluated based on the simulated device efficiency. Magnetohydrodynamic (MHD) fluid simulations will be implemented in the MACH2 modeling software, as detailed later.

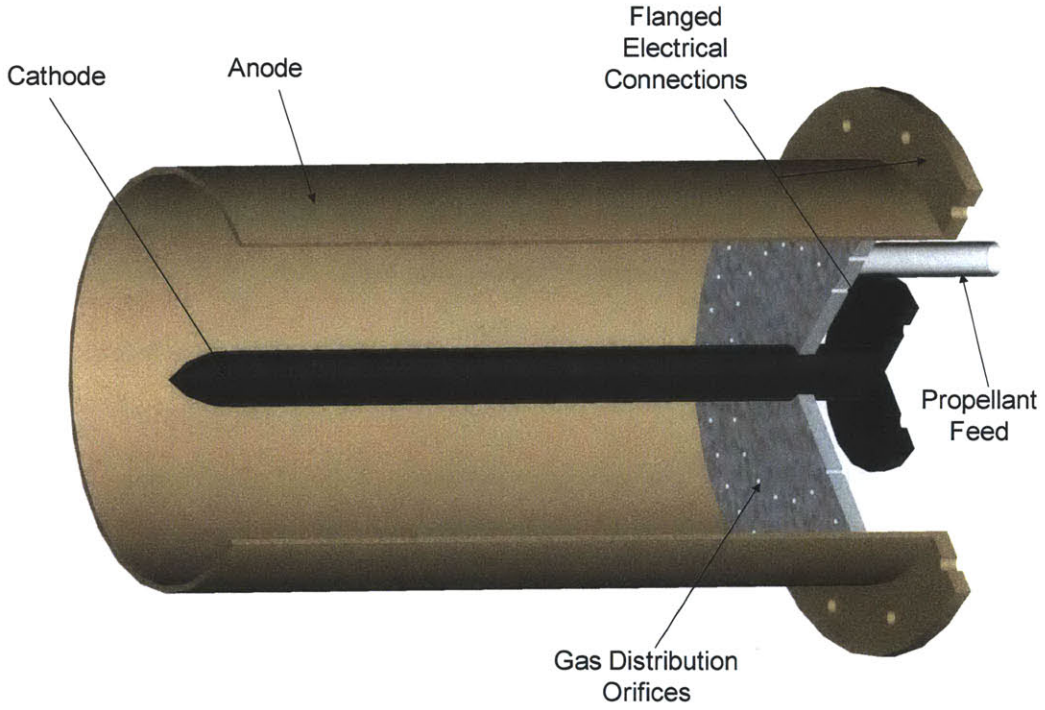

Figure 4.12. Coaxial magnetoplasmadynamic thruster

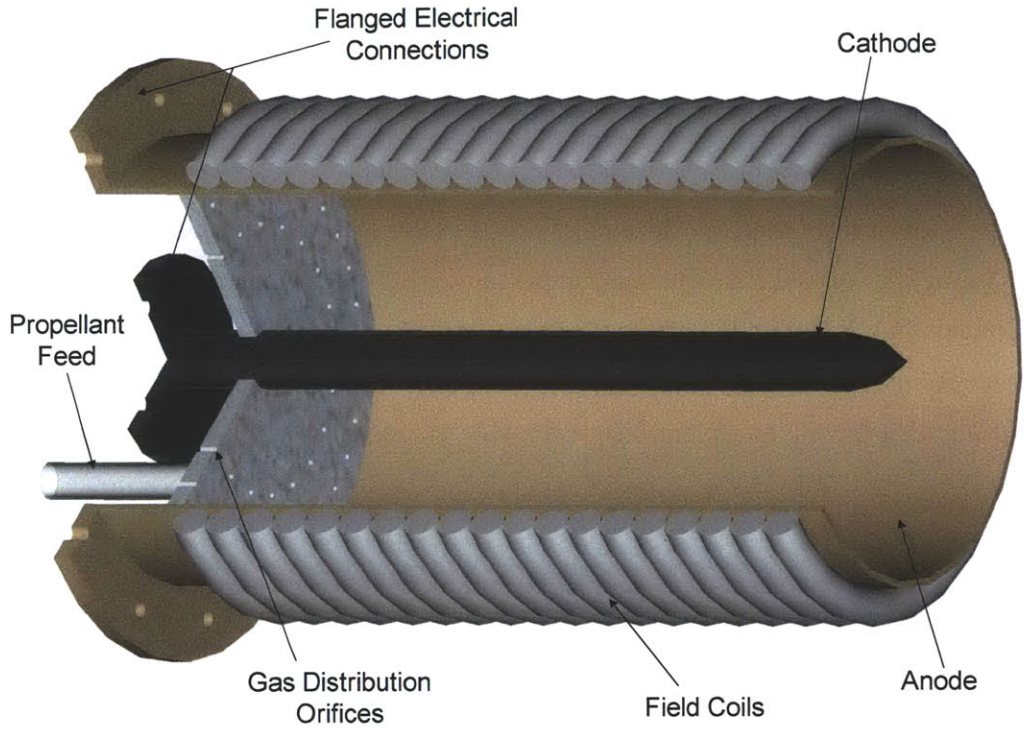

Figure 4.13. Applied field MPD

4.4.2 Pulsed Plasma Thrusters

Pulsed plasma thrusters (PPT) can the thought of as an unsteady variant of the MPD thruster described in the previous section. These devices use a solid propellant, typically Teflon or polyethylene, which is ablated during a current pulse applied between the device anode and cathode. The ablated propellant material is partially ionized by the current pulse, and accelerated to high exhaust velocity according to the same principles that govern MPD operation. An idealized model of a pulsed plasma thruster is shown in Figure 4.14, below.

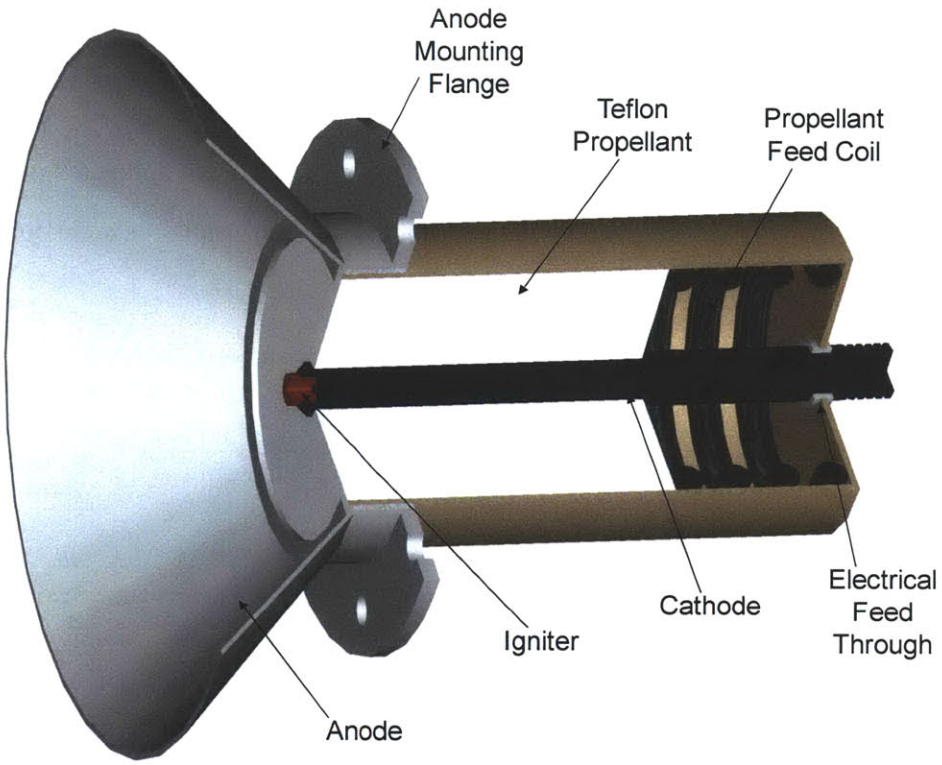

Figure 4.14. Coaxial pulsed plasma thruster using solid Teflon as propellant feedstock

An excellent overview of pulsed plasma thruster operation, as well as details of many operational thrusters is provided in [157]. Pulsed plasma thrusters are appealing for some applications because they can be implemented in a robust, monolithic system that incorporates non-toxic, solid phase propellant with a simple feed system. Output power and thrust can be varied by simply modulating the pulse rate of the device.

These devices have been used extensively for attitude and orbital control in satellite applications since the 1960s, including the Zond-2, the Lincoln Experimental Satellite (LES) series, the Transit Improvement Program (TIP), as well as the US Navy's NOVA program.

Efficiency of these pulsed devices is typically quite low, in the neighborhood of 10%, and specific impulse, similarly, is somewhat below the value that is shown to be useful for megawatt-level NEP missions, being typically less than 2000s. An additional element of risk common to all pulsed devices is the lifetime of the highly stressed energy storage components in the power processing unit, which must endure an extremely large number of repetitions if used for primary propulsion. These characteristics of PPTs make them ideally suited to attitude and orbital control applications, but undermine their utility for multi-megawatt primary electric propulsion.

4.4.3 Pulsed Inductive Thrusters

The pulsed inductive plasma accelerator concept can be traced back to the early 1960s [158, 159]. The concept was further developed by Loveberg and Daily beginning in the 1970s [160] explicitly for application to space propulsion. The thruster is an unsteady electromagnetic device which uses the induced electric field associated with a rapidly pulsed inductor to ionize and accelerate neutral propellant gas.

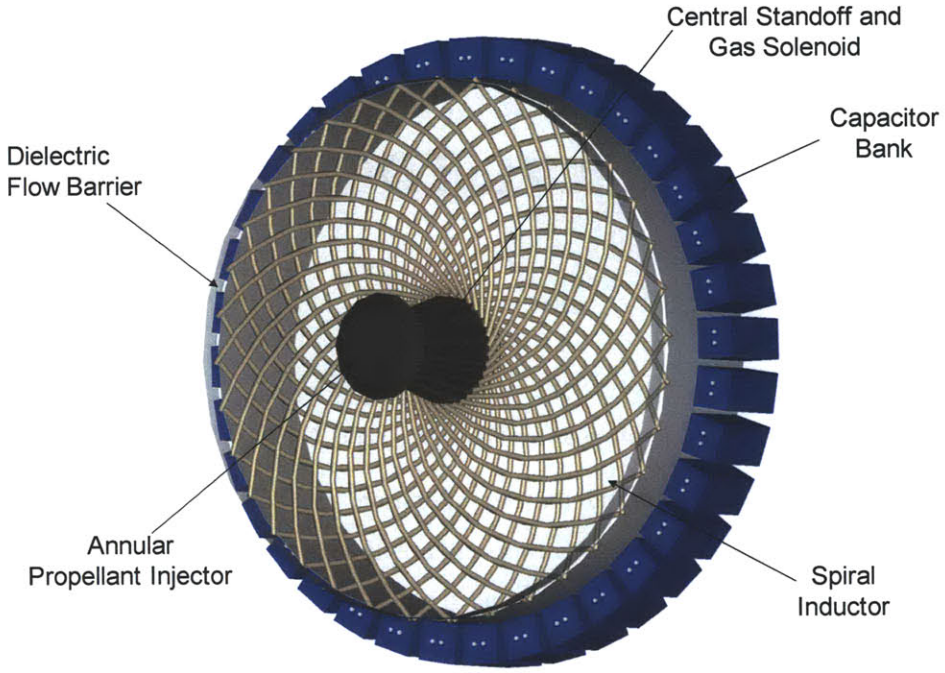

Figure 4.15. Idealized pulsed inductive thruster layout

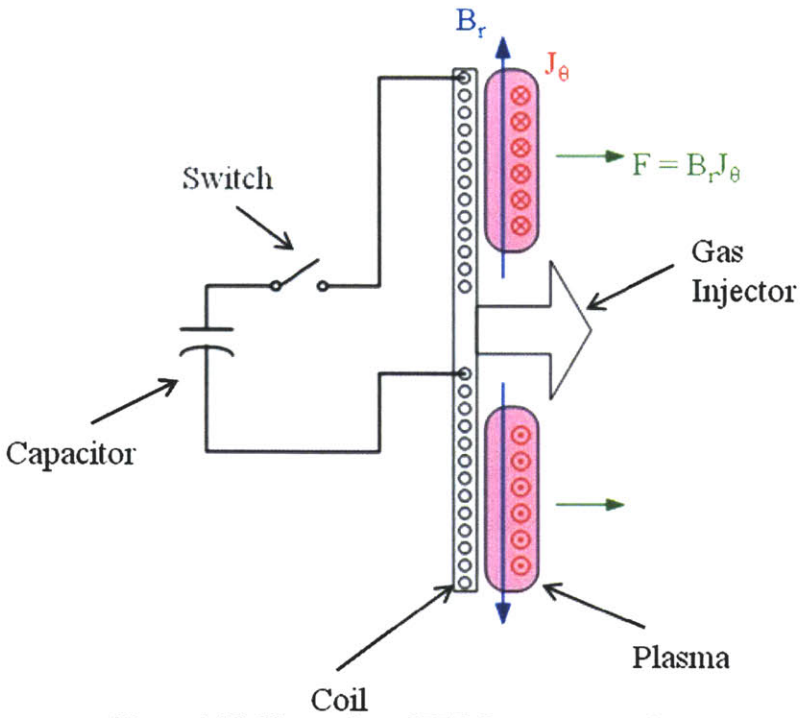

Figure 4.16. Illustration of PIT thruster operation

The layout of the PIT device is shown in Figure 4.15, and device operation is illustrated in cross section in Figure 4.16. Propellant gas is metered through a solenoid valve in the central standoff and is fed through the annular injector at an oblique angle toward the spiral. A large bank of energy storage capacitors discharges through the flat inductive spiral when the propellant is optimally distributed over the coil. This discharge generates a radial magnetic field with a large time-rate-of-change. This ionizes the neutral gas and generates an azimuthal electric field and current according to Faraday's law of induction:

$$\nabla \times \vec{E} = -\frac{\partial \vec{B}(\vec{r},t)}{\partial t} \qquad \text{(Eq. 4.23)}$$

For a generated magnetic field that is purely radial, the resulting θ-component of the electric field will drive an azimuthal current, J_θ. This current will, in turn, interact with the radial magnetic field to produce an axial force as described in Eq. 4.20. This means of accelerating plasma has several advantages for scaling to higher power. First, the PIT is an electrodeless concept. This means that it is possible to operate the PIT so that plasma is never in contact with thruster materials. This feature may eliminate many of the material lifetime limitations associated with hot plasma confinement. Second, as with the PPT, the operating power level for the PIT can be increased or decreased simply by modifying the pulse rate.

The specific impulse of a PIT thruster can be varied by varying the injected shot mass. Flight scale device demonstrations [161] have yielded 0.1 N-s of impulse per shot with variable specific impulse between 2500 – 8500 s at approximately 50% overall efficiency.

Demonstrated PIT performance and efficiency overlaps somewhat with other high thrust options including Hall effect thrusters, MPD thrusters, and possibly plasma phase electrothermal concepts. The advantage of PIT is primarily the promise of very long lifetime in the absence of plasma-contacting surfaces. Lifetime estimates are complicated somewhat by the extremely large number of pulses required to achieve the total impulse for missions likely to incorporate megawatt-level electric propulsion. For example, in order to meet the propulsive requirements of the manned Mars mission outlined in Chapter 3, a PIT thruster with comparable performance to the demonstrator described in [161] would execute 49 billion pulses at an average rate of approximately 1.8 kHz. In order to reduce the pulse rate to 100 Hz, a rate more realistic for a flight article, 18 such devices would be required.

4.5 Conclusions

Based on the derived propulsive requirements for missions of interest utilizing near-term nuclear power plant technologies, there is a developmental need for electric propulsion systems capable of producing total impulse values in the range of 0.5-5.0 GN-s with output powers typically in the range of 1.0 – 5.0 MW. Missions tend to optimize around relatively high values of specific impulse, $I_{SP} \geq 13{,}000$ s, with correspondingly low thrust and high total lifetime, or around relatively low I_{SP}, between 5000 – 6000 s, at high thrust, but with substantially reduced lifetime requirements.

In order to meet these systematic needs, design evolutions for conventional electric propulsion devices with the lowest perceived risks have been identified. In the area of high-I_{SP}, long life thruster development, the concept of multi-stage gridded ion thrusters seems to hold a great deal of promise. In order to evaluate this design evolution, erosion modeling of dual-stage gridded ion thrusters is undertaken. The two-dimensional simulations detailed in Chapter 5 allow not only an estimation of the achievable lifetime, but an evaluation of the performance limitations of these multi-grid thrusters.

Next, the performance and efficiency of high power Hall thrusters operating at high mass flow rate is evaluated for potential to meet the needs of high thrust applications. A one-dimensional model is developed that incorporates the pertinent plasma physics, and includes a rudimentary treatment of wall effects. The model allows for the variation of upstream properties, including mass flow rate, as well as thruster geometry and magnetic field topology. Sensitivities of device performance to variations in design are evaluated in Chapter 6.

Finally, the inherently high-power nature of MPD thrusters makes these devices attractive for high thrust missions as well. The greatest challenge in implementing these devices for next-generation space

missions is in improving their relatively low efficiency. Variations in thruster geometry are evaluated in Chapter 7 using a computational MHD simulation package to observe the effects of channel contouring in delaying the onset phenomenon that limits MPD thruster efficiency.

Conclusions derived from this work are provided in Chapter 8.

Chapter 5

Dual Stage Gridded Ion Thrusters

5.1 Introduction

Some missions enabled by high power nuclear electric propulsion systems optimize at values of specific impulse in excess of 20,000 seconds. These include missions with low initial mass, requiring low propellant mass, or missions that require exceptionally large total velocity increments unachievable with conventional electric propulsion systems. A variation on conventional gridded ion thruster design may provide a means of achieving exhaust velocities favorable for these applications while maintaining minimum technological and developmental risk. By utilizing a two-stage, four-grid optics design which decouples the extraction and acceleration processes in the grid assembly, the exhaust velocities achievable with gridded ion engines can be substantially increased. However, increased intergrid spacing in these systems poses the potential problem of enhanced charge exchange production and concomitant grid erosion, which will limit lifetime and undermine thruster utility. In this work, the issue of grid erosion in dual stage four grid ion thrusters is explored using a modified version of the JPL-developed CEX2D software package. Preliminary results indicate that with careful grid design, lifetimes comparable to those available in conventional systems are achievable in dual-stage four-grid configurations.

5.2 Background

The very high values of specific impulse around which some missions tend to optimize places a tight constraint on the type of EP system that might be used. Theoretical work [126] and recent experimental work [127] indicate that the specific impulse of traditional gridded ion engines can be substantially

improved upon by utilizing a two-stage system that effectively decouples the extraction and acceleration stages of the grid assembly. Contrasting configurations of such the three- and four-grid system are shown in Figures 5.1 and 5.2.

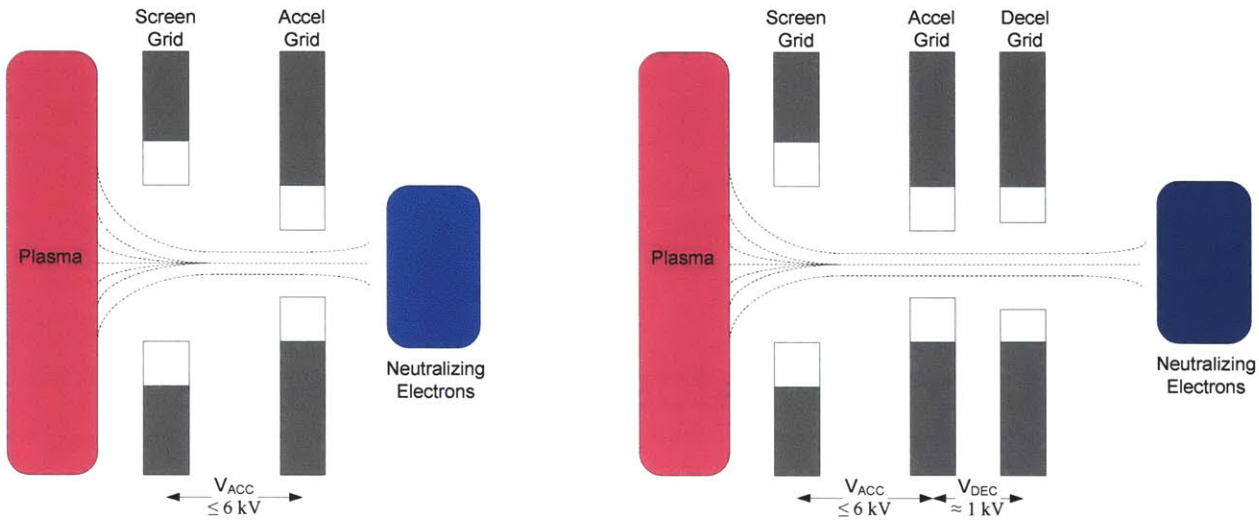

Figure 5.1. Conventional 2- and 3- grid arrangement for ion engines featuring a single extraction/acceleration stage

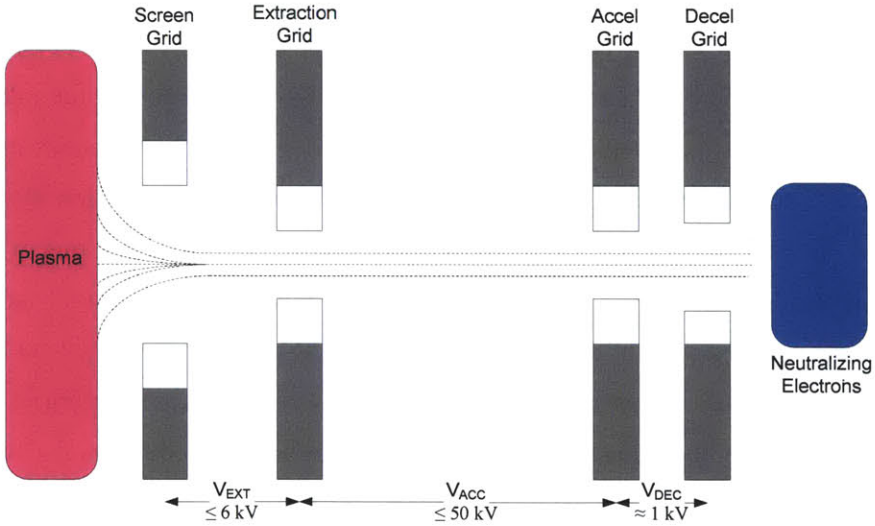

Figure 5.2. Optics geometry for the dual-stage configuration. This arrangement effectively decouples the extraction and acceleration processes, allowing for much higher exhaust velocity.

Because of its ability to generate very high values of specific impulse, dual-stage engines will tend to have lower thrust-to-weight ratios at a given power, necessitating longer thrust durations, and making engine lifetime a critical performance metric. Higher beam potentials present in dual-stage systems could make sputtering of the downstream grid structures due to charge-exchange ions created in the acceleration stage especially problematic.

Based on the results of the Deep Space 1 FT2 30,000 hour life test, there appear to be three critical lifetime limiting processes at work in gridded ion engines [162]. These include erosion of the discharge cathode keeper plate, neutralizer cathode orifice and keeper tube wall, and accelerator grid. One noteworthy finding in post-test evaluation of the neutralizer cathode keeper tube wall was that the surface with direct line of sight to the exhaust beam had eroded by 20% of the initial thickness. This erosion rate was found to be proportional to the square of the exhaust beam potential, making it a process of concern for high I_{SP} multi-grid designs. The most severely compromised component of the engine was the accelerator grid structure. Pits from the center of the grid webbing out to approximately 6.6 cm radially, compromised the full thickness of the grid structure. Furthermore, chamfering of acceleration grid apertures increases total electron backstreaming, degrading efficiency and performance [163].

Grid erosion is thought to represent the most detrimental process to enhanced thruster lifetime in conventional gridded ion engines. In order to make a quantitative assessment of the utility of dual-stage gridded ion thrusters for future high power electric propulsion applications, the effects of grid erosion must be well characterized. Because of the strong dependence of sputtering yield on incident ion energy, it is unlikely that application of erosion and lifetime data for conventional gridded ion engines to dual-stage devices will provide an accurate representation of operational behavior.

Several grid erosion software packages developed at NASA JPL [128,165,166] provide a promising means of characterizing the erosion processes at work in such unconventional gridded systems. The CEX2D software package is able to iteratively solve for the potentials and ion trajectories in order to predict the operating characteristics, erosion rates and erosion patterns associated with a given geometry of ion optics. Current modeling of conventional gridded ion thrusters provides strong predictive power for estimating thruster lifetime due to limits imposed by grid erosion [166]. These data can be used both to inform initial estimates for overall thruster operational lifetime, and to evaluate the impact of variations in grid design parameters on erosion characteristics and lifetime. The CEX2D simulation tool can accommodate changes in throttle conditions at user-specified time points during the simulated operational life. The program is written in FORTRAN, and provides a graphical user interface implemented in an Excel spreadsheet. The code simulates single aperture ion beamlet trajectories and ion currents resulting from impingement of charge exchange ions on grid surfaces.

Geometry and potentials for the ion optics to be simulated can be defined from the spreadsheet GUI. Additional required inputs include some user-defined plasma parameters such as the upstream neutral density, the discharge chamber electron temperature, and the downstream plasma potential. Some required inputs defining engine performance are the single aperture beamlet current, the total beam current and the propellant utilization efficiency, and the maximum allowable electron backstreaming

efficiency. Executing a case from the GUI casts the input data in the required format for compatibility with the CEX2D core, and generates a batch file to execute the simulation.

5.3 Algorithm Description

Beam ions enter the computational domain traveling axially at their Bohm velocity. Initial ion radial velocity is taken to be zero. The inter-grid neutral gas density is computed from a Monte-Carlo algorithm which calculates the Clausing factor appropriate to the grid geometry. This algorithm is detailed in Appendix G of [167]. Charge exchange ions are created by the resonant interaction of beam ions with this neutral background. Sputter yields are computed for these charge exchange ions, as well as for directly impinging beam ions. Using these yields, the required time to remove all the grid mass from a single computational grid node is determined. Finally, the beam ion trajectories, charge exchange ion production and erosion are computed using the new perturbed grid geometry for the next iteration. A flow diagram for the CEX2D program is given in Figure 5.3, below.

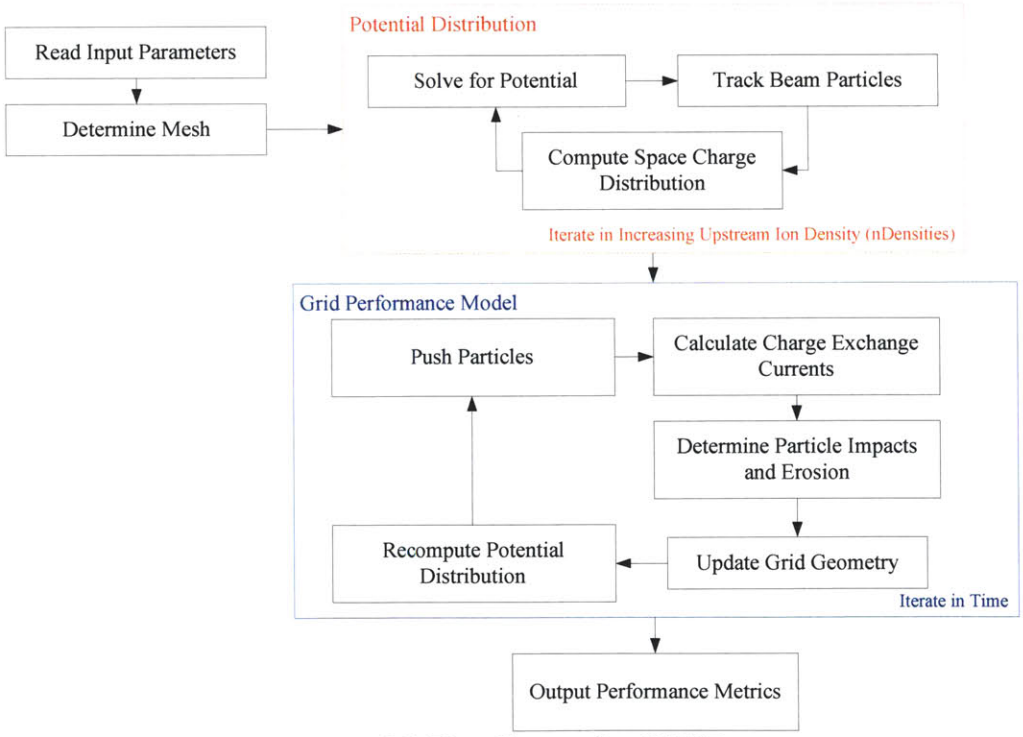

Figure 5.3. Flow diagram for CEX2D

5.4 Model Physics

As indicated in the algorithm description above, the potential distribution is first computed over a control volume using Gauss's law. Each control volume is bounded by the surface described by its adjacent radial and axial mesh lines, as shown in Figure 5.4.

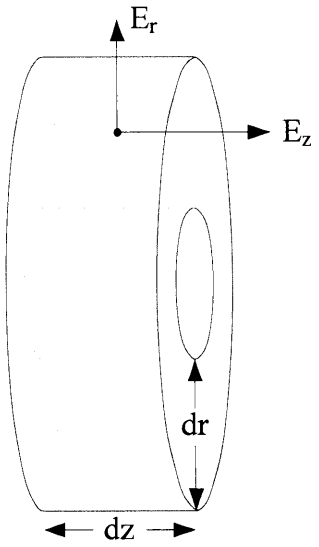

Figure 5.4. Differential volume element formed by the intersection of mesh lines in cylindrical coordinates

From Gauss's Law,

$$\frac{q}{\epsilon_0} = \oint \vec{E} \cdot d\vec{n} \qquad \text{(Eq. 5.1)}$$

The electric field is then assumed to be centered and the edges of the control volume element, and is given by the differences in potential across its adjacent volume element per differential length element.

$$E_r(i,j) = \frac{\phi_{i+1,j} - \phi_{i,j}}{dr} \qquad \text{(Eq. 5.2)}$$

$$E_z(i,j) = \frac{\phi_{i,j+1} - \phi_{i,j}}{dz} \qquad \text{(Eq. 5.3)}$$

Differential radial increments are denoted with the subscript i, and differential axial increments are denoted with the subscript j. Integrating over the control volume gives:

$$2\pi E_r(i,j)\left(r_{i,j} + 0.5dr\right)dz - 2\pi E_r(i-1,j)\left(r_{i,j} - 0.5dr\right)dz + 2\pi\left(E_z(i,j) - E_z(i,j-1)\right)r_{i,j}dr = -\frac{q}{\epsilon_0} \qquad \text{(Eq.5.4)}$$

In cylindrical coordinates this can be expressed:

$$a\phi_{i+1,j} + b\phi_{i,j+1} + c\phi_{i,j} + d\phi_{i-1,j} + e\phi_{i,j-1} + f = 0 \qquad \text{(Eq. 5.5)}$$

$$a = -2\pi(i - 0.5)dz \qquad \text{(Eq. 5.6)}$$

$$b = -2\pi(i-1)\frac{dr^2}{dz} \quad \text{(Eq. 5.7)}$$

$$c = -(a+b+d+e) \quad \text{(Eq. 5.8)}$$

$$d = -2\pi(i-1.5)dz \quad \text{(Eq. 5.9)}$$

$$e = b = -2\pi(i-1)\frac{dr^2}{dz} \quad \text{(Eq. 5.10)}$$

$$f = \frac{q}{\epsilon_0} \quad \text{(Eq. 5.11)}$$

To this system of equations we can apply the boundary conditions at $r = 0$ and $r = r_b$. Here we assume that the electric field $E_r(r = 0) = E_r(r = r_b) = 0$. These relations and conditions are sufficient to solve for the potential distribution within the computational domain. In the first iteration, the code computes the vacuum solution for the potential. In successive iterations, the upstream chamber plasma density is increased, producing a given beamlet current, and the potential is recomputed. This procedure is repeated until the desired beamlet current is produced.

Particle depletion is determined based on locality. For axial positions $z > z_{MAX}$ and $z < 0$ particles leave the computational domain. If particles enter a grid structure they also leave the simulation, and this process contributes to grid erosion. Particles are created with uniform spacing and velocity upstream of the screen grid.

5.5 Neutral Gas Model

The neutral gas density distribution model used in CEX2D was updated to accommodate the four-grid geometry. This is necessary to facilitate calculations of charge exchange ion production and grid erosion. In this model, the neutral gas density is assumed to be divided into three regions. Because of the large spacing between the extractor and accelerator grids, this region is treated as a neutral gas plenum, in which the neutral population is essentially isotropic. This geometry is shown in Figure 5.5.

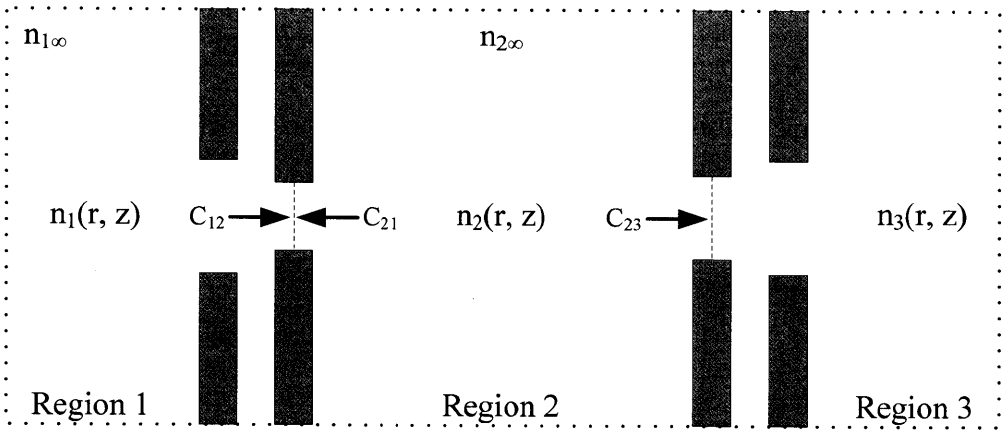

Figure 5.5. Geometry used for computing neutral particle density distribution

The neutral particle densities in each of these regions are given by:

$$n_1(r,z) = n_{1\infty}\left(1 - \frac{1}{2}D_{12}(r,z)\right) + \frac{n_{2\infty}}{2}D_{12}(r,z) \qquad \text{(Eq. 5.12)}$$

$$n_2(r,z) = n_{2\infty}\left(1 - \frac{1}{2}D_{12}(r,z) - \frac{1}{2}D_{23}(r,z)\right) + \frac{n_{1\infty}}{2}D_{12}(r,z) \qquad \text{(Eq. 5.13)}$$

$$n_3(r,z) = \frac{1}{2}f_{OPEN}n_{2\infty}\left(1 + \left(\frac{1}{f_{OPEN}} - 1\right)D_{23}(r,z)\right) \qquad \text{(Eq. 5.14)}$$

In this formulation, the function $D_{AB}(r,z)$ describes the downstream distribution behavior of a non-collisional gas with a known upstream density passing through an orifice. The background density of neutrals in the tank is given by $n_{n_{tank}}$. The open area fraction, denoted f_{OPEN}, is the ratio of beamlet area to total grid face area. The value of $n_{1\infty}$ is simply the user-defined neutral density far upstream in the chamber. The value $n_{2\infty}$ can be derived from continuity. In the steady state, the rate of particles entering into region 2 must be balanced by the rate of particle outflow:

$$\frac{n_{1\infty}\bar{c}}{4}C_{12}A_2 = \frac{n_{2\infty}\bar{c}}{4}C_{21}A_2 + \frac{n_{2\infty}\bar{c}}{4}C_{23}A_3 \qquad \text{(Eq. 5.15)}$$

The Clausing factors, C_{AB}, modify this flux based on the orifice geometries of area A_i. The derivation of the Clausing factors for each interface will be discussed in a subsequent section. The formulation in Eq. 5.15 assumes a uniform effective value for the neutral densities in regions 1 and 2. These are the same plenum values used in Eqs. (5.12-5.14) above. Assuming a constant thermal speed for neutral particles, we can obtain the effective neutral density in region 2 as a function of the Clausing factors and orifice areas bounding the plenum:

$$n_{2_\infty} = n_{1_\infty}\left(\frac{A_1 C_{12}(r_1, r_2)}{A_1 C_{12}(r_1, r_2) + A_3 C_{23}(r_2, r_3)}\right) \qquad \text{(Eq. 5.16)}$$

Figure 5.6 illustrates the typical resultant neutral distribution using this model, and Figure 5.7 shows the on-axis neutral density profile. In both figures the downstream direction is +z.

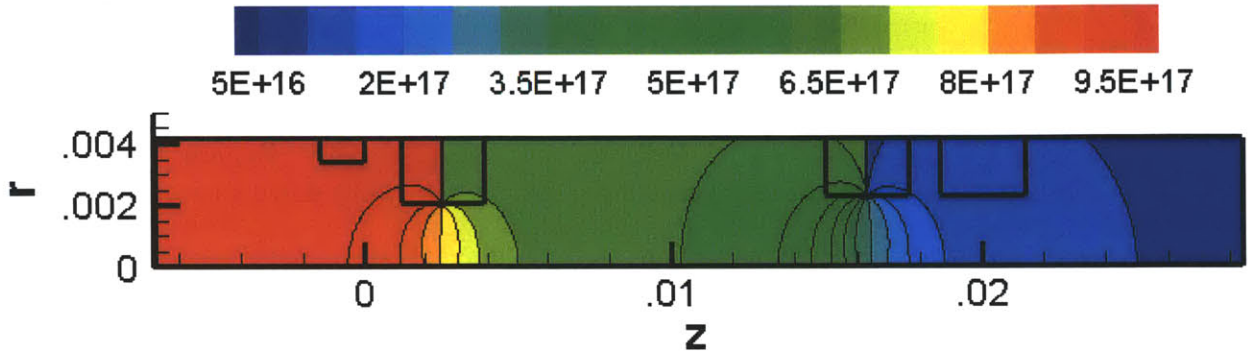

Figure 5.6. Neutral density distribution in a typical dual-stage four-grid configuration

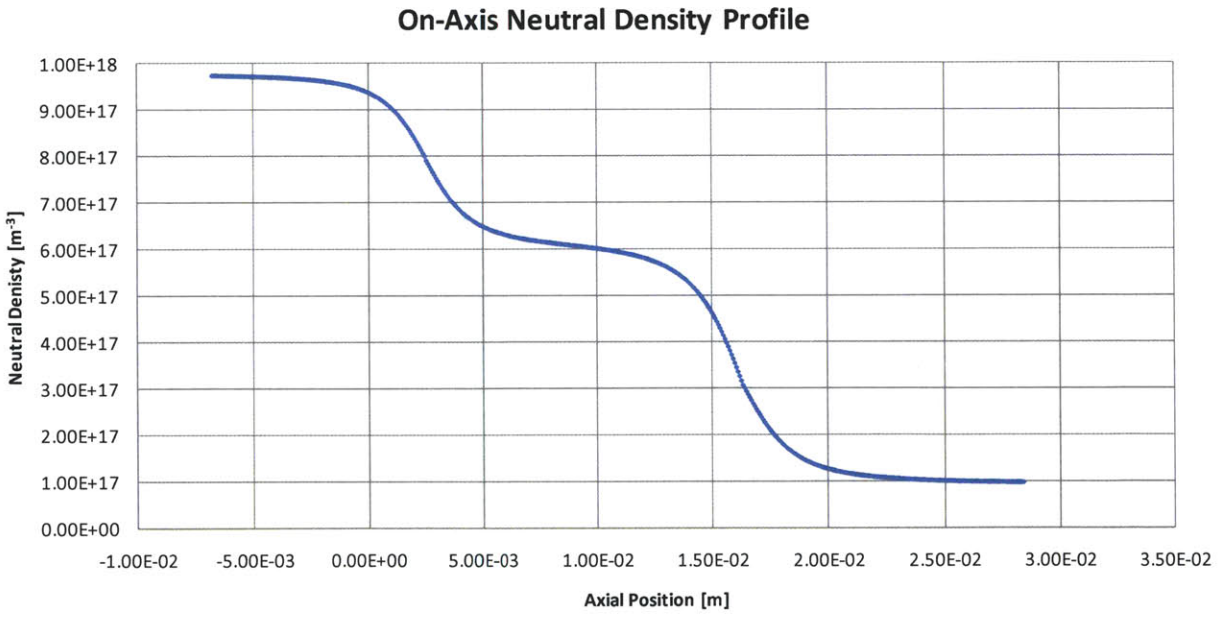

Figure 5.7. On-axis neutral density profile for model shown in Figure 5.6

5.5.1 Clausing Factor

The Clausing factor provides a means of quantifying the transmission probability of particles through grids of a given geometry. The ideas used in framing the analysis of neutral behavior in the inter-grid spaces of ion engines were originally developed by Knudsen [168] in the study of rarefied flow through long thin tubes and through thin orifices. The analysis was later refined [169], and extended to short tubes

of arbitrary cross section by Dushman [170]. Subsequent refinement of Dushman's treatment for short tubes by Clausing [171] yielded the theoretical framework which underlies the analysis that follows.

For highly rarified, isotropic, non-collisional particle distributions, the number of particles passing through a tube from one region 1 into region 2 is given by:

$$\dot{n}_n = C_{12}\Gamma_n A_1 = C_{12}\frac{n_n \bar{c}}{4}A_1 \qquad \text{(Eq. 5.17)}$$

The modifying factor, C_{12}, is referred to in this discussion as the Clausing factor, and the neutral particle flux is given by Γ_n. The Clausing factor is strictly a function of the geometry of the transmission region.

In CEX2D, the Clausing factor is computed using a Monte Carlo approach. Particles are injected into the computational domain from the upstream boundary and with a cosine distribution of velocity components. Once injected, the time of flight required for a particle to traverse the entire computational domain is determined. Using this time of flight, and given the known components of velocity, one can determine whether the particle will reach the computational boundary, or impact a grid surface before. Particles that intercept grid surfaces are re-emitted with a cosine distribution, and the process iterates. Particles that eventually reach the upstream or downstream boundary of a given region will enter a subsequent upstream or downstream region. Given a statistically significant number of particles, the ratio of particles escaping a region through the downstream boundary to the number of particles being simulated provides a quantitative representation of transmission efficiency. The geometry for the computation of the Clausing factor is shown in Figure 5.8, below.

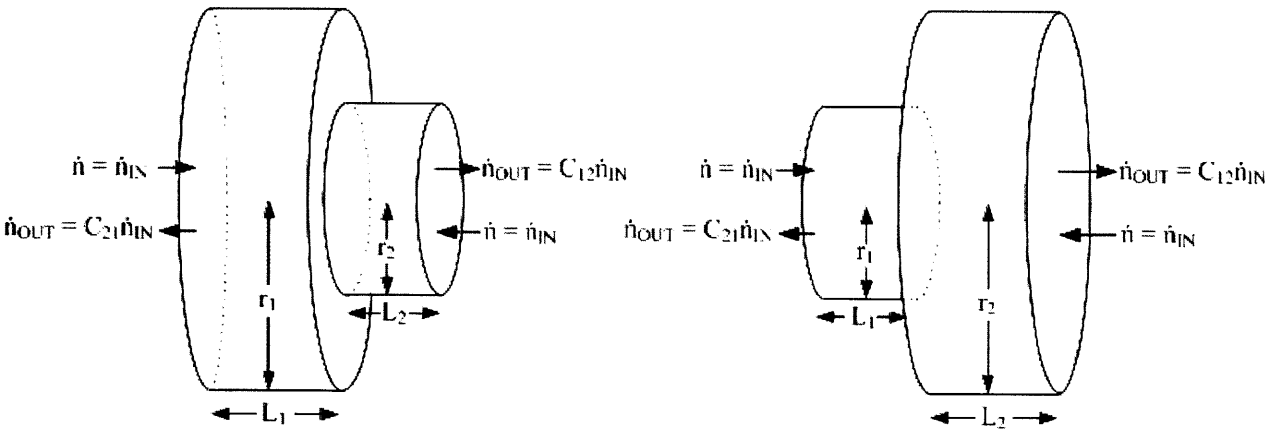

Figure 5.8. Geometric construction for Clausing factor calculations

The time of flight for particles traveling between arbitrary initial and final radial positions, r_0 and r_f can be derived from the kinematic relation with constant velocity:

$$(v_x t - r_0)^2 + (v_y t)^2 = r_f^2 \qquad \text{(Eq. 5.18)}$$

So that the time of flight is given simply by

$$t = \frac{v_x r_0 + \sqrt{(v_x^2 + v_y^2) r_f^2 - v_y^2 r_0^2}}{v_x^2 + v_y^2} \quad \text{(Eq. 5.19)}$$

In the particular cases of computing the time of flight from one region to another, the radial dimensions of the two given regions will replace r_0 and r_f.

The CEX2D software was modified to accept arbitrary upstream and downstream grid geometries. In previous versions of the software, the model for the Clausing factor presupposed an upstream grid radius greater than the downstream grid radius. While this is accurate for modeling conventional optics, in order to accommodate a four-grid system, the restrictions on grid radii have been relaxed.

5.6 Sputter Yield Model

As an alternative to, or in conjunction with the use of dual-stage four-grid systems to increase specific impulse, it may be helpful to utilize propellant gases of lower atomic mass. In order to characterize the erosion of grid materials under bombardment by lighter propellant gases, a simple piecewise model for sputter yield was implemented based on the model developed in [172] at lower energies, and a simple logarithmic fit for a variety of ion and target parameters. The model has the functional form

$$Y = Q \cdot Y_N(K, E) \quad \text{(Eq. 5.20)}$$

In this formulation, Q is the yield factor, Y_N is the energy function, and K is the energy parameter, given by

$$K = \frac{\gamma}{E_B} \quad \text{(Eq. 5.21)}$$

Where E_B is the surface binding energy, which is approximated by the heat of sublimation for the grid material. The factor γ is a reduced mass, given by:

$$\gamma = \frac{4 M_1 M_2}{(M_1 + M_2)^2} \quad \text{(Eq. 5.22)}$$

The masses M_1 and M_2 denote the incident ion and the target masses respectively. Finally, the sputtering yield is expressed in terms of a normalized incident ion energy:

$$E' = KE = \frac{E}{E_B}\gamma \qquad \text{(Eq. 5.23)}$$

In terms of these parameters, the empirically derived expression for sputtering yield can be written [172]:

$$Y \sim \gamma^{\frac{4}{3}} M_2^{\frac{8}{9}} E_B^{-\frac{2}{3}} E'^{-\frac{1}{2}} (E'^{\frac{5}{6}} - 1) \qquad \text{(Eq. 5.24)}$$

The units of the target mass in this expression are AMU. Comparison against tabulated data indicates that this model is accurate for values $E' < 20$, and ion-target combinations for which $M_1/M_2 < 1$. For neon ions incident to molybdenum grids, this corresponds to an incident energy of approximately 240 eV. In the case of carbon grids, this model for sputtering data is not appropriate, as the condition that $M_1/M_2 < 1$ is violated. In this case, the higher energy model is extended to lower incident ion energies, as discussed below.

In the region of higher energy, an analytic fit to the sputtering behavior of neon ions incident on both graphite and molybdenum targets was derived for this work from experimental data [173]. Results are given in Figure 5.9.

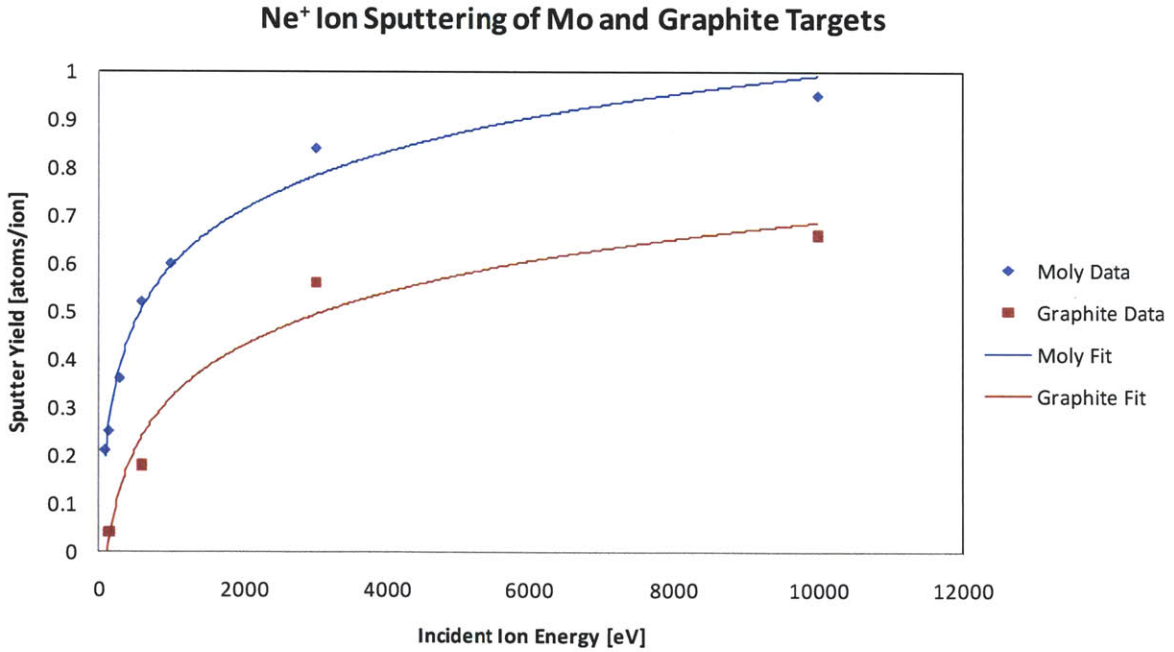

Figure 5.9. Sputtering yields for molybdenum and graphite under low energy neon ion bombardment

The expression for molybdenum is given by:

$$Y_{Mo} = 0.1722 \ln(E) - 0.5948 \qquad \text{(Eq. 5.25)}$$

The expression for graphite yield has an identical form:

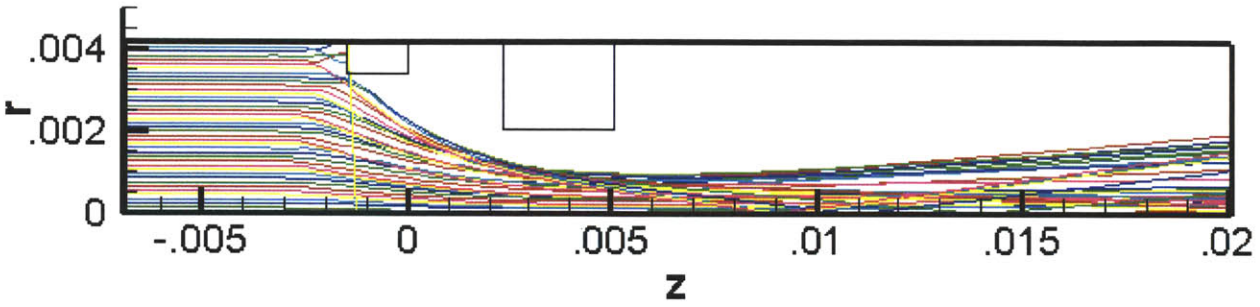

Figure 5.10. Tracer particle trajectories in the NEXIS geometry illustrating beam focusing; dimensions are in meters

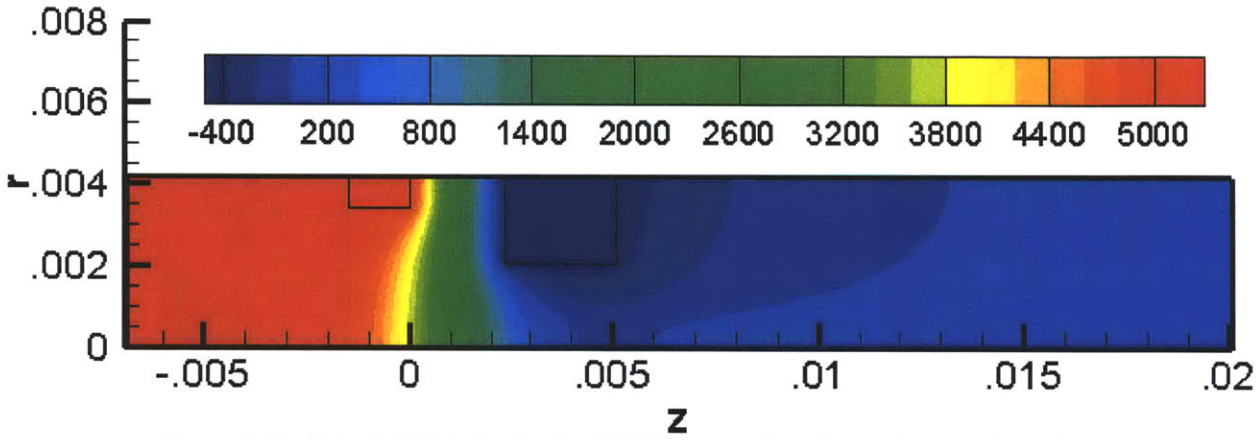

Figure 5.11. Potential Distribution for NEXIS geometry; dimensions are in meters

A composite illustration of the NEXIS grid erosion in time is given in Figure 5.12. The reproduction of these simulations from work originally performed in the design of the NEXIS system has served both as a troubleshooting tool in addressing issues related to functionality and operation of the CEX2D software package, as well as in providing a baseline for the evolutionary design of dual-stage systems. The NEXIS grid configuration will serve as an extraction stage for subsequent evolutionary designs utilizing a downstream acceleration grid.

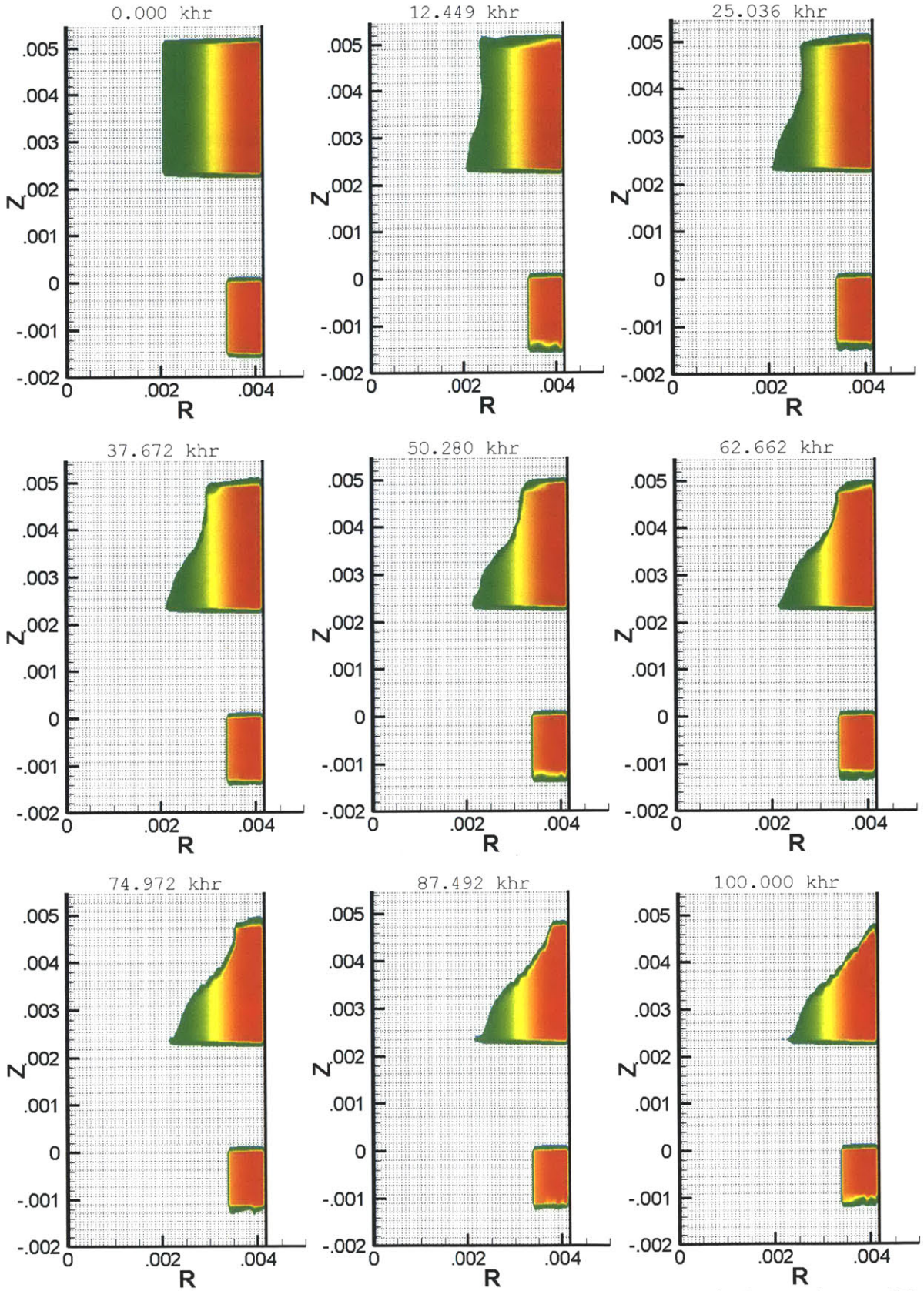

Figure 5.12. Composite simulated erosion profile of NEXIS ion optics under nominal operating conditions; dimensions are in meters

To accomplish the proposed grid erosion modeling, these codes are being modified to accommodate the dual-stage geometry. Several configurations using variable acceleration stage grid separation distances and applied potential are being investigated to observe the effect of these design variables on overall erosion processes.

5.7.1 Optics Design

In developing the simulated optics for a notional future high-I_{SP} dual-stage gridded ion thruster, the primary focus was on achieving high performance with long lifetime at a minimum of developmental risk. To that end, a series of parametric studies was conducted to evaluate the characteristics of several configurations. The family of configurations studied represents an incremental evolution on the NEXIS thruster ion optics. In order to determine grid spacing, the electric field between the screen and extractor grids, and the extractor and accelerator grids was varied. The goodness of each optics design can be evaluated on the basis of the current intercepted by each of the grids at the beginning of life (BOL). Additionally, some qualitative assessment of the beam focusing characteristics of each grid design can be conducted by inspection of the tracer particle trajectories. Geometries used in this evaluation are tabulated in Table 5.2.

Case	$E_{S\text{-}X}$ [kV/mm]	$E_{X\text{-}A}$ [kV/mm]	ϕ_B [V]	$\Delta\phi_{S\text{-}X}$ / $\Delta\phi_B$	$d_{S\text{-}X}$ [mm]	$d_{X\text{-}A}$ [mm]	$d_{A\text{-}D}$ [mm]	ϕ_S [V]	ϕ_X [V]	ϕ_A [V]	ϕ_D [V]	r_S [mm]	r_X [mm]	r_A [mm]	r_D [mm]	I_B [mA]	I_b/I_{CL}
1	2.5	2.5	30000	0.1	1.2	11.0	1.0	29975	26975	-500	0	3.415	2.05	2.292	2.292	1.437	0.200
2	2.5	2.5	30000	0.15	1.8	10.4	1.0	29975	25475	-500	0	3.415	2.05	2.292	2.292	1.173	0.200
3	2.5	2.5	30000	0.2	2.4	9.8	1.0	29975	23975	-500	0	3.415	2.05	2.292	2.292	1.270	0.250
4	2.5	2.5	30000	0.25	3.0	9.2	1.0	29975	22475	-500	0	3.415	2.05	2.292	2.292	1.817	0.400
5	2.5	2.5	30000	0.3	3.6	8.6	1.0	29975	20975	-500	0	3.415	2.05	2.292	2.292	1.866	0.450
6	2.5	2.5	30000	0.35	4.2	8.0	1.0	29975	19475	-500	0	3.415	2.05	2.292	2.292	1.920	0.500
7	3	2.5	30000	0.05	0.5	11.6	1.0	29975	28475	-500	0	3.415	2.05	2.292	2.292	0.439	0.030
8	3	2.5	30000	0.1	1.0	11.0	1.0	29975	26975	-500	0	3.415	2.05	2.292	2.292	1.551	0.150
9	3	2.5	30000	0.15	1.5	10.4	1.0	29975	25475	-500	0	3.415	2.05	2.292	2.292	1.689	0.200
10	3	2.5	30000	0.2	2.0	9.8	1.0	29975	23975	-500	0	3.415	2.05	2.292	2.292	1.463	0.200
11	3	2.5	30000	0.25	2.5	9.2	1.0	29975	22475	-500	0	3.415	2.05	2.292	2.292	1.962	0.300
12	3.5	2.5	30000	0.05	0.4	11.6	1.0	29975	28475	-500	0	3.415	2.05	2.292	2.292	0.597	0.030
13	3.5	2.5	30000	0.1	0.9	11.0	1.0	29975	26975	-500	0	3.415	2.05	2.292	2.292	1.408	0.100
14	3.5	2.5	30000	0.15	1.3	10.4	1.0	29975	25475	-500	0	3.415	2.05	2.292	2.292	2.299	0.200
15	3.5	2.5	30000	0.2	1.7	9.8	1.0	29975	23975	-500	0	3.415	2.05	2.292	2.292	1.991	0.200
16	3.5	2.5	30000	0.25	2.1	9.2	1.0	29975	22475	-500	0	3.415	2.05	2.292	2.292	2.048	0.230
17	3.5	2.5	30000	0.3	2.6	8.6	1.0	29975	20975	-500	0	3.415	2.05	2.292	2.292	2.438	0.300
1A - Xe	2.5	2.5	30000	0.1	1.2	11.0	1.0	29975	26975	-500	0	3.415	2.05	2.292	2.3	1.400	0.195
1B - Ne	2.5	2.5	30000	0.1	1.2	11.0	1.0	29975	26975	-500	0	3.415	2.05	2.292	2.3	3.570	0.195

Table 5.2 Table of Parametric Study Cases

In Table 5.2, the screen, extraction, accelerator, and decelerator grids are represented by the subscripts $S, X, A,$ and D. The average electric field, grid spacing, potentials and aperture radii are represented by E, d, ϕ and r. Values in red represent parameters that were varied in the evaluation. The case numbers highlighted in yellow denote configurations that exhibited good beam focusing, no direct beam

impingement on grid surfaces and a minimum of charge exchange current collection. The electric field in the extraction stage was varied between 2.5 – 3.5 kV/mm. For each value of electric field, the fraction of the total potential drop occurring across the extraction stage was varied between 0.05 – 0.35. In the case of $E_{S-X} = 3.0$ kV/mm, direct beam impingement on the accelerator grid structure was observed for extractor potential fractions greater than 25%. This was also observed for the case of $E_{S-X} = 3.5$ kV/mm at an extractor potential fraction of 35% and $E_{S-X} = 2.5$ kV/mm and extractor potential fraction of 5%. These cases were therefore excluded.

The current fraction given in the last column is the fraction of the ideal space-charge limited current which was extracted in the beamlet. This parameter was varied ad hoc for each case by varying the chamber plasma density to obtain good beam focusing.

Best performance was obtained for all values of extraction field when 10% of the total potential drop occurred across the extraction stage. Based on assessment of the performance of each of the geometries outlined in Table 2, an iteration of the geometry for case 1 was chosen. This geometry was run using both neon and xenon propellants in simulated long-duration tests. Both cases indicate that grid lifetimes in excess of 100,000 hours are possible. These results are discussed further in the sections that follow.

Finally, the potential distribution and tracer particle trajectories for Case 1A have been included in Figures 5.13 and 5.14, below.

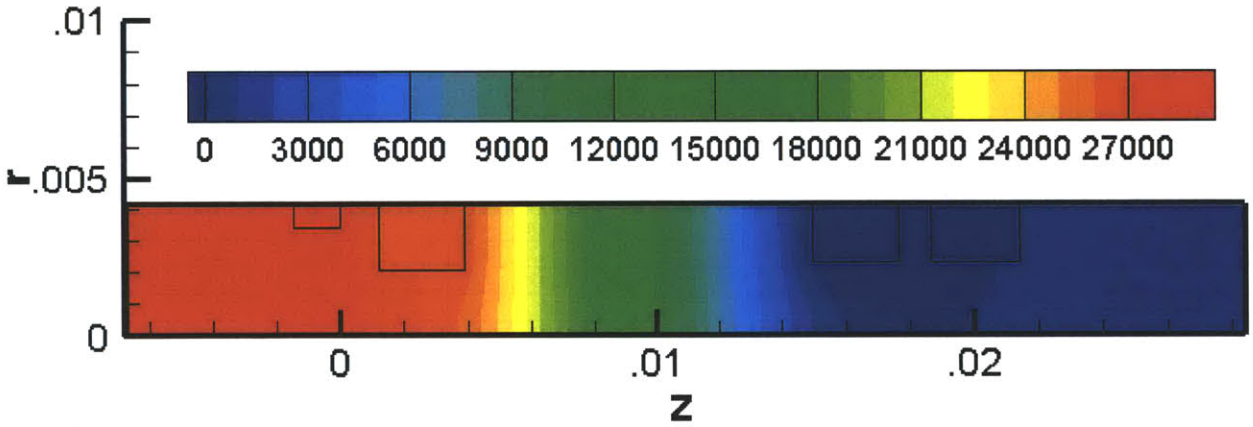

Figure 5.13. Potential Distribution for Case 1A; dimensions are in meters

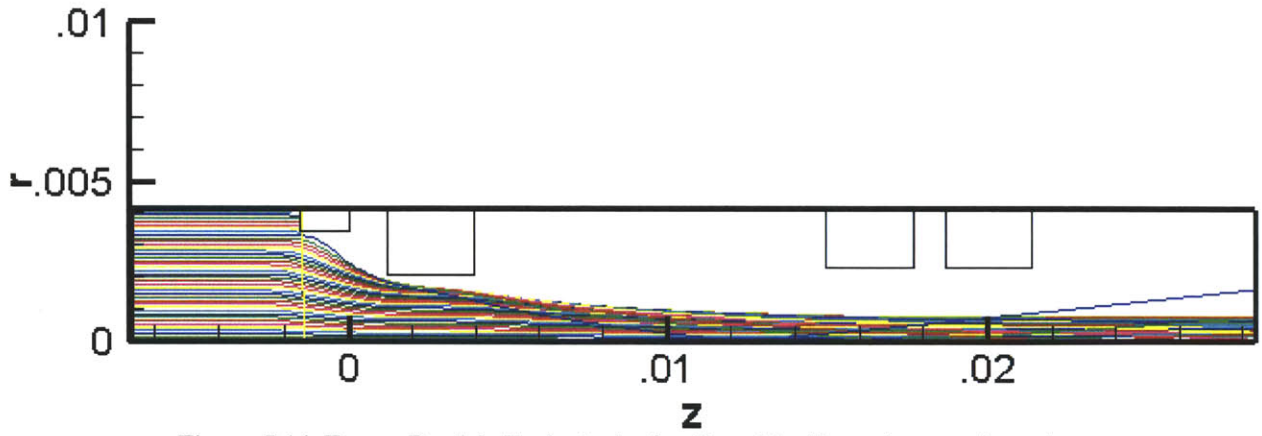

Figure 5.14. Tracer Particle Trajectories for Case 1A; dimensions are in meters

5.7.2 Erosion Results

Erosion modeling results for typical dual-stage four-grid configurations are shown in Figures 5.15 and 5.16. In Figure 5.15, the propellant gas is xenon. In Figure 5.16 the propellant gas is neon. One notable characteristic common to both simulations is the uneven barrel erosion of the third grid. This may be caused by activation of charge exchange ions downstream of the third grid centerline and subsequent acceleration into the third grid.

In the case of xenon, the extracted current per hole is 1.4 mA and the I_{SP} is approximately 21,000 s. Using the same hole spacing and grid diameter of the Nexis thruster, this corresponds to a total output power of approximately 200 kW. In the case of neon, the extracted current is 3.57 mA, corresponding to an output power of 500 kW at an I_{SP} of approximately 54,000 s.

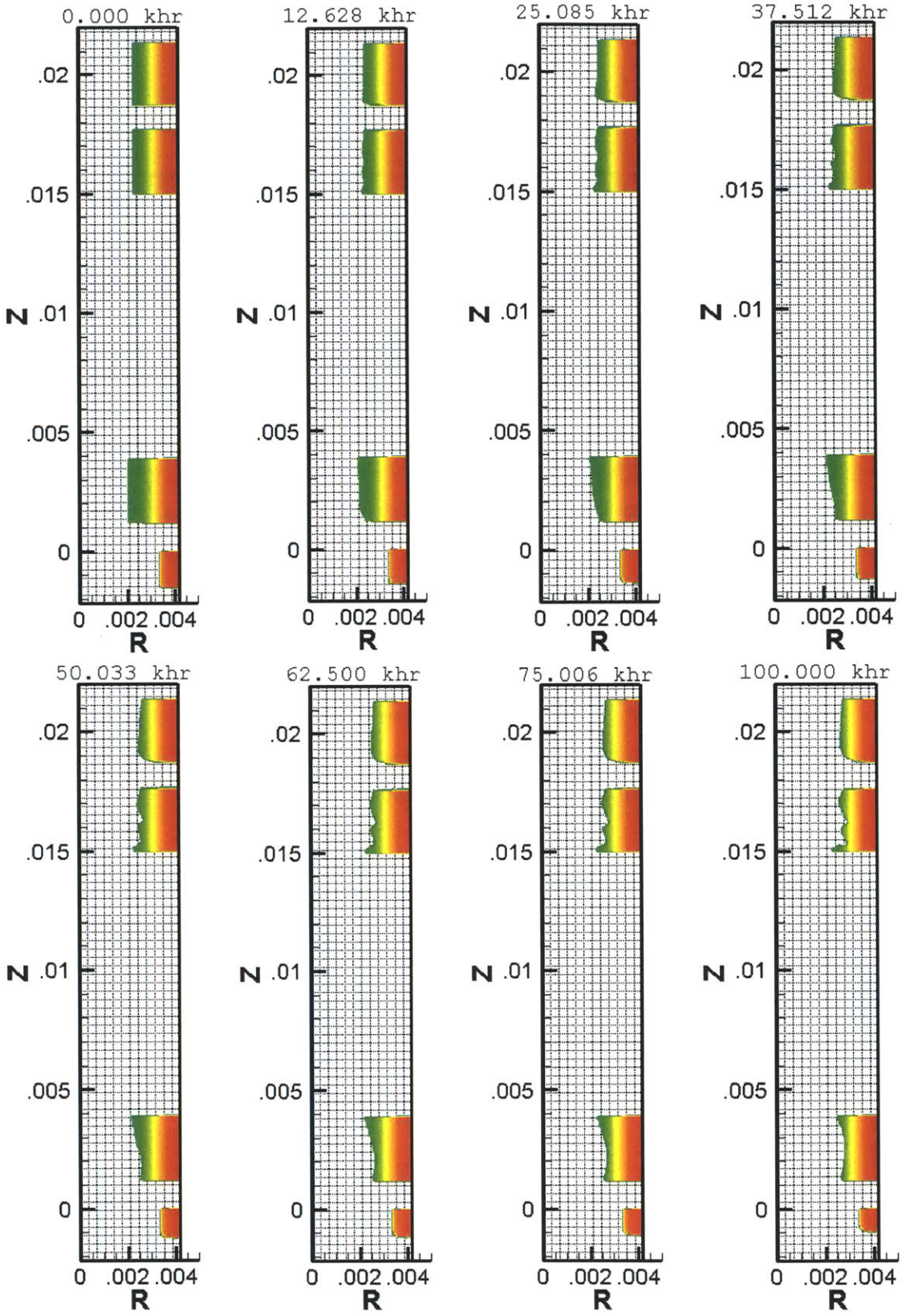

Figure 5.15. Composite Illustration of the Progression of Dual-Stage Grid Erosion using Xenon Propellant; dimensions are in meters

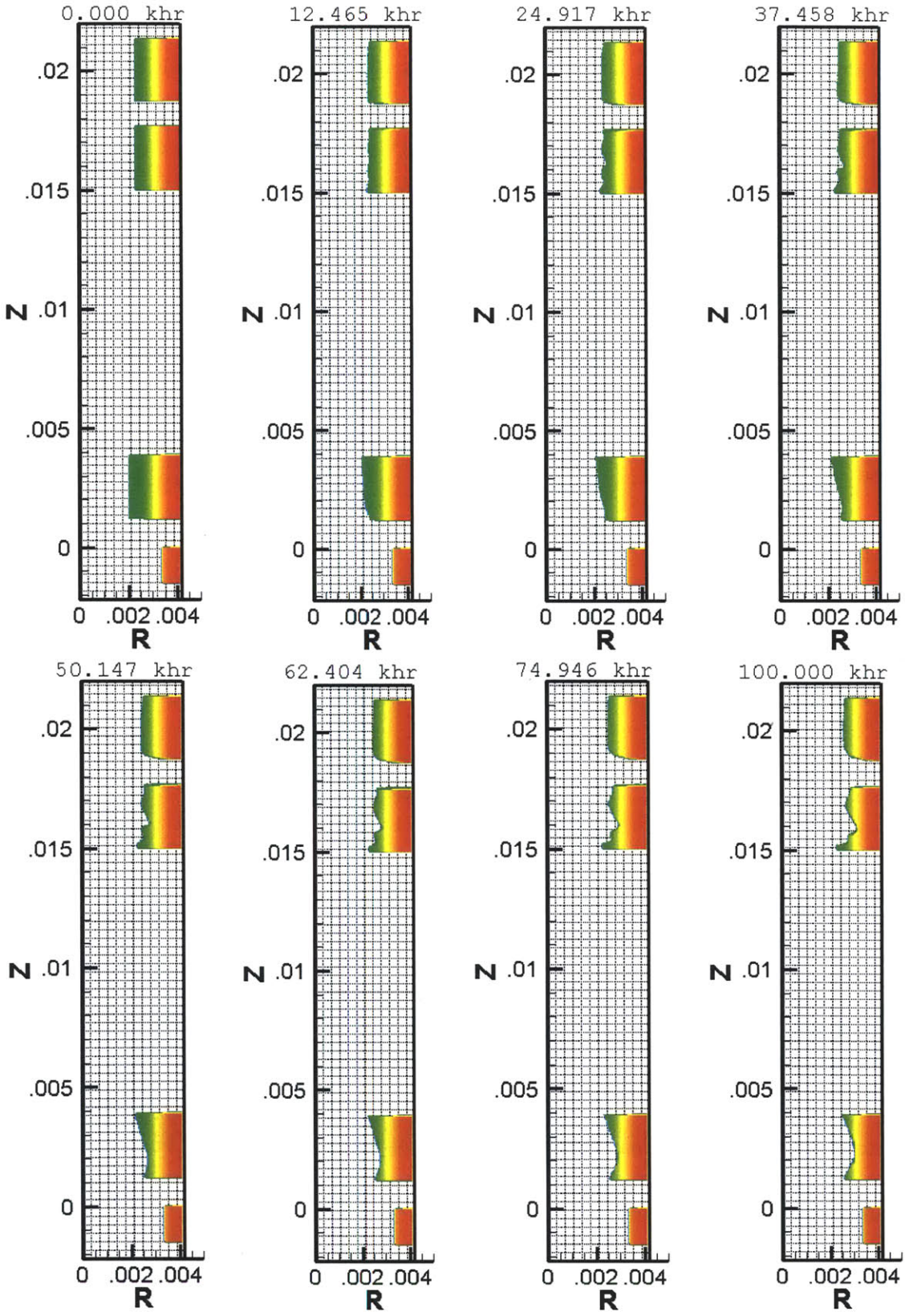

Figure 5.16. Composite Illustration of the Progression of Dual-Stage Grid Erosion using Neon Propellant; dimensions are in meters

5.7.3 Charge Exchange Production

In the absence of direct beam impingement on grid surfaces, grid erosion will be primarily due to bombardment by unfocused, high energy charge exchange ions activated in intergrid spaces. The CEX2D program is able to simulate charge exchange ion production, predict flight trajectories and determine impingement points. Because barrel erosion of grid surfaces is the dominant erosion type, it is of particular interest to identify activation regions for ions contributing to that process. This is shown in Figure 5.17.

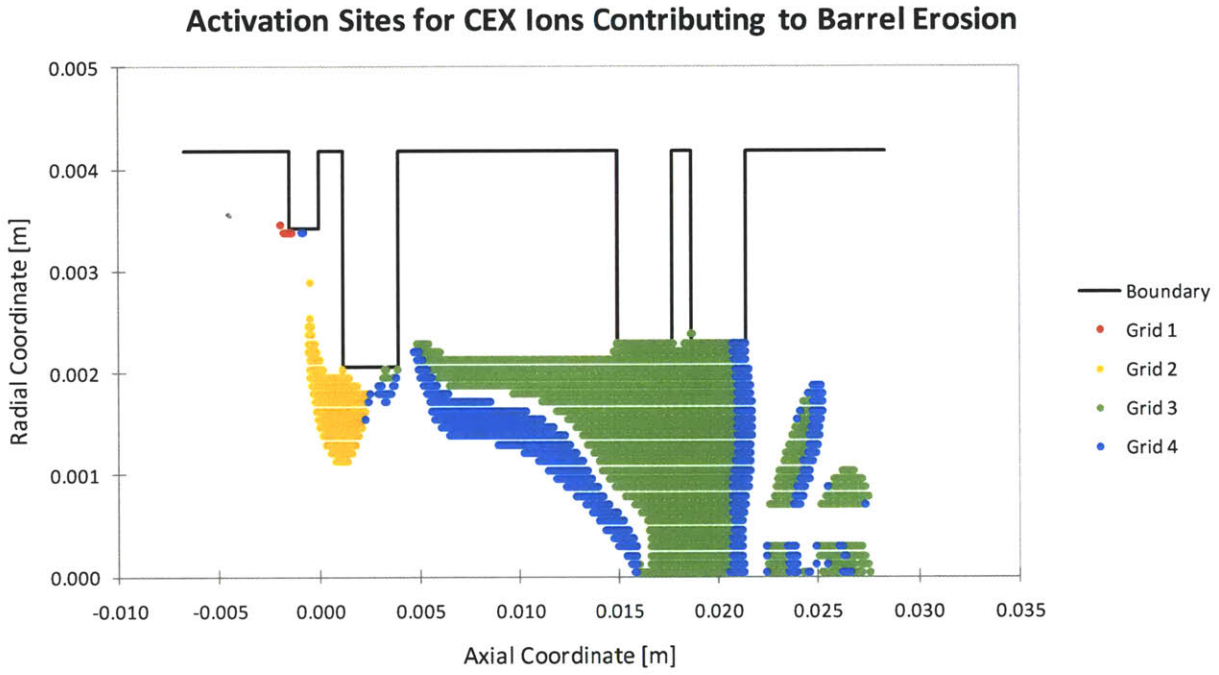

Figure 5.17. Location for charge exchange ion production contributing to barrel erosion at beginning-of-life for Case 1A, parsed according to the grid impinged

One noteworthy feature evident in this mapping is that the bulk of the charge exchange ions that contribute to erosion of the third grid structure are activated at axial coordinates near the exit. This indicates that the contribution to barrel erosion by ions activated in the grid gaps is less than that of the ions activated near the third and fourth grid planes. It is further worth noting that activation is greater for all grid structures at radial coordinates approaching the grid barrel surface.

5.8 Conclusions and Future Work

The dual-stage four-grid ion optics geometry has been implemented into CEX2D. The neutral background gas model, the near orifice neutral distribution, and the Clausing calculations have been revised to incorporate the dual-stage four-grid ion thruster design. Additionally, sputter models have been

developed which allow for the simulation of thruster operation using neon. Simulations indicate that lifetime limitations due to excessive charge exchange production in the increased intergrid gap and the accompanying increase in grid erosion will not prohibit the design and operation of a thruster of this type. Operational lifetimes consistent with anticipated mission needs for this class of thruster appear feasible based on these simulations, with achievable lifetimes up to or in excess of 100,000 hours.

One aspect of the physics of grid erosion that has not been incorporated into the CEX2D code is material re-deposition. In order to further increase the fidelity of erosion simulations undertaken in this work and others the impact of grid material re-deposition on erosion rates and achievable lifetime should be captured and incorporated. Finally, there is a need to evaluate the impact of 3D effects on grid erosion to investigate the pit and groove erosion patterns that are observed experimentally in conventional gridded ion thrusters. This might be accomplished by modifying the CEX3D code to incorporate a four-grid geometry.

Chapter 6

Hall Thruster Modeling

6.1 Background

Hall effect thrusters may provide a solution for obtaining multi-megawatt levels of output power at high thrust. Equally important, these devices may offer an incremental path to the implementation of a high power electric propulsion system. By varying some simple operational properties of Hall thrusters of constant geometry, it may be possible to increase device power handling, while simultaneously improving efficiency and performance. As discussed in Chapter 4, this is important, as the mass scaling behavior of Hall-effect thrusters with increasing radial dimension may result in unnecessarily massive thrusters. If, by implementing simple operational variations, possible mass scaling issues can be circumvented then one potential limitation for the design of megawatt-level Hall thrusters may be effectively overcome.

There has been a good deal of success in treating the structure of the equilibrium plasma flow in the Hall-effect thruster [176, 177]. Attempts at understanding the precise scaling relations and similarity criteria for the design of these devices have been undertaken relatively more recently, and have had a more evolutionary development [131 - 138]. More recently, numerical modeling of the plasma flow has provided some insight into the behavior of these devices, and may provide a tool for better understanding their scaling behavior [178].

One common aspect to previous scaling studies is a simplified analysis of the neutral population, which ignores ion-neutral coupling. Because the Hall thruster mass scales poorly with increasing diameter, it is important to ascertain how increased mass flow rate and input power will impact the

performance of a thruster of constant dimension. In the limit that the plasma becomes highly collisional, momentum exchange from the ion population to the neutral population may become significant, and important in accurately predicting thruster performance. Additionally, at some point the Hall current may become reduced by increased electron collisions in the ionization region, strongly affecting the magnetic thrust generation mechanism. Finally, there is some experimental evidence that substantially increased mass flow rate and input power for a given thruster can improve performance and efficiency [139].

6.2 Motivation

As discussed in Chapter 4, it may be possible to operate Hall effect thrusters at higher values of mass flow rate and input power given a fixed geometry. This would amount to increasing the power density of these devices over what is achieved in conventional thrusters, thereby circumventing some of the problems associated with Hall thruster mass scaling with increased dimension outlined previously.

An operational regime in which contributions from momentum exchange between the ions and neutrals is significant must meet three criteria. First, the rate at which electrons diffuse through the radial magnetic field must be sufficiently slow that efficient ionization can take place. The rate of electron diffusion varies inversely with electron-neutral collisions. We therefore require that the electron cyclotron frequency remain much greater than the electron-neutral collision frequency:

$$\frac{\omega_{ce}}{\nu_{en}} \gg 1 \rightarrow B \gg \frac{1}{e} m_e \bar{c}_e n_n Q_{en} \qquad \text{(Eq. 6.1)}$$

Next, in order to effectively couple and transfer momentum to the neutral fluid, there should be a large number of ion-neutral collisions, including charge exchange collisions. The mean free path for ion-neutral collisions must be much shorter than the channel length:

$$\frac{L}{\lambda_{in}} \gg 1 \rightarrow n_n \gg \frac{1}{Q_{in} L} \qquad \text{(Eq. 6.2)}$$

Finally, the radial magnetic field must be less than the critical value at which anode starvation occurs. In the segment between the anode and the ionization region the axial electric field is negligible and electrons diffuse toward the anode. The gradient in electron number density is related to the electron diffusion rate:

$$\frac{dn_e}{dz} = -\frac{\Gamma_e}{D_{e\perp}} \qquad \text{(Eq. 6.3)}$$

The electron diffusion rate is comprised of a classical and anomalous component. The diffusivity in this case is given by:

$$D_{e\perp} = \frac{kT_e}{m_e}\frac{\upsilon_{en} + \alpha_B\omega_{ce}}{\omega_{ce}^2} = \frac{m_e}{e^2}kT_e\frac{\upsilon_{en} + \alpha_B\frac{eB}{m_e}}{B^2} \qquad \text{(Eq. 6.4)}$$

The parameter α_B is the Bohm coefficient. Values are observed to lie in the range of $\frac{1}{16} - \frac{1}{80}$. In the limit that the number density at the anode is very small, we can express Eq. 6.3:

$$n_{e_{MAX}} - 0 = -\Gamma_e\int_0^L \frac{dz}{D_{e\perp}} \qquad \text{(Eq. 6.5)}$$

The upper limit of the integrand is the point at which the plasma density reaches a maximum. Substituting for the electron flux:

$$-\Gamma_e = \frac{I_{A,e}}{A_A e} \cong \frac{I_A}{A_A e} = \frac{n_{e_{MAX}}}{\int_0^L \frac{dz}{D_{e\perp}}} \qquad \text{(Eq. 6.6)}$$

By approximating the magnetic field and electron temperature through the channel as Gaussian, we can obtain a final bounding criterion on the B-n_n space:

$$\frac{I_A}{n_{e_{MAX}}A_A e}\int_0^L \frac{e^2}{m_e}kT_{e_M}\exp\left(-\frac{(z-L)^2}{L_m}\right)\left(\frac{n_nC_{en}Q_{en} + \alpha_B\frac{eB_M\exp\left(-\frac{(z-L)^2}{L_m}\right)}{m_e}}{B_M^2\exp\left(-\frac{(z-L)^2}{L_m}\right)^2}\right)dz - 1 = 0 \qquad \text{(Eq. 6.7)}$$

This final relationship between B_M and n_n can be solved using iterative methods.

Using values that approximate the plasma parameters in the ionization region of an SPT-type Hall thruster, it becomes clear that there is a region which is effectively bounded by these three conditions on neutral density and magnetic field strength.

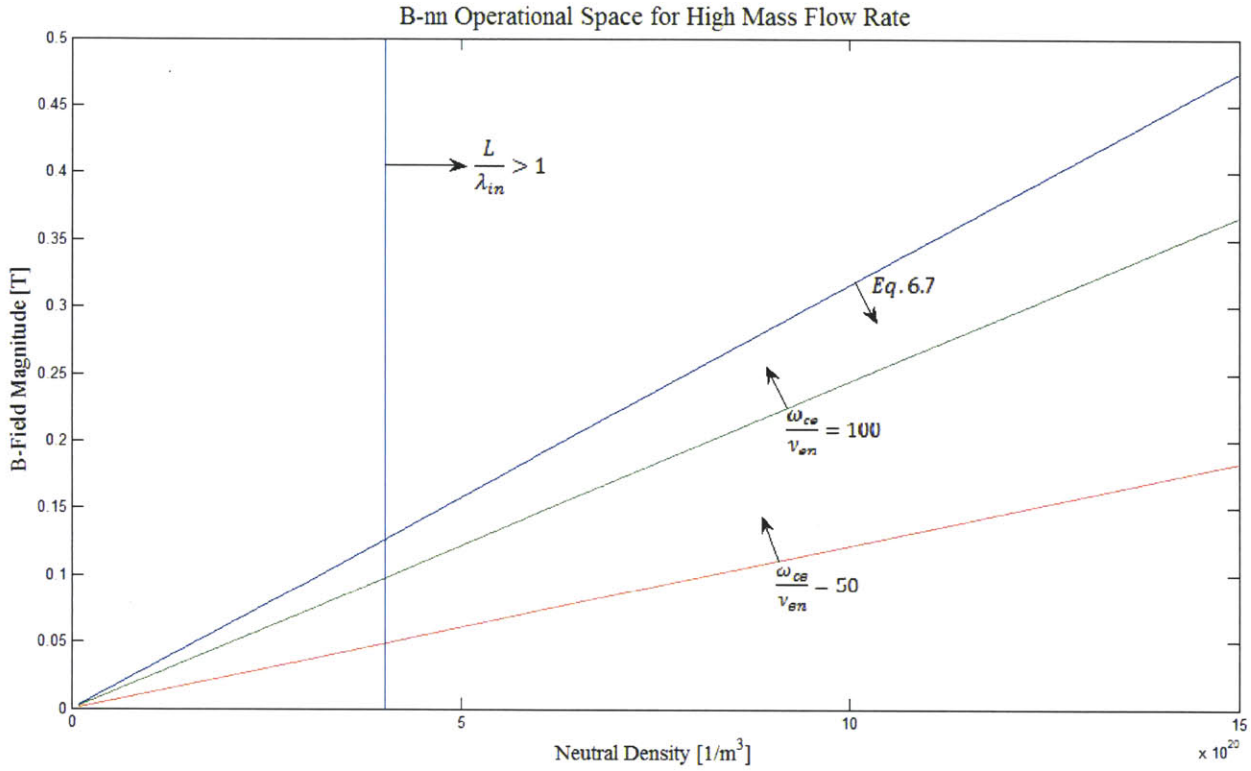

Figure 6.1. Constraints bounding the allowable space for neutral population density in the ionization region of a Hall thruster

It is clear that there is a solution space in which, for a given magnetic field, the neutral density in the ionization region can be varied without violating the three constraints outlined above. In order to study the effect of higher mass flow rate a one-dimensional code has been developed and implemented which incorporates the dynamics of the neutral population.

6.3 Model Formulation

Incorporating the effects of ionization in the consumption of neutrals and recombination in the production of neutrals, we can express continuity in terms of the individual particle fluxes:

$$\frac{d\Gamma_e}{dx} = \frac{d\Gamma_i}{dx} = -\frac{d\Gamma_n}{dx} = n_e(\nu_i - \nu_w) \qquad \text{(Eq. 6.8a -6.8c)}$$

The ionization frequency and effective wall collision frequencies are given by ν_i and ν_w respectively. Including momentum exchange between ions and neutrals due to charge exchange collisions and ion-neutral collisions, we can express the conservation of momentum in the electron, ion and neutral populations:

$$\frac{d}{dx}(n_e k T_e) = e n_e \frac{d\phi}{dx} - m_e n_e \nu_e \nu_e \qquad \text{(Eq. 6.9)}$$

$$m_i v_i \frac{dv_i}{dx} = -e\frac{d\phi}{dx} - m_i(\nu_i + \nu_{in} + \nu_{cex})(v_i - v_n) \quad \text{(Eq. 6.10)}$$

$$n_n m_i v_n \frac{dv_n}{dx} = n_n m_i(\nu_{in} + \nu_{cex})(v_i - v_n) - \frac{d}{dx}(n_n k T_n) \quad \text{(Eq. 6.11)}$$

The effective 1D electron collision frequency is given by ν_e in Eq. 6.9. This collision frequency incorporates magnetic effects so that $\nu_e = \frac{\omega_{ce}^2}{\nu_{en} + \alpha_B \omega_{ce}}$. In this model, the neutral temperature is taken as constant. Finally, the electron energy is given by:

$$\frac{d}{dx}\left(\frac{5}{2} k T_e \Gamma_e\right) = e\Gamma_e \frac{d\phi}{dx} - n_e \nu_i E_i - n_e \nu_{Ew} k T_e \quad \text{(Eq. 6.12)}$$

In order to avoid singularities in the solution to this system of equations that occur at the ion and neutral sonic speeds, we can recast the system using the ion flux as the independent variable. From Eq. 6.8b:

$$\frac{d}{dx} = (\nu_i - \nu_w) n_e \frac{d}{d\Gamma_i} \quad \text{(Eq. 6.13)}$$

In the case where the number of wall collisions is greater than the number of ionizing collisions, as might occur upstream near the anode, the ion flux is no longer increasing monotonically in axial coordinate. In this case, the model must be evaluated in terms of the axial coordinate, rather than the ion flux. This analysis is outlined beginning in Eq. 6.57, using a constant channel area.

We can reformulate Eq. 6.8-6.12 in terms of the ion flux.

$$\frac{d\Gamma_e}{d\Gamma_i} = -\frac{d\Gamma_n}{d\Gamma_i} = 1 \quad \text{(Eq. 6.14a, b)}$$

$$m_i v_i \frac{dv_i}{d\Gamma_i} = -e\frac{d\phi}{d\Gamma_i} - \frac{m_i(\nu_i + \nu_{in} + \nu_{cex})}{n_e(\nu_i - \nu_w)}(v_i - v_n) \quad \text{(Eq. 6.15)}$$

$$\frac{d}{d\Gamma_i}(n_e k T_e) = e n_e \frac{d\phi}{d\Gamma_i} - m_e \frac{\nu_e}{(\nu_i - \nu_w)} v_e \quad \text{(Eq. 6.16)}$$

$$n_n m_i v_n \frac{dv_n}{d\Gamma_i} = \frac{n_n m_i(\nu_{in} + \nu_{cex})}{n_e(\nu_i - \nu_w)}(v_i - v_n) - \frac{d}{d\Gamma_i}(n_n k T_n) \quad \text{(Eq. 6.17)}$$

$$\frac{d}{d\Gamma_i}\left(\frac{5}{2} k T_e \Gamma_e\right) = e\Gamma_e \frac{d\phi}{d\Gamma_i} - \frac{\nu_i E_i}{(\nu_i - \nu_w)} - \frac{\nu_{Ew} k T_e}{(\nu_i - \nu_w)} \quad \text{(Eq. 6.18)}$$

Finally, in order to evaluate position in the hall thruster channel corresponding to a given ion flux, we can just take the reciprocal of Eq. 6.8b:

$$\frac{dx}{d\Gamma_i} = \frac{1}{n_e(\nu_i - \nu_w)} \tag{Eq. 6.19}$$

Next, we can consider the constants of the plasma flow and evaluate their variation in ion flux. First, we consider the electron enthalpy. We can rearrange the second term in Eq. 6.18:

$$e\Gamma_e \frac{d\phi}{d\Gamma_i} = \frac{d}{d\Gamma_i}(e\Gamma_e\phi) - e\phi\frac{d\Gamma_e}{d\Gamma_i} = \frac{d}{d\Gamma_i}(e\Gamma_e\phi) - e\phi \tag{Eq. 6.20}$$

And the third term in Eq. 6.18 can be expressed:

$$\begin{aligned} -\frac{\nu_i}{\nu_i - \nu_w}E_i &= -E_i - \frac{\nu_w}{\nu_i - \nu_w}E_i = -\frac{d}{d\Gamma_i}(\Gamma_e E_i) - \frac{\nu_w}{\nu_i - \nu_w}E_i \\ &= -E_i - \Gamma_e\frac{dE_i}{d\Gamma_i} - \frac{\nu_w}{\nu_i - \nu_w}E_i \end{aligned} \tag{Eq. 6.21}$$

Substituting these into Eq. 6.18 and simplifying gives:

$$\Gamma_e\frac{d}{d\Gamma_i}\left(\frac{5}{2}kT_e + E_i - e\phi\right) + \left(\frac{5}{2} + \frac{\nu_{Ew}}{\nu_i - \nu_w}\right)kT_e + \left(1 + \frac{\nu_w}{\nu_i - \nu_w}\right)E_i = 0 \tag{Eq. 6.22}$$

Defining the electron enthalpy:

$$h_e = \frac{5}{2}kT_e + E_i - e\phi \tag{Eq. 6.23}$$

We can substitute and solve to find the variation in electron enthalpy with ion flux:

$$\frac{dh_e}{d\Gamma_i} = \frac{-1}{\Gamma_e}\left(\left(\frac{5}{2} + \frac{\nu_{Ew}}{\nu_i - \nu_w}\right)kT_e + \left(1 + \frac{\nu_w}{\nu_i - \nu_w}\right)E_i\right) \tag{Eq. 6.24}$$

The next property of interest is the ion enthalpy. The variation of ion enthalpy with ion flux can be found by rearranging Eq. 6.15:

$$\frac{d}{d\Gamma_i}\left(m_i\frac{v_i^2}{2} + e\phi\right) = -\frac{m_i(\nu_i + \nu_{in} + \nu_{cex})}{n_e(\nu_i - \nu_w)}(v_i - v_n) \tag{Eq. 6.25}$$

We can define the ion enthalpy:

$$h_i = m_i\frac{v_i^2}{2} + e\phi \tag{Eq. 6.26}$$

By substituting and combining the ion collision frequencies, we finally obtain the variation of ion enthalpy in ion flux:

$$\frac{dh_i}{d\Gamma_i} = -\frac{\nu_{iT}}{(\nu_i - \nu_w)}\frac{m_i(v_i - v_n)}{n_e} \quad \text{(Eq. 6.27)}$$

Next, we can consider the ambipolar momentum density. The electric field can be eliminated by multiplying both sides of Eq. 6.15 by the plasma density, n_e, and combining it with Eq. 6.16:

$$m_i\Gamma_i\frac{dv_i}{d\Gamma_i} + \frac{d}{d\Gamma_i}(n_e kT_e) = -m_i\frac{\nu_{iT}}{(\nu_i - \nu_w)}(v_i - v_n) - m_e\frac{\nu_e}{(\nu_i - \nu_w)}v_e \quad \text{(Eq. 6.28)}$$

To simplify this expression, we first use the fact that:

$$m_i\Gamma_i\frac{dv_i}{d\Gamma_i} = \frac{d}{d\Gamma_i}(m_i\Gamma_i v_i) - m_i v_i \quad \text{(Eq. 6.29)}$$

The ambipolar momentum density can be defined:

$$A = m_i v_i \Gamma_i + n_e kT_e \quad \text{(Eq. 6.30)}$$

Finally, we can substitute back into Eq. 6.28 and simplify to obtain:

$$\frac{dA}{d\Gamma_i} = m_i\left[v_i - \frac{\nu_{iT}}{(\nu_i - \nu_w)}(v_i - v_n)\right] - m_e\frac{\nu_e}{(\nu_i - \nu_w)}v_e \quad \text{(Eq. 6.31)}$$

Following the variation of ambipolar momentum density with ion flux, we next consider the neutral momentum density. Based on the definition of the flux, it must be true that:

$$\Gamma_n\frac{dv_n}{d\Gamma_i} = \frac{d}{d\Gamma_i}(\Gamma_n v_v) - v_n\frac{d\Gamma_n}{d\Gamma_i} \quad \text{(Eq. 6.32)}$$

We can define the neutral momentum density:

$$N = m_i v_n \Gamma_n + n_n kT_n \quad \text{(Eq. 6.33)}$$

We can substitute into Eq. 6.17 to obtain

$$\frac{dN}{d\Gamma_i} = -m_i v_n + m_i\frac{n_n}{n_e}\frac{\nu_{in} + \nu_{cex}}{(\nu_i - \nu_w)}(v_i - v_n) \quad \text{(Eq. 6.34)}$$

This formulation is useful because we can now use the constants of the flow, coupled with the three continuity equations to solve for seven properties of interest: $v_i, v_e, v_n, n_e, n_n, \phi$, and T_e. We first wish to solve for the ion velocity. We can combine Eq. 6.23 and Eq. 6.26 to obtain the total enthalpy:

$$h = h_e + h_i = m_i\frac{v_i^2}{2} + \frac{5}{2}kT_e + E_i \quad \text{(Eq. 6.35)}$$

Next we can solve Eq. 6.8b for the plasma density and substitute into Eq. 6.30 to find an expression for the electron temperature:

$$kT_e = \frac{v_i}{\Gamma_i} A - m_i v_i^2 \qquad \text{(Eq. 6.36)}$$

By substituting into Eq. 6.35 and regrouping, we obtain a quadratic in the ion velocity:

$$2m_i v_i^2 + \frac{5}{2}\frac{A}{\Gamma_i} v_i + (h - E_i) = 0 \qquad \text{(Eq. 6.37)}$$

Solving for ion velocity:

$$v_i = \frac{5}{8}\frac{A}{m_i \Gamma_i} \pm \sqrt{\left(\frac{5}{8}\frac{A}{m_i \Gamma_i}\right)^2 - \frac{h - E_i}{2m_i}} \qquad \text{(Eq. 6.38)}$$

It is clear that the radicand becomes zero at the ion sonic speed:

$$c_i = \frac{5}{8}\frac{A}{m_i \Gamma_i} = \sqrt{\frac{5}{3}\frac{kT_e}{m_i}} \qquad \text{(Eq. 6.39)}$$

The plus sign in Eq. 6.38 corresponds to ion supersonic flow, and the negative sign to ion subsonic flow. At the point at which the radicand goes to zero, the sign in the expression for ion velocity must be switched. Once the ion velocity has been obtained, the other four variables relating to the charged species, n_e, v_e, T_e, and ϕ, can be solved for using back substitution.

Solving for the neutral velocity is much simpler. Substituting the neutral flux into the expression for the neutral momentum density in Eq. 6.33 to eliminate n_n gives:

$$\frac{N}{m_i \Gamma_n} = v_n + \frac{kT_n}{m_i}\frac{1}{v_n} \qquad \text{(Eq. 6.40)}$$

This also gives a quadratic expression in neutral velocity:

$$v_n^2 - \frac{N}{m_i \Gamma_n} v_n + \frac{kT_n}{m_i} = 0 \qquad \text{(Eq. 6.41)}$$

This expression has a solution similar to that for the ion velocity:

$$v_n = \frac{N}{2m_i \Gamma_n} \pm \sqrt{\left(\frac{N}{2m_i \Gamma_n}\right)^2 - \frac{kT_n}{m_i}} \qquad \text{(Eq. 6.42)}$$

This form indicates that the neutral population also reaches a sonic passage. Again, we find that when the radicand goes to zero:

$$c_n = \frac{N}{2m_i\Gamma_n} = \sqrt{\frac{kT_n}{m_i}} \qquad \text{(Eq. 6.43)}$$

The sign in Eq. 6.42 is negative for subsonic neutral flow, becoming sonic when the radicand goes to zero, and positive for supersonic flow.

This treatment of the ion and neutral population dynamics poses a problem in implementation. As outlined thus far, the ions and neutrals are forced to cross smoothly through two distinct sonic points. Because their dynamics are coupled, the difficulty in implementation is compounded. It would be helpful to avoid the neutral sonic transition altogether by imposing a supersonic inlet condition on the neutral population. To evaluate the impact and potential utility of this simplification in modeling the flow, it is necessary to observe the sensitivity of downstream neutral behavior to upstream inlet conditions.

It is possible to formulate the neutral fluid behavior in a different way. Assuming a constant temperature for the neutral population, as in the formulation above, we can express the conservation of momentum for the neutrals:

$$\rho_n v_n \frac{dv_n}{dx} + \frac{kT_n}{m_i}\frac{d\rho_n}{dx} = -m_i n_n n_e \bar{c}_{in} Q_{in}(v_n - v_i) \qquad \text{(Eq. 6.44)}$$

The flux of neutrals can be expressed in terms of an ionization rate:

$$\frac{dn_n v_n}{dx} = -R_i n_n n_e = -R_i n_e \frac{\Gamma_n}{v_n} \qquad \text{(Eq. 6.45)}$$

Eliminating the mass in Eq. 6.44 and substituting for the neutral density gives:

$$\Gamma_n \frac{dv_n}{dx} + \frac{kT_n}{m_i}\frac{d}{dx}\left(\frac{\Gamma_n}{v_n}\right) = \frac{-\Gamma_n}{v_n} n_e \bar{c}_{in} Q_{in}(v_n - v_i) \qquad \text{(Eq. 6.46)}$$

The second term in Eq. 6.46 can be recast:

$$\frac{kT_n}{m_i}\frac{d}{dx}\left(\frac{\Gamma_n}{v_n}\right) = \frac{c_s^2}{v_n}\left(\frac{dn_n v_n}{dx} - n_n\frac{dv_n}{dx}\right) = c_s^2\left(-R_i n_e \frac{\Gamma_n}{c_s^2 M^2} - \frac{\Gamma_n}{c_s M^2}\frac{dM}{dx}\right) \qquad \text{(Eq. 6.47)}$$

Substituting Eq. 6.47 into Eq. 6.46, and eliminating the neutral flux gives:

$$c_s\frac{dM}{dx} - \frac{1}{M^2}\left(R_i n_e + c_s\frac{dM}{dx}\right) = \frac{-1}{c_s M} n_e \bar{c}_{in} Q_{in}(c_s M - v_i) \qquad \text{(Eq. 6.48)}$$

Dividing through by the neutral sonic speed, c_s, and solving for the gradient in Mach number gives:

$$\frac{dM}{dx} = \frac{\frac{\bar{c}_{in} Q_{in} n_e}{c_s M}\left(M - \frac{v_i(x)}{c_s}\right) + \frac{R_i n_e}{c_s M^2}}{\left(1 - \frac{1}{M^2}\right)} \quad \text{(Eq. 6.49)}$$

We can define the scattering and ionization mean free paths for a neutral:

$$\lambda_c = \frac{c_s}{\bar{c}_{in} Q_{in} n_e} \quad \text{(Eq. 6.50)}$$

$$\lambda_i = \frac{c_s}{R_i n_e} \quad \text{(Eq. 6.51)}$$

Using these characteristic lengths and multiplying the top and bottom of Eq. 6.49 by the square of the Mach number gives:

$$\frac{dM}{dx} = \frac{\frac{-M}{\lambda_c}\left(M - \frac{v_i(x)}{c_s}\right) + \frac{1}{\lambda_i}}{(M^2 - 1)} \quad \text{(Eq. 6.52)}$$

In this way, by computing the plasma properties first, we can determine the neutral Mach number at any point, x, along the channel. The neutral density can be computed from the known relationship for neutral flux in Eq. 6.8c. A useful analog for understanding the dynamics implied by Eq. 6.52 is a simplified linear ion velocity:

$$v_i(x) = c_i\left(\frac{x}{x_0} - 1\right) \quad \text{(Eq. 6.53)}$$

The ion velocity begins with reverse sonic flow, crosses zero at $x = x_0$, makes a smooth sonic transition and continues supersonically until the end of the simulation. For this simplified model, the plasma density and ionization rate are assumed to be constant. Near the Hall thruster anode the density will be quite low. Taking values $n_e = 6 \times 10^{17}$ and $R_i = 2.78 \times 10^{-20}$ to demonstrate this behavior yields the response illustrated in Figure 6.2.

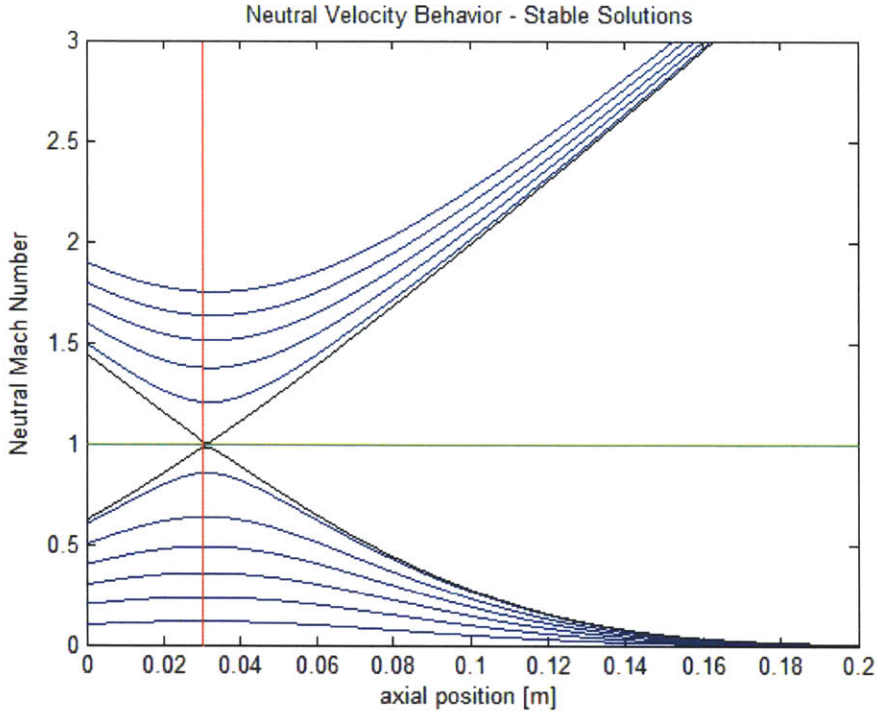

Figure 6.2. Neutral dynamics for a linear ion velocity profile at various inlet Mach numbers; $x_0 = 0.03, \lambda_c = 1.65, \lambda_i = 15083, c_s = 251.6\frac{m}{s}, c_i = 4283.2\frac{m}{s}$.

In Figure 6.2, the inlet Mach number is varied from M = 0.1 – 1.9. The ion zero velocity crossing is shown in red. Non-transonic neutral trajectories are shown in blue. The two bounding solutions shown in black correspond to subsonic inlet Mach number $M = 0.62043$ and supersonic inlet Mach number $M = 1.4471$. Trajectories starting with Mach numbers less than the subsonic limiting value asymptotically approach zero velocity at the outlet. The trajectory starting at the subsonic limiting value makes a smooth supersonic transition. Trajectories starting above the supersonic limit will continue supersonically into the exhaust, asymptotically approaching the smooth subsonic-supersonic transition trajectory.

We can evaluate Eq. 6.32 using some approximations to provide an analytic check on limiting inlet Mach numbers obtained numerically in Figure 6.2. First, given that $\lambda_i \gg \lambda_c$ in the region where the neutral fluid undergoes sonic transition the $\frac{1}{\lambda_i}$ term in Eq. 6.32 may be ignored. Next, because $c_i \gg c_s$ we can express Eq. 6.32:

$$\frac{dM}{dx} = \frac{1}{\lambda_c}\left(\frac{M}{M^2 - 1}\right)\left(\frac{c_i}{c_s}\right)\left(\frac{x}{x_0} - 1\right) \qquad \text{(Eq. 6.54)}$$

Integrating we find that:

$$\frac{M^2}{2} - \ln M = \frac{1}{\lambda_c}\frac{c_i}{c_s}\left(\frac{x^2}{2x_0} - x\right) + C \qquad \text{(Eq. 6.55)}$$

In order to traverse the sonic point smoothly, it must be true that the Mach number $M = 1$ at $x = x_0$. Imposing these conditions, we can solve for a value of C:

$$C = \frac{1}{2} + \left(\frac{c_i}{\lambda_c c_s}\right)\left(\frac{1}{2x_0}\right) \qquad \text{(Eq. 6.56)}$$

Plugging in the appropriate values for the sonic speeds and characteristic length, and imposing $x_0 = 0.03\,m$, we find critical Mach numbers $M = 0.636$ and $M = 1.417$, which are similar to the values obtained numerically.

One counter-intuitive characteristic of the neutral behavior for subsonic inlet Mach numbers below the critical subsonic value ($M_0 < 0.62$) is that, in the region of ion reverse flow, the subsonic neutral population is accelerated. In the region of forward ion flow, the subsonic neutral population is decelerated. This behavior is somewhat analogous to compressible, viscous flow in a pipe. Ion counter-flow provides a frictional force on the neutral fluid. This frictional force results in a pressure drop in the direction of flow, which implies decreasing neutral density. To the extent that neutral depletion due to ionization can be neglected in this region, the overall flux of neutrals is approximately constant. Neutral velocity must therefore be increasing.

It is also noteworthy that in the case of a supersonic downstream neutral velocity, there is little dependence on the neutral inlet conditions. It is clear from Figure 6.2 that neutral trajectories that begin with high inlet Mach number ($M_0 > 1.447$) will tend to converge to the stable subsonic-supersonic transitional trajectory. This provides a basis for the simplification of supersonic neutral injection, which will be used in the model.

We finally wish to evaluate the plasma properties in the plume region. Expression of the dynamics of the system in the plume region is complicated by the variation of area in the expanding plume. Radial expansion of the plume is assumed to vary according to the ratio of Bohm velocity to ion velocity:

$$\frac{dr}{dx} = \frac{v_B}{v_i} \qquad \text{(Eq. 6.57)}$$

Given this axial variation of radius, it is straightforward to evaluate the corresponding axial variation in area:

$$\frac{dA}{dx} = 2\pi(r_o + r_{in})\frac{v_B}{v_i} \qquad \text{(Eq. 6.58)}$$

This expression can be manipulated to give the usual rule for plume expansion:

$$\frac{d}{dx}\ln A = \frac{1}{A}\frac{dA}{dx} = \frac{2v_B}{(r_o - r_{in})v_i} \quad \text{(Eq. 6.59)}$$

The governing equations cannot be expressed in terms of the differential variation in ion flux, as in the preceding treatment. In this region, the equations must be rendered more conventionally, in terms of the variation in the axial coordinate. This is not problematic, as no singular points occur in the expansion region. Including the effects due to non-constant flow area, the system of equations given in Eq. 6.8 – 6.12 becomes:

$$\frac{1}{A}\frac{\partial}{\partial x}(A\Gamma_e) = n_e v_i \quad \text{(Eq. 6.60)}$$

$$\frac{1}{A}\frac{\partial}{\partial x}(A\Gamma_i) = n_e v_i \quad \text{(Eq. 6.61)}$$

$$\frac{1}{A}\frac{\partial}{\partial x}(A\Gamma_n) = -n_e v_i \quad \text{(Eq. 6.62)}$$

$$\frac{1}{A}\frac{\partial}{\partial x}\left(Am_i n_e v_i^2\right) = -en_e\frac{\partial \phi}{\partial x} - m_i n_e v_{iT}(v_i - v_n) \quad \text{(Eq. 6.63)}$$

$$\frac{1}{A}\frac{\partial}{\partial x}(Am_i n_n v_n^2) = -m_i n_n(v_{in} + v_{CEX})(v_i - v_n) - \frac{\partial}{\partial x}(n_n k T_n) \quad \text{(Eq. 6.64)}$$

$$\frac{\partial}{\partial x}(n_e k T_e) = en_e\frac{\partial \phi}{\partial x} - m_e n_e v_e v_e \quad \text{(Eq. 6.65)}$$

$$\frac{1}{A}\frac{\partial}{\partial x}\left(\frac{5}{2}AkT_e n_e v_e\right) = en_e v_e\frac{\partial \phi}{\partial x} - n_e v_i a_i E_i \quad \text{(Eq. 6.66)}$$

Expanding this system of equations we can obtain a system of seven equations in seven unknown derivatives:

$$\frac{\partial v_e}{\partial x} + \frac{v_e}{n_e}\frac{\partial n_e}{\partial x} = v_i - \frac{2v_e c_p}{\delta v_i} \quad \text{(Eq. 6.67)}$$

$$\frac{\partial v_i}{\partial x} + \frac{v_i}{n_e}\frac{\partial n_e}{\partial x} = v_i - \frac{2c_p}{\delta} \quad \text{(Eq. 6.68)}$$

$$n_n\frac{\partial v_n}{\partial x} + v_n\frac{\partial n_n}{\partial x} = -n_e v_i - \frac{2n_n v_n c_p}{\delta v_i} \quad \text{(Eq. 6.69)}$$

$$\frac{2v_i c_p}{\delta} + \frac{v_i^2}{n_e}\frac{\partial n_e}{\partial x} + 2v_i\frac{\partial v_i}{\partial x} = -\frac{e}{m_i}\frac{\partial \phi}{\partial x} - v_{iT}(v_i - v_n) \quad \text{(Eq. 6.70)}$$

$$\frac{2v_n^2 c_p}{\delta v_i} + \frac{v_n^2}{n_n}\frac{\partial n_n}{\partial x} + 2v_n\frac{\partial v_n}{\partial x} = (v_{in} + v_{CEX})(v_i - v_n) - \frac{kT_n}{m_i n_n}\frac{\partial n_n}{\partial x} \quad \text{(Eq. 6.71)}$$

$$kT_e\frac{\partial n_e}{\partial x} + n_e k\frac{\partial T_e}{\partial x} = en_e\frac{\partial \phi}{\partial x} - m_e n_e v_e v_e \quad \text{(Eq. 6.72)}$$

$$\frac{5}{2}\left[\frac{2kT_e v_e c_p}{\delta v_i} + v_e\frac{\partial kT_e}{\partial x} + \frac{kT_e v_e}{n_e}\frac{\partial n_e}{\partial x} + kT_e\frac{\partial v_e}{\partial x}\right] = ev_e\frac{\partial \phi}{\partial x} - v_i E_i \quad \text{(Eq. 6.73)}$$

Solving this system of equations for the axial variation in the plasma density, we find that:

$$\frac{\partial n_e}{\partial x} = \frac{5m_e n_e v_e v_e + 3n_e m_i v_{iT}(v_i - v_n) - 6n_e m_i \frac{v_i v_B}{(r_o - r_i)}}{3m_i v_i^2 - 5kT_e} \quad \text{(Eq. 6.74)}$$

Given the neutral variation, we can progressively back solve for the variations of each of the other plasma parameters:

$$\frac{dv_e}{dx} = -\frac{2v_e v_B}{v_i(r_o - r_i)} - \frac{v_e}{n_e}\frac{dn_e}{dx} \quad \text{(Eq. 6.75)}$$

$$\frac{dv_i}{dx} = -\frac{2v_B}{(r_o - r_i)} - \frac{v_i}{n_e}\frac{dn_e}{dx} \quad \text{(Eq. 6.76)}$$

$$\frac{d\phi}{dx} = -\frac{m_h}{e}\left(\frac{2v_i v_B}{(r_o - r_i)} + \frac{v_i^2}{n_e}\frac{dn_e}{dx} + 2v_i\frac{dv_i}{dx} + v_{iT}(v_i - v_n)\right) \quad \text{(Eq. 6.77)}$$

$$\frac{dT_e}{dx} = \frac{1}{k}\left(e\frac{d\phi}{dx} - m_e v_e v_e - \frac{kT_e}{n_e}\frac{dn_e}{dx}\right) \quad \text{(Eq. 6.78)}$$

The variation in neutral density is given by:

$$\frac{dn_n}{dx} = \frac{(v_{in} + v_{CEX})(v_i - v_n) + \frac{2v_B v_n^2}{v_i(r_o - r_i)}}{\frac{kT_n}{m_i n_n} - \frac{v_n^2}{n_n}} \quad \text{(Eq. 6.79)}$$

This gives a variation in neutral velocity:

$$\frac{dv_n}{dx} = -\frac{2v_n v_B}{v_i(r_o - r_i)} - \frac{v_n}{n_n}\frac{dn_n}{dx} \quad \text{(Eq. 6.80)}$$

In order to begin the integration, we need to first establish a sufficient set of boundary conditions. First, we assume reverse choking at the anode. To avoid the singular ion sonic point we approximate:

$$v_i(0) \cong -0.999\sqrt{\frac{5}{3}\frac{kTe(0)}{m_i}} \qquad \text{(Eq. 6.81)}$$

The anode is taken at zero potential. Anode values of input current, electron temperature, and plasma density are varied to obtain smooth passage through the ion sonic point. For the neutral fluid, the inlet velocity is a approximated as a low supersonic value sufficiently high to continue supersonically throughout the thruster. As discussed above and illustrated in Figure 6.2, a stable supersonic inlet velocity for the neutral propellant gas will tend toward asymptotically toward the smooth sonic passage value, while avoiding the computational difficulties of finding the two dependent smooth passage trajectories for both the ions and neutrals. These boundary conditions, as well as the geometry and magnetic field characteristics are sufficient to model the behavior of the plasma flow inside the Hall thruster channel.

The integration procedure is shown graphically in Figure 6.3 below.

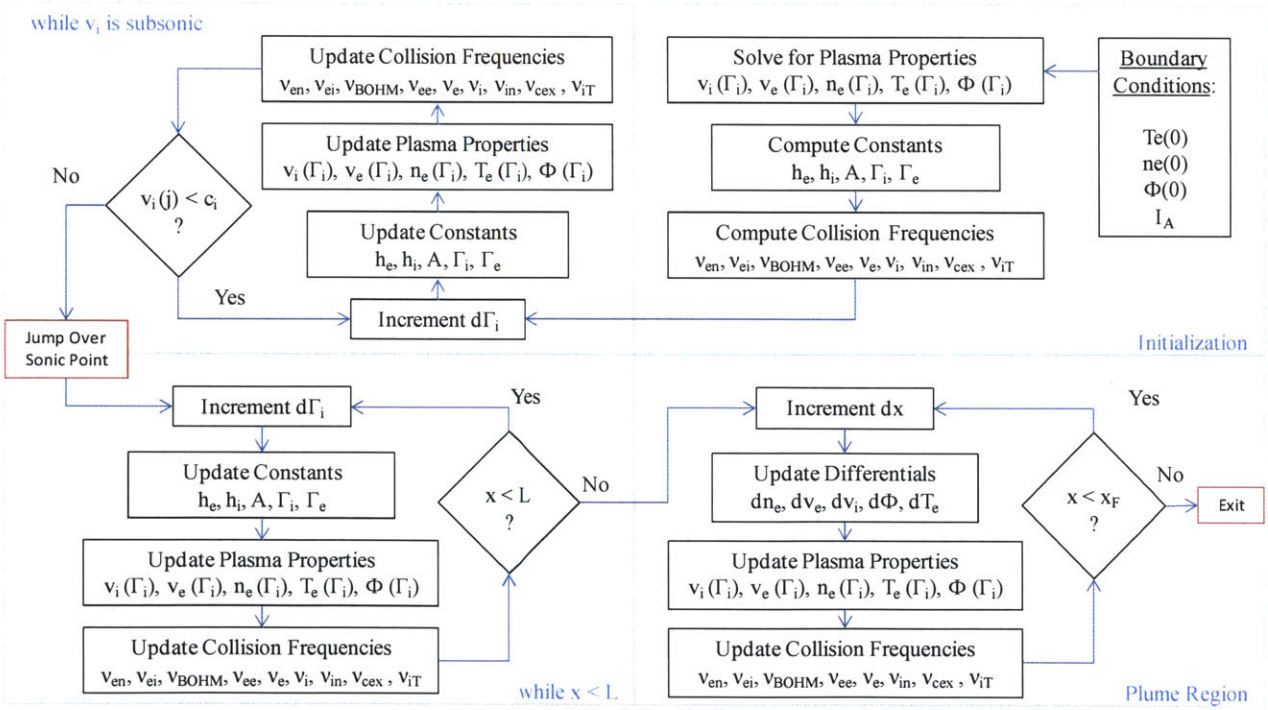

Figure 6.3. Flow diagram illustrating the integration process associated with the Hall thruster simulation.

The simulation consists of three sequential loops. The first loop describes the plasma properties and dynamics for the case in which the ion flow is subsonic. The second loop describes the system for the case in which the ion flow is supersonic within the thruster channel. The third loop treats the case in which the plume is expanding outside the thruster channel. The transition from subsonic to supersonic ion flow is accomplished in one iteration. When the ion velocity is within 0.1% of the sonic velocity, the

subsonic loop terminates. In the matching iteration, the ion velocity is set slightly above the sonic speed and the other plasma properties are adjusted accordingly. After the matching iteration, the simulation enters the supersonic loop and iterates until reaching the specified channel length. At the thruster exit, the simulation enters the third loop and the plasma is allowed to expand to a specified downstream point.

The magnetic field is modeled as a Gaussian, given by:

$$B(x) = B_M \exp\left(\frac{x_0 - x}{2\sigma^2}\right) \quad \text{(Eq. 6.82)}$$

The development of this model can be completed with the analytical expressions for the relevant collision frequencies. The expression for the ionization collision frequency:

$$\upsilon_i = n_n \sigma_{i_0} \sqrt{\frac{8kT_e}{\pi m_e}} \frac{1 + kT_e E_i}{(kT_e + E_i)^2} e^{\frac{-E_i}{kT_e}} \quad \text{(Eq. 6.83)}$$

Electron-Neutral Collisions:

$$\upsilon_{eN} = \frac{n_n \sigma_{eN} \left(\frac{T_e}{4 \times 11594} - 0.1\right)}{\left(1 + \left(\frac{T_e}{4 \times 11594}\right)^{1.6}\right)} \sqrt{\frac{8kT_e}{\pi m_e}} \quad \text{(Eq. 6.84)}$$

Electron Ion Collisions:

$$\upsilon_{ei} = \frac{n_e 2.9 \times 10^{-12} \ln \Lambda}{\left(\frac{T_e}{11594}\right)^{\frac{3}{2}}} \quad \text{(Eq. 6.85)}$$

The Coulomb Logarithm is given by:

$$\ln \Lambda = 23 - \frac{1}{2} \log \frac{10^{-6} n_e}{\left(\frac{T_e}{11594}\right)^3} \quad \text{(Eq. 6.86)}$$

The Bohm effective collision frequency:

$$\upsilon_B = \frac{1}{80} \frac{eB}{m_e} \quad \text{(Eq. 6.87)}$$

The loss of ions to the wall is modeled using an effective wall collision frequency. Following the axial model used by Ahedo [178]:

$$\upsilon_w = \frac{\upsilon_0}{r_o - r_i}\sqrt{\frac{kT_e}{m_i}} \qquad \text{(Eq. 6.88)}$$

The energy loss to the walls is related to the secondary electron emission yield due to impacts with the walls. This can be approximated:

$$\upsilon_{Ew} = \upsilon_w\left(5.62 + \frac{1.65}{1-\delta_\omega}\right) \qquad \text{(Eq. 6.89)}$$

And the secondary electron yield is well approximated by:

$$\delta_\omega(T_e) = min\left\{\delta_\omega^*, \sqrt{\frac{kT_e}{E_w}}\right\} \qquad \text{(Eq. 6.90)}$$

The limiting value of $\delta_\omega = \delta_\omega^*$ can be physically interpreted as the secondary electron yield for which the sheath at the insulating wall disappears. Herein this value is taken as $\delta_\omega^* = 0.983$. The total effective electron collision frequency is given by:

$$\upsilon_e = \frac{e^2B^2}{m_e^2(\upsilon_{eN} + \upsilon_{ei} + \upsilon_B + \upsilon_w)} \qquad \text{(Eq. 6.91)}$$

The charge exchange collision frequency:

$$\upsilon_{CEX} = n_n\sigma_{CEX}\left[|v_i - v_n| + \sqrt{\frac{kT_i}{m_h}}\right] \qquad \text{(Eq. 6.92)}$$

The non-exchange ion-neutral collision frequency is approximately equal in magnitude to the charge exchange collision frequency:

$$\upsilon_{iN} = \upsilon_{CEX} \qquad \text{(Eq. 6.93)}$$

Finally, the total ion collision frequency is just the scalar sum of the different ion collision frequencies:

$$\upsilon_{iT} = \upsilon_{iN} + \upsilon_{CEX} + \upsilon_i \qquad \text{(Eq. 6.94)}$$

6.4 Model Calibration and Operation

In order to validate the predictive power of this model for Hall thruster plasma dynamics, it is important that it accurately reproduce the performance parameters of well-characterized thrusters at the thruster exit plane. The thruster used for validation of the simulation is the Russian SPT-100 [179, 180].

	SPT-100 Experimental	1D3F Model - Incl. Wall Losses	Error
Thrust [mN]	82	82	0.00%
I_{SP} [s]	1600	1571	-1.81%
Anode Current [A]	4.5	5.5642	23.65%
Voltage	350	185.3	-47.06%
Efficiency	0.52	0.612	17.69%

Table 6.1. Comparison of Experimental and simulated performance of the Russian SPT-100 Hall Thruster at the baseline mass flow rate $\dot{m} = 5.32 \frac{mg}{s}$; simulated results are shown for the three fluid model developed in this work.

The baseline operating conditions for the SPT-100 are used to calibrate the model. In particular, in this work the anode plasma parameters, input current and total potential drop are chosen to reproduce the thrust of the SPT-100. The model requires input values of the anode current, anode electron temperature and anode plasma density. Using these values, the plasma properties are evaluated along the channel until reaching the ion sonic point. At this point, the radicand in Eq. 6.38 will go to zero. If the upstream plasma properties are set correctly, this radicand will pass smoothly through zero in a single iteration, and begin increasing again thereafter.

In a typical run, however, the upstream plasma properties and anode current will not be set correctly from the outset. In these cases, the value under the radicand will cross through zero and become negative, forcing the simulation to diverge. To facilitate iteration in setting the upstream parameters, the radicand in these cases is forced to zero and the number of iterations in which the radicand is locked at zero is recorded. In the stuck-at-zero condition, the simulation continues marching downstream until the radicand becomes positive again. The simulation will terminate normally and stuck-at-zero iterations will be reported. Upstream quantities can then be varied systematically to reduce the number of stuck-at-zero iterations until the upstream quantities for which the ion fluid passes smoothly through the sonic point is found. Solutions so obtained are invariant to changes of the order of 10^{-5} Amps in anode current, 10^{14} m^{-3} in plasma density and 10^{-2} - 10^{-3} eV in electron temperature. Variations in upstream quantities that are smaller than these values will not generally demonstrate an effect on the convergence of a solution.

In using the SPT-100 experimental values to calibrate the model, the anode current, plasma density and electron temperature are set to accurately reproduce the measured thrust at the nominal mass flow

rate. The model then reports the specific impulse and the potential drop through the thruster channel. This is executed first for the baseline operation of the SPT-100 thruster. Simulations run at increasing mass flow rates are then forced to the same downstream potential of 185.3 Volts. Implicit in this constraint is the assumption that the potential "lost" to recombination is insensitive to variations in propellant mass flow rate.

In the following section, results obtained from this model for the SPT-100 are provided for increasing values from the nominal case at $\dot{m} = 5.32$ mg/s, up to $\dot{m} = 50.0$ mg/s.

6.5 Results

Using the model developed in the preceding treatment, four numerical experiments are conducted. First, the inlet mass flow rate is increased with a constant geometry and constant magnetic field strength. Variations in plasma properties and derived performance are presented. Next, the magnetic field strength is varied for several values of mass flow rate and geometry is held constant. Effects on the thruster efficiency and performance are presented. Third, the magnetic field shape is varied at a fixed position and field strength. Variations in efficiency are presented. Finally, a series of runs are conducted to observe the maximum achievable thruster efficiency for cases in which the thruster geometry and magnetic field topology are allowed to vary. Details of field topology are presented, along with thruster performance parameters.

6.5.1 Variable Flow Rate at Fixed Field and Geometry

Figures 6.4 – 6.11 provide a snapshot of calculated plasma parameters along the channel of the SPT-100. Figure 6.12 illustrates the relative importance of Bohm diffusion compared to other contributors to electron diffusion. The relevant variations in performance metrics and plasma parameters are observed in Figures 6.13 – 6.17. Conclusions derived from these results outlined below.

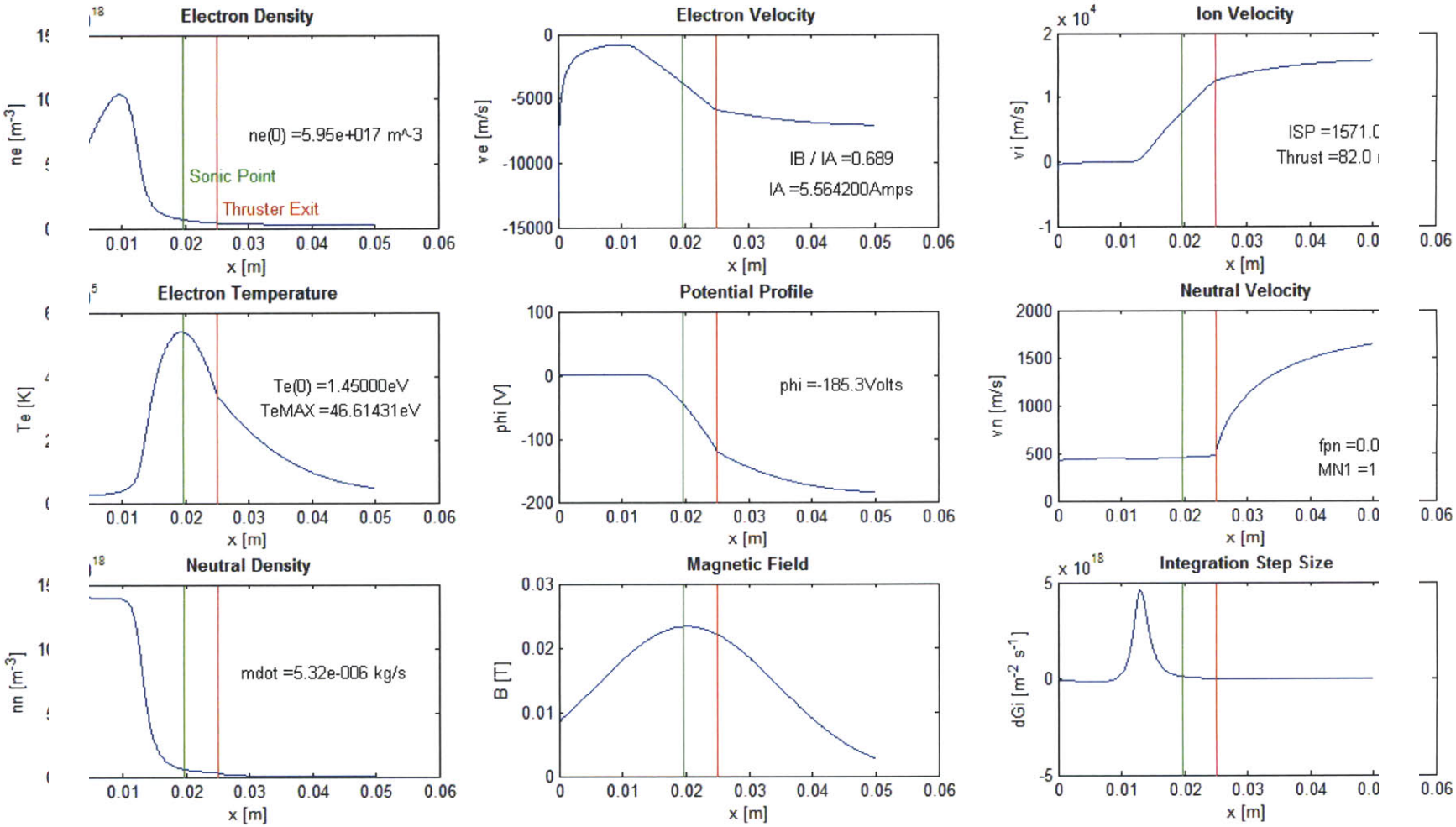

Figure 6.4. Simulated baseline performance of the SPT-100 at the nominal mass flow rate $\dot{m} = 5.32$ mg/s

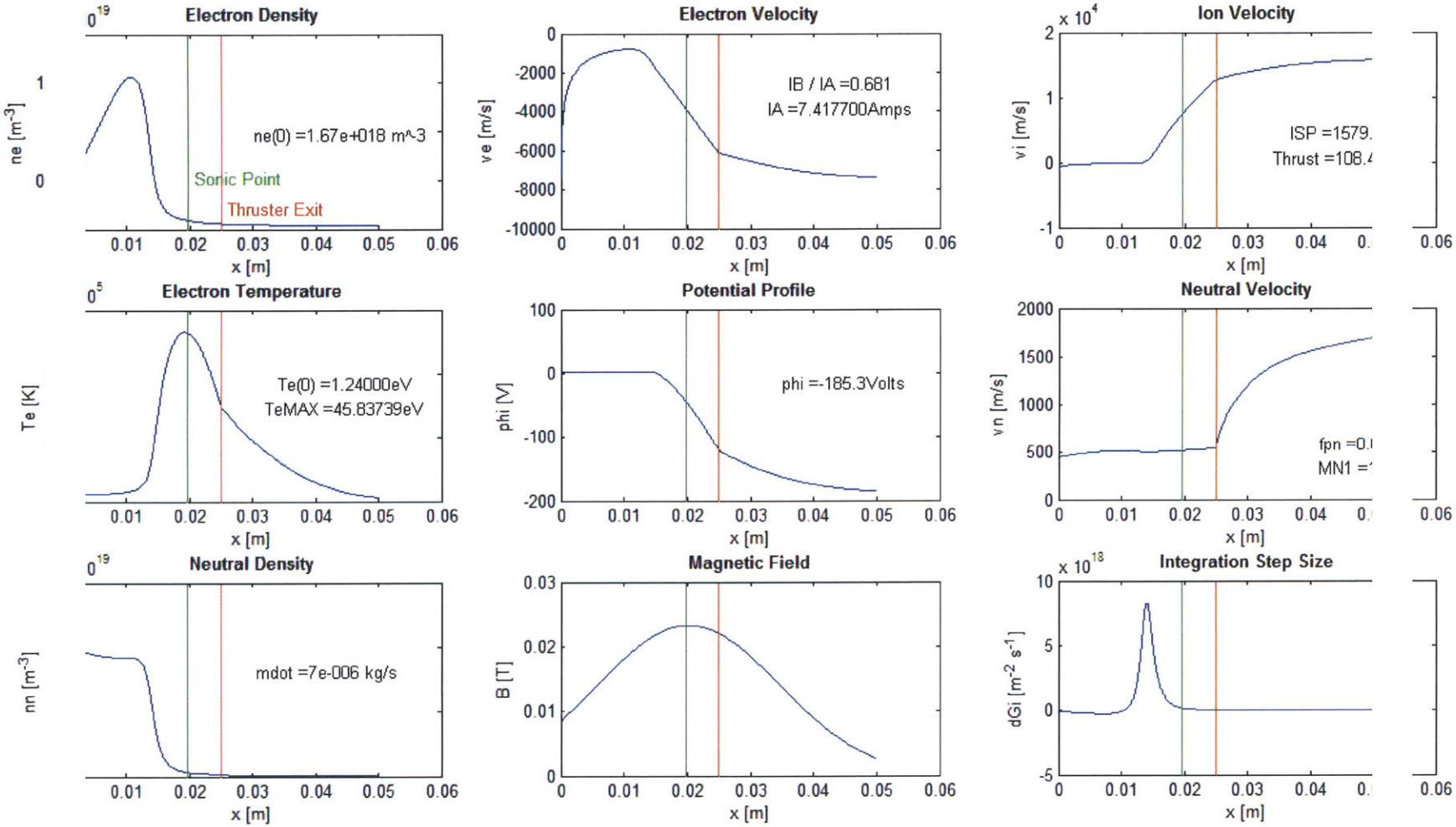

Figure 6.5. Simulated performance of the SPT-100 at mass flow rate $\dot{m} = 7.0$ mg/s

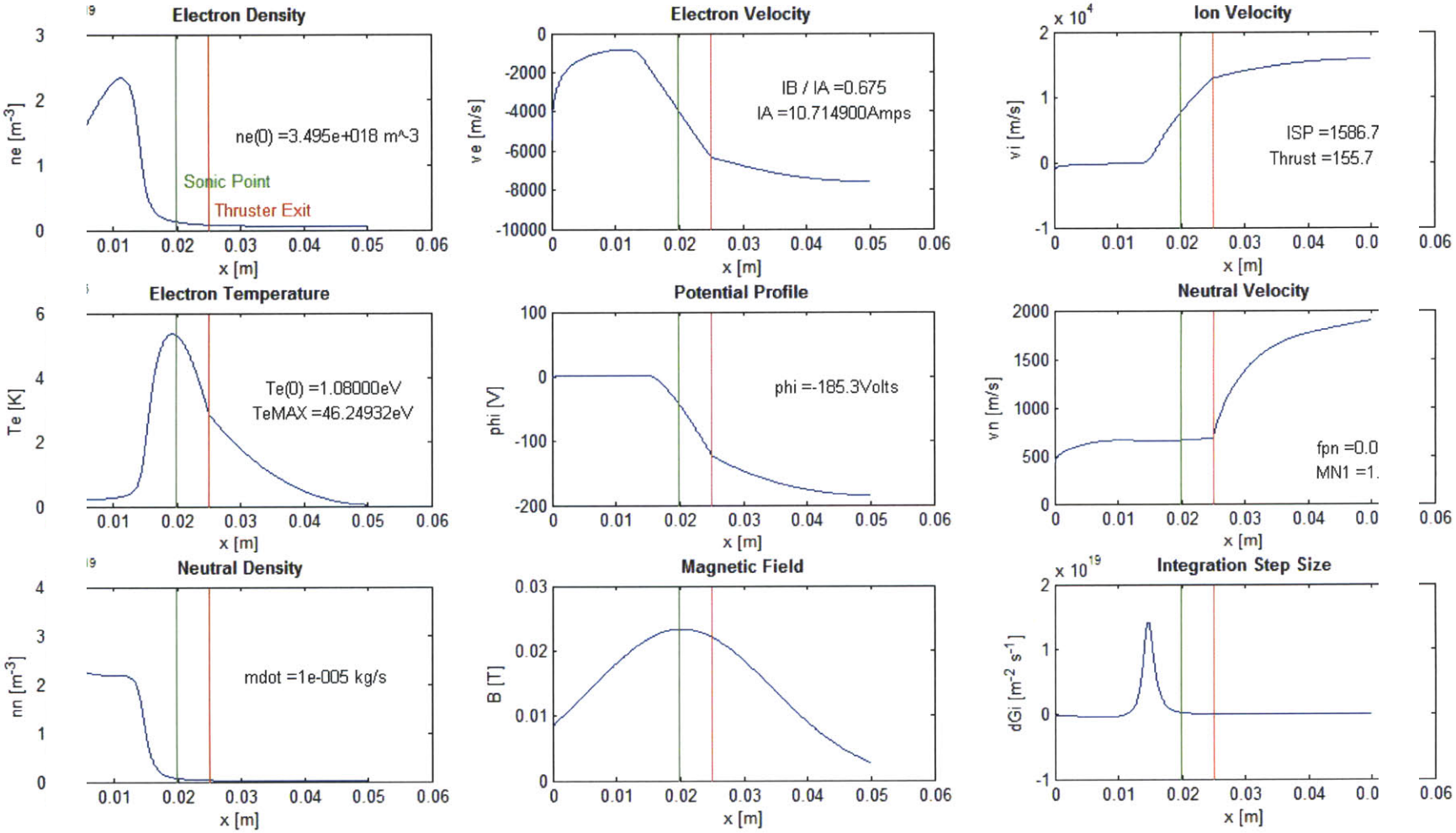

Figure 6.6. Simulated performance of the SPT-100 at mass flow rate $\dot{m} = 10.0$ mg/s

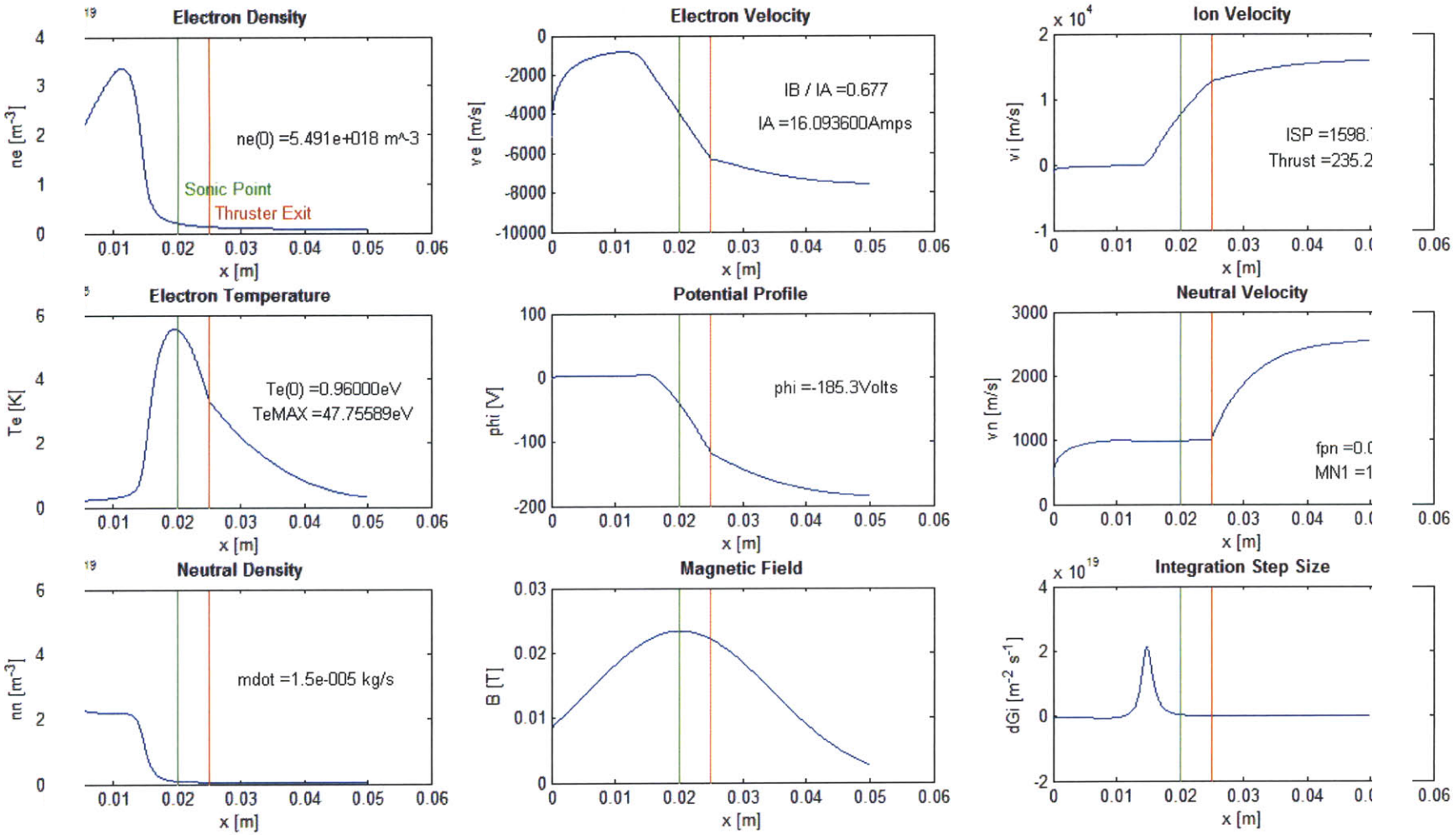

Figure 6.7. Simulated performance of the SPT-100 at mass flow rate $\dot{m} = 15.0$ mg/s

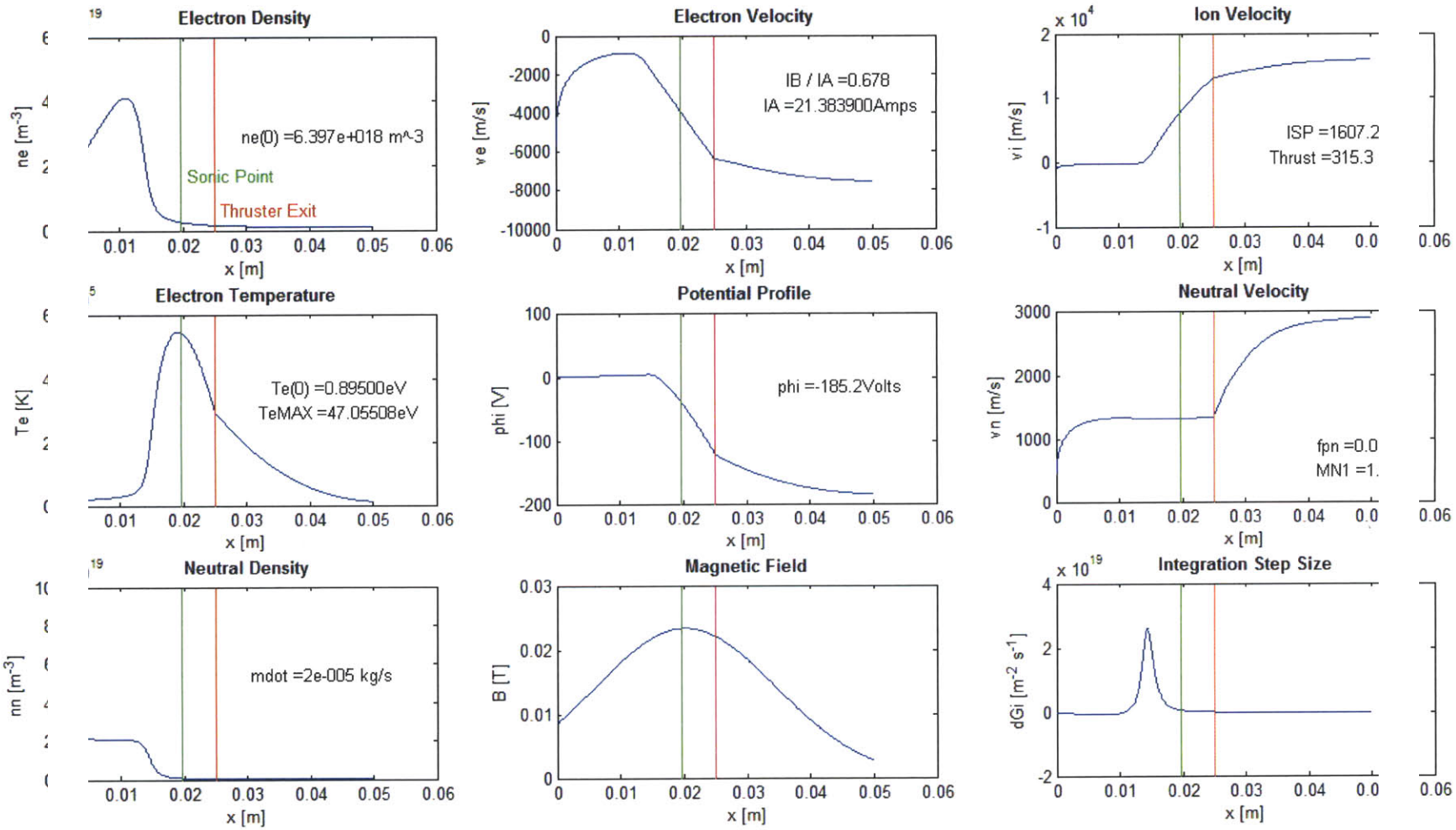

Figure 6.8. Simulated performance of the SPT-100 at mass flow rate $\dot{m} = 20.0$ mg/s

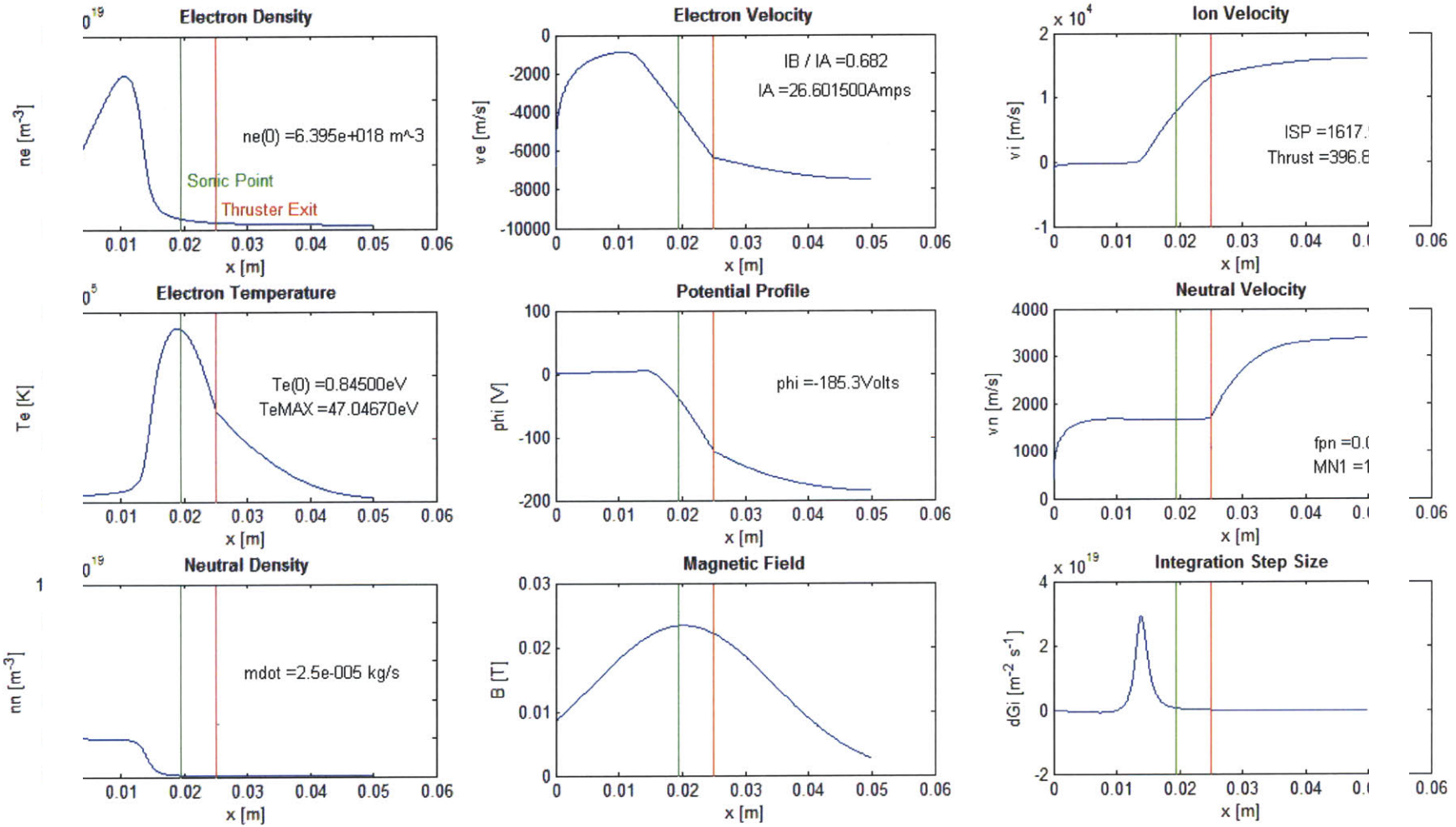

Figure 6.9. Simulated performance of the SPT-100 at mass flow rate $\dot{m} = 25.0$ mg/s

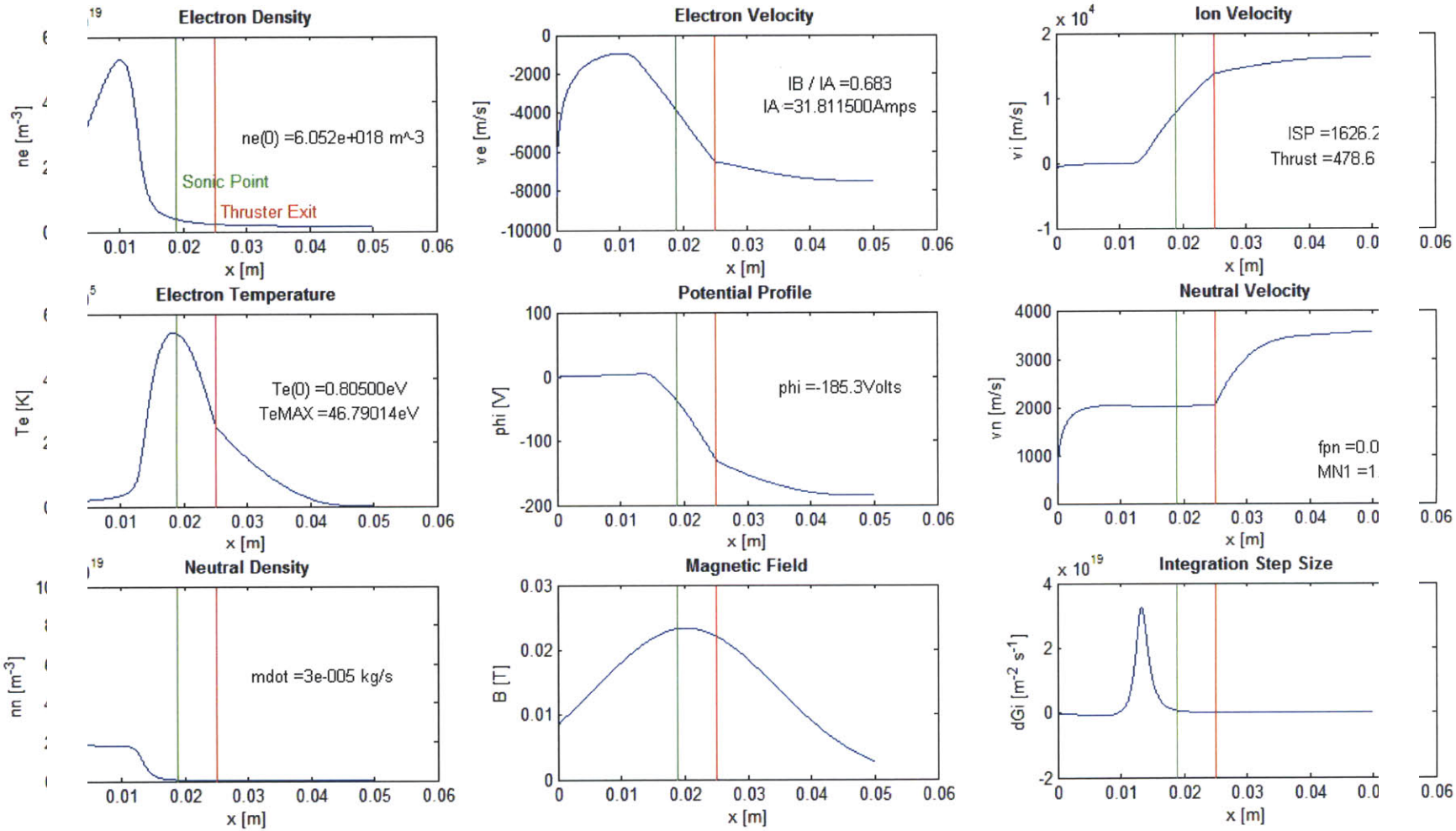

Figure 6.10. Simulated performance of the SPT-100 at mass flow rate $\dot{m} = 30.0$ mg/s

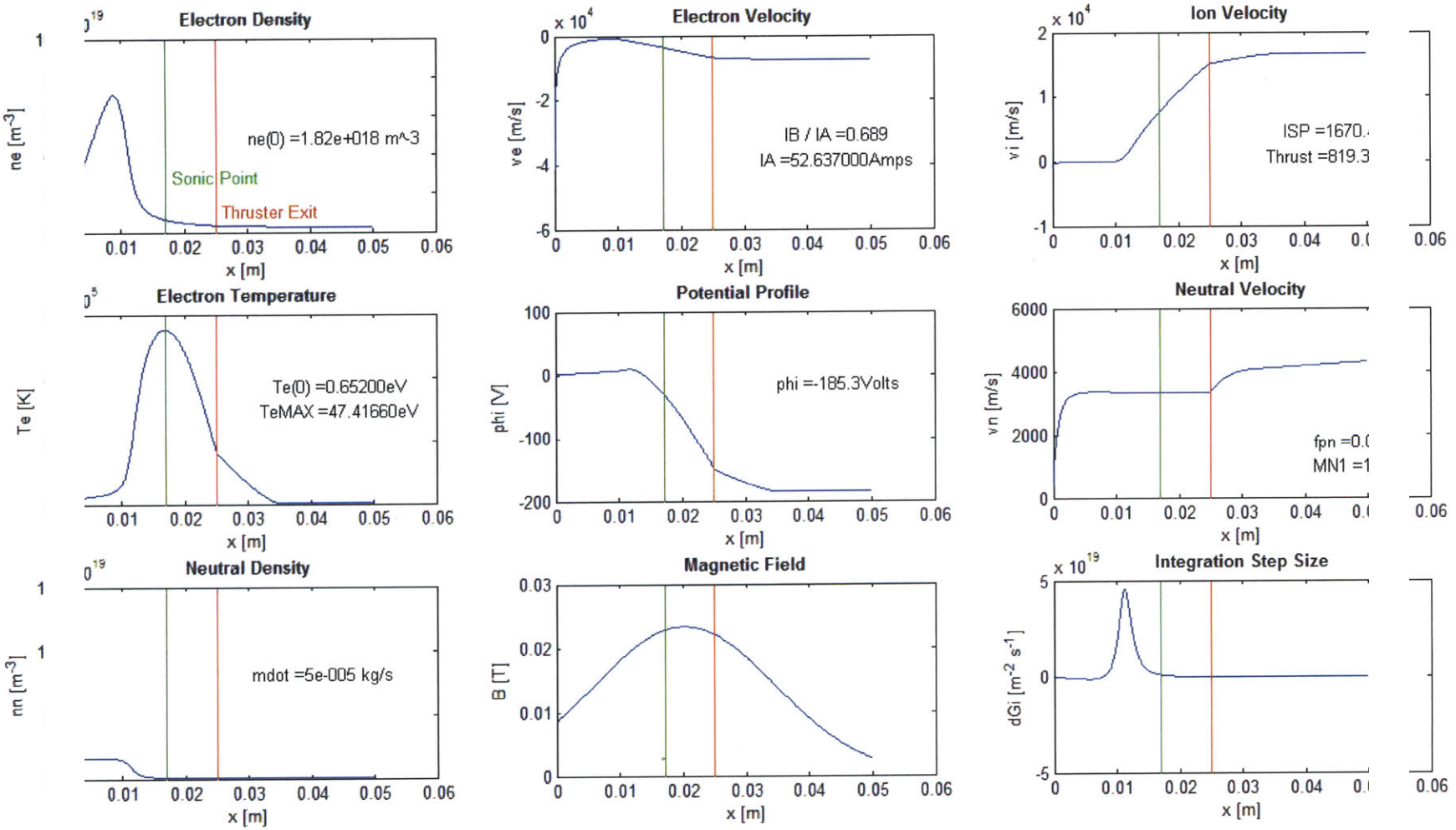

Figure 6.11. Simulated performance of the SPT-100 at mass flow rate $\dot{m} = 50.0$ mg/s

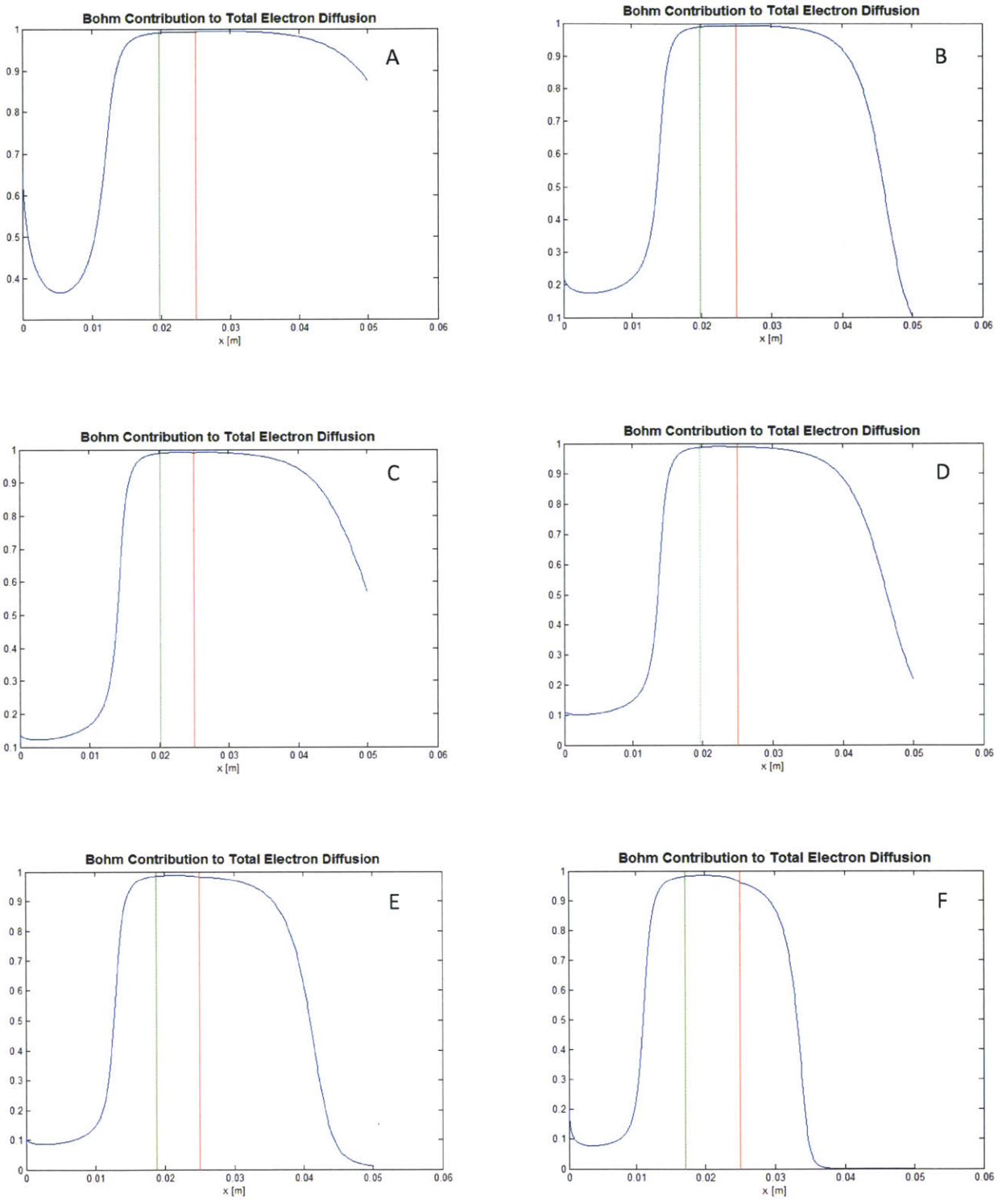

Figure 6.12. Variation in the ratio of Bohm collision frequency to total collision frequency at propellant mass flow rates of A) 5.32 mg/s; B) 10 mg/s; C) 15 mg/s; D) 20 mg/s; E) 30 mg/s; and F) 50 mg/s

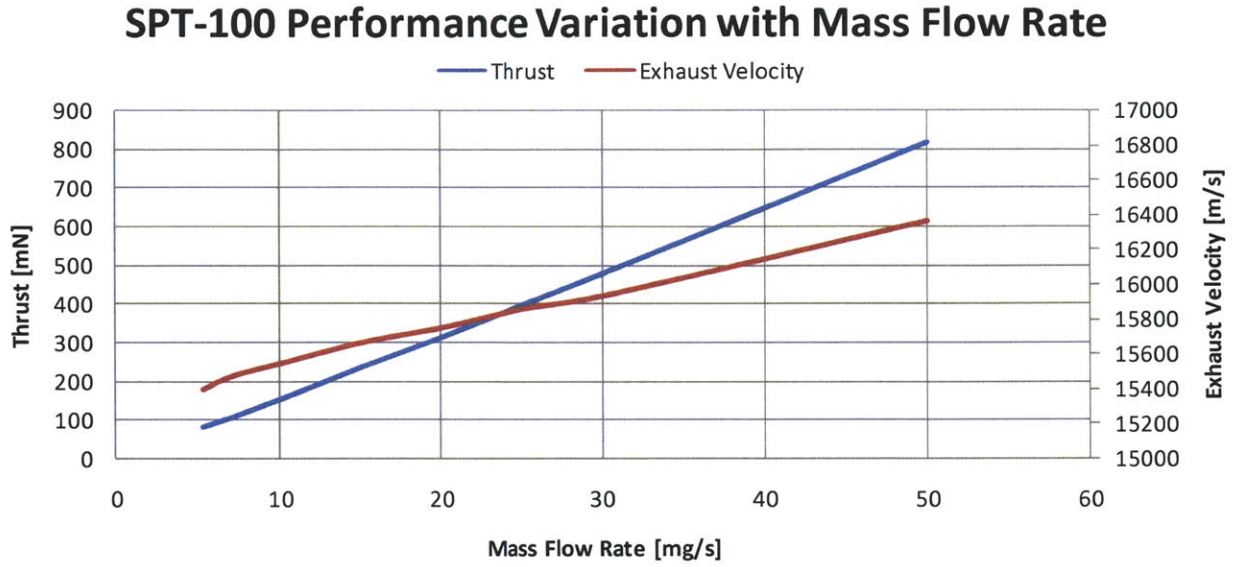

Figure 6.13. Simulated thrust and exhaust velocity for the SPT-100 Hall thruster operated with variable propellant mass flow rate; operating conditions are detailed in preceding Figures 6.4-6.11.

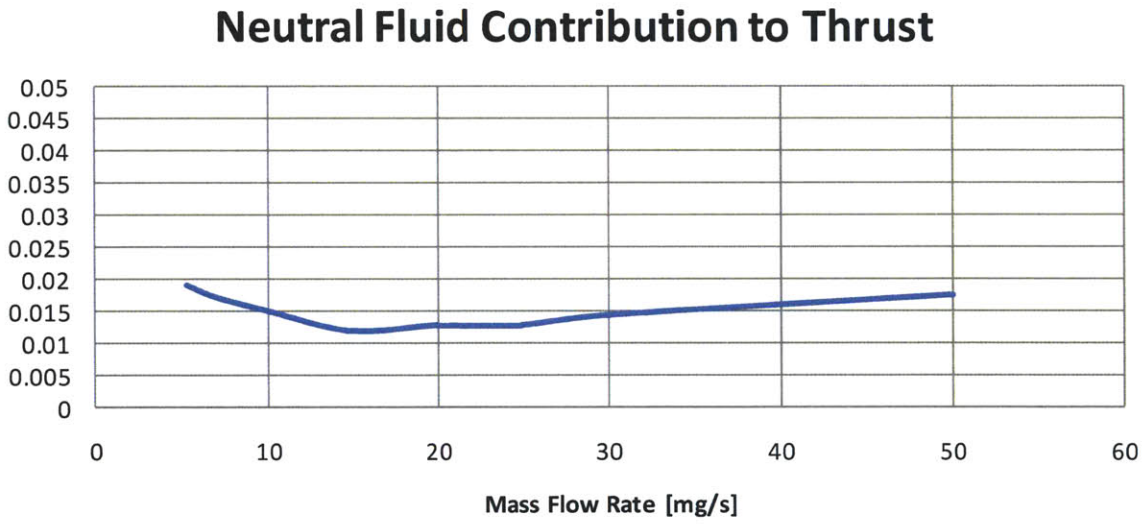

Figure 6.14. The fractional contribution of neutral momentum to the overall thrust achieved is a weakly increasing function of mass flow rate beyond a mass flow rate of approximately 7 mg/s.

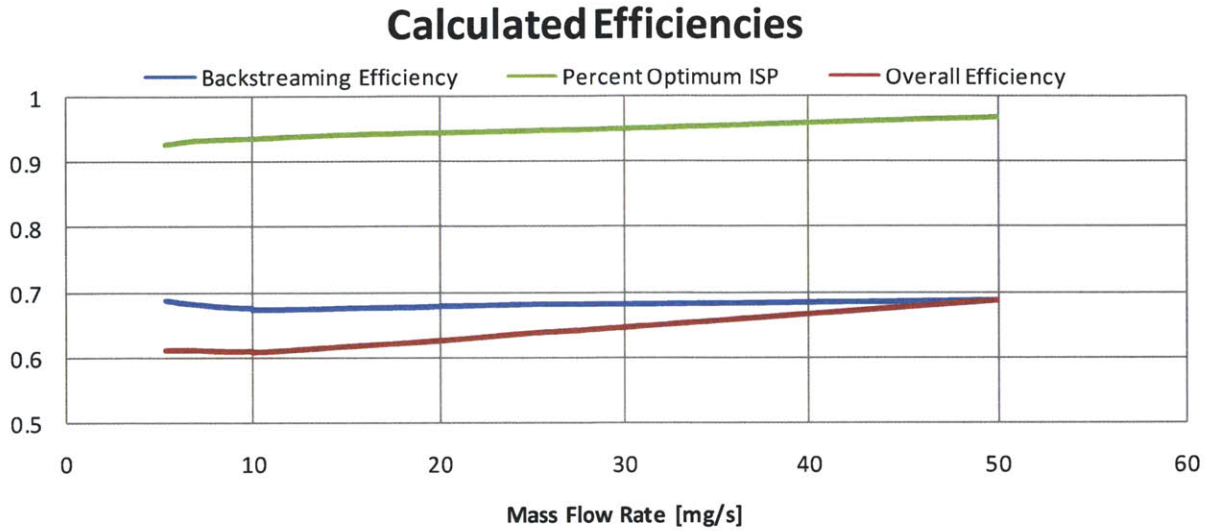

Figure 6.15. The actual specific impulse achieved increases as a function of mass flow rate. This may indicate that ionization is occurring at higher potentials. Increases in the utilization efficiency will also contribute to the increase in overall efficiency.

It is worth noting that the ideal specific impulse shown in Figure 6.15 is defined for the maximum potential drop through the channel, $\Delta\phi = \phi_{MAX} - \phi_{EXIT}$, which incorporates the small increase in potential that occurs upstream of the ion sonic point.

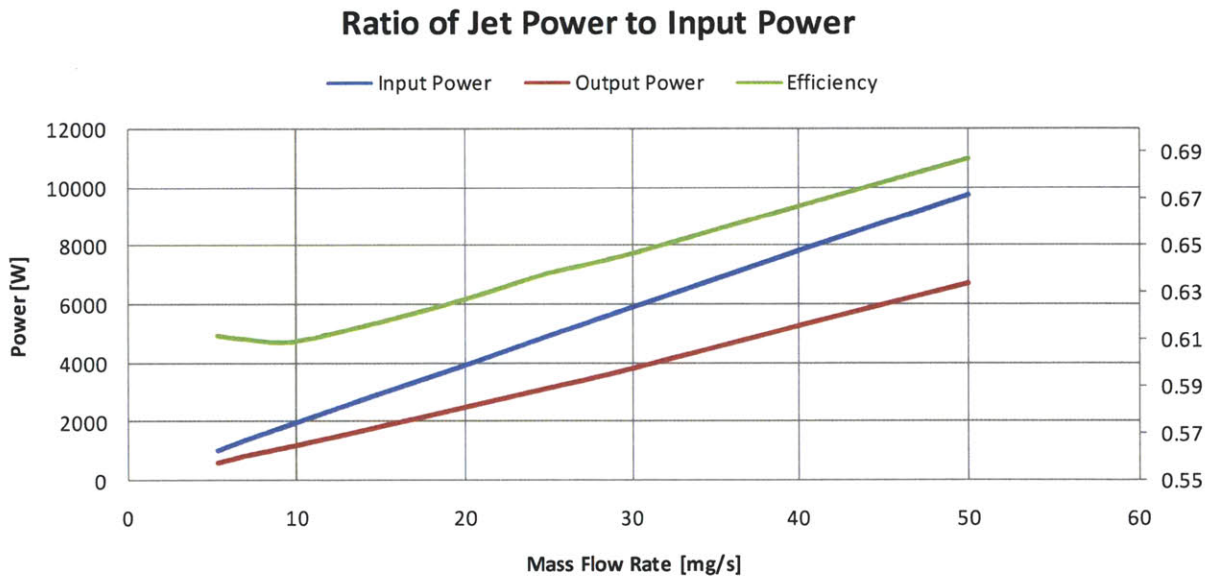

Figure 6.16. Variation in the input and output powers with increasing propellant mass flow rate

The results given in Figure 6.16 indicate that, including the effects of recombinant losses, and at a fixed effective potential, both input power and jet kinetic power are linear in mass flow rate. The efficiency is observed first to drop off as mass flow rate is increased, then grow approximately linearly as mass flow

rate is increased further. As one might expect, this behavior is mirrored in the variations in beam and anode current with increasing mass flow rate, as observed in Figure 6.17, below:

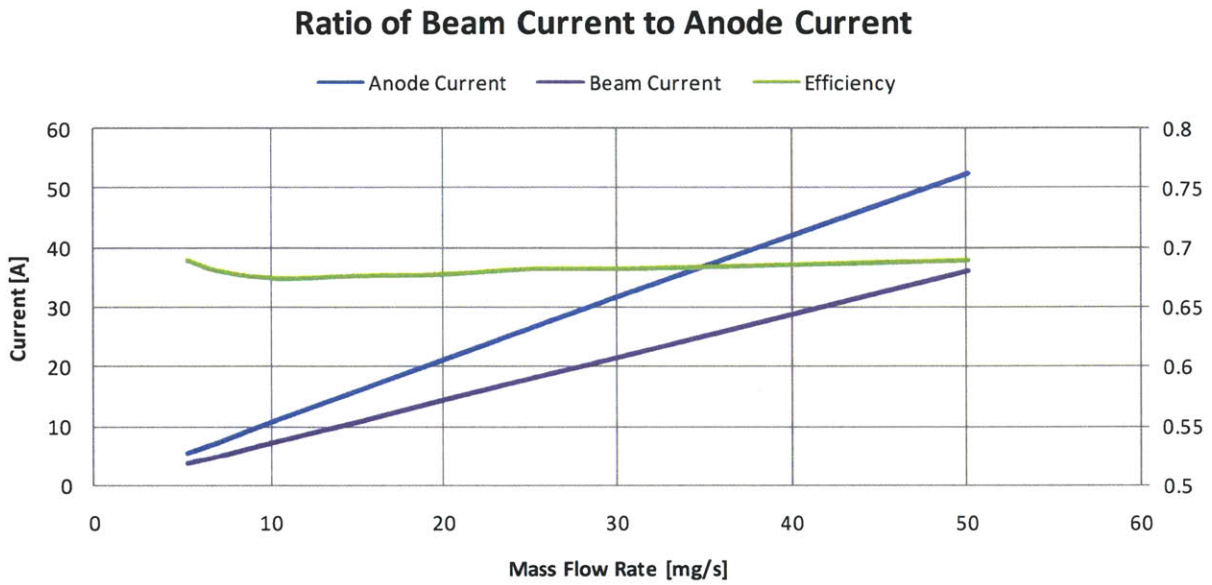

Figure 6.17. Variation in the beam and anode currents with increasing propellant mass flow rate

While the physics incorporated in this model are sufficient to identify trends in important operational parameters as a function of propellant mass flow rate, an important limitation deserves consideration. In treating the performance variations in mass flow rate, the potential drop in the thruster, which was determined by matching the thrust to the experimental value in the baseline case, was held constant, as can be seen in Figures 6.4 – 6.11. This treatment is adequate for evaluating changes in relative thruster performance and efficiency. This methodology is carried through in the sections that follow.

6.5.2 Variations in Mass Flow Rate and Peak Field

The flexibility in defining the thruster and magnetic field geometry and magnetic field strength afforded by this model permit interrogation of thruster performance as a function of these design variables. In particular, it may be useful to explore thruster capabilities at enhanced peak magnetic field strength, peak field location, as well as sensitivities to variation in field shape through the channel. The magnetic field for the baseline SPT-100 operation is well modeled as Gaussian, with a peak field strength of 233 Gauss, centered at $x_0 = 0.0203$ with a variance of $\sigma^2 = 0.0101$.

Variations in the field topology may be evaluated on the basis of their impact on device efficiency given a constant output power. In the design studies that follow, each of the three parameters will be varied independently, and the effects of those variations on operating efficiency will be evaluated for

three values of propellant mass flow rate. At each value of mass flow rate, the thruster output power will be held constant and converged solutions for required input power used to calculate efficiency.

The first element of the magnetic field topology that is of interest is the peak field strength. By varying the peak field and generating solutions for several values of propellant mass flow rate, each at the same output powers as those obtained for the baseline field case, we can identify trends in efficiency as a function of input mass flow rate and peak magnetic field.

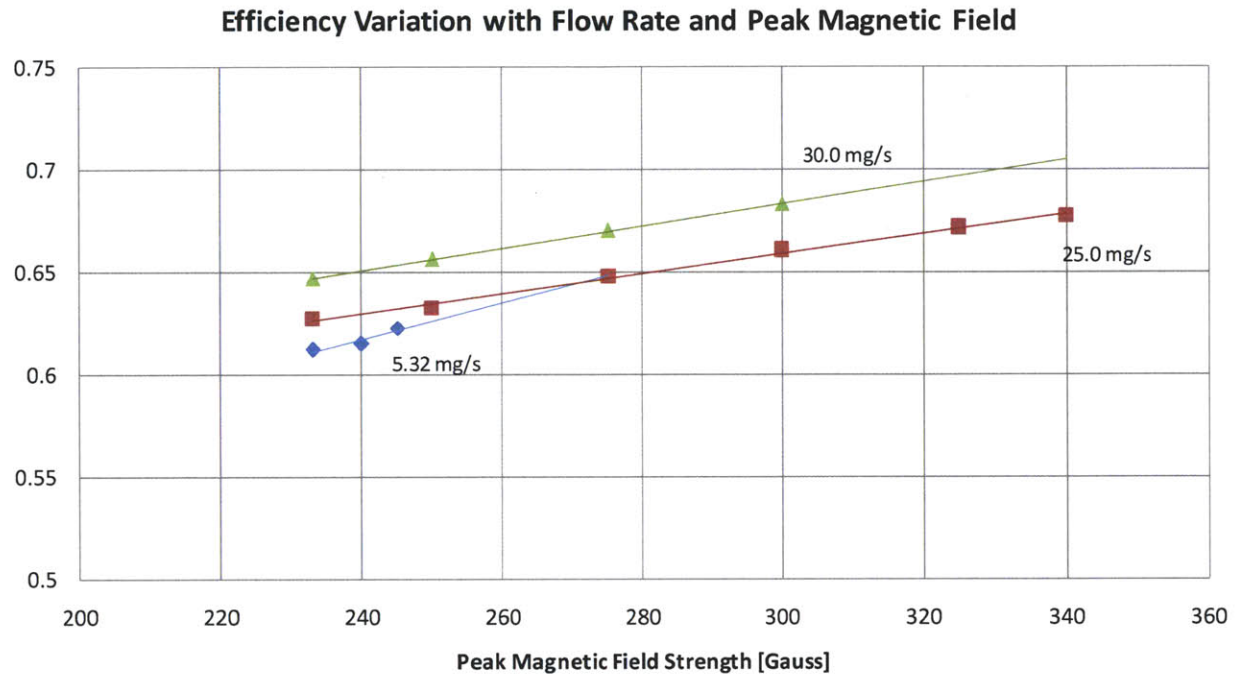

Figure 6.18. Increasing the propellant mass flow rate gives higher achievable values of peak magnetic field and overall device efficiency; peak field location and variance are identical to those for the baseline SPT-100 geometry; maximum peak field obtained for $\dot{m} = 5.32, 25.0$, and 30.0 mg/s are 245, 340 and 300 G respectively.

As peak magnetic field strength is increased, the anode plasma density decreases. Increasing the peak magnetic field has the effect of reducing the anomalous contribution to electron diffusion, forcing the diffusion to become more and more classically dominated, thereby enhancing the barrier to electron diffusion through the channel. The result is an increase in backstreaming efficiency and overall efficiency, as seen in Figure 6.18.

At some critical value of peak field the anode density will tend toward zero, effectively starving the anode. This phenomenon is captured in the model, as seen in Figure 6.19, below for the simulated case of 25.0 mg/s mass flow rate.

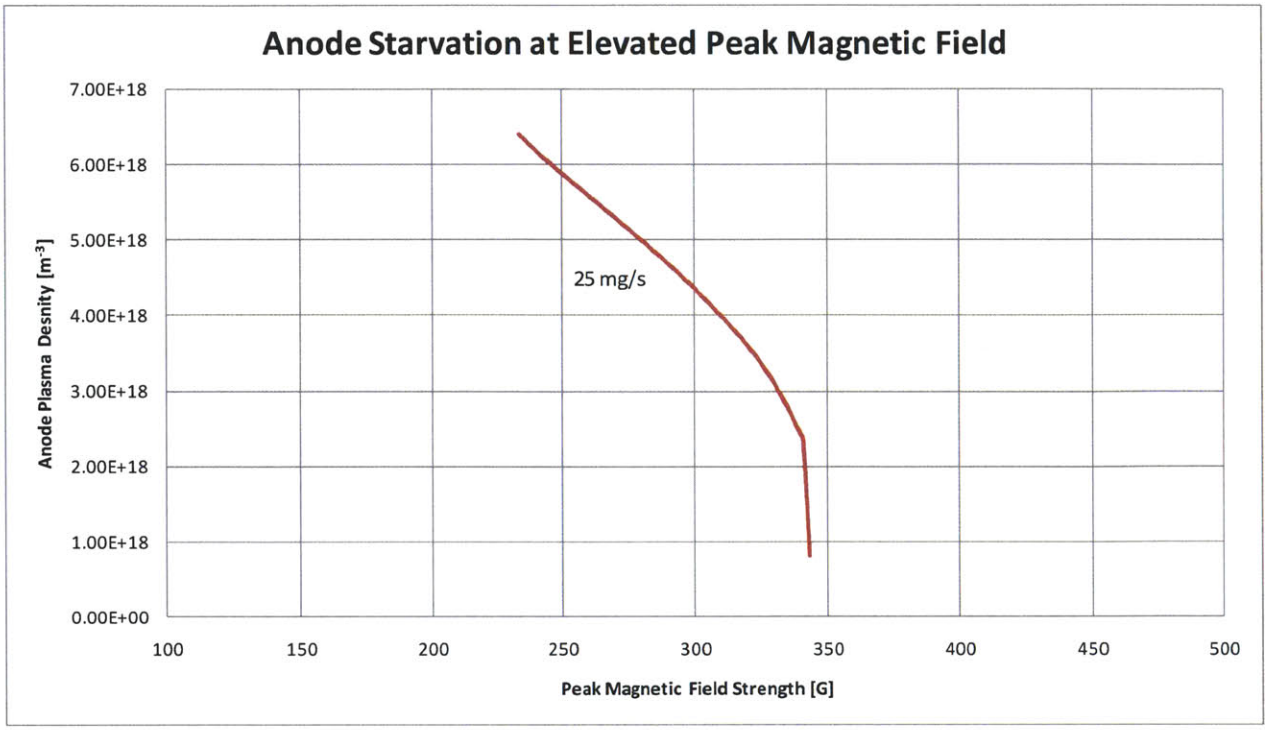

Figure 6.19. Onset of anode starvation is characterized by a sharp decrease in the anode plasma density as peak magnetic field strength in the channel is increased above a certain critical value. Operating conditions are identical to those given for Figure 6.18 for a mass flow rate of 25.0 mg/s.

The critical value of peak magnetic field for which anode starvation occurs is observed to increase with increasing mass flow rate. At a given magnetic field strength, higher propellant mass flow rates yield higher anode plasma densities. The range of achievable peak magnetic field is thus extended for these elevated mass flow rates.

6.5.3 Variations in Peak Field Location and Flow Rate

The next variable of interest is the placement of the peak magnetic field. In order to investigate the effects of the peak placement on device performance, we will follow a procedure similar to that described above. Peak field placement within the channel will be manipulated for several values of propellant mass flow rate, with all simulations of a given flow rate operating at a fixed output power. The variations in the input power so calculated will then be used to evaluate impact on device efficiency.

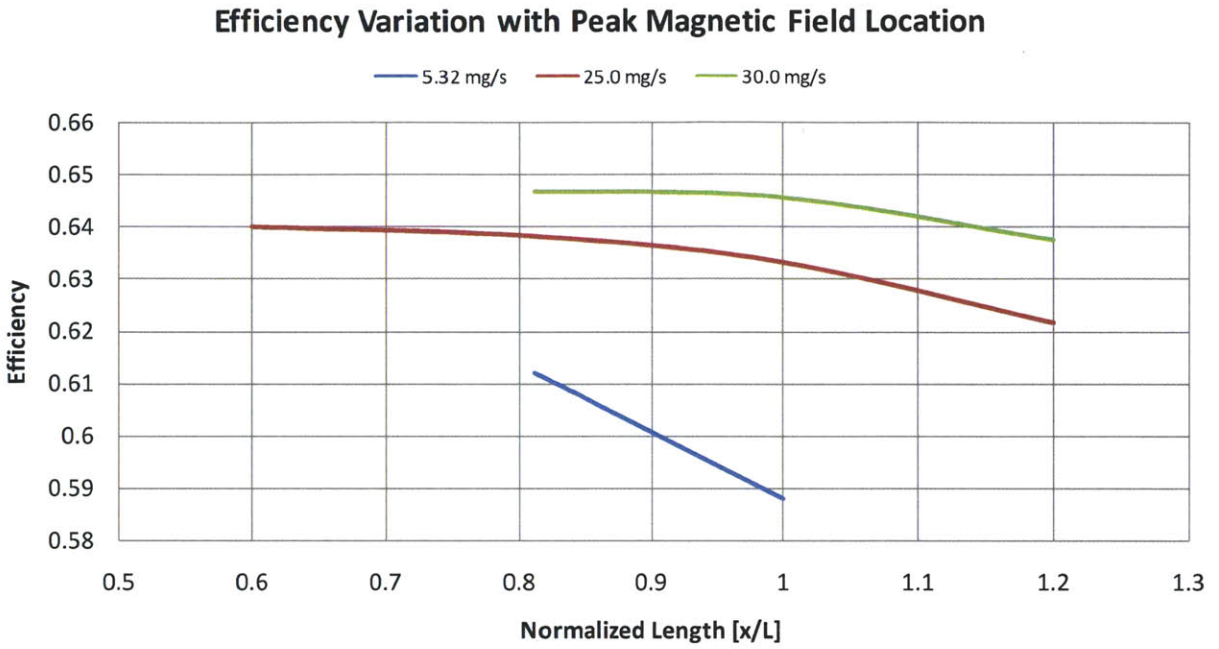

Figure 6.20. Thruster efficiency for a given mass flow rate at a fixed output power is maximized for peak magnetic field upstream of the thruster exit.

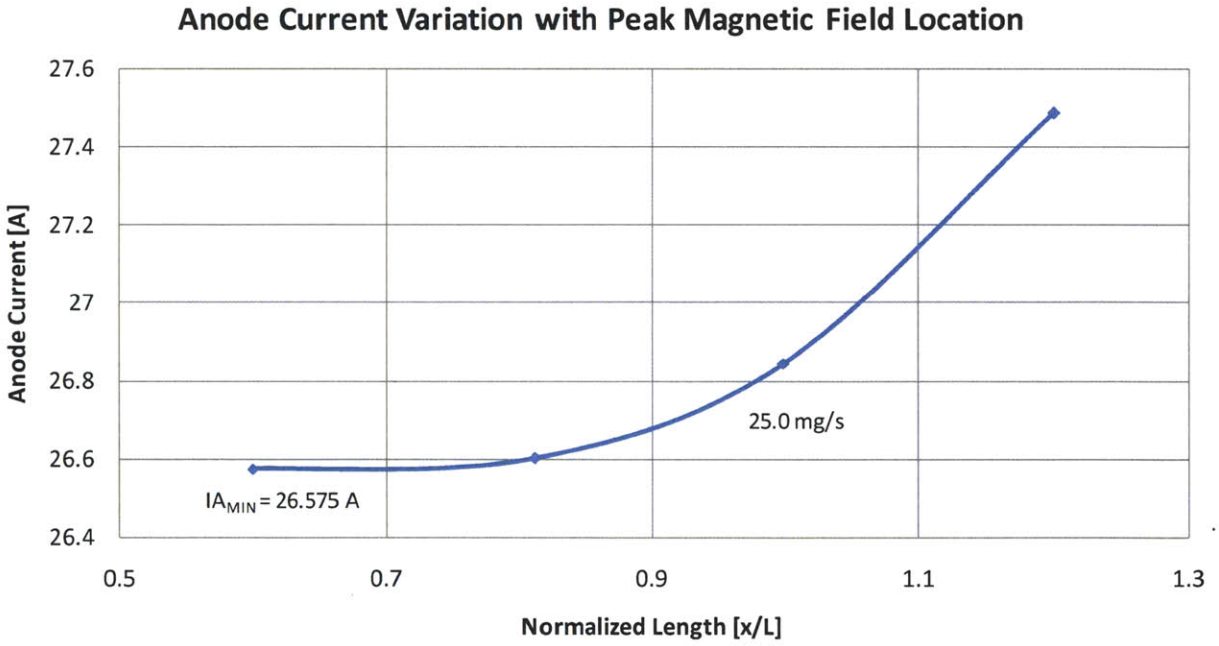

Figure 6.21. For elevated mass flow rates at fixed output power the minimum in required anode current occurs when the peak magnetic field is located nearest to the anode; peak field placement nearer than 0.6L force the electron temperature to drop to zero inside the thruster channel, a non-physical solution.

Results of these simulations seem to indicate that the required anode current is minimized and efficiency is maximized for peak magnetic fields which lie near the anode. It should be noted that, for the fixed geometry assumed in this test case, a very narrow range of peak field locations is possible. If the

anode value of electron temperature is constant, then for all elevated mass flow rates, peak field placement nearer to the anode than 0.6L forces the electron temperature to fall to zero inside the thruster channel, a non-physical solution. In Section 6.5.5, this problem will be circumvented by allowing a variable thruster channel length.

6.5.4 Variations in Field Flatness

The final design variable considered in this work is the shape of the magnetic field in the channel. The effect of variations in magnetic field shape will be explored by modifying the variance of a field whose peak location is fixed. In this case field strength and location are identical to those in the baseline thruster design. The results of these simulations for a mass flow rate of 25.0 mg/s are given in Figure 6.22 below.

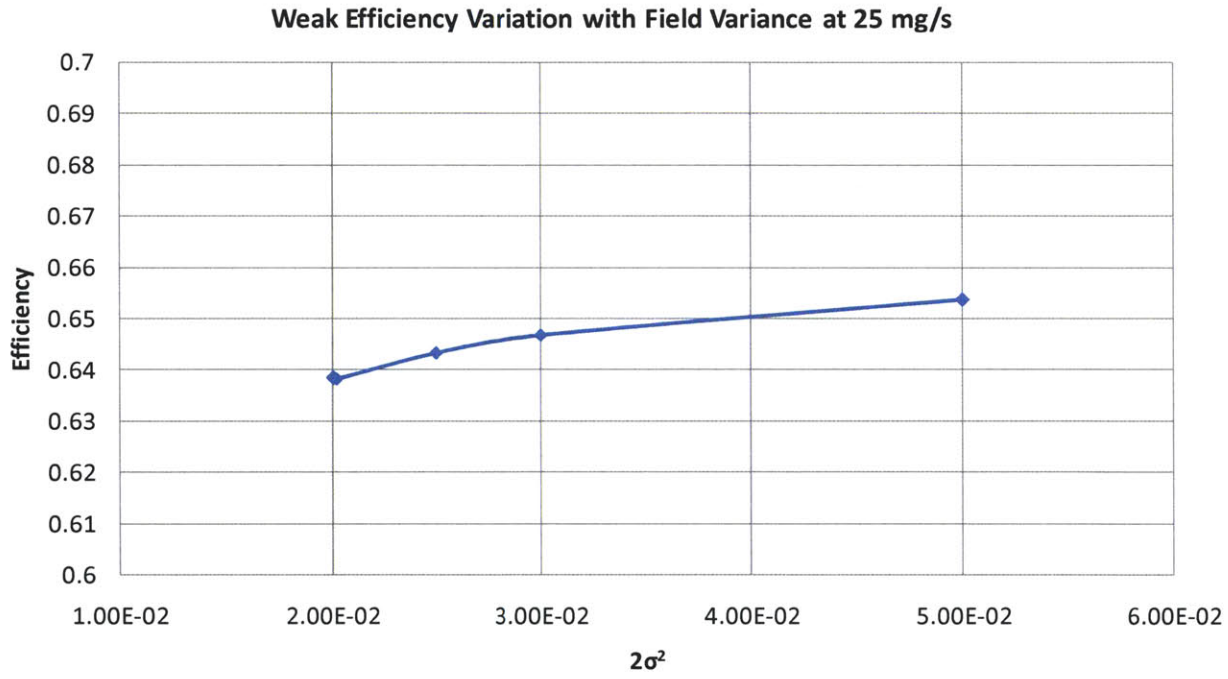

Figure 6.22. Effect of magnetic field variance on device efficiency

No solution could be found for cases with $0.05 < 2\sigma^2 < 0.02$ at the required output power. In the range of variances evaluated, a weak increase in the efficiency is observed as the magnetic field flattens in the channel. For the cases run, this value appears to approach $\eta_{MAX} = 66\%$.

6.5.5 Incorporating Best Practices

The goal of the last numerical experiment that was conducted using this simulation tool was to operate a thruster of assumed variable geometry at the anode starvation limit by varying peak field strength and placement. As the peak of the magnetic field is shifted toward the anode, there is a limiting point at

which smooth sonic passage will no longer occur. When the peak of the magnetic field is held just upstream of this point, the minimum field strength required to operate at the anode starvation condition is achieved. This is desirable from a design standpoint, as it will offer the lowest mass and power conditions for the applied magnetic field coils in the thruster. Results of this exercise are given in Table 6.2, and the effects of peak field and efficiency are shown graphically in Figure 6.23.

M_{DOT}	15.0	20.0	25.0	30.0	50.0	mg/s
Thrust	235.4	315.9	396.7	478.7	819.8	mN
$\Delta\varphi_{APP}$	-186.7	-187.5	-187.2	-186.9	-187.1	V
n_{e0}	1.00E+17	1.00E+17	1.00E+17	1.00E+17	1.00E+17	m^{-3}
x_S	2.11E-02	2.15E-02	2.10E-02	1.99E-02	1.68E-02	m
Te_{MAX}	50.3	50.7	50.8	50.8	50.8	eV
I_A	15.0971	20.2129	25.308	30.3158	51.7626	A
I_B	10.9152	14.5735	18.2218	21.8577	36.2856	A
B_{MAX}	0.0291	0.02858	0.02787	0.0276	0.02155	Tesla
I_{SP}	1599.7	1610.0	1617.5	1626.7	1671.4	s
η_{TOT}	65.447%	65.738%	66.364%	67.331%	69.338%	

Table 6.2. Performance data for SPT-100 thruster geometry operating at anode starvation and incorporating observed best practices for magnetic field configuration

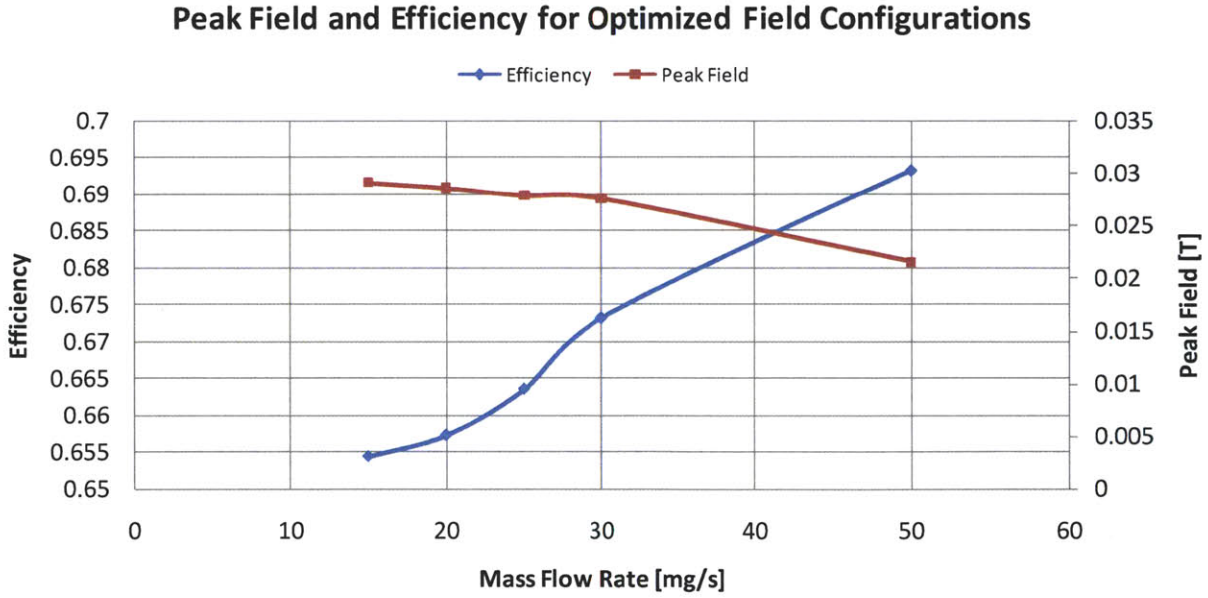

Figure 6.23. Peak field requirements and computed overall efficiencies for several cases of propellant mass flow rate and optimized field configuration

The observed decrease in the peak field required to operate the Hall thruster in the anode starvation limit as mass flow rate is increased deserves some discussion. As mass flow rate is increased, the anode electron temperature must also decrease in order to satisfy the downstream boundary condition on the potential drop. Returning to Eq. 6.6, we find that the effect driving the upstream anode current condition is primarily that of the electron diffusion, $D_{e_\perp}$. By inspection of Eq. 6.4, the electron diffusion will depend linearly on the electron temperature. Furthermore, inspection of the functional dependence of electron-neutral scattering in Eq. 6.84 on the electron temperature demonstrates a linear dependence on the neutral density, n_n, and thus the mass flow rate, but a stronger dependence on electron temperature, approximately $T_e^{\frac{3}{2}}$ for lower temperature values. Thus, while increased anode neutral density alone may tend to increase diffusion of electrons toward the anode because of increased scattering, the concurrent decrease in the required anode electron temperature exerts a greater influence on scattering, as well as the overall diffusion rate. This is an important conclusion in the broader context of this work, as it indicates that mass savings associated with improving the dimensional scaling of Hall thrusters will not be offset by the requirement for increased magnetic field coil mass.

Noting the apparent desirability of operating at the anode starvation limit, it may be worthwhile to derive a suitable design criterion for this operating regime. Returning to the treatment of the anode starvation limit given in Eq. 6.3-6.6, we find:

$$\int_0^L \frac{dx}{D_{e\perp}} = \frac{\eta_a}{0.61 v_{BOHM}} \qquad \text{(Eq. 6.95)}$$

If we assume the electron temperature, T_e, can be represented as some constant approximate value which we will evaluate later, we can further simplify this expression:

$$\int_0^L \frac{B^2 dz}{v_{en} + \alpha\omega_c} = kT_e \frac{m_e \eta_a}{0.61 e^2 v_{BOHM}} \qquad \text{(Eq. 6.96)}$$

Dividing the top and bottom of the integral by the cyclotron frequency gives:

$$\frac{m_e}{e}\int_0^L \frac{B dz}{\frac{1}{\beta} + \alpha} = kT_e \frac{m_e \eta_a}{0.61 e^2 v_{BOHM}} \qquad \text{(Eq. 6.97)}$$

Simplifying this expression and dividing through by the Bohm coefficient, α, gives:

$$\int_0^L \frac{B dz}{1 + \frac{1}{\alpha\beta}} = kT_e \frac{\alpha \eta_a}{0.61 e v_{BOHM}} \qquad \text{(Eq. 6.98)}$$

In the model developed in this work, the Bohm coefficient is taken as $\alpha = \frac{1}{64}$. By evaluating the integral on the left side of Eq. 6.98 numerically using the 1D model, for several of the optimized, anode starved cases in this work, we can back solve for the required value of T_e to force the equality. We find that, for all cases so evaluated, $T_e = T_{e_{MAX}}$ as computed in the 1D model appears to offer the highest degree of accuracy. Note that the value of the Bohm velocity is also evaluated at this temperature. Imposing this condition and evaluating Eq. 6.98 numerically using the 1D model for each of the cases detailed in Table 6.2, we see that this equality is satisfied within a small error band, especially near the lower limit of propellant mass flow rate. These results are given in Table 6.3.

$\dot{M}_{DOT}$ [mg/s]	$\int_0^L \frac{Bdz}{1+\frac{1}{\alpha\beta}}$	$kT_e \frac{\alpha\eta_a}{0.61ev_{BOHM}}$	Error
15	1.435E-04	1.396E-04	2.71%
20	1.375E-04	1.390E-04	-1.10%
25	1.320E-04	1.396E-04	-5.80%
30	1.241E-04	1.395E-04	-12.46%
50	1.025E-04	1.410E-04	-37.59%

Table 6.3. Evaluation of the utility of Eq. 6.98 as a design criterion for the design of magnetic field required to achieve anode starvation; the error is normalized by the integral term on the LHS of Eq. 6.98.

By using projected, approximate values for the maximum electron temperature, backstreaming efficiency and an approximate length for the thruster ionization region, the peak magnetic field required to approach anode starvation may be estimated in a more straightforward way.

6.6 Conclusions and Future Work

Because this treatment has involved the development and application of a simplified one dimensional model of the Hall thruster discharge, the accuracy of the predicted values for final efficiencies are questionable. Nonetheless, the physics incorporated into the model as described in the preceding sections are sufficient to identify trends in relative performance and provide insights into the best design and operational practices for Hall effect thrusters intended to operate at high power and high mass flow rate. These best practices are summarized below.

In a thruster of fixed geometry and magnetic field configuration, the specific impulse is observed to increase with increasing propellant mass flow rate, approaching the ideal value. This is likely because ionization occurs at a higher potential as the flow rate increases. For the SPT-100 thruster model developed in this work, the overall efficiency of the thruster appears to increase gradually as propellant mass flow rate is increased to approximately ten times the nominal value. The results in Figure 6.12

show that the fractional contribution of anomalous diffusion to overall electron diffusion decreases with increasing mass flow rate. This may contribute to the incremental improvement in backstreaming efficiency evident in Figure 6.16, and thus overall efficiency as well.

The effect of magnetic field configuration on overall thruster efficiency has been explored. To evaluate these effects, the peak magnetic field strength, peak location in the channel, and field flatness were each varied individually. Output power in all cases was maintained at a constant value, and the required input power evaluated by simulation. The results of these experiments seem to point to four general conclusions regarding field configuration and elevated flow rate effects:

- Increasing peak magnetic field strength at a fixed mass flow rate appears to result in decreased anode plasma density. Above a certain critical magnetic field strength, anode plasma density tends to very small values. In this case, the anode has reached its so-called starvation limit.

- Maximum efficiency is consistently obtained if the thruster is operated near the anode starvation limit. The required peak magnetic field strength and the overall thruster efficiency increase with increasing mass flow rate when operated in this limit.

- The minimum field strength required to approach the anode starvation limit for the cases considered in this work is obtained when the magnetic field peak is placed a distance of 0.15 m from the thruster anode.

- A weak increase in efficiency is observed for flat magnetic field profiles in the channel.

Results obtained in this work suggest that more comprehensive numerical work and perhaps experimental work are merited in assessing the utility of these design evolutions in developing thrusters designed to operate at high power. A great deal of additional work will be required to validate the reality of any trends identified in the four conclusions above.

Finally, a separate, equally critical aspect of the physics not treated in this work relates to maintaining discharge stability at elevated mass flow rate. It is possible that, at the higher plasma densities associated with increased mass flow rate designs, arc development may occur, creating losses that will undermine any potential gains in performance or efficiency.

Chapter 7

Magnetoplasmadynamic Thrusters

7.1 Introduction

As discussed in Chapter 4, MPD thrusters utilize crossed currents and magnetic fields to generate electro-magnetic body forces in a plasma. The plasma is accelerated through the thruster channel, and subsequently exhausted with high jet velocity. Conventional MPD thruster configurations are unique in that they are the only devices which are able to make use of electromagnetic body forces for acceleration in steady-state operation.

The MPD thruster tends to optimize at higher values of input power, with several megawatts being a typical design point for a self-field MPD thruster. In order to achieve the efficient generation of electromagnetic body forces, large values of azimuthal magnetic field are required. In a self-field MPD thruster this field is generated by the applied radial current, which must, in turn be large. Typical values of input current for self-field MPD thrusters are several tens of kiloamperes.

Several characteristics of MPD thrusters make them attractive for implementation in multi-megawatt NEP applications. First, they seem to fall within the range of specific impulse suitable for NEP missions requiring high thrust as discussed in Chapter 3. Next, these thrusters optimize at relatively high output power relative to competing devices. Finally, the small envelope of these thrusters means that they may achieve very large values of power density and specific power.

Perhaps the greatest engineering challenge associated with the development of high power MPD thrusters for primary propulsion is overcoming lifetime limitations due to cathode erosion. Erosion rates have been measured for two regimes of operation: a relatively short ignition phase characterized by high

erosion rates, and a thermionic phase, characterized by a lower erosion rate [181]. For an operational MPD thruster, the thermionic erosion rate will govern lifetime. In a pure thermionic emission regime, electrode erosion will be dominated by material sublimation. The rate of sublimation is governed by the modified Dushman equation [182]:

$$s(T) = \frac{\dot{m}_S}{I_{TOT}} = \sqrt{\frac{M}{2\pi RT}}\frac{P_V(T)}{J} \qquad \text{(Eq. 7.1)}$$

In this expression, $P_V(T)$ denotes the temperature-dependent vapor pressure of the cathode material, J is the current density at the cathode, and M is the molecular mass of the cathode material. The sublimation rate is usually expressed in units of kg/C.

It has been demonstrated that thrusters utilizing alkali metals (especially lithium) tend to experience less cathode wear than gas-fed thrusters for a given power [183]. The inclusion of small amounts of barium with alkali metal propellants has also been demonstrated as a means of enhancing thermoelectric emission at a given temperature, thereby lowering the required plasma temperature and accompanying material sublimation rates. The use of barium compound impregnation is common practice in the development of hollow cathodes for electrostatic thrusters [184].

The second challenge in developing MPD thrusters for flight applications is improving device efficiency. Efficiency is typically seen to increase in thrusters operating at or near critical current, as discussed in Chapter 4. Increases in efficiency typically occur concurrently with increases in thruster specific impulse.

The challenges of increasing lifetime, performance and efficiency are intimately connected with the onset of the terminal voltage instability phenomenon extensively observed and described in the literature [144-150]. In order to increase the performance and efficiency of MPD thrusters, several means of delaying the onset have been explored, including channel contouring [185-188], and variations in propellant injection [189].

Identifying means of reducing electrode erosion, increasing I_{SP} and improving total efficiency will be required to characterize the utility of MPD thrusters in future high power applications. In Appendix B, a method of characteristics is developed for a thruster operating in the ideal MHD limit that yields an optimal two-dimensional MPD channel contour for thruster performance. This tool is used to inform the design of axisymmetric thruster geometries, which are simulated using an MHD fluid software package to evaluate thruster performance. Gross nozzle parameters, including the area ratio between the thruster throat and exit, as well as the thruster length are calculated from this 2D code, and implemented in an axisymmetric geometry. The intervening nozzle contour is approximate. Based on the observed behavior for this baseline thruster concept, numerous geometry evolutions are implemented and simulated in an

effort to maximize thruster performance. Results of this design effort are described beginning in Section 7.3.

7.2 MACH Code

The Multiblock Arbitrary Coordinate Hydromagnetic (MACH) codes have been designed to simulate highly collisional plasmas, appropriately studied using magnetohydrodynamics (MHD) [189]. MACH2 is able to solve the time-dependent single-fluid multi-temperature resistive MHD equations, including the effects of finite thermal and electrical conductivities and energy losses from radiation on an adaptive computational mesh comprised of arbitrarily shaped hexahedral cells [190]. The program also has the ability to incorporate elastic stress modeling and plastic deformation of materials for relevant problem types. The MACH codes were developed from an earlier software package developed at Los Alamos National Laboratories called MOQUI [191]. Including the elastic stress model, the MACH2 code is able to solve the time-dependent system of equations outlined below.

Mass continuity is given by:

$$\frac{\partial \rho}{\partial t} = -\nabla \cdot (\rho \vec{v}) \qquad \text{(Eq. 7.2)}$$

The equations for fluid momentum can be written compactly:

$$\rho \frac{dv^i}{dt} = -\rho v^j \nabla_j v^i + \nabla_j \left[-\left(P + Q + \frac{1}{3} u_R \right) \delta^{ji} + \frac{1}{\mu_0} \left(B^j B^i - \frac{1}{2} B^2 \delta^{ji} \right) + \sigma^d_{ji} \right] \qquad \text{(Eq. 7.3)}$$

Summation over repeated indices $(i, j) \in \{1, 2, 3\}$ is assumed in the fluid momentum equation above, as well as in the equations following. The electron specific internal energy is given by:

$$\rho \frac{\partial \epsilon_e}{\partial t} = -\rho \vec{v} \cdot \nabla \epsilon_e - P_e \delta^{ij} \nabla_i v_j + \eta J^2 - \vec{J} \cdot \left(\frac{\nabla P_e}{e n_e} \right) + \nabla \cdot (\kappa_e \nabla T_e) - \Phi_{eR} - \rho c_{ve} \frac{T_e - T_i}{\tau_{ei}} \qquad \text{(Eq. 7.4)}$$

And the ion specific internal energy, similarly:

$$\rho \frac{\partial \epsilon_i}{\partial t} = -\rho \vec{v} \cdot \nabla \epsilon_i + \left[-(P_i + Q) \delta^{ij} + \sigma^d_{ji} \right] \nabla_i v_j + \nabla \cdot (\kappa_i \nabla T_i) + \rho c_{vi} \frac{T_e - T_i}{\tau_{ei}} \qquad \text{(Eq. 7.5)}$$

The radiation energy density may be expressed:

$$\frac{\partial u_R}{\partial t} = -\rho \vec{v} \cdot \nabla u_R - \frac{4}{3} u_R \nabla \cdot \vec{v} + \nabla \cdot (\rho \chi_r \nabla u_R) + \Phi_{eR} \qquad \text{(Eq. 7.6)}$$

The magnetic induction equation:

$$\frac{\partial \vec{B}}{dt} = \nabla \times (\vec{v} \times \vec{B}) - \nabla \times (\eta \vec{J}) - \nabla \times \left(\frac{\vec{J} \times \vec{B}}{en_e}\right) + \nabla \times \left(\frac{\nabla P_e}{en_e}\right) \quad \text{(Eq. 7.7)}$$

And, finally, the material elastic stress:

$$\frac{\partial \sigma_{ji}^d}{\partial t} = 2\mu d_{ij}^d - v^k \nabla_k \sigma_{ji}^d \quad \text{(Eq. 7.8)}$$

In this system of equations, the fluid mass density is given by ρ, the fluid velocity by $\vec{v}$, and the magnetic induction by $\vec{B}$. The electron and ion specific internal energies are given by ϵ_e and ϵ_i respectively. The radiant flux $u_R = \sigma T_R^4$, where T_R is the radiation temperature. The electron and ion temperatures and pressures are denoted T_e, T_i, P_e, and P_i. The artificial numerical compressional viscosity is represented by Q. The current density is given by $\vec{J}$. The sum of the classical and anomalous electrical resistivity is denoted by η. The electron number density is given by n_e, the electron and ion thermal conductivities by κ_e and κ_i respectively, and the Rosseland mean opacity by χ_r. The electron and ion specific heats are denoted by c_{ve} and c_{vi}, the shear modulus μ, the electron-ion equilibration time τ_{ei}, the fundamental charge, e, and the permeability of free space μ_0. The components of the elastic stress deviators are denoted by in indexed term σ_{ji}^d, and the components of the unit dyad are similarly expressed as δ^{ij}. Finally, the radiation coupling term is related to the radiation and electron temperatures:

$$\Phi_{eR} = 4\sigma\rho\chi_r(T_e^4 - T_R^4) \quad \text{(Eq. 7.9)}$$

MACH is also able to incorporate several externally applied inputs, including external circuits, a laser model, and the inclusion of explosive materials in the problem domain. The external circuit subroutine is especially useful in simulating the operation of the plasma thrusters which application is the focus of this chapter. External circuits may be driven by voltage sources or current sources, each with a variety of options for tailoring time dependent response of the source, including a model for the pulse-forming network which is quite useful in performing experimental work in pulsed or quasi-steady MPD thruster operation. In this work, external sources are modeled as constant current sources. The required voltage to drive the fixed current can be modeled during the simulation. This may allow observation of the onset of terminal voltage instability during operation beyond the threshold of performance onset.

Both axisymmetric cylindrical and planar geometries can be simulated using MACH. In cylindrical geometries, the axis of revolution is the y-axis. In the case of MACH2, simulation geometries are developed using one or more blocks which lie in the xy- or rz-plane. Each block must be specified by four points in the xy- or rz-plane, but the block sides need not necessarily be straight lines. Boundary

conditions may be applied to any of the four sides of a given block. Each block is surrounded by a band of so-called "ghost cells," which are used to implement these boundary conditions computationally. Geometries supported by MACH2 include both straight lines and arcs. Arc shapes may be defined using a starting and ending point, as well as either a third point lying on the arc, or the initial slope of the arc. This choice of geometries makes the development of complex surfaces, including compound curves, somewhat difficult. In order to facilitate more complex geometries, the MACH routine MSMKUCRV may be modified by the user. Such modifications were not necessary for the geometries considered in this work. Figure 7.1 illustrates the block constructions and resulting meshes for several of the MPD thruster geometries that were developed in this work.

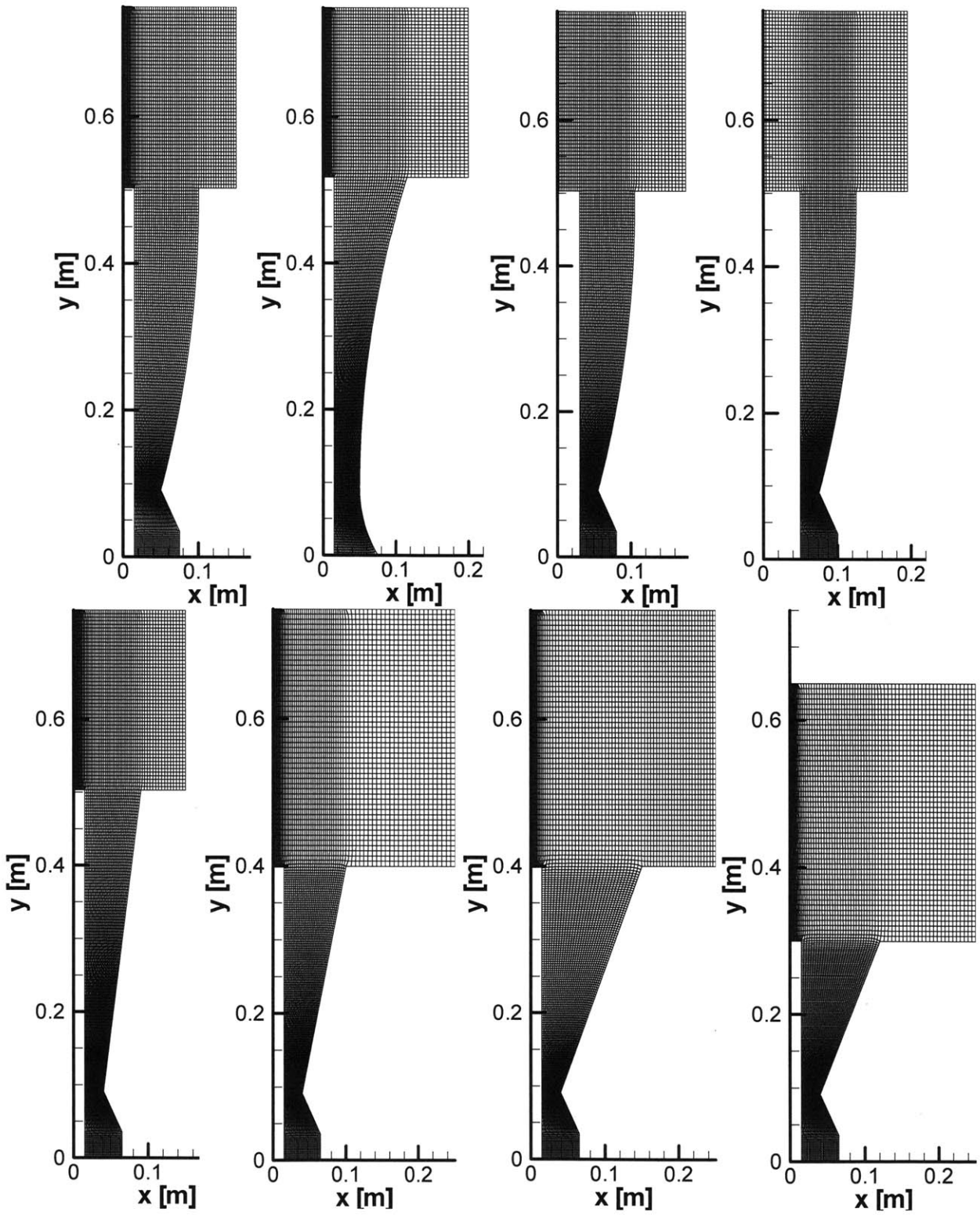

Figure 7.1. A selected set of the axisymmetric MPD thruster channel geometries considered in this work; in all geometries considered in this work, the cathode lies on the y-axis.

One of the strengths of the MACH code is the ease with which a wide variety of boundary conditions may be specified by the user to reflect the structure of a real system to be simulated. Boundary conditions are fundamentally hydrodynamic, electromagnetic, or thermal. Typical hydrodynamic boundary conditions allow the user to specify components of fluid velocity, temperature and density at the boundary. This allows for the development of no-slip or free-slip conditions at solid surfaces, as well as the implementation of propellant injection at boundaries. The electromagnetic boundary conditions allow users to specify whether surfaces or conducting or insulating. These also provide the user with the ability to attach external circuits to boundaries to simulate the operation of plasma devices, for example. Finally, thermal boundary conditions give the user the ability to specify whether surfaces are thermally conducting or insulating to specify the flow of thermal energy out of the system.

Simulations are constructed in MACH using an input file or deck. Input files in MACH2 are comprised of up to eleven namelists. These namelists allow the user to supply the values for a variety of input parameters, as well as activate or deactivate code components which may or may not be needed in simulating a system of interest. An exhaustive description of these namelists and corresponding variables is given in Chapter 7 of [190]. Files supplementing the input file may also be required to specify, for example, external magnetic field geometry.

7.3 Results

In this section the results of the MPD channel contouring simulations conducted using MACH are presented. In all cases lithium is used as the propellant, consistent with the previous discussion of best practices. The axisymmetric geometries of all the contour design evolutions evaluated in this work are summarized in Table 7.1. The accompanying performance data for each thruster is presented in Table 7.2. Also included in Table 7.2 are some calculations related to the onset conditions for MPD thrusters, as discussed briefly in Chapter 4. The onset parameters are precisely those outlined in Section 4.4.1 previously:

$$\frac{I^{*2}}{\dot{m}\sqrt{E_i M_M}} = const. \qquad \text{(Eq. 7.10)}$$

The Bakhst prediction for onset current [145] is given by:

$$I_{ON} = \left[\dot{m}^4 \left(\frac{945}{8}\right) \frac{e}{\mu_0^4 m_i^2} \frac{kT}{\sigma} \frac{LH^3}{d^5}\right]^{\frac{1}{7}} \qquad \text{(Eq. 7.11)}$$

In Eq. 7.11 the plasma conductance is given by σ, and is assumed to have a value of 8000 mho/m, L is the thruster length, H is taken as the circumference of the thruster exit and d is the throat radius. As in

previous sections, the ion mass is denoted by m_i, the permeability of free space, μ_0, and the electric charge, e. Plasma temperature is taken at 30,000 K. Dimensional values are as tabulated in Table 7.1. Mass flow rate is given in Table 7.2.

For the first case considered in this work, the time-evolution of the axial velocity and density distributions are also included to demonstrate that the thruster reaches steady operating conditions in the allotted simulation time. These distributions are shown in Figure 7.2 and 7.3. Beginning with the channel contour corresponding to the 2D ideal MHD limit, the results of each simulation are presented, including the steady state axial velocity distribution of propellant plasma in the channel, density evolution, a mapping of the Alfven and the Mach-Alfven number throughout the channel in the steady state, and the steady-state current distributions. These data are presented for Case 1 of Tables 7.1 and 7.2 in Figure 7.4. In Figure 7.4 and following the Alfven number is based on the magnetosonic speed:

$$A = \sqrt{\frac{\mu_0 \rho v^2}{B_Z^2}} \qquad \text{(Eq. 7.12)}$$

The Mach-Alfven number incorporates the gasdynamic speed of sound:

$$M_A = \sqrt{\frac{v^2}{\frac{\gamma p}{\rho} + \frac{B_z^2}{\mu_0 \rho}}} \qquad \text{(Eq. 7.13)}$$

Based on insights obtained by inspection of these results, design evolutions to improve performance are implemented and tested.

Case No.	Inlet Radius [m]	Throat Radius [m]	Exit Radius [m]	Cathode Radius [m]	Thruster Length [m]	Divergence / Takeoff Angle [deg]	Area Ratio [A_e/A_{th}]	Shape Description
1	0.075	0.05	0.1	0.015	0.503	14.40	4.30	2D Approximated Method of Characteristics
2	0.075	0.05	0.115	0.015	0.518	14.40	5.71	Evolution of Case 1 - Smoothed Anode Lip
3	0.075	0.05	0.115	0.015	0.518	14.40	5.71	Smooth Convergent Divergent
4	0.065	0.04	0.09	0.015	0.503	14.40	5.73	2D Approximated Method of Characteristics
5	0.055	0.03	0.08	0.015	0.503	14.40	9.15	2D Approximated Method of Characteristics
6	0.080	0.055	0.105	0.030	0.503	14.40	4.76	2D Approximated Method of Characteristics
7	0.100	0.075	0.125	0.050	0.503	14.40	4.20	2D Approximated Method of Characteristics
8	0.065	0.04	0.09	0.015	0.503	6.90	5.73	Linear Convergent-Divergent
9	0.065	0.04	0.1	0.015	0.503	8.27	7.11	Linear Convergent-Divergent
10	0.065	0.04	0.12	0.015	0.503	10.96	10.31	Linear Convergent-Divergent
11	0.065	0.04	0.15	0.015	0.503	14.91	16.20	Linear Convergent-Divergent
12	0.065	0.04	0.1	0.015	0.4	10.95	7.11	Linear Convergent-Divergent
13	0.065	0.04	0.12	0.015	0.4	14.47	10.31	Linear Convergent-Divergent
14	0.065	0.04	0.15	0.015	0.4	19.54	16.20	Linear Convergent-Divergent
15	0.065	0.04	0.1	0.015	0.3	15.95	7.11	Linear Convergent-Divergent
16	0.065	0.04	0.12	0.015	0.3	20.85	10.31	Linear Convergent-Divergent
17	0.065	0.04	0.12	0.015	0.503	14.40	10.31	Contoured Evolution of Case 10
18	0.065	0.04	0.12	0.015	0.503	20	10.31	Contoured Evolution of Case 10
19	0.065	0.04	0.12	0.015	0.503	25	10.31	Contoured Evolution of Case 10

Table 7.1. Geometric Data for each of the 19 MPD thruster channel configurations considered in this work; cases exhibiting overall efficiencies greater than 30% are highlighted in yellow.

Case No.	Applied Current [kA]	Voltage [V]	Mass Flow Rate [kg/s]	Average Jet Velocity [m/s]	Applied Power [MW]	Simulated Onset Parameter	Calculated Onset Parameter	Bakhst [192] Predicted Onset Current	Actual / Calculated Onset Condition	Efficiency [%]
1	29.98	49.83	4.75E-04	42113.0	1.494	6.30E+14	6.28E+13	1.35E+04	10.04	28.2%
2	11.00	33.26	4.54E-04	16749.0	0.366	8.89E+13	6.58E+13	1.40E+04	1.35	17.4%
3	11.00	40.03	4.51E-04	19768.0	0.440	8.94E+13	6.62E+13	1.39E+04	1.35	20.0%
4	25.00	50.59	3.65E-04	47222.0	1.265	5.71E+14	8.18E+13	1.30E+04	6.98	32.2%
5	15.00	57.29	2.64E-04	38933.5	0.859	2.84E+14	1.13E+14	1.26E+04	2.51	23.3%
6	30.998	54.25	4.88E-04	43319.4	1.682	6.56E+14	6.12E+13	1.30E+04	10.73	27.2%
7	38.998	60.40	6.29E-04	41697.1	2.355	8.06E+14	4.75E+13	1.30E+04	16.98	23.2%
8	15.999	46.43	3.57E-04	34709.1	0.743	2.39E+14	8.36E+13	1.28E+04	2.86	28.9%
9	14.999	45.07	3.54E-04	33124.5	0.676	2.12E+14	8.43E+13	1.33E+04	2.51	28.7%
10	13.999	36.19	3.51E-04	31439.4	0.507	1.86E+14	8.50E+13	1.44E+04	2.19	34.2%
11	9.995	32.42	3.43E-04	21479.4	0.324	9.71E+13	8.70E+13	1.56E+04	1.12	24.4%
12	12.999	43.91	3.50E-04	25710.2	0.571	1.61E+14	8.53E+13	1.28E+04	1.89	20.3%
13	10.999	38.66	3.45E-04	21835.0	0.425	1.17E+14	8.65E+13	1.38E+04	1.35	19.3%
14	8.995	35.02	3.42E-04	19680.3	0.315	7.89E+13	8.73E+13	1.51E+04	0.90	21.0%
15	8.996	37.97	3.42E-04	18311.4	0.342	7.89E+13	8.73E+13	1.22E+04	0.90	16.8%
16	7.996	31.65	3.41E-04	17877.0	0.253	6.25E+13	8.75E+13	1.31E+04	0.71	21.5%
17	14.999	38.06	3.50E-04	33048.9	0.571	2.14E+14	8.53E+13	1.43E+04	2.51	33.5%
18	21.999	46.85	3.57E-04	44911.3	1.031	4.52E+14	8.36E+13	1.45E+04	5.40	34.9%
19	16.999	44.33	3.45E-04	30904.2	0.754	2.79E+14	8.65E+13	1.42E+04	3.23	21.9%

Table 7.2. Performance Data for the various thruster geometries considered in this work; cases exhibiting overall efficiencies greater than 30% are highlighted in yellow.

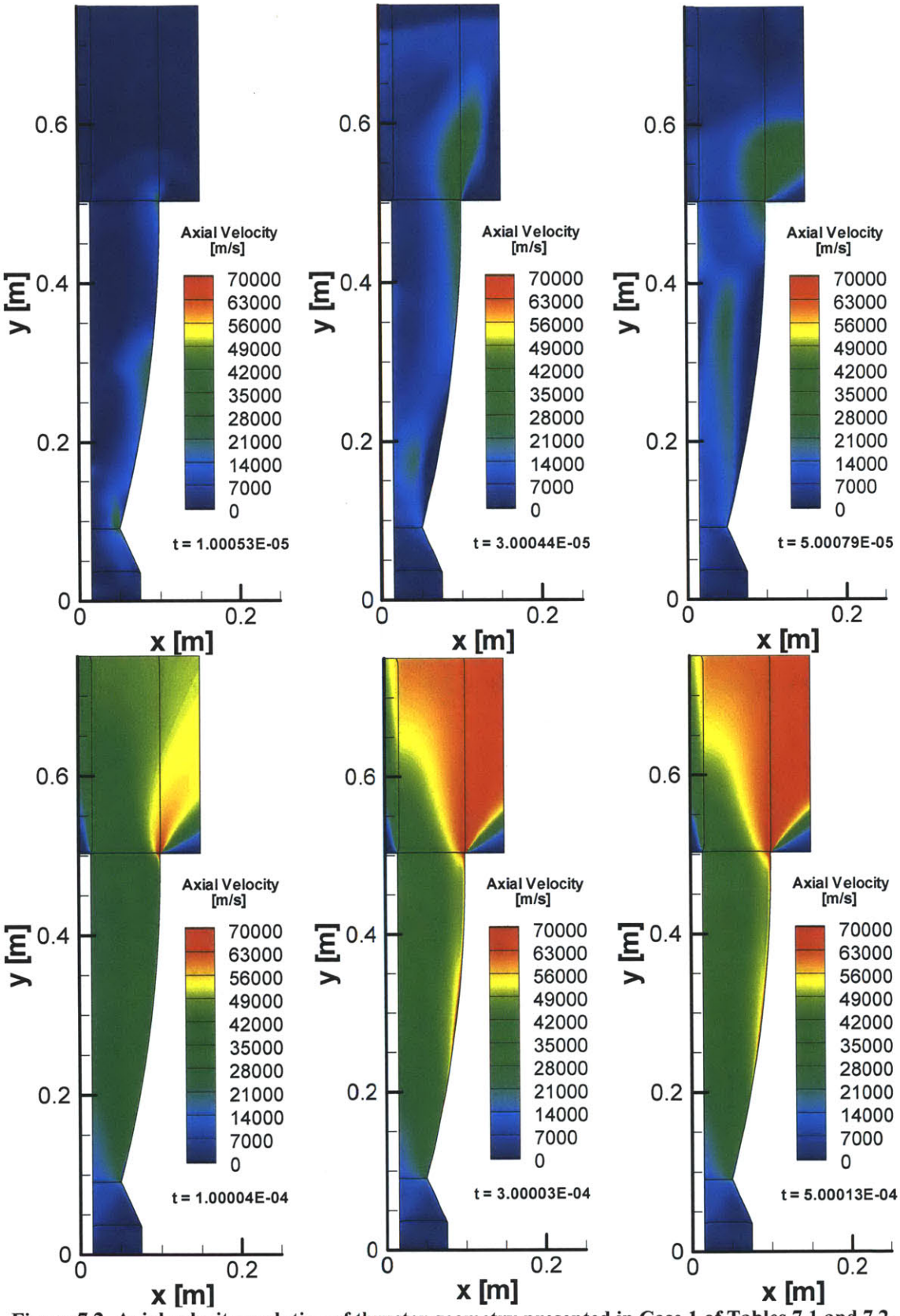

Figure 7.2. Axial velocity evolution of thruster geometry presented in Case 1 of Tables 7.1 and 7.2.

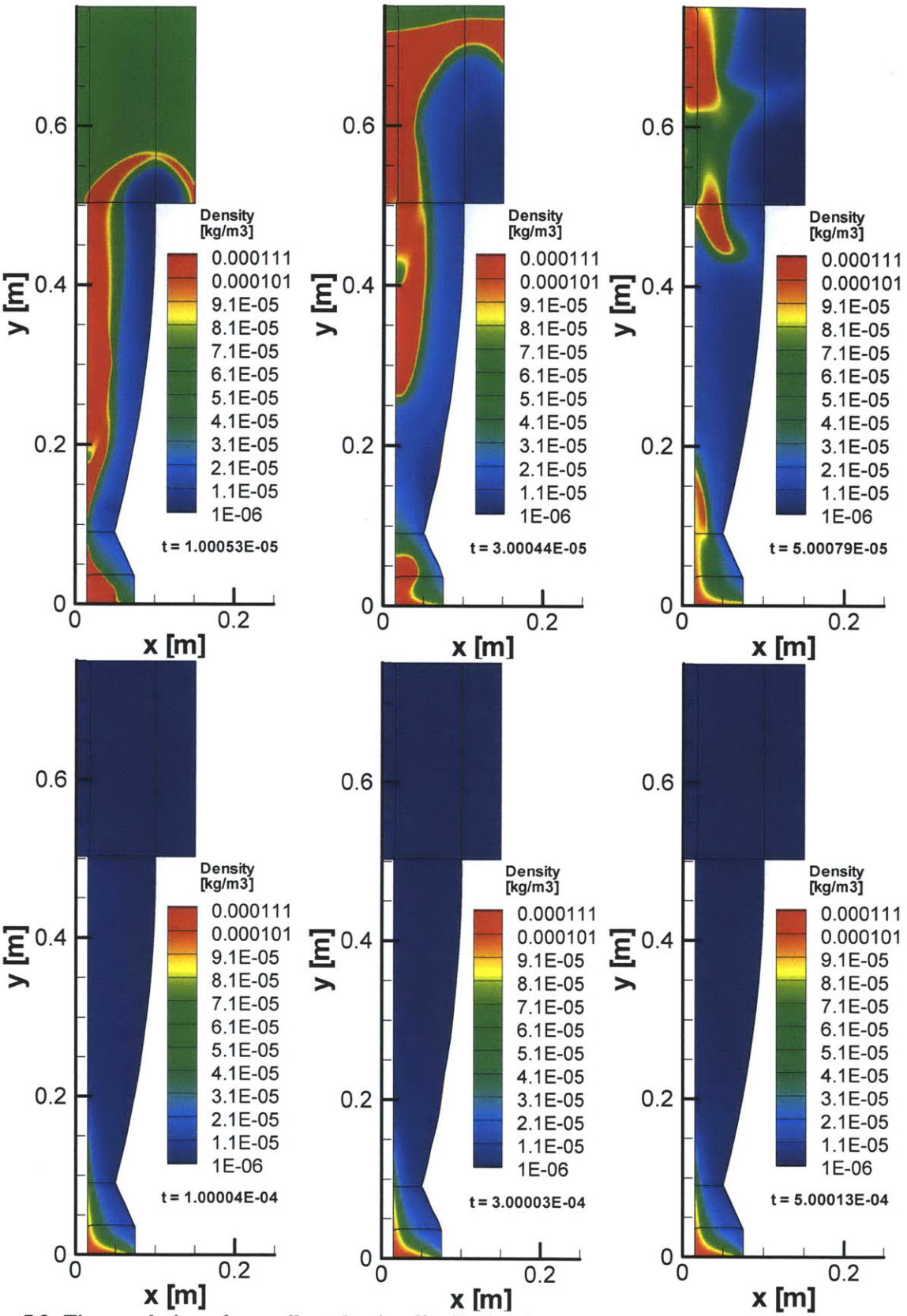

Figure 7.3. Time evolution of propellant density distribution for thruster geometry presented in Case 1 of Tables 7.1 and 7.2.

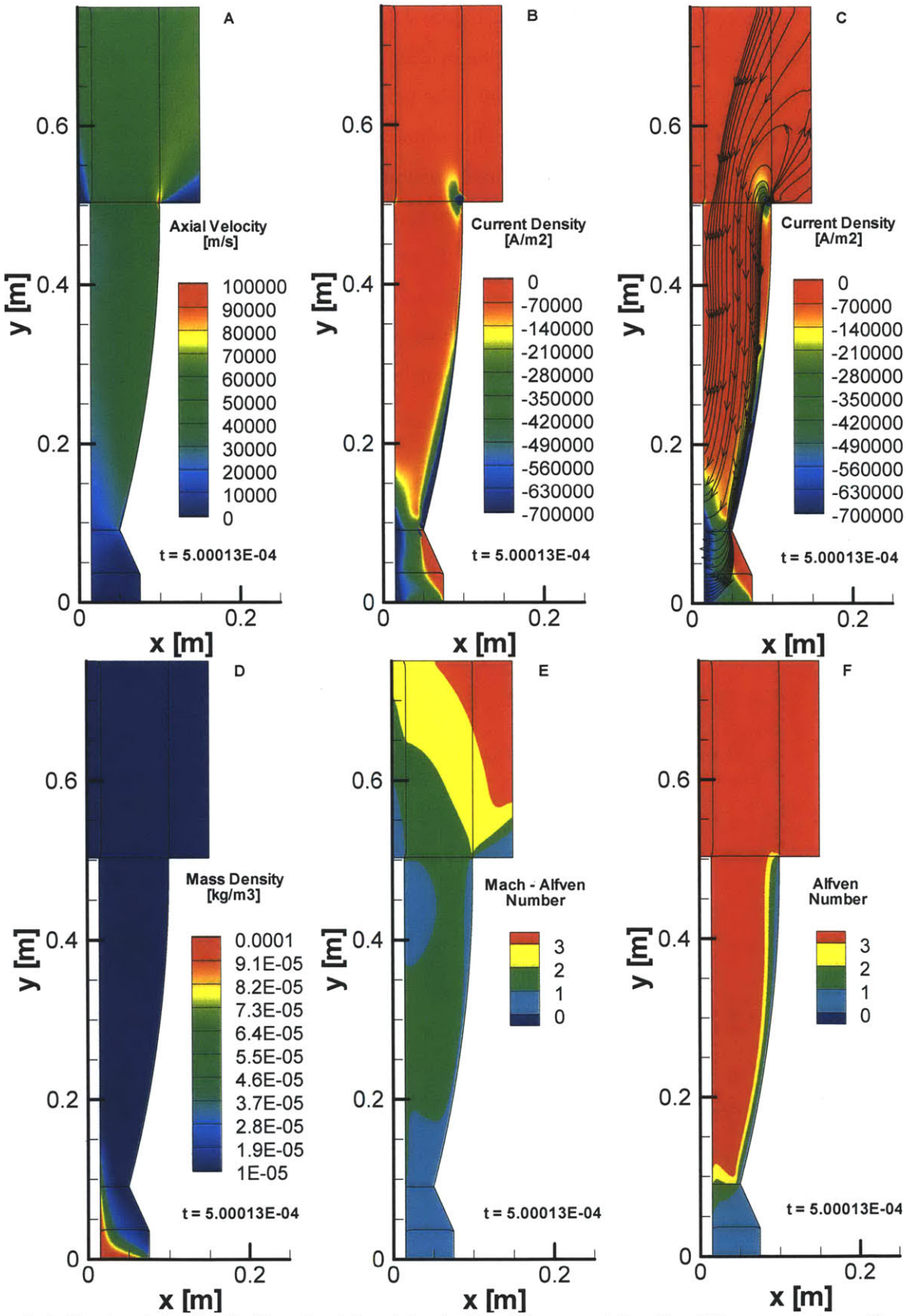

Figure 7.4. Steady state distributions for (A) axial velocity; (B) current density; (C) current streamlines; (D) propellant density; (E) Mach-Alfven number; and (F) Alfven number for Case 1 in Tables 7.1 and 7.2

Inspection of the steady state distributions in Figure 7.4 offers some potential paths for improvement in thruster performance. The current concentration evident at the anode lip motivates an effort to smooth this region, eliminating the sharp attachment point. The next geometry considered in this work included a flared anode exit, as shown in Figure 7.1 (b). This simulation demonstrated that stable operation could only be obtained for currents below 11 kA. Stable operation in this context indicates operation at the maximum current prior to the onset of anode starvation. Performance and efficiency are similarly reduced in this case. A further attempt was made to smooth thruster geometry by eliminating the channel contour in favor of a smooth converging-diverging geometry, as shown in Figure 7.2 (c). The inlet, throat and exit areas in the third geometry are identical to those previously considered. As in the previous case, this geometry produced stable operation for currents below 11 kA, with concurrent reductions in performance compared to that obtained using the first geometry. Steady state distributions for Cases 2 and 3 are presented in Figures 7.5 and 7.6.

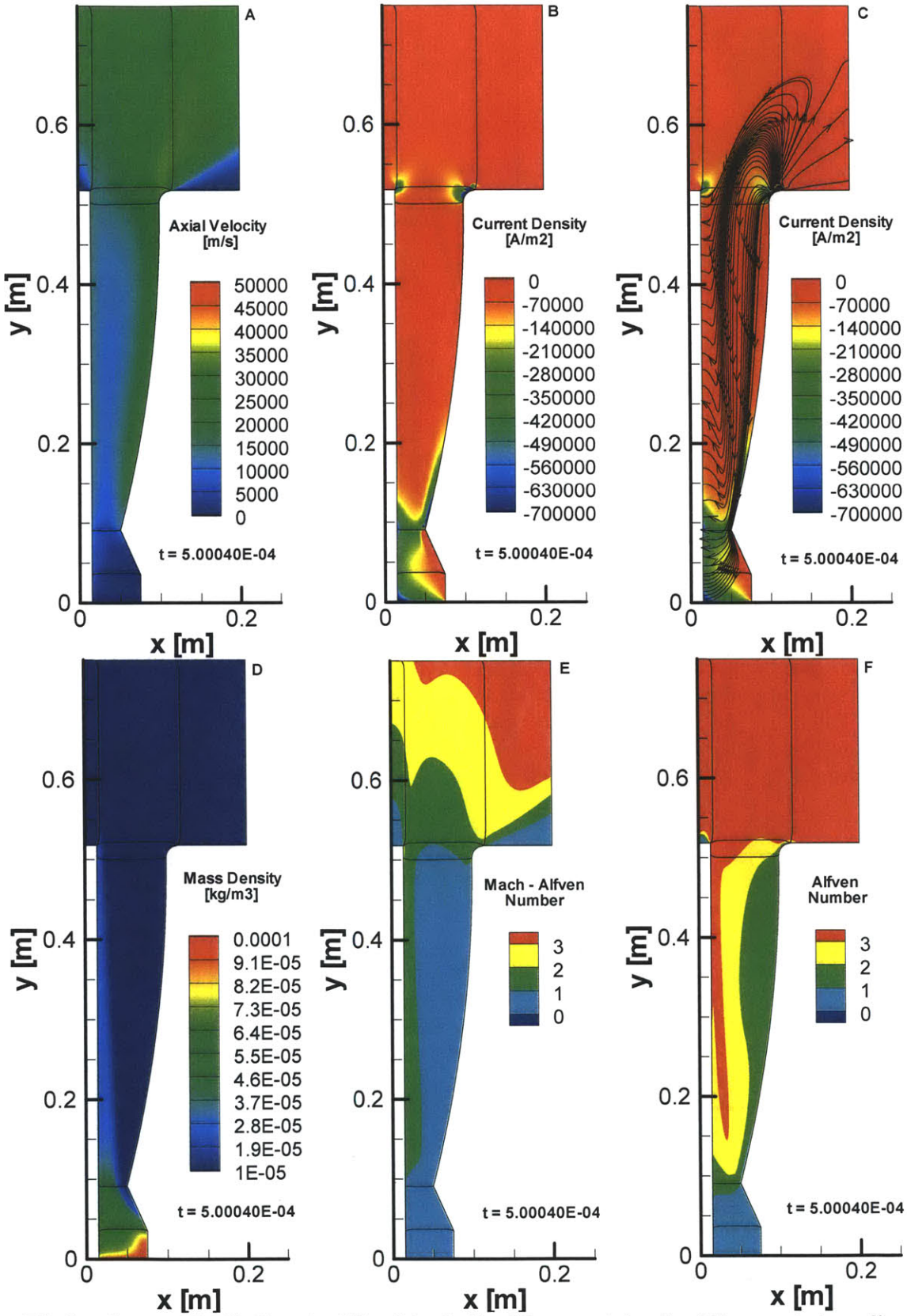

Figure 7.5. Steady state distributions for (A) axial velocity; (B) current density; (C) current streamlines; (D) propellant density; (E) Mach-Alfven number; and (F) Alfven number for Case 2 in Tables 7.1 and 7.2

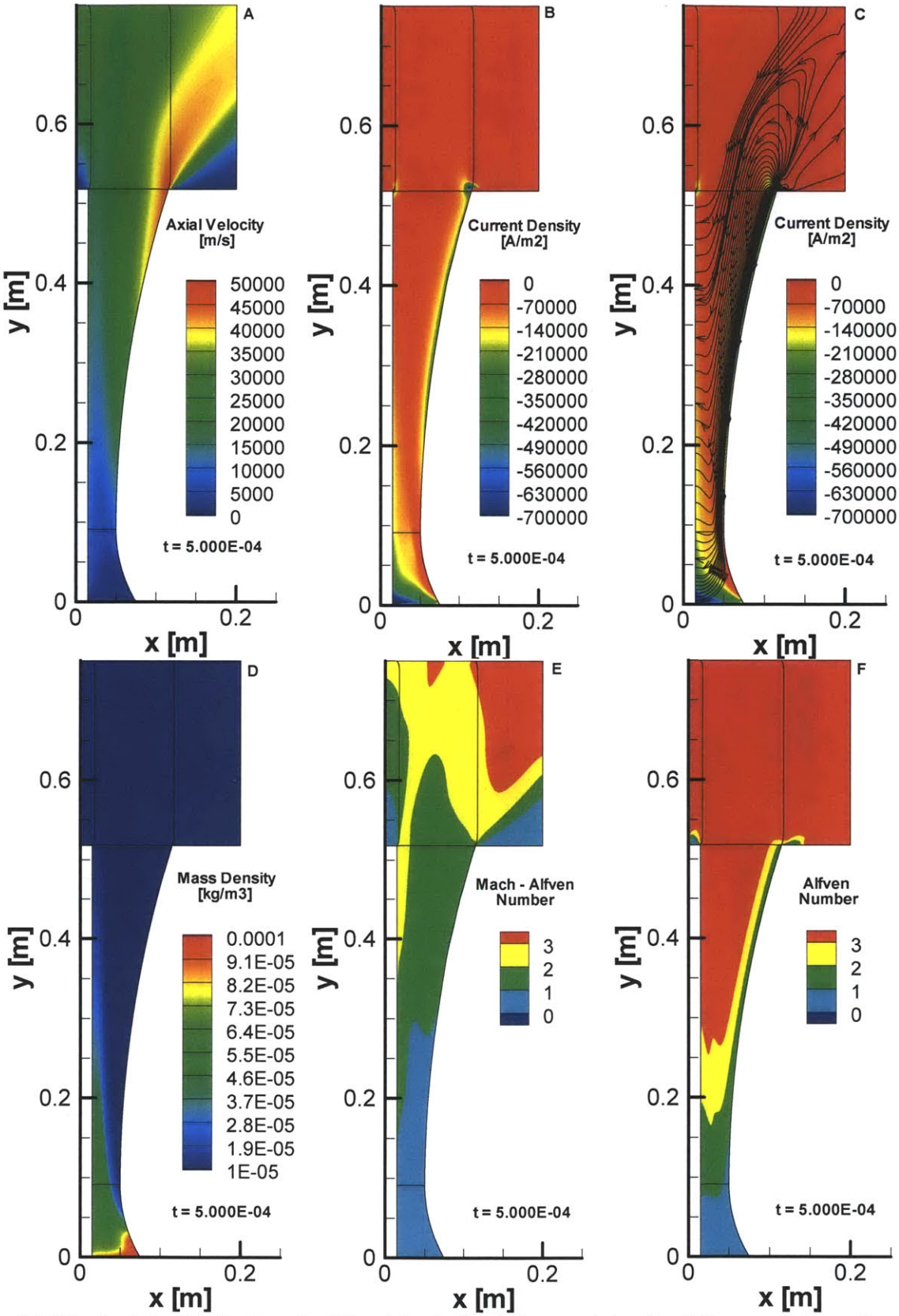

Figure 7.6. Steady state distributions for (A) axial velocity; (B) current density; (C) current streamlines; (D) propellant density; (E) Mach-Alfven number; and (F) Alfven number for Case 3 in Tables 7.1 and 7.2

Returning to the first geometry considered, it is useful to examine the effects of variation on the throat area. In Cases 4 and 5 the anode contour was identical to that of Case 1, but the anode-to-cathode spacing was decreased by 1 cm in each run. In both cases a decrease in the maximum current was observed. The maximum sustained current yielding stable operation in Case 4 was 25 kA. This decrease in current, however, was accompanied by a substantial increase in overall thruster efficiency, reaching approximately 32.2%. Further reduction of the throat area in Case 5 resulted in a sharp decrease in overall thruster efficiency. The apparent conclusion is that there is will optimal throat area for a given thruster and a given set of propellant inlet conditions. The steady state distributions for Cases 4 and 5 are presented in Figures 7.7 and 7.8, below.

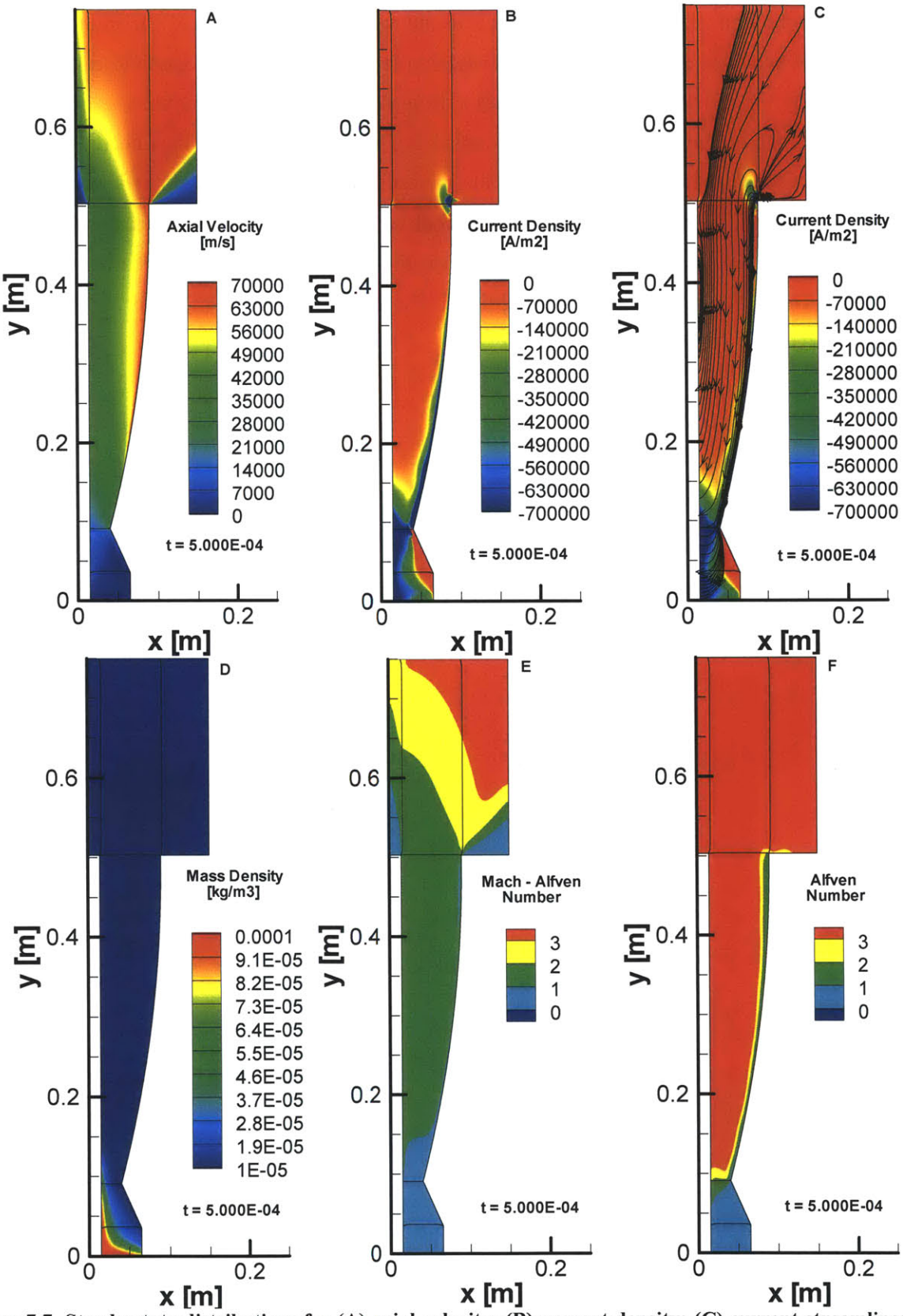

Figure 7.7. Steady state distributions for (A) axial velocity; (B) current density; (C) current streamlines; (D) propellant density; (E) Mach-Alfven number; and (F) Alfven number for Case 4 in Tables 7.1 and 7.2

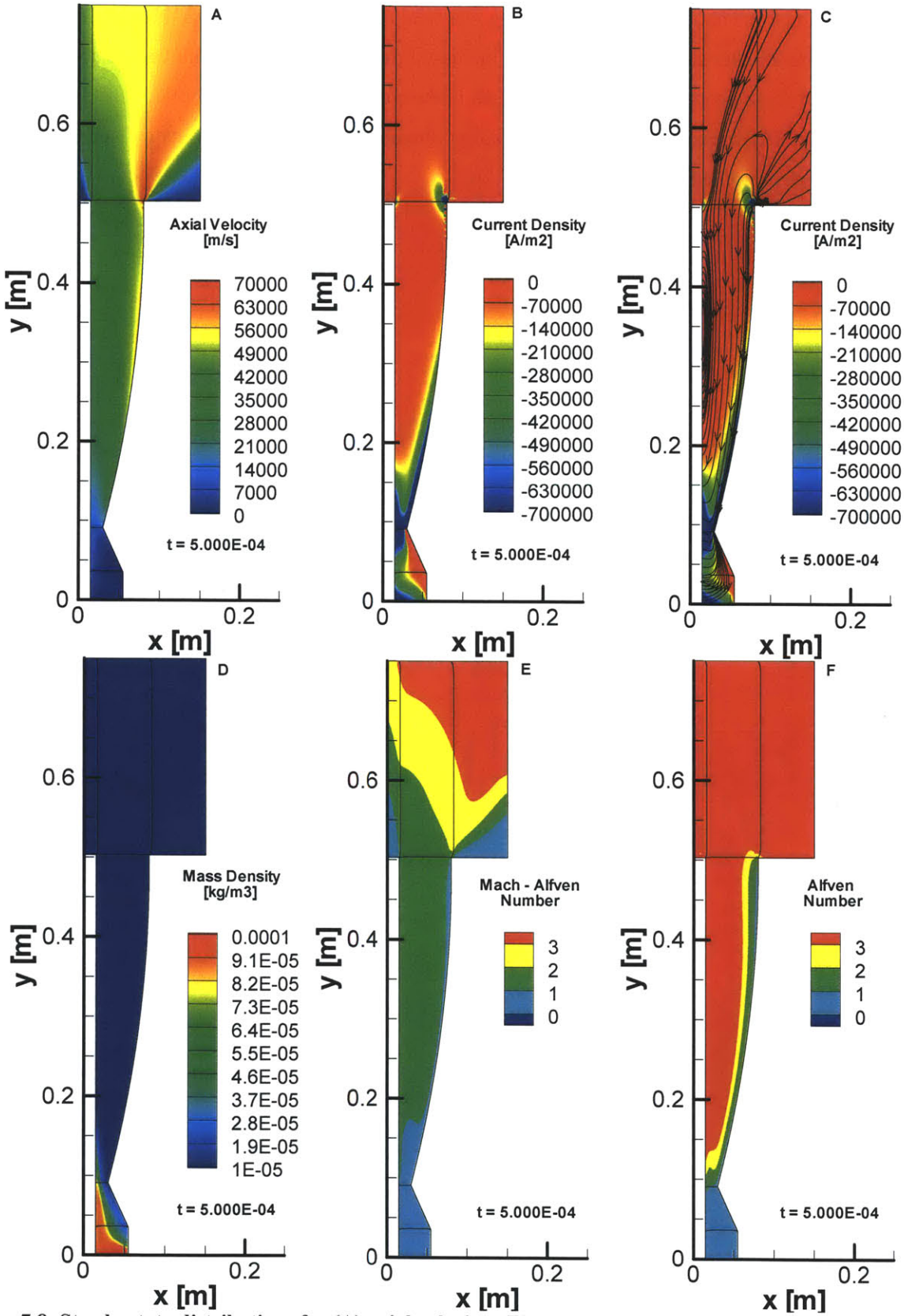

Figure 7.8. Steady state distributions for (A) axial velocity; (B) current density; (C) current streamlines; (D) propellant density; (E) Mach-Alfven number; and (F) Alfven number for Case 5 in Tables 7.1 and 7.2

In Cases 6 and 7 the anode-to-cathode spacing was held constant at the value of 4 cm obtained from Case 4, while the thruster cathode diameter was increased from 1.5 cm to 3.0 cm in Case 6 and 5.0 cm in Case 7. Both of these geometries yielded increases in the current that could be applied to the thruster, but the overall thruster efficiency was degraded from that obtained in Case 4. Steady state distributions for Cases 6 and 7 are presented in Figures 7.9 and 7.10.

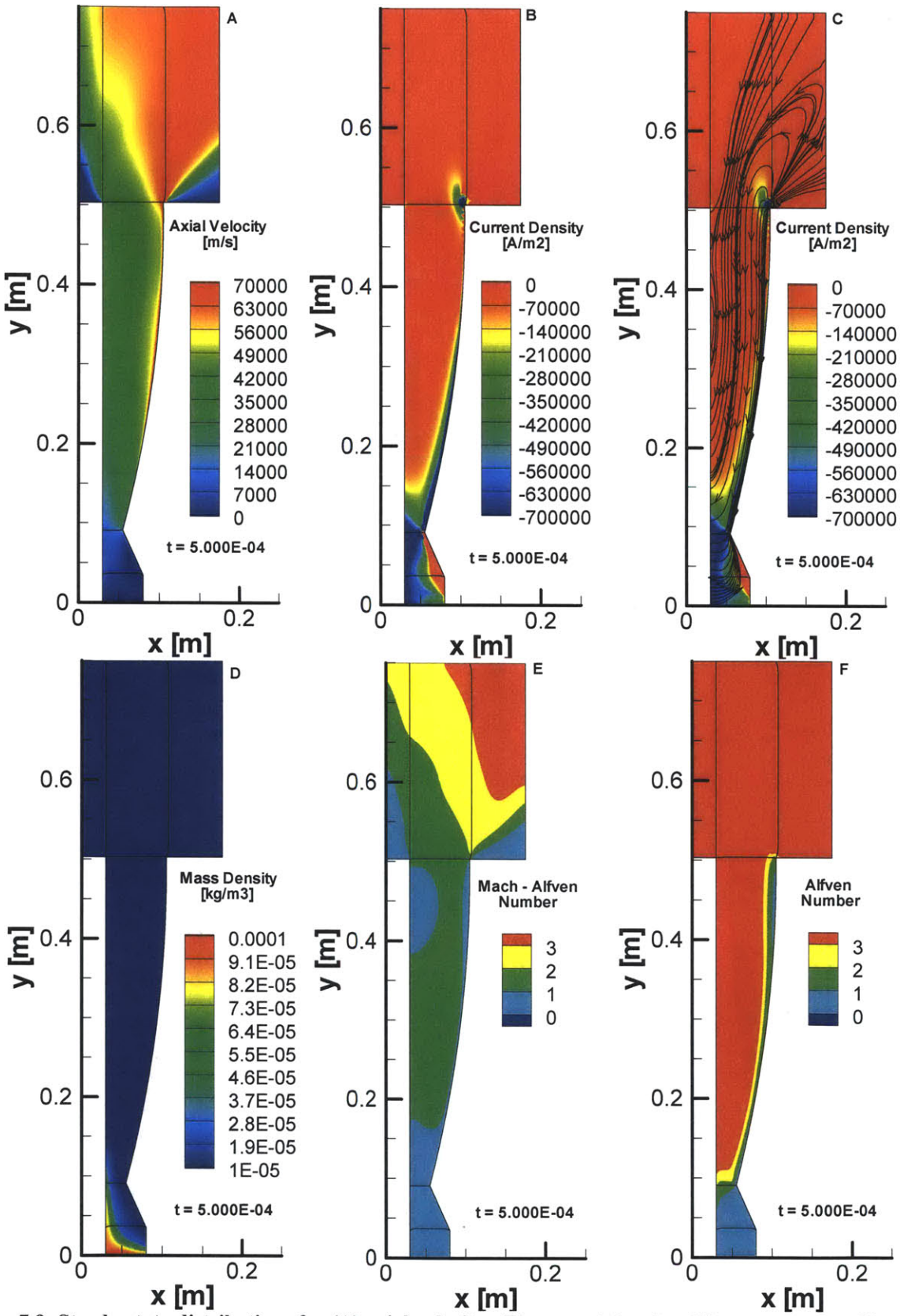

Figure 7.9. Steady state distributions for (A) axial velocity; (B) current density; (C) current streamlines; (D) propellant density; (E) Mach-Alfven number; and (F) Alfven number for Case 6 in Tables 7.1 and 7.2

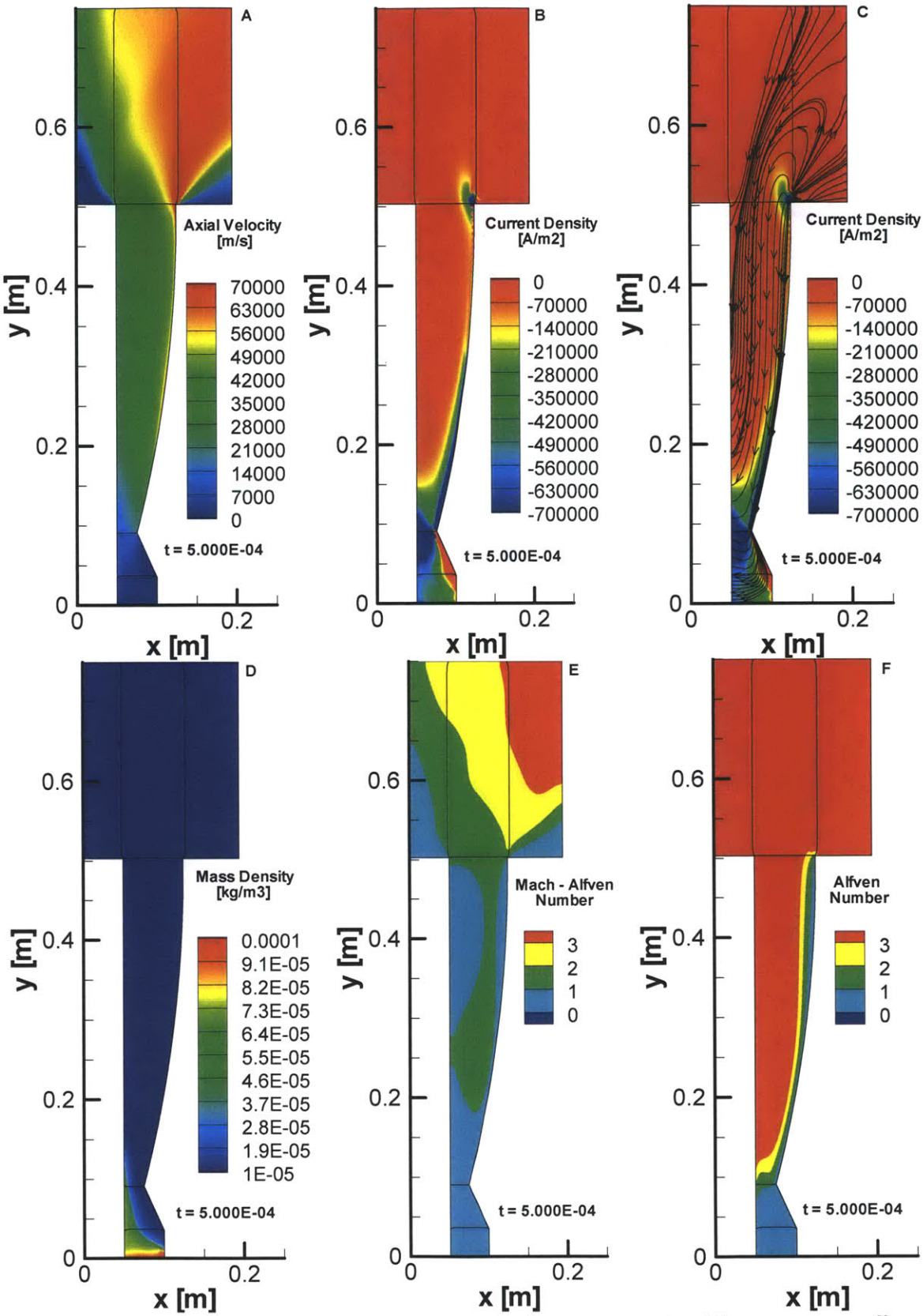

Figure 7.10. Steady state distributions for (A) axial velocity; (B) current density; (C) current streamlines; (D) propellant density; (E) Mach-Alfven number; and (F) Alfven number for Case 7 in Tables 7.1 and 7.2

Beginning with Case 8, thruster designs were transitioned to a simplified straight convergent-divergent geometry. In particular, Case 8 is a duplication of the geometry presented in Case 4, with a constant divergence angle. In Cases 9 – 11 following, the exit radius of the thruster was increased and the effects on thruster efficiency observed. As shown in Table 7.2, the second best performance of all configurations considered in this study was obtained in Case 10, with an exit radius of 0.12 m. The steady state distributions for Cases 8 – 11 are presented in Figures 7.11 – 7.14.

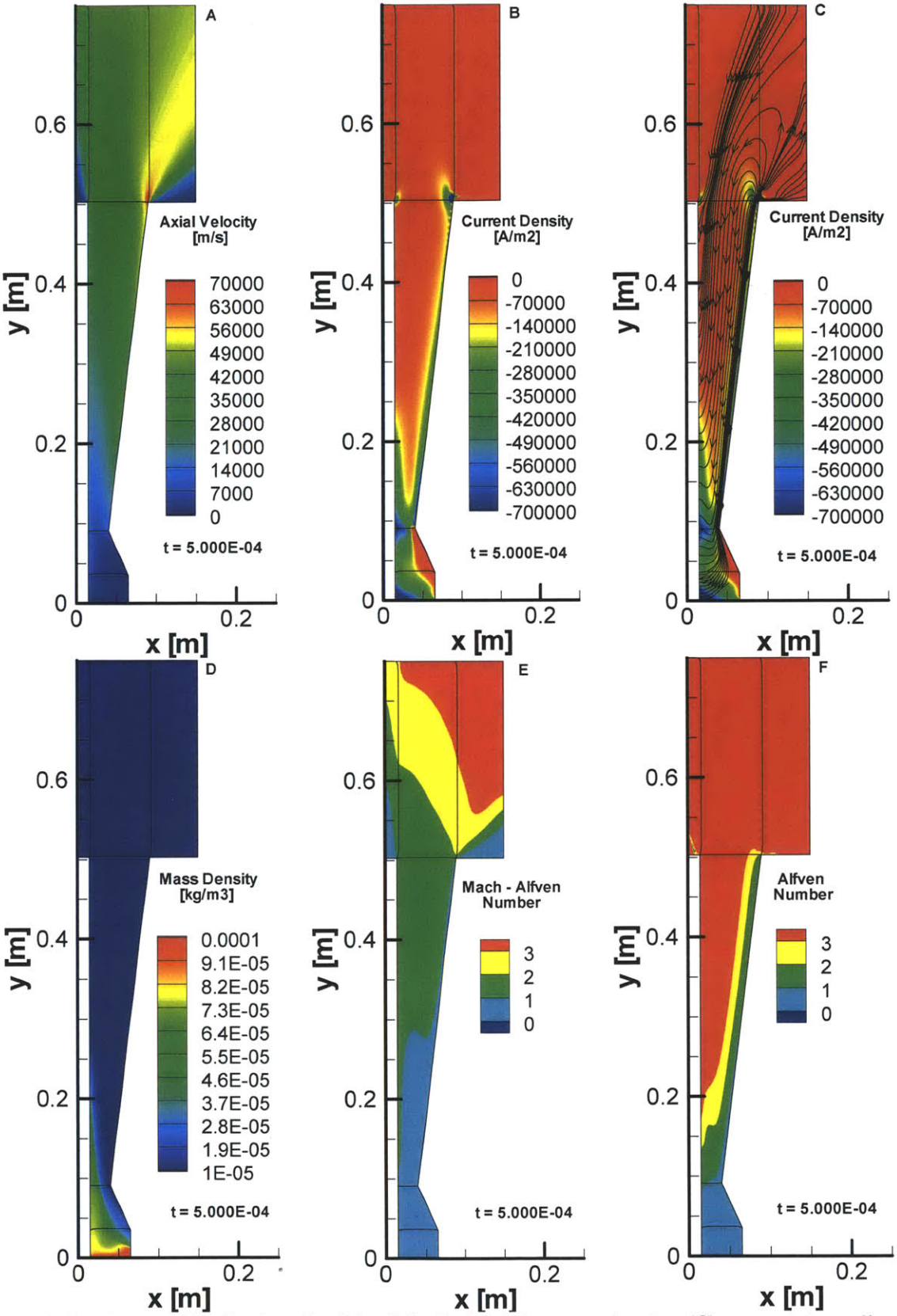

Figure 7.11. Steady state distributions for (A) axial velocity; (B) current density; (C) current streamlines; (D) propellant density; (E) Mach-Alfven number; and (F) Alfven number for Case 8 in Tables 7.1 and 7.2

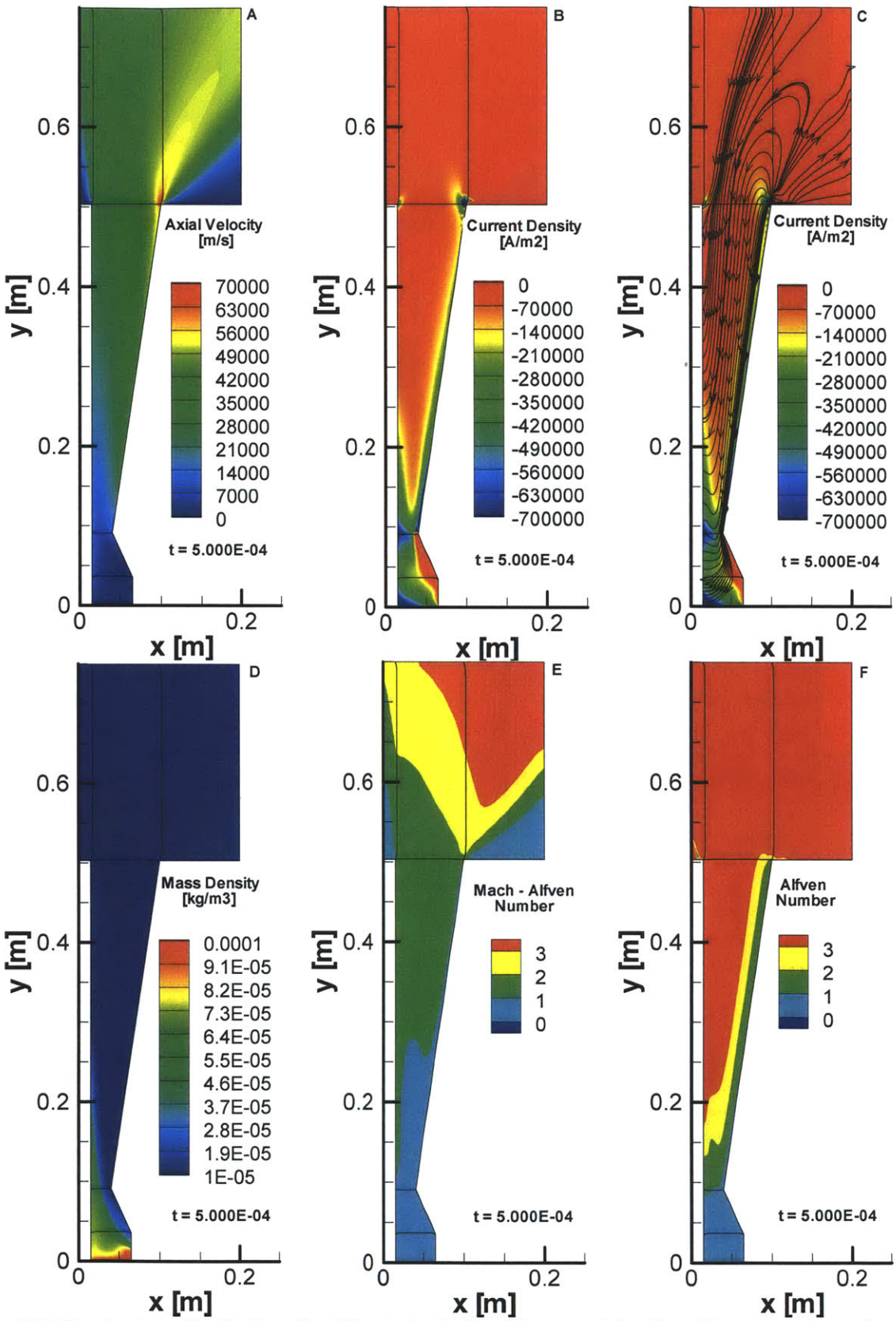

Figure 7.12 Steady state distributions for (A) axial velocity; (B) current density; (C) current streamlines; (D) propellant density; (E) Mach-Alfven number; and (F) Alfven number for Case 9 in Tables 7.1 and 7.2

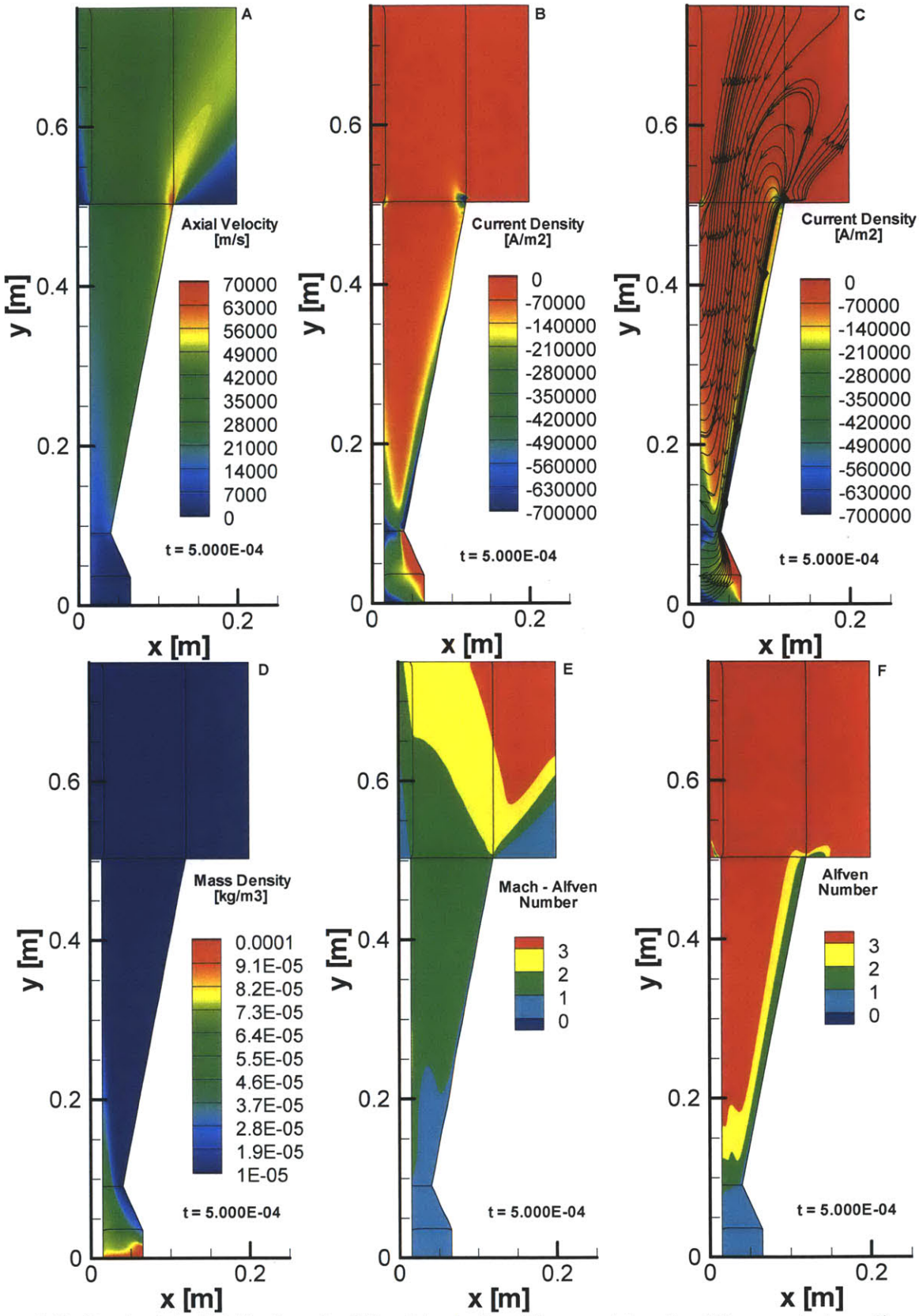

Figure 7.13. Steady state distributions for (A) axial velocity; (B) current density; (C) current streamlines; (D) propellant density; (E) Mach-Alfven number; and (F) Alfven number for Case 10 in Tables 7.1 and 7.2

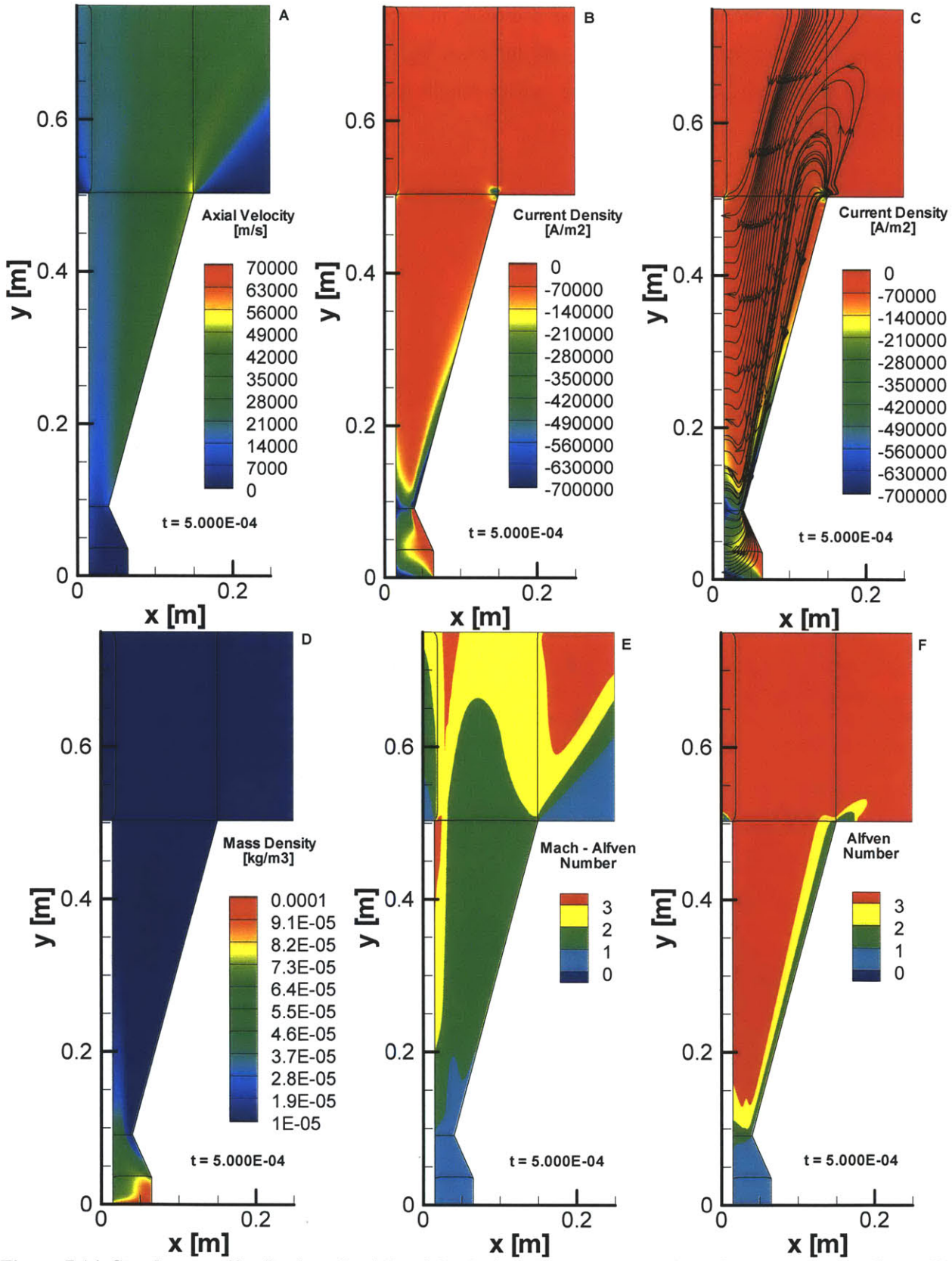

Figure 7.14. Steady state distributions for (A) axial velocity; (B) current density; (C) current streamlines; (D) propellant density; (E) Mach-Alfven number; and (F) Alfven number for Case 11 in Tables 7.1 and 7.2

In cases 12 – 16, the thruster length was decreased in steps of 0.10 m to 0.4 m and 0.3 m. At each length, the area ratio was again varied. As indicated by the data in Table 7.2, the overall thruster efficiency was generally diminished as the thruster length decreased. Data for these runs are shown in Figures 7.15 – 7.19.

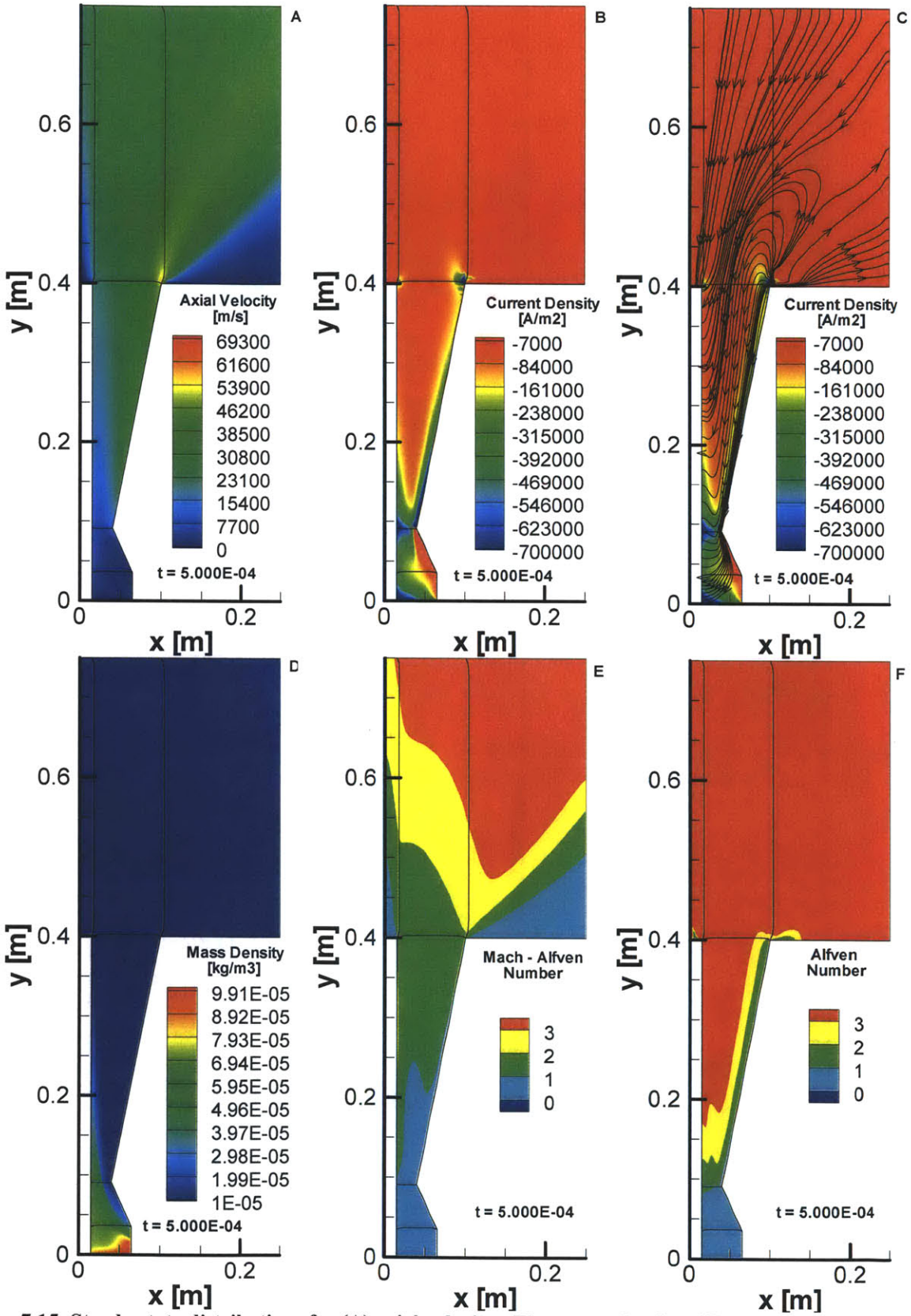

Figure 7.15. Steady state distributions for (A) axial velocity; (B) current density; (C) current streamlines; (D) propellant density; (E) Mach-Alfven number; and (F) Alfven number for Case 12 in Tables 7.1 and 7.2

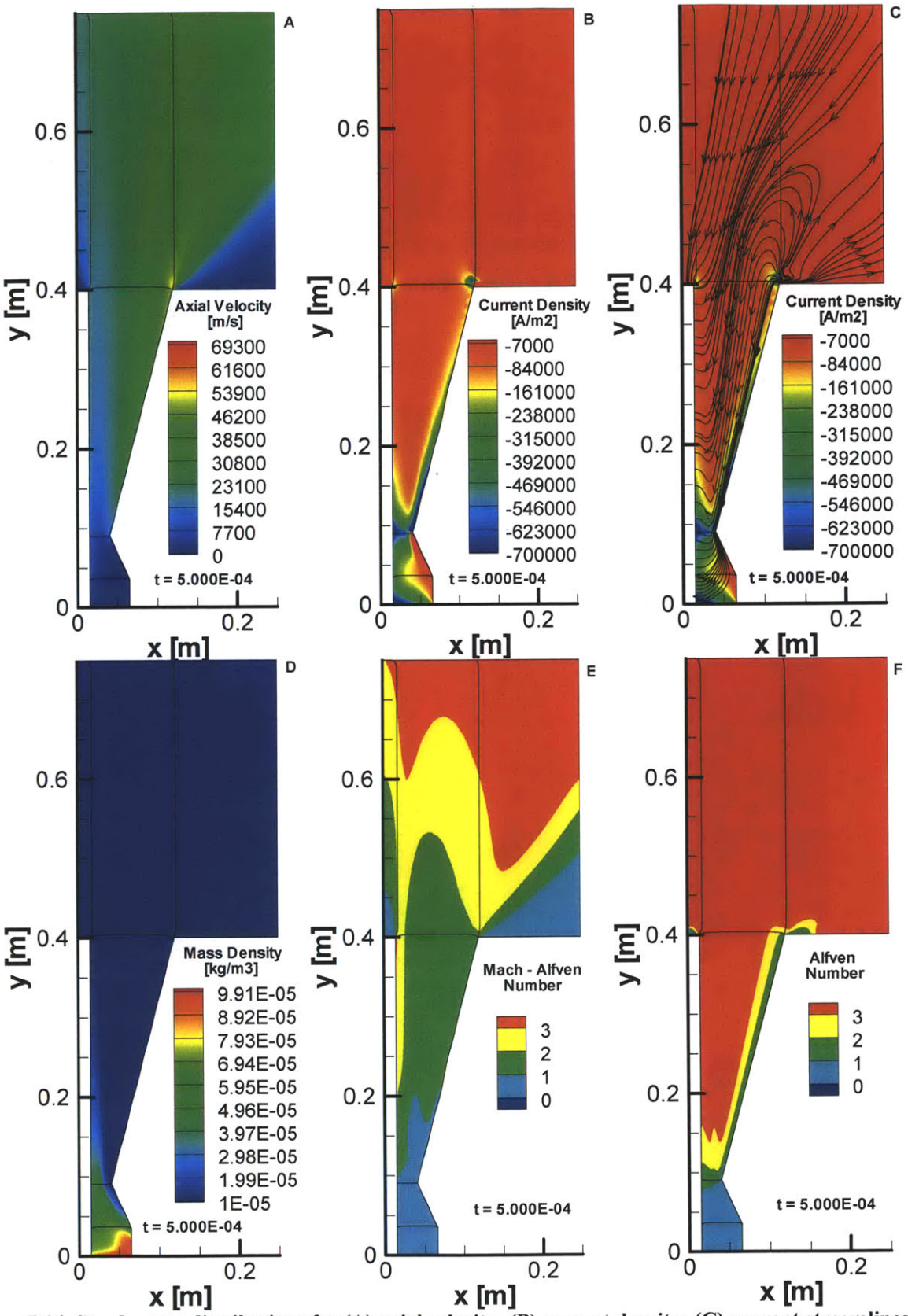

Figure 7.16. Steady state distributions for (A) axial velocity; (B) current density; (C) current streamlines; (D) propellant density; (E) Mach-Alfven number; and (F) Alfven number for Case 13 in Tables 7.1 and 7.2

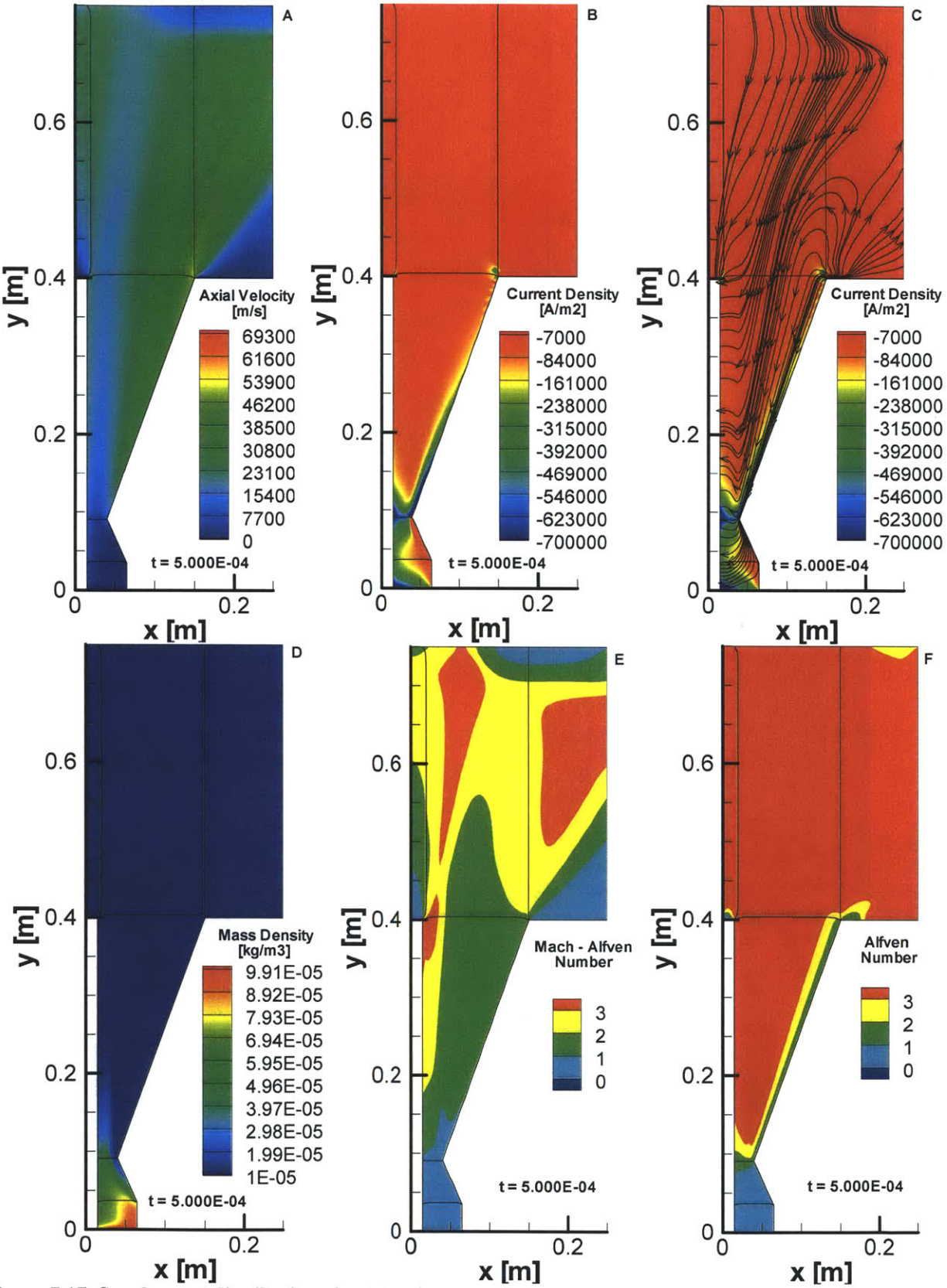

Figure 7.17. Steady state distributions for (A) axial velocity; (B) current density; (C) current streamlines; (D) propellant density; (E) Mach-Alfven number; and (F) Alfven number for Case 14 in Tables 7.1 and 7.2

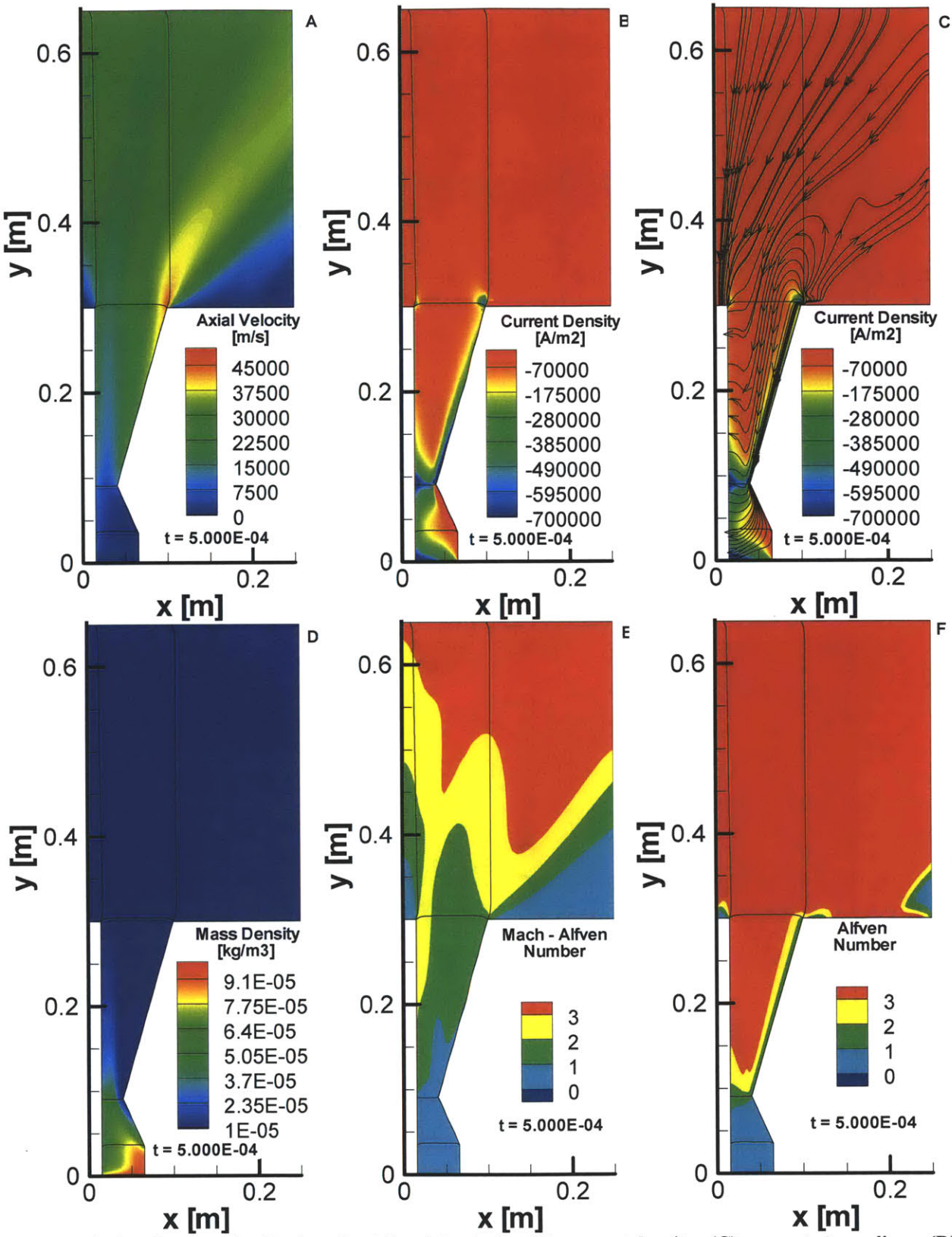

Figure 7.18. Steady state distributions for (A) axial velocity; (B) current density; (C) current streamlines; (D) propellant density; (E) Mach-Alfven number; and (F) Alfven number for Case 15 in Tables 7.1 and 7.2

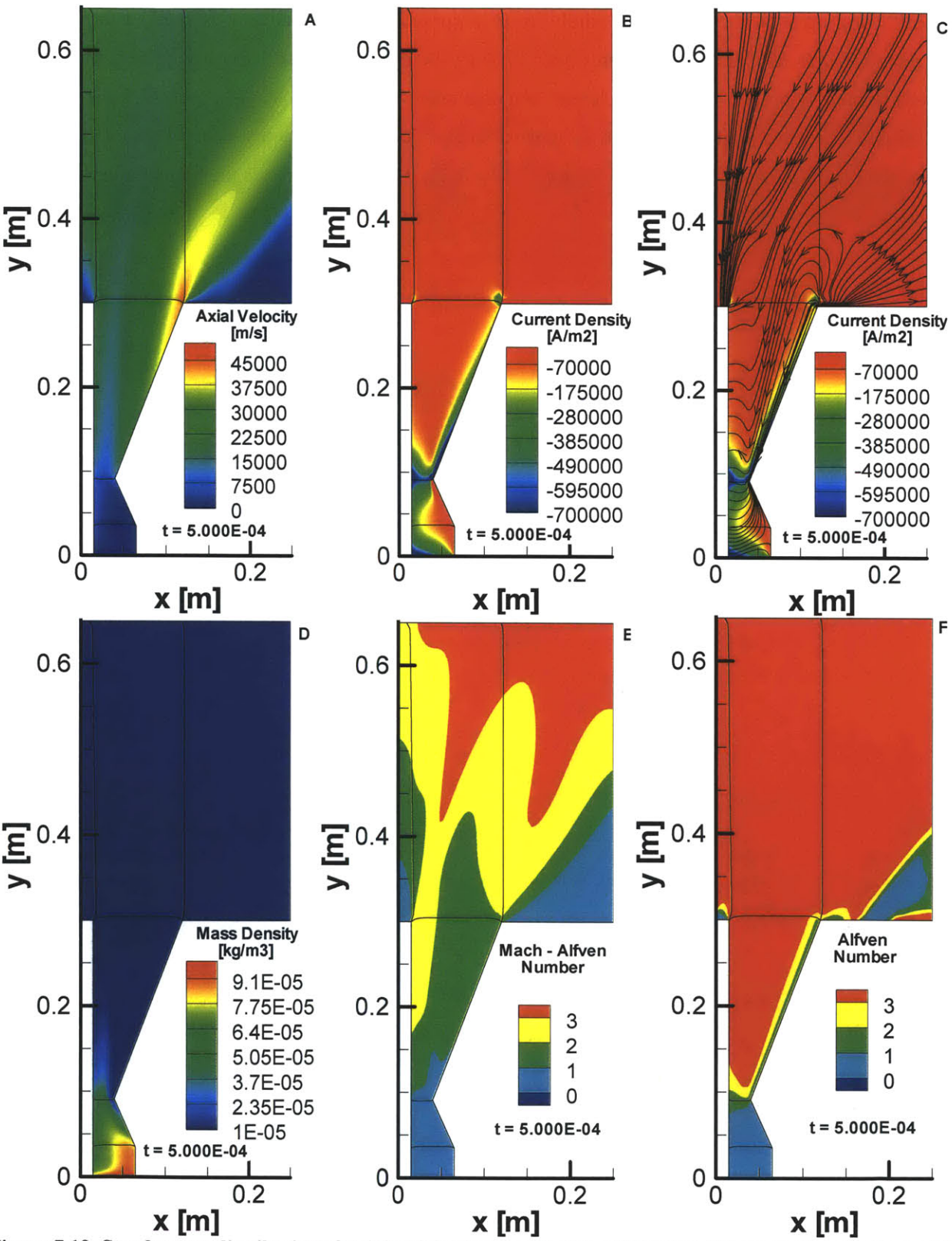

Figure 7.19. Steady state distributions for (A) axial velocity; (B) current density; (C) current streamlines; (D) propellant density; (E) Mach-Alfven number; and (F) Alfven number for Case 16 in Tables 7.1 and 7.2

Following up with the apparent desirability of a curved channel contour observed in the operating efficiency figures of Cases 4 and 8, in Cases 17 – 19 the design in Case 10 was modified to include a curved channel contour. The thruster length and area ratio were held constant in each of these cases and the initial divergence angle was varied in approximately 5 degree increments from 14.4 to 25.0 degrees. These final test cases are illustrated in Figures 7.20 – 7.22. Case 18 represents the highest overall thruster efficiency obtained in this work.

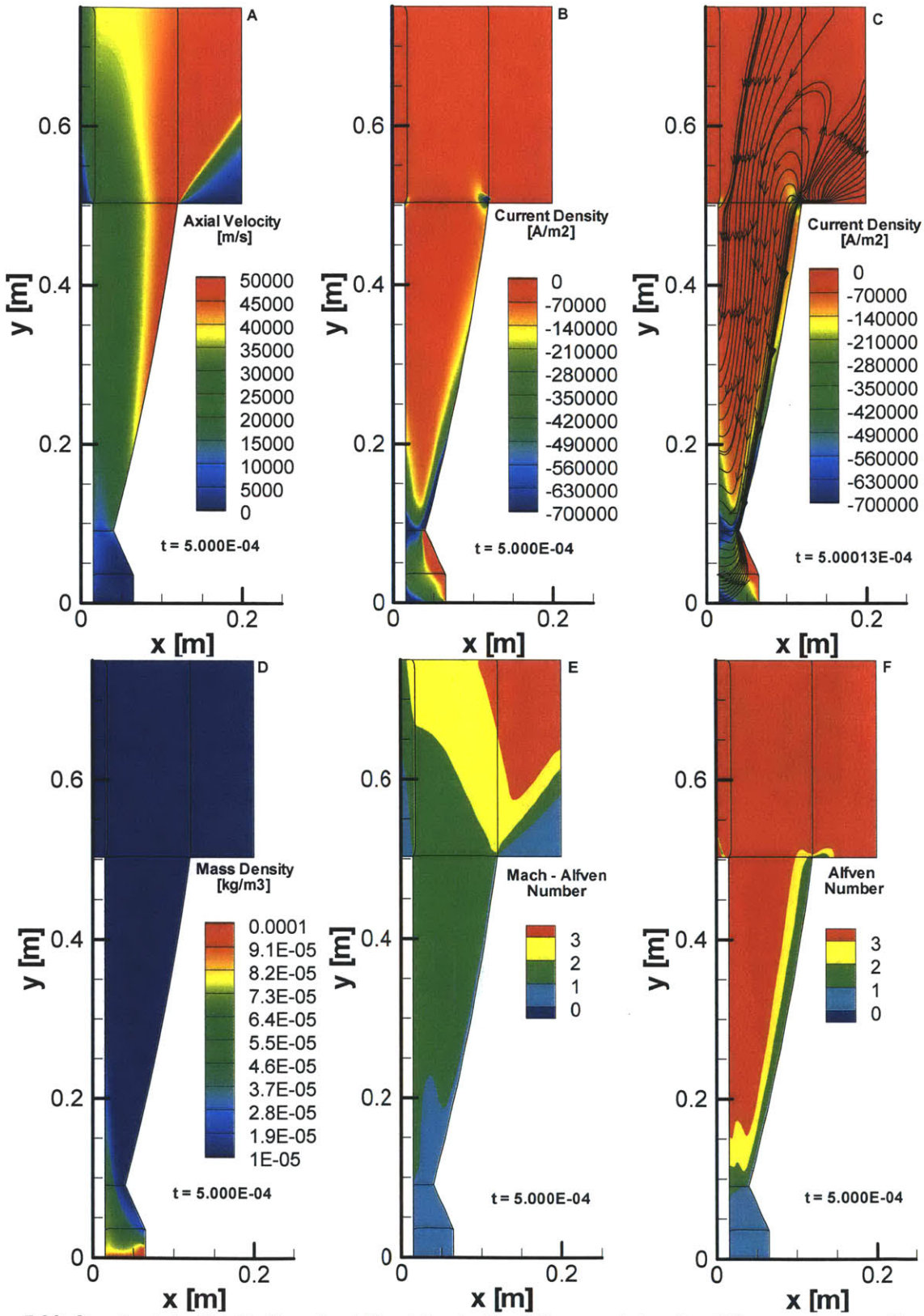

Figure 7.20. Steady state distributions for (A) axial velocity; (B) current density; (C) current streamlines; (D) propellant density; (E) Mach-Alfven number; and (F) Alfven number for Case 17 in Tables 7.1 and 7.2

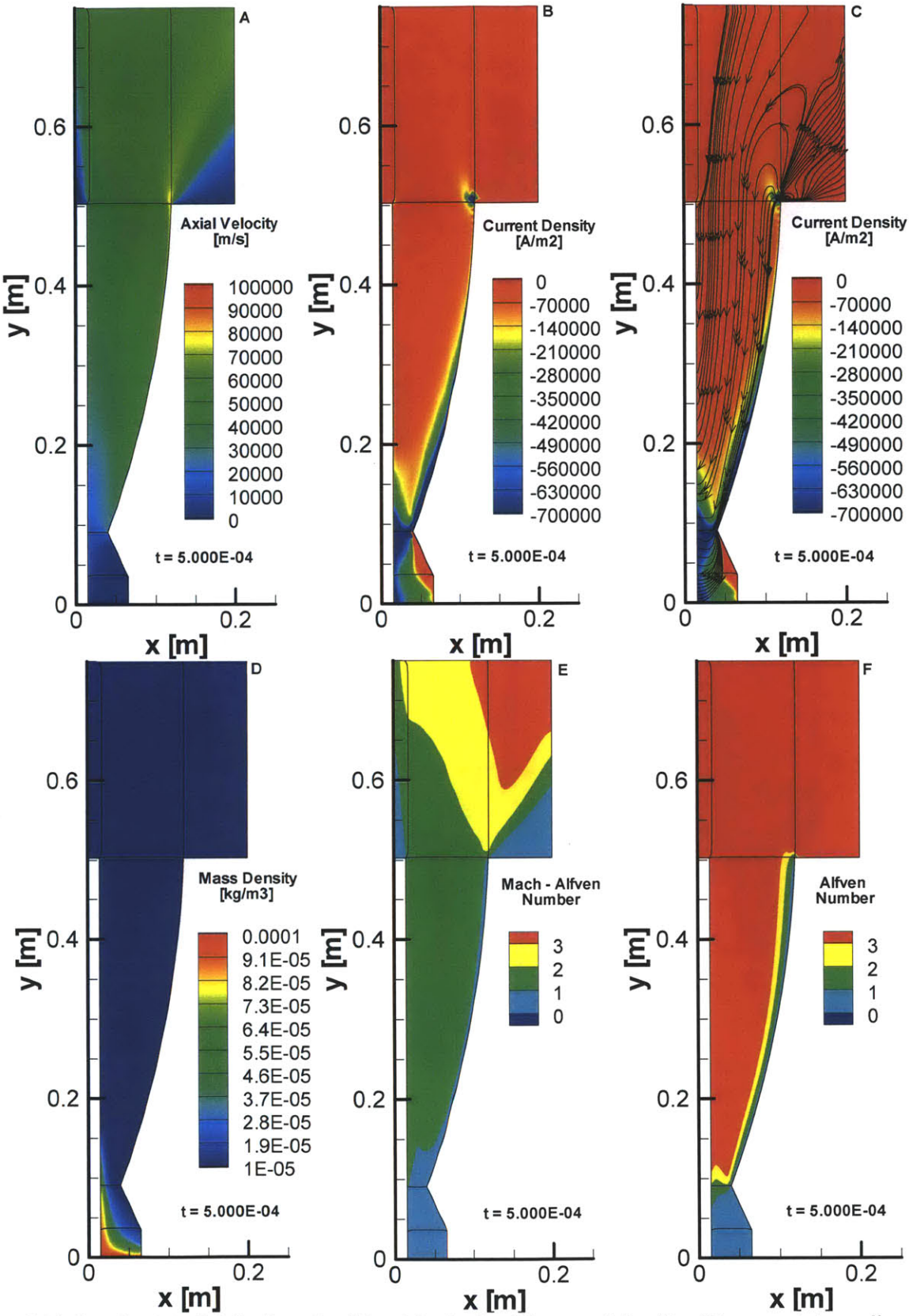

Figure 7.21. Steady state distributions for (A) axial velocity; (B) current density; (C) current streamlines; (D) propellant density; (E) Mach-Alfven number; and (F) Alfven number for Case 18 in Tables 7.1 and 7.2

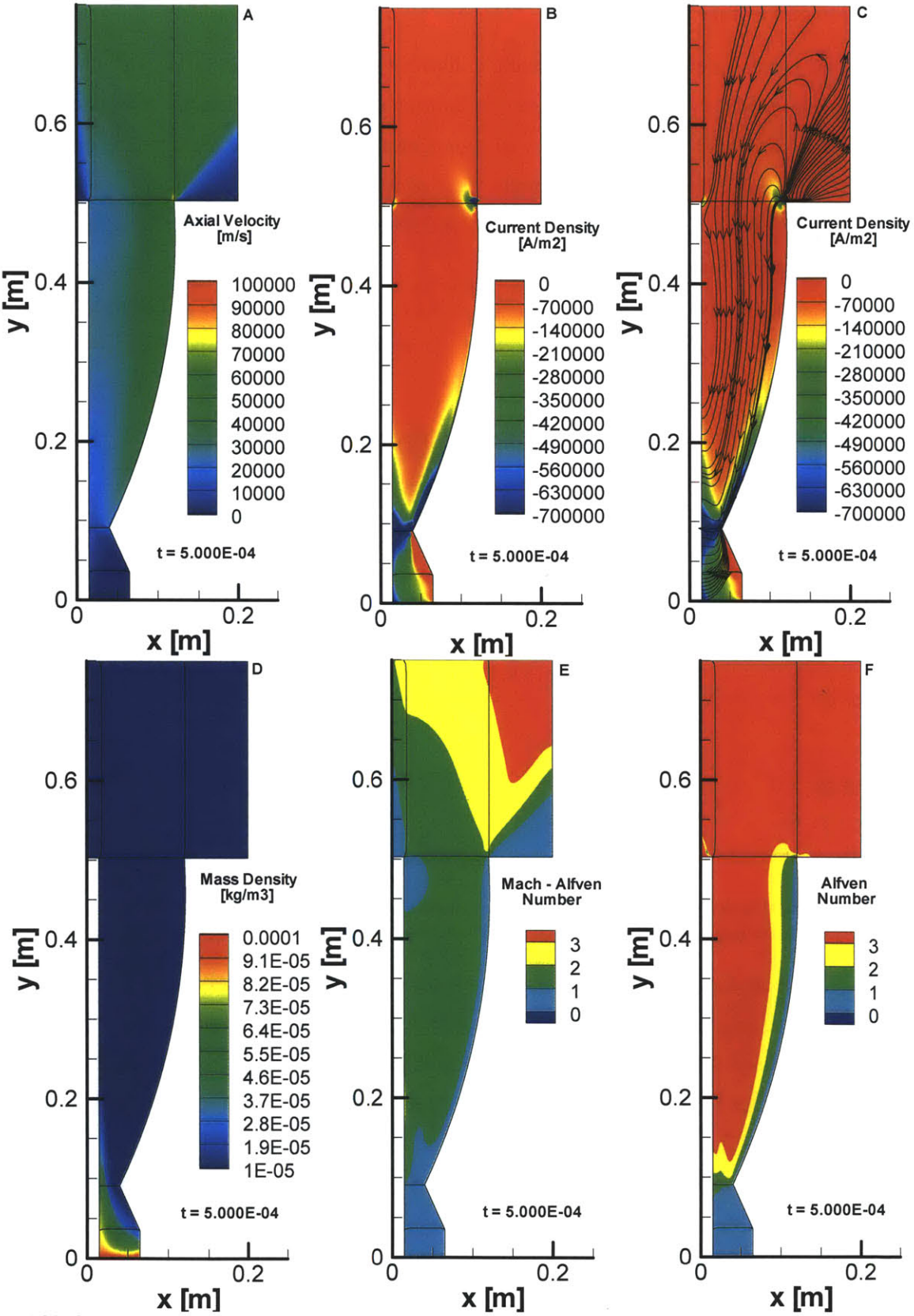

Figure 7.22. Steady state distributions for (A) axial velocity; (B) current density; (C) current streamlines; (D) propellant density; (E) Mach-Alfven number; and (F) Alfven number for Case 19 in Tables 7.1 and 7.2

7.4 Discussion and Future Work

Based on the test cases evaluated in this work, it does not appear likely that variations in MPD thruster channel geometry alone will provide increases in thruster efficiency sufficient to make these thrusters competitive with other high-thrust options for multi-megawatt nuclear power applications, including Hall thrusters. More refined geometric design might yield additional increases in efficiency. Based on the results obtained in this work, an aggressive goal of 35% - 40% overall thruster efficiency might be achievable with careful design.

The anode starvation phenomenon can be observed in the thruster contours developed in this work. The radial density profile for the thruster geometry developed in Case 18 is presented in Figure 7.23, below.

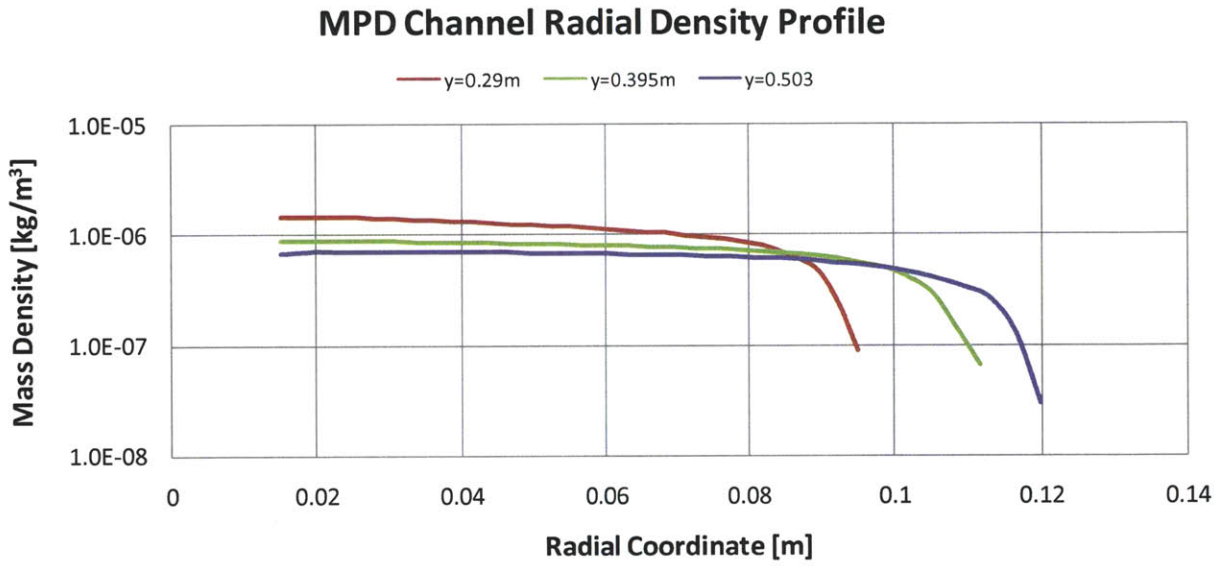

Figure 7.23. Radial density profiles for the thruster geometry presented in Case 18 at three axial coordinates; a sharp decrease in density is observed at each axial location near the thruster anode.

Additional proposed approaches to increasing thruster efficiency may yield additional improvements, including variations in propellant injection, and segmented anode configurations. Going forward, these design evolutions may also be effectively modeled using the MACH software package. An avenue of research that may offer some future benefit is to evaluate the achievable thruster efficiency given two or more anode segments located on an upstream and downstream portion of the thruster channel each operating at constant current. Furthermore, rather than model the propellant injection as taking place exclusively in the upstream portion of the thruster, some amount of propellant might be injected along the cathode surface, simulating propellant sublimation from the cathode.

Chapter 8

Conclusions

8.1 Summary of Current Work

The purpose of this work has been to explore the problem of implementing multi-megawatt nuclear electric spacecraft power and propulsion systems to facilitate expanded space exploration goals. The approach began with an in-depth mass modeling of potassium Rankine cycle space nuclear power plants using the ORNL-developed ALKASYS-PC modeling tool. Two power plant configurations, each representing different plant technology levels were considered to provide limits on the plant specific power. In the first case conventional reactor packaging, suitable for integration into a single launch vehicle was assumed. The second case assumed some level of on-orbit assembly to allow for the application of two-sided radiator surfaces and longer reactor-to-payload separation distance. In both cases the plant is assumed to utilize a conventional fast reactor incorporating pin-type fuel rod assemblies using uranium nitride fuel pellets. The power plant included a shadow shield comprised of a layer of lithium hydride to reduce neutron fluence at the payload plane, as well as a tungsten layer to stop gamma radiation. It was observed that the required shield mass can be reduced by increasing the distance between the reactor and the payload. Finally, the radiator subsystem is assumed to use interwoven carbon fiber heat pipes with Nb-1% Zr foil for compatibility with the potassium metal working fluid. Areal mass density is conservatively estimated at 4.0 kg/m^2 for single sided radiating surface.

Results of this modeling demonstrate that near-term plant specific powers will lie in the range of 0.19 – 0.33 kW/kg, depending on the allowed level of on-orbit assembly and relaxed redundancy. In all cases the required plant full-power lifetime is taken to be 10 years.

Once a range is established for power plant specific power, it is possible to begin implementing models for missions of interest that are enabled or enhanced by the use of NEP platforms. The trajectory for each of the mission was optimized using the JPL-developed MALTO software package. In this work, five missions were considered. Each mission was derived from a previous mission study performed by one of the national space agencies.

The first mission, the Galilean Satellites Orbiter is a derivative of the NASA JIMO concept. The Galilean Satellites Orbiter would orbit each of the four Galilean satellites for a period of approximately 1 year, beginning with Callisto, ending with Io. The required mission time was approximately six years from the beginning of Earth spiral-out until the end of one year at Io.

The second mission, the Saturn Transit Stage, had as its premise the emplacement of a 10 metric ton NEP platform with deployable payloads in orbit of the Saturn system using low-capability launch system. The goal of this mission was to obtain the minimum initial mass in low Earth orbit required to achieve this goal. Based on the parametric study of the IMLEO as a function of Earth-Saturn transit time, four years was selected as the allowed transit time between Earth escape and Saturn capture.

An interstellar precursor was chosen for the third mission. The goals of this mission were to deliver an NEP powered spacecraft with a burnout mass of 6.5 metric tons to a distance of 250 AU in ten years or less. Because the mass constraints for this particular mission were extremely demanding, the spacecraft is assumed to incorporate a somewhat more advanced power plant. On arrival at the 250 AU required distance, the spacecraft will be travelling at a velocity of nearly 38 AU/year.

Next, an evolution of the Neptune Orbiter with Probe and Triton Lander mission was developed. The NEP version of this mission considered in this work required a transfer time of less than 4.5 years, compared to the 13 years in the initial mission design. Additionally, the estimated payload for the NEP variant was increased by 1 metric ton to 2.5 metric tons.

Finally, an NEP-powered variation on the NASA Design Reference Mission 5.0 crewed Mars Mission was simulated. In particular, only the crewed component of the DRM 5.0 was considered in this work. The flight time for the outbound leg of the trajectory was 277 days including spacecraft spiral-out and spiral-in times. Assuming the crew in not present during the escape and capture spirals results in an outbound crew flight duration of 191 days, which is competitive with other mission concepts. The inbound flight time was 203 days, including the escape time from Mars orbit. Neglecting this again gives a crewed flight time of approximately 187 days, or 378 total crewed days. A surface stay of between 540-575 days is included in the mission, depending on whether or not the crew is assumed to be on board during the spacecraft capture and escape spirals around Mars. If the crew is required to be onboard the spacecraft during the capture and escape maneuvers, crew flight time will increase by approximately 100 days.

The development of optimal trajectories and timelines for each of these missions allowed for the derivation of several key power and propulsion system requirements that are likely to drive the development of future NEP systems. In particular, the following key observations may be made:

- Two ranges of specific impulse are needed to service the full spectrum of future NEP missions. There is a need for relatively low specific impulse, approximately 5000 s, with correspondingly high thrust, as well as high specific impulse, around 13,000s and up.

- The required total impulse in all cases falls into an envelope of less than one order of magnitude, from 0.5 – 5 GN-s.

- All the missions simulated in this work can be accomplished with 1-5 MW of propulsive output power. For propulsion system efficiencies $\eta \geq 0.70$, required reactor output powers will likely fall into a range of 1.5 – 7 MW.

The mission total impulse and required plant input power are strongly functions of the spacecraft initial mass, and thus the assumed launch vehicle capacity. These figures may be assumed to be fairly general, given current and near-term technology levels for earth-to-orbit launch vehicles. More advanced far-term missions may incorporate extensive on-orbit construction. One such mission is considered in Section 8.4, below.

Following the development of key power and propulsion system requirements, a survey was made of the electric propulsion devices most commonly studied in the literature. These were shown to fall into three very general categories: electrothermal, electrostatic and electromagnetic. The thruster implementations particular to each of these three classes were described. Design evolutions for the gridded ion engine, the Hall effect thruster and the magnetoplasmadynamic thruster that may enhance their operation at high power are identified.

The first design evolution evaluated in this work is the application of staged extraction systems to gridded ion thrusters. By decoupling the extraction and acceleration functions of ion thruster grids, it becomes possible to operate gridded ion thrusters at much higher voltages, and thus exhaust velocities, than is otherwise possible using conventional grid systems. Because the thrust, or accumulation rate of total impulse, for high-I_{SP} thrusters is lower than for other systems, the required operating lifetime for these thrusters is high. The challenge of achieving high lifetime in thrusters operating at very high I_{SP} is complicated by the fact that impacting ions contributing to grid erosion may have extremely high energies and increased sputter yields. To evaluate the potential lifetime for these thrusters, the grid erosion

simulation tool CEX2D was employed. Results of iterative design evolutions demonstrated that it was possible to design four-grid systems operating at 20,000 – 50,000 seconds of specific impulse in which grid aperture erosion is not the life-limiting process. It is also shown that additional grid structures impede the escape of neutral gas from the thruster ionization chamber, providing an additional improvement on the achievable efficiency of staged gridded ion thruster concepts. Future work for this particular design evolution includes 3D modeling of erosion processes.

The next two design evolutions considered in this work related to high-thrust EP devices. The first was the Hall-effect thruster. It is observed that conventionally designed Hall thrusters will tend to exhibit poor mass scaling with increasing thruster power. There is, however, evidence in the literature that Hall thrusters operated at higher mass flow rates and increased input power may obtain higher operating efficiency and increased power density, alleviating some of the design challenges associated with the mass scaling of Hall thrusters designed to operate at high power. In order to examine this effect as a potential avenue to circumvent the poor mass scaling, a one-dimensional three fluid thruster model was developed. This model is novel in that it incorporates the dynamics of the neutral species. Using this model, the effects of mass flow rate, thruster input power, thruster geometry and magnetic field topology have been investigated. Results of a large number of numerical experiments seem to support four general conclusions that may have utility for thruster design:

- Increasing peak magnetic field strength at a fixed mass flow rate appears to result in decreased anode plasma density. Above a certain critical magnetic field strength, anode plasma density tends to very small values. In this case, the anode has reached its so-called starvation limit.

- Maximum efficiency is consistently obtained if the thruster is operated near the anode starvation limit. The required peak magnetic field strength and the overall thruster efficiency increase with increasing mass flow rate when operated in this limit.

- The minimum field strength required to approach the anode starvation limit for the cases considered in this work is obtained when the magnetic field peak is placed a distance of 0.15 m from the thruster anode.

- A weak increase in efficiency is observed for flat magnetic field profiles in the channel.

Within the limitations of the model it does appear feasible to operate a conventional Hall thruster at up to ten times the current mass flux. Some limitations of the model deserve further consideration, however. In particular, the impact of thruster arcing and the mass of active cooling hardware on overall thruster utility must be evaluated.

The final design evolution considered in this work is related to the onset phenomenon in MPD thrusters and its impact on achievable thruster efficiency. Based on the ideal MHD equations, a method of characteristics is developed which enables the design of an optimum channel contour for plasma expansion in the super-magneto-sonic acceleration region of a 2D thruster. Using the MACH modeling tool developed by AFRL, the effects of a variety of channel contouring schemes on thruster performance and efficiency can be observed. Beginning with the approximate 2D contour for a thruster channel derived from the ideal MHD equations, a number of geometry variations were implemented, and a final design that maximized thruster overall efficiency was evolved. This work demonstrated that channel contouring alone will likely prove insufficient for achieving the gains in thruster efficiency necessary for supporting future multi-megawatt nuclear electric propulsion applications. An aggressive efficiency goal for MPD thrusters utilizing channel contouring alone to improve performance over conventional constant-area devices is approximately 35%-40%. Finally, there appears to be a demonstrable advantage in terms of achievable efficiency for thrusters that utilize some contouring, compared to thrusters that use straight convergent-divergent geometries.

8.2 Considerations for Subsequent Design Iterations

In this work the contribution of the thruster and the thruster cooling hardware to the overall specific power has been neglected. We can evaluate the additional mass of thruster cooling hardware required as a function of the thruster efficiency:

$$m_{PP} = \frac{P_{in}}{\alpha_0} + \frac{(1-\eta)P_{in}\rho_R}{\epsilon\sigma T_R^4} \qquad \text{(Eq. 8.1)}$$

In this expression the specific power without including thruster cooling is denoted by α_0, the radiator areal density ρ_R and the radiating temperature T_R. If thruster cooling is provided by the low-temperature coolant loop extant on the power plant we find that this is, indeed a relatively small contribution to the overall mass of the power and propulsion system. Using $\alpha_0 = 0.2$ kW/kg, $\eta = 0.7$, $P_{in} = 1.5$ MW, $\rho_R = 4.0$ kg/m^2, $T_R = 600$ K and ideal emissivity, we find that the additional mass is less than 250 kg, or an increase in mass of about 3.2%.

The contribution of thruster mass to the overall specific power is somewhat more difficult to quantify precisely at this level of design. It will necessarily depend on the type of thruster implemented. In general, the contributions of additional subsystems to overall specific power take the form:

$$\frac{1}{\alpha_T} = \sum_i \frac{1}{\alpha_i}; i \in \{Plant, Thruster\ Cooling, Thruster, \ldots\} \quad \text{(Eq. 8.2)}$$

Subsystems characterized by increasingly large values of specific power will contribute correspondingly less to the overall system specific power.

8.3 Future Work

The needs going forward for the development of high power nuclear electric spacecraft platforms can be broadly cast into three categories. The first are large scale national programmatic needs. Next, some research and development needs related to the design of space-based nuclear power plants may be identified. Finally, several future research paths are enumerated with respect to the design of EP thrusters.

8.3.1 Programmatic Needs

The first set of needs required in moving forward with the design of high power nuclear electric power and propulsion systems may be understood as large-scale programmatic needs. Two such requirements are identified. First, because of the enormous scale and projected cost of developing multi-megawatt nuclear power systems for spacecraft applications, it is essential that one or more national space programs implement adequately funded initiatives related to the development of these systems.

The second programmatic requirement is the development of an orbital test bed for high power electric thrusters and nuclear electric power plants. This might be most easily realized onboard the International Space Station.

8.3.2 Nuclear Power Plant Subsystems Design

As shown earlier in this work, the largest contribution to total plant mass in advanced nuclear power plants constructed in orbit comes from the reactor. This means that research and development efforts in designing lower mass reactors have the greatest leverage in ultimately fielding plants with high specific power. Several of the Gen IV reactor configurations may provide mass advantages over the conventional pin-type reactors considered in this work.

8.3.3 Electric Thruster Design

In this work preliminary study of several design evolutions for EP thrusters that offer the lowest programmatic risk for development of megawatt-level systems have been evaluated. Based on these results, several needs for refined simulation and experimental validation may be identified. First, the 3D erosion effects of multi-stage ion thruster grids should be evaluated. This might be accomplished using the CEX3D simulation software [164, 165], or other equivalent packages. In particular the effects of so-called "pits and grooves" erosion patterns observed numerically and experimentally in conventional gridded ion thrusters must be quantified for dual stage four grid thrusters, along with the impact on thruster lifetime.

Study of the effects of mass flow rate, thruster geometry and magnetic topology in Hall thrusters conducted in this work appear to yield some paths to improving the scaling behavior of these devices. In particular, the design for operation at the anode starvation condition seems to offer an avenue for improving thruster performance and efficiency in any power regime. These observations should be subjected to further testing using capable two-dimensional modeling. If more rigorous simulations continue to bear out the utility of this effect, it should ultimately be subjected to experimental validation.

Further simulation work is needed to tailor the design of MPD thrusters for maximum performance and efficiency. Avenues that might yield positive results include anode segmentation and variations in propellant injection.

8.4 Far-Term NEP Systems

As a final exercise, it is perhaps interesting to consider the design of highly advanced far-term nuclear electric propulsion systems and their accompanying performance requirements. In the following section, this is done for the Human Outer Planet Exploration (HOPE) mission. The premise of the HOPE mission is to send a crew of 6 humans to Jupiter's moon Callisto [192 - 194]. Because the mission is manned, round trip time is limited to 5 years, with a minimum surface stay of 30 days on Callisto.

Detailed spacecraft mass breakdowns are developed in [195] for this mission. The power system specific power assumed in that work is inconsistent with estimations for advanced reactors developed in this work. The power system mass breakdown that follows has been revised up to be consistent with the more conservative modeling included herein. As in prior modeling of the HOPE concept, the manned spacecraft is assumed to leave from the Earth-Moon L1 point at an altitude of 326,054 km. Total transit time for the mission is constrained to be less than five years, including a surface stay of 30 days at Callisto. Upon Jupiter rendezvous, the spacecraft must spiral down to the orbit of Callisto, where it is subsequently captured into orbit.

Several changes to the mission design have been incorporated into this simulation. First, the spacecraft mass breakdown has been modified to include two TransHab modules and supplies. This will allow the TransHab modules to be rotated about their center of mass independently of the rest of the spacecraft. The power and propulsion system is assumed to provide 30 MW of output power at a specific power of 0.33 kW/kg. The goal of this treatment is to incorporate all the required mission hardware as outlined in [195] in a single spacecraft while keeping the total initial mass of the spacecraft less than the combined mass of the three vehicles considered in that work. The mass budget for the mission variant considered herein is provided in Table 8.1. The resulting optimized trajectory is given in Figure 8.1. The derived propulsion system performance requirements are presented in Table 8.2.

Subsystem	Mass	
Power	90909	kg
Propulsion	30000	kg
RCS + COMM	7527	kg
ISRU Lander	37909	kg
Crew Lander	25009	kg
Surface Habitat	36616	kg
TransHab	104802	kg
Structure	25294	kg
Callisto Drop Mass	99534	kg
Spacecraft Burnout Mass	363334	kg
Initial Mass in LEO	850000	kg

Table 8.1. Proposed mass budget for the HOPE-Advanced crewed mission to Callisto

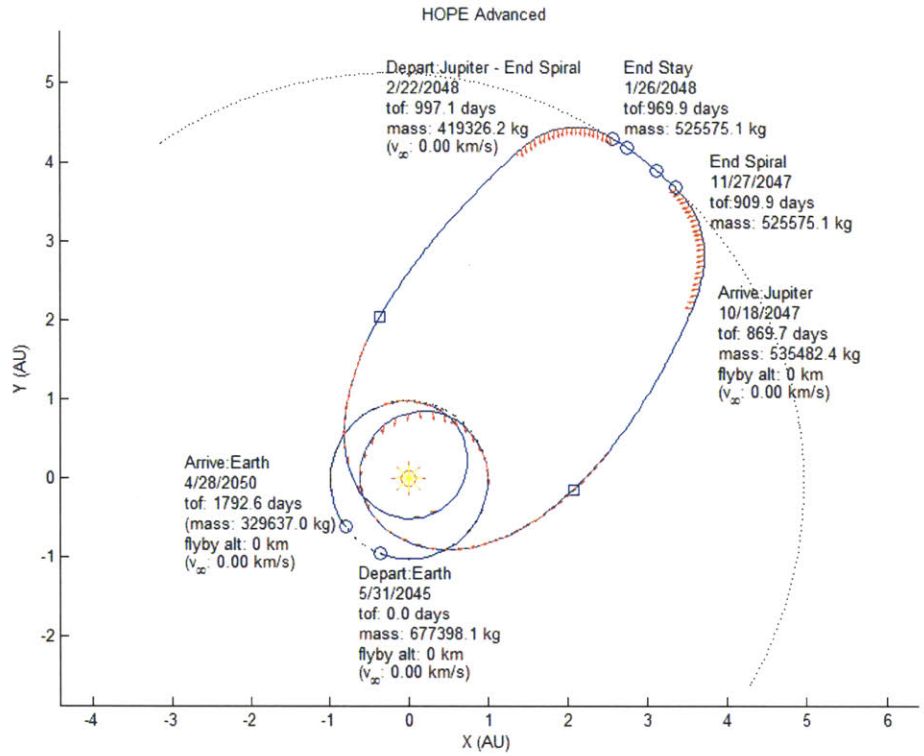

Figure 8.1. Earth-Jupiter-Earth mission trajectory for the HOPE-Advanced mission

	P_{OUT} [MW]	Thrust [N]	I_{SP} [s]	Lifetime [hr]	I_{TOT} [N-s]
HOPE Advanced Mission	30.00	413.63	14791.7	22896	3.63E+10

Table 8.2. Derived propulsion system requirements for the HOPE Advanced mission developed in this work

It should be noted that the converged solution developed in this work results is a final spacecraft burnout mass that is approximately 9% less than that proposed in Table 8.1. Based on the derived propulsion system requirements to enable the monolithic HOPE Advanced spacecraft, distant far-term applications such as these will likely require an order of magnitude increase in total output power and total impulse. It is also noteworthy that the optimum specific impulse for this mission is somewhat high by current and near-term technology standards at almost 15,000 seconds.

8.5 Beyond Electric Propulsion

In closing, it is illustrative to consider this work in the context of the extended range of power requirements likely to be encountered in distant far-term applications. In the case of electric propulsion systems using nuclear power sources, there may be a limiting plant output energy in which the amount of nuclear fuel consumed in generating thermal energy, coupled with the required mass overhead associated with the thermal conversion cycle, approaches an infeasible limit. To achieve total energies beyond this

limit, it may become more favorable to exhaust hot nuclear fuel fission products directly to generate thrust. Indeed, several concepts exist for such a system [196-198]. Alternatively, if nuclear fusion becomes a viable technology for in-space propulsion, fission-fusion hybrid systems may become possible in which fusion products are used to bootstrap neutron economy [199], or to increase system output power by exhausting fusion products directly [200]. It should be emphasized that propulsion systems incorporating fusion concepts are subject to requirements and constraints that are somewhat less technologically demanding than fusion reactors designed for electrical power production. Fusion power reactors must achieve fusion thermal power outputs that are many multiples of the input power in order to overcome limits of thermodynamic cycle efficiency and produce a positive net power output. In fission-fusion hybrid propulsion systems, however, this is not necessarily the case. This can be seen by considering the simple case of an NEP-powered plasma-phase electrothermal thruster. For an appropriately selected propellant combination such as D-T, D-^{3}He, or p-^{11}B, given adequate confinement and plasma density, a fraction of the collisions occurring in the plasma will result in a fusion event, liberating excess thermal energy. This additional thermal energy can be converted to jet kinetic energy by, for example, exhausting the plasma through a magnetic nozzle. In such a system the contribution of fusion power to the overall power balance would be observed as an increase in total efficiency. In highly advanced systems the apparent efficiency, the ratio of jet kinetic power to electrical input power, could in principle exceed unity. Regardless of the particulars of distant far-term propulsion system implementation, what seems likely is that these engines will make increasingly direct use of hot fission fragments or fusion products as reaction mass, rather than for the intermediate production of electrical power. It is likely that all such systems will remain largely conceptual into the foreseeable future, as space exploration activities world-wide may be enormously enhanced over the current state of the art by using more conventional closed-cycle nuclear power systems for electric propulsion at input power levels of several megawatts.

Appendix A

HET1D Simulation Code

```
function HET1DSim

%%%%%%%%%%%%%%%%%%%%%%%%%%%%%%%%%%%%%%%%%%%%%%%%%%%%%%%%%%%%%%%%%%%%%%%%%%%%%%%%
% HET1DSim MATLAB Script
% B. J. White
% 12/2010
%
% This MATLAB script provides a three-fluid, one dimensional model of
% Hall effect thruster discharge properties and performance.  Based on
% conditions at the anode, including mass flow rate, anode current, plasma
% density and electron temperature, downstream properties are evaluated.
% Upstream properties must be carefully tailored to generate solutions that
% pass smoothly through the ion sonic point.
%
% The model also provides the flexibility to accept variations on thruster
% geometry, magnetic field configuration, peak magnetic field strength, as
% well as propellant properties including atomic mass and ionization
% energy.
%                                                                [White, 2010]
%%%%%%%%%%%%%%%%%%%%%%%%%%%%%%%%%%%%%%%%%%%%%%%%%%%%%%%%%%%%%%%%%%%%%%%%%%%%%%%%

clear all; close all; format long g; j=1;

%%%%%%%%%%%%%%%%%%%%%%%%%%%%%%%%%%%%%%%%%%%%%%%%%%%%%%%%%%%%%%%%%%%%%%%%%%%%%%%%
%                       Constants and Thruster Geometry
%%%%%%%%%%%%%%%%%%%%%%%%%%%%%%%%%%%%%%%%%%%%%%%%%%%%%%%%%%%%%%%%%%%%%%%%%%%%%%%%
rout=.0503; %Channel Outer Radius in m
rin=.0331; %Channel Inner Radius in m
L=0.025; %Length of thruster channel in m
mh=0.1313/(6.02214179*10^23); %Heavy Particle Mass in kg/ion
Ac=3.14159*(rout^2-rin^2); %Channel Area
k=1.38*10^-23; %Boltzmann's Constant
```

```
Ei=k*12.13*11594; %propellant ionization energy in Joules
ai=2.5; % ai*Ei is the "average" ionization energy in Joules
ech=1.602*10^-19; %Fundamental Charge in C
me=9.109*10^-31; %Electron Mass in kg
Bm=0.0233; %Bmax in T
xm=0.0203; %Center of Gaussian B-Field Distribution
Lm=0.0202; %Constant
sig_i0=5*10^-20; %Ionization cross section constant in m^2
Tn=1000; %Neutral Temperature in K (assumed constant)
Ti=0.5*11594; %Ion Temperature in K (assumed constant)
cinbar=sqrt(8*k*Ti/(3.14*mh))-sqrt(8*k*Tn/(3.14*mh));

%%%%%%%%%%%%%%%%%%%%%%%%%%%%%%%%%%%%%%%%%%%%%%%%%%%%%%%%%%%%%%%%%%%%%%%%%%%
%                           Control Variables
%%%%%%%%%%%%%%%%%%%%%%%%%%%%%%%%%%%%%%%%%%%%%%%%%%%%%%%%%%%%%%%%%%%%%%%%%%%
m_dot=50e-6; %Propellant Mass Flow Rate in kg/s
IA=52.637; %Anode current in A
ne(j)=18.2*10^17; %Neutral Density in m^-3
Te(j)=0.652*11594; %Electron Temperature in eV*(e/k) = Kelvin

%%%%%%%%%%%%%%%%%%%%%%%%%%%%%%%%%%%%%%%%%%%%%%%%%%%%%%%%%%%%%%%%%%%%%%%%%%%
%                 Initialization and Initial Conditions
%%%%%%%%%%%%%%%%%%%%%%%%%%%%%%%%%%%%%%%%%%%%%%%%%%%%%%%%%%%%%%%%%%%%%%%%%%%
x(j)=0;
dAdx(j)=0;
Ac(j)=Ac;
rout(j)=rout;
rin(j)=rin;
B(j)=Bm*exp(-(x(j)-xm)^2/Lm^2);
vi(j)=-0.99*sqrt((5/3)*k*Te(j)/mh); %Reverse Sonic Ions @ anode
Gi(j)=ne(j)*vi(j); %Ion Flux
phi(j)=0; %Anode Potential
he(j)=(5/2)*k*Te(j)+ai*Ei-ech*phi(j); %Electron Enthalpy
hi(j)=(1/2)*mh*vi(j)^2+ech*phi(j); %Ion Enthalpy
A(j)=mh*vi(j)*Gi(j)+ne(j)*k*Te(j); %Ambipolar Momentum Density
Gn(j)=m_dot/(Ac*mh)-Gi(j); %Neutral Flux
vn(j)=1.72*sqrt(k*Tn/mh); %Neutral Inlet Velocity
M(j)=vn(j)/sqrt(k*Tn/mh); %Neutral Inlet Mach Number
nn(j)=Gn(j)/vn(j); %Neutral Number Density
Ge(j)=-IA/(Ac*ech)+Gi(j); %Electron Flux
ve(j)=Ge(j)/ne(j); %Electron Velocity
PlasmaRad(j)=(1-((8/5)*mh*Gi(j)/A(j))^2*(he(j)+hi(j)-ai*Ei)/(2*mh));
Li(j)=sqrt(k*Tn/mh)/(ne(j)*2.78*10^-20);
Lc(j)=2*sqrt(k*Tn/mh)/(cinbar*90*10^-20*ne(j));
bion(j)=0;

%%%%%%%%%%%%%%%%%%%%%%%%%%%%%%%%%%%%%%%%%%%%%%%%%%%%%%%%%%%%%%%%%%%%%%%%%%%
%                      Initialize Collision Frequencies
%%%%%%%%%%%%%%%%%%%%%%%%%%%%%%%%%%%%%%%%%%%%%%%%%%%%%%%%%%%%%%%%%%%%%%%%%%%
nuen(j)=nn(j)*6.6*10^-19*(((Te(j)/(4*11594))-
0.1)/(1+(Te(j)/(4*11594))^1.6))*sqrt(8*k*Te(j)/(3.14*me));
CouLog(j)=23-0.5*log((10^-6*ne(j))/(Te(j)/11594)^3);
nuei(j)=2^0.5*ne(j)*ech^4*CouLog(j)/(12*3.14159^1.5*(8.854e-
12)^2*me^0.5*(k*Te(j))^1.5);
nub(j)=(1/64)*ech*B(j)/me;
```

```
nui(j)=nn(j)*sig_i0*sqrt(8*k*Te(j)/(3.14159*me))*(1+k*Te(j)*Ei/(k*Te(j)+Ei)^2
)*exp(-Ei/(k*Te(j)));
nucex(j)=nn(j)*90*10^-20*(abs(vi(j)-vn(j))+sqrt(k*Ti/mh));
nuin(j)=nucex(j);
nuiT(j)=nui(j)+nuin(j)+nucex(j);
if 0.983 < 0.832*(k*Te(j)/(55*11594*k))^0.576
    dw(j)=0.983;
else
    dw(j)=0.832*(k*Te(j)/(55*11594*k))^0.576;
end
nuw(j)=0.15*sqrt(k*Te(j)/mh)/(rout(j)-rin(j));
nuEw(j)=(5.62+1.65/(1-dw(j)))*nuw(j);
nue(j)=(ech^2*B(j)^2/(me^2))/(nuen(j)+nuei(j)+nub(j)+nuw(j));
fnub(j)=1/(1+80*(nuen(j)+nuei(j))/(ech*B(j)/me));
IntBdL(j)=0;

%%%%%%%%%%%%%%%%%%%%%%%%%%%%%%%%%%%%%%%%%%%%%%%%%%%%%%%%%%%%%%%%%%%%%%%%%%%%%%%
%                                Subsonic Ion Region
%%%%%%%%%%%%%%%%%%%%%%%%%%%%%%%%%%%%%%%%%%%%%%%%%%%%%%%%%%%%%%%%%%%%%%%%%%%%%%%
while PlasmaRad(j)>0 && j<20000
    FI=0; %number of failed iterations preceding sonic passage
    j=j+1;
    dAdx(j)=0;
    Ac(j)=Ac(j-1);
    rout(j)=rout(j-1);
    rin(j)=rin(j-1);

    %Computing the constants & Current Position
    dGi(j)=ne(j-1)*(nui(j-1)-nuw(j-1))*(L/10^4);
    if nui(j-1)<nuw(j-1)
        dx=10^-5;
        Ge(j)=Ge(j-1)+dGi(j);
        Gi(j)=Gi(j-1)+dGi(j);
        Gn(j)=Gn(j-1)-dGi(j);
        A(j)=A(j-1)+dx*ne(j-1)*(nui(j-1)-nuw(j-1))*(mh*(vi(j-1)-(nuiT(j-
1)/(nui(j-1)-nuw(j-1)))*(vi(j-1)-vn(j-1)))-me*(nue(j-1)/(nui(j-1)-nuw(j-
1)))*ve(j-1));
        he(j)=he(j-1)+dx*ne(j-1)*(nui(j-1)-nuw(j-1))*(-(2.5+nuEw(j-1)/(nui(j-
1)-nuw(j-1)))*k*Te(j-1)-(1+nuw(j-1)/(nui(j-1)-nuw(j-1)))*ai*Ei)/Ge(j-1);
        hi(j)=hi(j-1)+dx*ne(j-1)*(nui(j-1)-nuw(j-1))*(-(nuiT(j-1)/(nui(j-1)-
nuw(j-1)))*(mh*(vi(j-1)-vn(j-1))/ne(j-1)));
        x(j)=x(j-1)+dx;
    else
        Ge(j)=Ge(j-1)+dGi(j);
        Gi(j)=Gi(j-1)+dGi(j);
        Gn(j)=Gn(j-1)-dGi(j);
        A(j)=A(j-1)+dGi(j)*(mh*(vi(j-1)-(nuiT(j-1)/(nui(j-1)-nuw(j-
1)))*(vi(j-1)-vn(j-1)))-me*(nue(j-1)/(nui(j-1)-nuw(j-1)))*ve(j-1));
        he(j)=he(j-1)+dGi(j)*(-(2.5+nuEw(j-1)/(nui(j-1)-nuw(j-1)))*k*Te(j-1)-
(1+nuw(j-1)/(nui(j-1)-nuw(j-1)))*ai*Ei)/Ge(j-1);
        hi(j)=hi(j-1)+dGi(j)*(-(nuiT(j-1)/(nui(j-1)-nuw(j-1)))*(mh*(vi(j-1)-
vn(j-1))/ne(j-1)));
        x(j)=x(j-1)+dGi(j-1)/(ne(j-1)*(nui(j-1)-nuw(j-1)));
    end

    B(j)=Bm*exp(-(x(j)-xm)^2/Lm^2);
```

```
    bion(j)=((he(j)+hi(j)-ai*Ei)/(2*mh))*((8/5)*mh*Gi(j)/A(j))^2;
    PlasmaRad(j)=1-bion(j);

    if bion(j) > 1
        PlasmaRad(j)=0;
    end

    vi(j)=(5/8)*A(j)/(mh*Gi(j))*(1-sqrt(PlasmaRad(j)));
    ne(j)=Gi(j)/vi(j);
    ve(j)=Ge(j)/ne(j);
    Te(j)=(hi(j)+he(j)-ai*Ei-mh*vi(j)^2/2)*(2/(5*k));
    phi(j)=(hi(j)-mh*vi(j)^2/2)/ech;

    %Solve for the neutral properties
    Lc(j)=2*sqrt(k*Tn/mh)/(cinbar*90*10^-20*ne(j));
    Li(j)=sqrt(k*Tn/mh)/(ne(j)*2.78*10^-20);
    dMdx(j)=(-M(j-1)/Lc(j)*(M(j-1)-vi(j)/sqrt(k*Tn/mh))+1/Li(j))/(M(j-1)^2-
1);
    vn(j)=vn(j-1)+sqrt(k*Tn/mh)*dMdx(j)*dGi(j-1)/(ne(j-1)*nui(j-1));
    M(j)=vn(j)/sqrt(k*Tn/mh);
    nn(j)=Gn(j)/vn(j);

    %Recomputing Collision Frequencies:
    nuen(j)=nn(j)*6.6*10^-19*(((Te(j)/(4*11594))-
0.1)/(1+(Te(j)/(4*11594))^1.6))*sqrt(8*k*Te(j)/(3.14*me));
    CouLog(j)=23-0.5*log((10^-6*ne(j))/(Te(j)/11594)^3);
    nuei(j)=2^0.5*ne(j)*ech^4*CouLog(j)/(12*3.14159^1.5*(8.854e-
12)^2*me^0.5*(k*Te(j))^1.5);
    nub(j)=(1/64)*ech*B(j)/me;

nui(j)=nn(j)*sig_i0*sqrt(8*k*Te(j)/(3.14*me))*(1+k*Te(j)*Ei/(k*Te(j)+Ei)^2)*e
xp(-Ei/(k*Te(j)));
    nucex(j)=nn(j)*90*10^-20*(abs(vi(j)-vn(j))+sqrt(k*Ti/mh));
    nuin(j)=nucex(j);
    nuiT(j)=nui(j)+nuin(j)+nucex(j);
    if 0.983 < 0.832*(k*Te(j)/(55*11594*k))^0.576
        dw(j)=0.983;
    else
        dw(j)=0.832*(k*Te(j)/(55*11594*k))^0.576;
    end
    nuw(j)=0.15*sqrt(k*Te(j)/mh)/(rout(j)-rin(j));
    nuEw(j)=(5.62+1.65/(1-dw(j)))*nuw(j);
    nue(j)=(ech^2*B(j)^2/(me^2))/(nuen(j)+nuei(j)+nub(j)+nuw(j));
    fnub(j)=1/(1+64*(nuen(j)+nuei(j))/(ech*B(j)/me));
    if ne(j)>ne(j-1)
        IntBdL(j)=IntBdL(j-1)+B(j)*(x(j)-x(j-
1))/(1+64*me*nuen(j)/(ech*B(j)));
    else
        IntBdL(j)=IntBdL(j-1);
    end
end

%%%%%%%%%%%%%%%%%%%%%%%%%%%%%%%%%%%%%%%%%%%%%%%%%%%%%%%%%%%%%%%%%%%%%%%%%%%%
%                              Ion Sonic Transition
%%%%%%%%%%%%%%%%%%%%%%%%%%%%%%%%%%%%%%%%%%%%%%%%%%%%%%%%%%%%%%%%%%%%%%%%%%%%
j=j+1;
```

```
dAdx(j)=0;
Ac(j)=Ac(j-1);
rout(j)=rout(j-1);
rin(j)=rin(j-1);
if nui(j-1)>nuw(j-1)
    dGi(j)=ne(j-1)*(nui(j-1)-nuw(j-1))*(L/10^6);
else
    disp('Theres a Problem')
    pause
end
x(j)=x(j-1)+dGi(j-1)/(ne(j-1)*(nui(j-1)-nuw(j-1)));
B(j)=Bm*exp(-(x(j)-xm)^2/Lm^2);
Gi(j)=Gi(j-1)+dGi(j);
Ge(j)=Ge(j-1)+dGi(j);
vi(j)=1.0001*sqrt((5/3)*k*Te(j-1)/mh);
Te(j)=fsolve(@(x)1.2.*sqrt(5.*k.*x+mh.*vi(j).^2)-sqrt(mh.*vi(j).^2)-
k.*x/sqrt(mh.*vi(j).^2),Te(j-1));
ne(j)=Gi(j)/vi(j);
ve(j)=Ge(j)/ne(j);
A(j)=mh*vi(j)*Gi(j)+ne(j)*k*Te(j);
phi(j)=phi(j-1);
he(j)=(5/2)*k*Te(j)+ai*Ei-ech*phi(j);
hi(j)=(1/2)*mh*vi(j)^2+ech*phi(j);

% Neutral Properties
Gn(j)=Gn(j-1)-dGi(j);
vn(j)=vn(j-1);
nn(j)=Gn(j)/vn(j);
M(j)=M(j-1);

bion(j)=((he(j)+hi(j)-ai*Ei)/(2*mh))*((8/5)*mh*Gi(j)/A(j))^2;
PlasmaRad(j)=1-bion(j);

%Collision Frequencies:
nuen(j)=nn(j)*6.6*10^-19*(((Te(j)/(4*11594))-
0.1)/(1+(Te(j)/(4*11594))^1.6))*sqrt(8*k*Te(j)/(3.14*me));
CouLog(j)=23-0.5*log((10^-6*ne(j))/(Te(j)/11594)^3);
nuei(j)=2^0.5*ne(j)*ech^4*CouLog(j)/(12*3.14159^1.5*(8.854e-
12)^2*me^0.5*(k*Te(j))^1.5);
nub(j)=(1/64)*ech*B(j)/me;
nui(j)=nn(j)*sig_i0*sqrt(8*k*Te(j)/(3.14*me))*(1+k*Te(j)*Ei/(k*Te(j)+Ei)^2)*e
xp(-Ei/(k*Te(j)));
nucex(j)=nn(j)*90*10^-20*(abs(vi(j)-vn(j))+sqrt(k*Ti/mh));
nuin(j)=nucex(j);
nuiT(j)=nui(j)+nuin(j)+nucex(j);
if 0.983 < 0.832*(k*Te(j)/(55*11594*k))^0.576
    dw(j)=0.983;
else
    dw(j)=0.832*(k*Te(j)/(55*11594*k))^0.576;
end
nuw(j)=0.15*sqrt(k*Te(j)/mh)/(rout(j)-rin(j));
nuEw(j)=(5.62+1.65/(1-dw(j)))*nuw(j);
nue(j)=(ech^2*B(j)^2/(me^2))/(nuen(j)+nuei(j)+nub(j)+nuw(j));
fnub(j)=1/(1+64*(nuen(j)+nuei(j))/(ech*B(j)/me));
if ne(j)>ne(j-1)
    IntBdL(j)=IntBdL(j-1)+B(j)*(x(j)-x(j-1))/(1+64*me*nuen(j)/(ech*B(j)));
```

```
else
    IntBdL(j)=IntBdL(j-1);
end
x(j)
xS=x(j);
exitflag=0;

%%%%%%%%%%%%%%%%%%%%%%%%%%%%%%%%%%%%%%%%%%%%%%%%%%%%%%%%%%%%%%%%%%%%%%%%%%%%%%%
%                          Supersonic Ions inside Channel
%%%%%%%%%%%%%%%%%%%%%%%%%%%%%%%%%%%%%%%%%%%%%%%%%%%%%%%%%%%%%%%%%%%%%%%%%%%%%%%
while x(j)<L  && j<20000 && exitflag<1
    j=j+1;
    dAdx(j)=0;
    Ac(j)=Ac(j-1);
    rout(j)=rout(j-1);
    rin(j)=rin(j-1);
    dGi(j)=ne(j-1)*(nui(j-1)-nuw(j-1))*(L/10^4);

    %Resolve current position
    x(j)=x(j-1)+dGi(j-1)/(ne(j-1)*(nui(j-1)-nuw(j-1)));
    B(j)=Bm*exp(-(x(j)-xm)^2/Lm^2);

    %Computing the constants
    Ge(j)=Ge(j-1)+dGi(j);
    Gi(j)=Gi(j-1)+dGi(j);
    Gn(j)=Gn(j-1)-dGi(j);
    A(j)=A(j-1)+dGi(j)*(mh*(vi(j-1)-(nuiT(j-1)/(nui(j-1)-nuw(j-1)))*(vi(j-1)-
vn(j-1)))-me*(nue(j-1)/(nui(j-1)-nuw(j-1)))*ve(j-1));
    he(j)=he(j-1)+dGi(j)*(-(2.5+nuEw(j-1)/(nui(j-1)-nuw(j-1)))*k*Te(j-1)-
(1+nuw(j-1)/(nui(j-1)-nuw(j-1)))*ai*Ei)/Ge(j-1);
    hi(j)=hi(j-1)+dGi(j)*(-(nuiT(j-1)/(nui(j-1)-nuw(j-1)))*(mh*(vi(j-1)-vn(j-
1))/ne(j-1)));
    bion(j)=((he(j)+hi(j)-ai*Ei)/(2*mh))*((8/5)*mh*Gi(j)/A(j))^2;
    PlasmaRad(j)=1-bion(j);

    if PlasmaRad(j)<0
        FI=FI+1; %Smooth sonic passage condition not met
        PlasmaRad(j)=0;
        vi(j)=sqrt((5/3)*k*Te(j-1)/mh);
        Te(j)=Te(j-1);
        ne(j)=Gi(j)/vi(j);
        ve(j)=Ge(j)/ne(j);
        phi(j)=phi(j-1);
        A(j)=mh*vi(j)*Gi(j)+ne(j)*k*Te(j);
        he(j)=(5/2)*k*Te(j)+ai*Ei-ech*phi(j);
        hi(j)=(1/2)*mh*vi(j)^2+ech*phi(j);
    elseif PlasmaRad(j)>1
        PlasmaRad(j)=1;
        vi(j)=(5/8)*A(j)/(mh*Gi(j))*(1+sqrt(PlasmaRad(j)));
        ne(j)=Gi(j)/vi(j);
        ve(j)=Ge(j)/ne(j);
        phi(j)=(hi(j)-mh*vi(j)^2/2)/ech;
        Te(j)=2*(he(j)+ech*phi(j)-ai*Ei)/(5*k);
    else
        vi(j)=(5/8)*A(j)/(mh*Gi(j))*(1+sqrt(PlasmaRad(j)));
        ne(j)=Gi(j)/vi(j);
```

```
        ve(j)=Ge(j)/ne(j);
        phi(j)=(hi(j)-mh*vi(j)^2/2)/ech;
        Te(j)=2*(he(j)+ech*phi(j)-ai*Ei)/(5*k);
    end

    %Solve for the neutral properties
    Lc(j)=2*sqrt(k*Tn/mh)/(cinbar*90*10^-20*ne(j));
    Li(j)=sqrt(k*Tn/mh)/(ne(j)*2.78*10^-20);
    dMdx(j)=(-M(j-1)/Lc(j)*(M(j-1)-vi(j)/sqrt(k*Tn/mh))+1/Li(j))/(M(j-1)^2-
1);
    vn(j)=vn(j-1)+sqrt(k*Tn/mh)*dMdx(j)*dGi(j-1)/(ne(j-1)*(nui(j-1)-nuw(j-
1)));
    M(j)=vn(j)/sqrt(k*Tn/mh);
    nn(j)=Gn(j)/vn(j);

    if Te(j)<100
        ne(j)=ne(j-1);
        ve(j)=ve(j-1);
        vi(j)=vi(j-1);
        Te(j)=Te(j-1);
        phi(j)=phi(j-1);
    end

    if x(j)>=L && PlasmaRad(j)==0
        disp('Sonic Passage Failed')
        exitflag=1;
    end

    %Recomputing Collision Frequencies:
    nuen(j)=nn(j)*6.6*10^-19*(((Te(j)/(4*11594))-
0.1)/(1+(Te(j)/(4*11594))^1.6))*sqrt(8*k*Te(j)/(3.14*me));
    CouLog(j)=23-0.5*log((10^-6*ne(j))/(Te(j)/11594)^3);
    nuei(j)=2^0.5*ne(j)*ech^4*CouLog(j)/(12*3.14159^1.5*(8.854e-
12)^2*me^0.5*(k*Te(j))^1.5);
    nub(j)=(1/64)*ech*B(j)/me;

nui(j)=nn(j)*sig_i0*sqrt(8*k*Te(j)/(3.14*me))*(1+k*Te(j)*Ei/(k*Te(j)+Ei)^2)*e
xp(-Ei/(k*Te(j)));
    if nui(j)<100
        nui(j)=nui(j-1);
    end
    nucex(j)=nn(j)*90*10^-20*(abs(vi(j)-vn(j))+sqrt(k*Ti/mh));
    nuin(j)=nucex(j);
    nuiT(j)=nui(j)+nuin(j)+nucex(j);
    if 0.983 < 0.832*(k*Te(j)/(55*11594*k))^0.576
        dw(j)=0.983;
    else
        dw(j)=0.832*(k*Te(j)/(55*11594*k))^0.576;
    end
    nuw(j)=0.15*sqrt(k*Te(j)/mh)/(rout(j)-rin(j));
    nuEw(j)=(5.62+1.65/(1-dw(j)))*nuw(j);
    nue(j)=(ech^2*B(j)^2/(me^2))/(nuen(j)+nuei(j)+nub(j)+nuw(j));
    fnub(j)=1/(1+64*(nuen(j)+nuei(j))/(ech*B(j)/me));
    if ne(j)>ne(j-1)
        IntBdL(j)=IntBdL(j-1)+B(j)*(x(j)-x(j-
1))/(1+64*me*nuen(j)/(ech*B(j)));
```

```
    else
        IntBdL(j)=IntBdL(j-1);
    end
end
xE=x(j);
ind=j;
%%%%%%%%%%%%%%%%%%%%%%%%%%%%%%%%%%%%%%%%%%%%%%%%%%%%%%%%%%%%%%%%%%%%%%%%%%%
%                             Plume Region
%%%%%%%%%%%%%%%%%%%%%%%%%%%%%%%%%%%%%%%%%%%%%%%%%%%%%%%%%%%%%%%%%%%%%%%%%%%
while x(j)<2*L && exitflag<1 && Te(j)>1000
    j=j+1;
    cp=sqrt(k*Te(j-1)/mh);
    dx=1e-4;
    dAdx(j)=Ac(j-1)*2*cp/((rout(j-1)-rin(j-1))*vi(j-1));
    Ac(j)=Ac(j-1)+dAdx(j)*dx;
    dr=dAdx(j)*dx/(2*3.14159*(rout(j-1)-rin(j-1)));
    rout(j)=rout(j-1)+dr;
    rin(j)=rin(j-1)-dr;
    if rin(j)<0
        rin(j)=0;
    end
    d=rout(j)-rin(j);

    %Resolve current position
    x(j)=x(j-1)+dx;
    B(j)=Bm*exp(-(x(j)-xm)^2/Lm^2);

    %Find the derivatives and properties
    dnedx=(5*me*ne(j-1)*nue(j-1)*ve(j-1)+3*ne(j-1)*mh*nuiT(j-1)*(vi(j-1)-
vn(j-1))+6*ne(j-1)*mh*vi(j-1)*(nui(j-1)-cp/d)-(2*ne(j-1)*nui(j-1)/ve(j-
1))*((5/2)*k*Te(j-1)+ai*Ei))/(3*mh*vi(j-1)^2-5*k*Te(j-1));
    dvedx=nui(j-1)-2*cp*ve(j-1)/(d*vi(j-1))-ve(j-1)*dnedx/ne(j-1);
    dvidx=nui(j-1)-2*cp/d-vi(j-1)*dnedx/ne(j-1);
    dphidx=(-mh/ech)*(2*vi(j-1)*nui(j-1)-vi(j-1)^2*dnedx/ne(j-1)-2*vi(j-
1)*cp/d+nuiT(j-1)*(vi(j-1)-vn(j-1)));
    dTedx=(1/k)*(ech*dphidx-me*nue(j-1)*ve(j-1)-k*Te(j-1)*dnedx/ne(j-1));
    dnndx=(2*nn(j-1)*mh*vn(j-1)^2*cp/(d*vi(j-1))+2*mh*vn(j-1)*ne(j-1)*nui(j-
1)+mh*nn(j-1)*(nuin(j-1)+nucex(j-1))*(vi(j-1)-vn(j-1)))/(k*Tn-mh*vn(j-1)^2);
    dvndx=-ne(j-1)*nui(j-1)/nn(j-1)-2*vn(j-1)*cp/(d*vi(j-1))-vn(j-
1)*dnndx/nn(j-1);
    ne(j)=ne(j-1)+dnedx*dx;
    ve(j)=ve(j-1)+dvedx*dx;
    vi(j)=vi(j-1)+dvidx*dx;
    phi(j)=phi(j-1)+dphidx*dx;
    Te(j)=Te(j-1)+dTedx*dx;
    nn(j)=nn(j-1)+dnndx*dx;
    vn(j)=vn(j-1)+dvndx*dx;
    Ge(j)=ne(j)*ve(j);
    Gi(j)=ne(j)*vi(j);
    Gn(j)=vn(j)*nn(j);
    dGi(j)=0;

    if Te(j)<100
        ne(j)=ne(j-1);
        ve(j)=ve(j-1);
        vi(j)=vi(j-1);
```

```
        Te(j)=Te(j-1);
        phi(j)=phi(j-1);
    end

    %Recomputing Collision Frequencies:
    nuen(j)=nn(j)*6.6*10^-19*(((Te(j)/(4*11594))-
0.1)/(1+(Te(j)/(4*11594))^1.6))*sqrt(8*k*Te(j)/(3.14*me));
    CouLog(j)=23-0.5*log((10^-6*ne(j))/(Te(j)/11594)^3);
    nuei(j)=2^0.5*ne(j)*ech^4*CouLog(j)/(12*3.14159^1.5*(8.854e-
12)^2*me^0.5*(k*Te(j))^1.5);
    nub(j)=(1/16)*ech*B(j)/me;

nui(j)=nn(j)*sig_i0*sqrt(8*k*Te(j)/(3.14*me))*(1+k*Te(j)*Ei/(k*Te(j)+Ei)^2)*e
xp(-Ei/(k*Te(j)));
    if nui(j)<=0
        nui(j)=1;
    end
    nucex(j)=nn(j)*90*10^-20*(vi(j)-vn(j)+sqrt(k*Ti/mh));
    nuin(j)=nucex(j);
    nuiT(j)=nui(j)+nuin(j)+nucex(j);
    dw(j)=dw(j-1);
    nuw(j)=0;
    nuEw(j)=0;
    nue(j)=(ech^2*B(j)^2/(me^2))/(nuen(j)+nuei(j)+nub(j)+nuw(j));
    fnub(j)=1/(1+64*(nuen(j)+nuei(j))/(ech*B(j)/me));
    if ne(j)>ne(j-1)
        IntBdL(j)=IntBdL(j-1)+B(j)*(x(j)-x(j-
1))/(1+16*me*nuen(j)/(ech*B(j)));
    else
        IntBdL(j)=IntBdL(j-1);
    end
    PlasmaRad(j)=PlasmaRad(j-1);
    bion(j)=bion(j-1);
end

%%%%%%%%%%%%%%%%%%%%%%%%%%%%%%%%%%%%%%%%%%%%%%%%%%%%%%%%%%%%%%%%%%%%%%%%%%%%
%                       Outputs & Performance Metrics
%%%%%%%%%%%%%%%%%%%%%%%%%%%%%%%%%%%%%%%%%%%%%%%%%%%%%%%%%%%%%%%%%%%%%%%%%%%%
FI
%Note:  The output 'FI' is a useful metric for obtaining converged
%solutions.  By adjusting anode control variables (IA, mdot, ne(1) and
%Te(1)) appropriatley, one can force the value of 'FI' to decrease.
%Converged solutions must have zero failed iterations --- FI = 0.
%                                                          [White, 2010]
fpn=Gn(j)/(Gi(j)+Gn(j))
phimax=max(phi)
dphi=phi(j)
NA2=Gi(j)*Ac(j)*ech/IA
Thrust=1000*Gi(j)*Ac(j)*mh*vi(j)+1000*Gn(j)*Ac(j)*mh*vn(j)
ISP=(Thrust/(1000*9.81*m_dot))

%%%%%%%%%%%%%%%%%%%%%%%%%%%%%%%%%%%%%%%%%%%%%%%%%%%%%%%%%%%%%%%%%%%%%%%%%%%%
%                                    Plotting
%%%%%%%%%%%%%%%%%%%%%%%%%%%%%%%%%%%%%%%%%%%%%%%%%%%%%%%%%%%%%%%%%%%%%%%%%%%%
hold on
```

```
ne1=num2str(ne(1),'%11.4g'); Str1='ne(0) = '; Str2=' m^-3'; ne1=strcat(Str1,
ne1, Str2);
subplot(3,3,1); plot(x,ne); vline([xS xE],{'g','r'},{'Sonic Point','Thruster
Exit'}); xlabel('x [m]'); ylabel('ne [m^-^3]'); title('Electron
Density','Fontweight','Bold')
TB1=uicontrol('style','text'); set(TB1, 'Units','inches'); set(TB1,'String',
ne1); set(TB1,'Position', [3.258 5.781 1.6 0.22]);
set(TB1, 'FontName', 'Helvetica'); set(TB1, 'FontSize', 10.0); set(TB1,
'BackgroundColor', [1 1 1]);

IBIA=num2str(NA2,'%11.3f'); Str1='IB / IA = '; IBIA=strcat(Str1, IBIA);
IAN=num2str(IA,'%11.6f'); Str2='IA = '; Str3='Amps'; IAN=strcat(Str2, IAN,
Str3);
subplot(3,3,2); plot(x,ve); vline([xS xE],{'g','r'}); xlabel('x [m]');
ylabel('ve [m/s]'); title('Electron Velocity','Fontweight','Bold')
TB2=uicontrol('style','text'); set(TB2, 'Units','inches'); set(TB2,'String',
IBIA); set(TB2,'Position', [7.4 5.781 1.4 0.22]);
set(TB2, 'FontName', 'Helvetica'); set(TB2, 'FontSize', 10.0); set(TB2,
'BackgroundColor', [1 1 1]);
TB9=uicontrol('style','text'); set(TB9, 'Units','inches'); set(TB9,'String',
IAN); set(TB9,'Position', [7.4 5.581 1.4 0.22]);
set(TB9, 'FontName', 'Helvetica'); set(TB9, 'FontSize', 10.0); set(TB9,
'BackgroundColor', [1 1 1]);

ISP=num2str(ISP,'%11.1f'); Str1='ISP = '; Str2='s'; ISP=strcat(Str1, ISP,
Str2);
FTHR=num2str(Thrust,'%11.1f'); Str2='Thrust = '; Str3=' mN';
FTHR=strcat(Str2, FTHR, Str3);
subplot(3,3,3); plot(x,vi); vline([xS xE],{'g','r'}); xlabel('x [m]');
ylabel('vi [m/s]'); title('Ion Velocity','Fontweight','Bold')
TB3=uicontrol('style','text'); set(TB3, 'Units','inches'); set(TB3,'String',
ISP); set(TB3,'Position', [11.4 5.781 1.4 0.22]);
set(TB3, 'FontName', 'Helvetica'); set(TB3, 'FontSize', 10.0); set(TB3,
'BackgroundColor', [1 1 1]);
TB4=uicontrol('style','text'); set(TB4, 'Units','inches'); set(TB4,'String',
FTHR); set(TB4,'Position', [11.4 5.581 1.4 0.22]);
set(TB4, 'FontName', 'Helvetica'); set(TB4, 'FontSize', 10.0); set(TB4,
'BackgroundColor', [1 1 1]);

Te1=num2str(Te(1)/11594, '%11.5f'); Str1='Te(0) = '; Str2='eV';
Te1=strcat(Str1, Te1, Str2);
TeMAX=num2str(max(Te)/11594, '%11.5f'); Str3='TeMAX = ';
TeMAX=strcat(Str3,TeMAX,Str2);
subplot(3,3,4); plot(x,Te); vline([xS xE],{'g','r'}); xlabel('x [m]');
ylabel('Te [K]'); title('Electron Temperature','Fontweight','Bold')
TB5=uicontrol('style','text'); set(TB5, 'Units','inches'); set(TB5,'String',
Te1); set(TB5,'Position', [3.4 3.8 1.4 0.22]);
set(TB5, 'FontName', 'Helvetica'); set(TB5, 'FontSize', 10.0); set(TB5,
'BackgroundColor', [1 1 1]);
TB6=uicontrol('style','text'); set(TB6, 'Units','inches'); set(TB6,'String',
TeMAX); set(TB6,'Position', [3.4 3.6 1.4 0.22]);
set(TB6, 'FontName', 'Helvetica'); set(TB6, 'FontSize', 10.0); set(TB6,
'BackgroundColor', [1 1 1]);

dphi=num2str(dphi,'%11.1f'); Str1=('phi ='); Str2 = 'Volts'; dphi=
strcat(Str1, dphi, Str2);
```

```
subplot(3,3,5); plot(x,phi); vline([xS xE],{'g','r'}); xlabel('x [m]');
ylabel('phi [V]'); title('Potential Profile','Fontweight','Bold')
TB7=uicontrol('style','text'); set(TB7, 'Units','inches'); set(TB7,'String',
dphi); set(TB7,'Position', [7.4 3.8 1.4 0.22]);
set(TB7, 'FontName', 'Helvetica'); set(TB7, 'FontSize', 10.0); set(TB7,
'BackgroundColor', [1 1 1]);

fpn=num2str(fpn, '%11.3f'); Str1='fpn = '; fpn=strcat(Str1,fpn);
MN1=num2str(vn(1)/sqrt(k*Tn/mh),'%10.2f'); Str2='MN1 = ';
MN1=strcat(Str2,MN1);
subplot(3,3,6); plot(x,vn); vline([xS xE],{'g','r'}); xlabel('x [m]');
ylabel('vn [m/s]'); title('Neutral Velocity','Fontweight','Bold')
TB10=uicontrol('style','text'); set(TB10, 'Units','inches');
set(TB10,'String', fpn); set(TB10,'Position', [11.8 3.3 0.9 0.22]);
set(TB10, 'FontName', 'Helvetica'); set(TB10, 'FontSize', 10.0); set(TB10,
'BackgroundColor', [1 1 1]);
TB11=uicontrol('style','text'); set(TB11, 'Units','inches');
set(TB11,'String', MN1); set(TB11,'Position', [11.8 3.1 0.9 0.22]);
set(TB11, 'FontName', 'Helvetica'); set(TB11, 'FontSize', 10.0); set(TB11,
'BackgroundColor', [1 1 1]);

mdot=num2str(m_dot,'%11.4g'); Str1='mdot = '; Str2=' kg/s'; mdot=strcat(Str1,
mdot, Str2);
subplot(3,3,7); plot(x,nn); vline([xS xE],{'g','r'}); xlabel('x [m]');
ylabel('nn [m^-^3]'); title('Neutral Density','Fontweight','Bold')
TB8=uicontrol('style','text'); set(TB8, 'Units','inches'); set(TB8,'String',
mdot); set(TB8,'Position', [3.258 1.5 1.4 0.22]);
set(TB8, 'FontName', 'Helvetica'); set(TB8, 'FontSize', 10.0); set(TB8,
'BackgroundColor', [1 1 1]);

subplot(3,3,8); plot(x,B); vline([xS xE],{'g','r'}); xlabel('x [m]');
ylabel('B [T]'); title('Magnetic Field','Fontweight','Bold')
subplot (3,3,9); plot(x,dGi); vline([xS xE],{'g','r'}); xlabel('x [m]');
ylabel('dGi [m^-^2 s^-^1]'); title('Integration Step
Size','Fontweight','Bold')

end
```

Appendix B

Method of Characteristics for MPD

In the limit of a large magnetic Reynold's number, $\beta \gg 1$, MPD thruster operation may be approximately described by the ideal MHD equations. To develop a method of characteristics we first select a coordinate system aligned with a streamline in the MPD thruster. The conservation of momentum along the streamline can be expressed:

$$u\frac{\partial u}{\partial s}+\frac{B}{\mu_0\rho}\frac{\partial B}{\partial s}=0 \qquad \text{(Eq. B.1)}$$

The conservation of momentum normal to a streamline is given by:

$$\frac{\partial u}{\partial n}+u\frac{\partial \theta}{\partial s}=0 \qquad \text{(Eq. B.2)}$$

The conservation of mass in this coordinate system becomes:

$$\frac{1}{\rho}\frac{\partial \rho}{\partial s}+\frac{1}{u}\frac{\partial u}{\partial s}-\frac{\partial \theta}{\partial n}=-\frac{1}{r}\sin\theta \qquad \text{(Eq. B.3)}$$

Finally, the induction equation can be written simply:

$$\frac{\partial}{\partial s}\left(\frac{B}{\rho}\right)=\frac{B}{\rho r}\sin\theta \qquad \text{(Eq. B.4)}$$

Combining the expressions for conservation of momentum along a streamline with continuity, we find that:

$$\left(\frac{\mu_0 \rho u^2}{B^2} - 1\right)\frac{\partial u}{\partial s} + u\frac{\partial \theta}{\partial n} = 0 \qquad \text{(Eq. B.5)}$$

Recognizing the magneto-sonic speed in the expression above, we can define the Mach-Alfven number:

$$\frac{\mu_0 \rho u^2}{B^2} = \frac{u^2}{a^2} = A^2 \qquad \text{(Eq. B.6)}$$

Next, we can define the Mach-Alfven angle:

$$\mu = \sin^{-1}\frac{1}{A} = \tan^{-1}\frac{1}{\sqrt{A^2 - 1}} \qquad \text{(Eq. B.7)}$$

Recasting the conservation of momentum normal to a streamline in terms of the Mach-Alfven angle gives:

$$\tan\mu\frac{\sqrt{A^2 - 1}}{u}\frac{\partial u}{\partial n} + \frac{\partial \theta}{\partial s} = 0 \qquad \text{(Eq. B.8)}$$

Recasting Eq. B.5 in a similar way yields:

$$\frac{\sqrt{A^2 - 1}}{u}\frac{\partial u}{\partial s} + \tan\mu\frac{\partial \theta}{\partial n} = 0 \qquad \text{(Eq. B.9)}$$

The next step in developing a method of characteristics is to combine the two preceding equations by adding and subtracting them.

$$\frac{\sqrt{A^2 - 1}}{u}\frac{\partial u}{\partial s} + \tan\mu\frac{\partial \theta}{\partial n} + \tan\mu\frac{\sqrt{A^2 - 1}}{u}\frac{\partial u}{\partial n} + \frac{\partial \theta}{\partial s} = 0 \qquad \text{(Eq. B.10)}$$

$$\tan\mu\frac{\sqrt{A^2 - 1}}{u}\frac{\partial u}{\partial n} + \frac{\partial \theta}{\partial s} - \frac{\sqrt{A^2 - 1}}{u}\frac{\partial u}{\partial s} - \tan\mu\frac{\partial \theta}{\partial n} = 0 \qquad \text{(Eq. B.11)}$$

We can introduce an analog to the Prandtl-Meyer function:

$$d\omega = \frac{du}{u}\sqrt{A^2 - 1} = \frac{du}{u}\sqrt{\frac{\frac{3}{2}u^2 - a_0^2}{a_0^2 - \frac{u^2}{2}}} \qquad \text{(Eq. B.12)}$$

This expression can be integrated to find:

$$\omega = \sqrt{3}\tan^{-1}\left(\sqrt{\frac{A^2-1}{3}}\right) - \tan^{-1}\left(\sqrt{A^2-1}\right) \qquad \text{(Eq. B.13)}$$

Finally, in terms of the velocity u, we have:

$$\omega = \sqrt{3}\tan^{-1}\left(\sqrt{\frac{\frac{1}{3}\frac{3}{2}u^2 - a_0^2}{a_0^2 - \frac{1}{2}u^2}}\right) - \tan^{-1}\left(\sqrt{\frac{\frac{3}{2}u^2 - a_0^2}{a_0^2 - \frac{1}{2}u^2}}\right) \qquad \text{(Eq. B.14)}$$

It should be noted that this treatment is only valid for describing 2D geometries. Returning to Eq. B.10 and B.11 above and using the Prandtl-Meyer analog, we can rearrange terms to obtain:

$$\left(\frac{\partial}{\partial s} + \tan\mu\frac{\partial}{\partial n}\right)(\omega+\theta) - \tan\mu\frac{\partial\omega}{\partial(B/\rho)} - \frac{\partial\omega}{\partial(B/\rho)}\frac{B\sin\theta}{\rho r} = 0 \qquad \text{(Eq. B.15)}$$

$$\left(\frac{\partial}{\partial s} - \tan\mu\frac{\partial}{\partial n}\right)(\omega-\theta) - \tan\mu\frac{\partial\omega}{\partial(B/\rho)} + \frac{\partial\omega}{\partial(B/\rho)}\frac{B\sin\theta}{\rho r} = 0 \qquad \text{(Eq. B.16)}$$

Noting that the Prandtl-Meyer analog bears no explicit dependence on the variable quantity $\frac{B}{\rho}$, we can immediately simplify:

$$\left(\frac{\partial}{\partial s} + \tan\mu\frac{\partial}{\partial n}\right)(\omega+\theta) = \frac{\partial}{\partial m^+}(\omega+\theta) = 0 \qquad \text{(Eq. B.17)}$$

$$\left(\frac{\partial}{\partial s} - \tan\mu\frac{\partial}{\partial n}\right)(\omega-\theta) = \frac{\partial}{\partial m^-}(\omega-\theta) = 0 \qquad \text{(Eq. B.18)}$$

This is sufficient for the construction of a supersonic nozzle design tool for an MPD thruster in a 2D geometry. This algorithm was implemented in a simple Matlab script (Appendix C), to assist in the development of candidate geometries for simulation using a sophisticated magnetohydrodynamics code called MACH2, described previously in Chapter 7. By specifying a desired number of characteristic lines, the input Mach-Alfven number, and the required output Mach-Alfven number, the script is able to output the coordinates of a number of points that lie on the ideal nozzle contour. These coordinates are normalized to the radius of the nozzle throat.

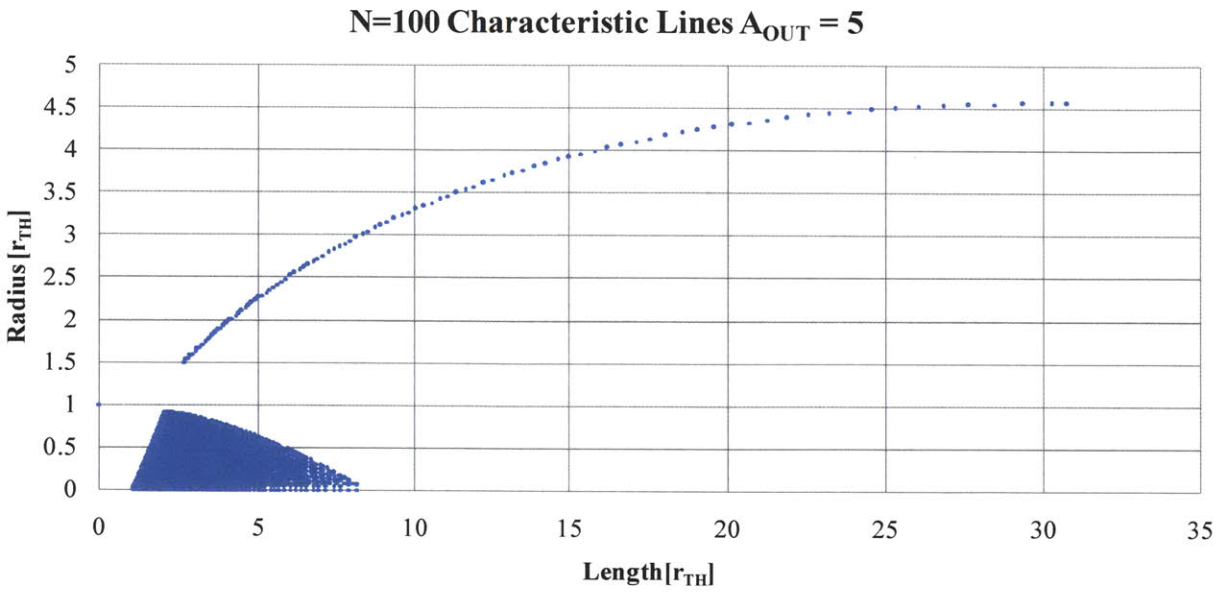

Figure B.1. Points lying on the ideal 2D nozzle contour derived from the method of characteristics; points interior to the nozzle contour represent the intersections of characteristics in the non-simple region.

Appendix C

MPD Method of Characteristics Code

```
function MPDMOC(nc, Ain, Ae)

%Calculate the number of points
i=nc+1; np=0;
while i>0
    np=np+i;
    i=i-1;
end

%Evaluate known quantities
w(1)=sqrt(3)*atan((1/sqrt(3))*sqrt(Ain^2-1))-atan(sqrt(Ain^2-1));
w(np)=sqrt(3)*atan((1/sqrt(3))*sqrt(Ae^2-1))-atan(sqrt(Ae^2-1));
Ip(1)=w(1);
Ip(np)=w(np);
Im(1)=-w(1);

%Find the values of the invariant I- at all points:
i=1; CL(i)=2; WALL(i)=CL(i)+nc;
for k=1:nc
    w(CL(i))=-w(1)-(k-1)*(w(np)-w(1))/(nc-1);
    for j=CL(i):WALL(i)
        Im(j)=w(CL(i));
    end
    if k~=nc
        i=i+1;
        CL(i)=CL(i-1)+nc+2-k;
        WALL(i)=WALL(i-1)+nc+1-k;
    end
end

%Find the values of the invariant I+ at all points:
```

```
for k=1:nc+1
    a=nc;
    j=k+1;
    while a>(nc-k)&&j<np
        Ip(j)=w(1)+((k-1)/nc)*(w(np)-w(1));
        j=j+a;
        a=a-1;
    end
end

%Compute the Angles at each point
for m=1:np
    theta(m)=(Ip(m)+Im(m))/2;
    if theta(m)<0
        theta(m)=0;
    end
    w(m)=(Ip(m)-Im(m))/2;
    A(m)=fzero(@(x)sqrt(3)*atan((1/sqrt(3))*sqrt(x.^2-1))-atan(sqrt(x.^2-1))-
w(m),[(Ain-10^-10) (Ae+10^-10)]);
    mu(m)=atan(1/A(m));
    a(m)=mu(m)-theta(m);
    b(m)=mu(m)+theta(m);
end

%Find the corresponding coordinates (r,z) for each point
z(1)=0; r(1)=1;
z(2)=1/tan(mu(2)); r(2)=0;
for k=1:nc
    for j=CL(k):WALL(k)
        if j==CL(k) && k~=1;
            a(j)=0.5*(theta(j-nc-2+k)+theta(j))+0.5*(mu(j-nc-2+k)+mu(CL(k)));
            b(j)=0.5*(theta(CL(k-1))+theta(j))+0.5*(mu(CL(k-1))+mu(j));
            z(j)=(r(j-nc-2+k)-r(CL(k-1))+z(j-nc-2+k)*tan(a(j))+z(CL(k-
1))*tan(b(j)))/(tan(a(j))+tan(b(j)));
            r(j)=0;
        end
        if j==WALL(k) && k==1
            a(j)=-(theta(1)+theta(j-1))/2;
            b(j)=theta(j-1)+mu(j-1);
            z(j)=(r(1)-r(j-1)+z(1)*tan(a(j))+z(j-
1)*tan(b(j)))/(tan(a(j))+tan(b(j)));
            r(j)=r(j-1)+(z(j)-z(j-1))*tan(b(j));
            %r(j)=(r(j-1)*tan(a(j))+r(1)*tan(b(j))+(z(1)-z(j-
1))*tan(a(j))*tan(b(j)))/(tan(a(j))+tan(b(j)));
        end
        if j==WALL(k) && k~=1
            a(j)=-(theta(WALL(k-1))+theta(j-1))/2;
            b(j)=theta(j-1)+mu(j-1);
            z(j)=(r(WALL(k-1))-r(j-1)+z(WALL(k-1))*tan(a(j))+z(j-
1)*tan(b(j)))/(tan(a(j))+tan(b(j)));
            r(j)=r(j-1)+(z(j)-z(j-1))*tan(b(j));
            %r(j)=(r(j-1)*tan(a(j))+r(CL(k-1))*tan(b(j))+(z(CL(k-1))-z(j-
1))*tan(a(j))*tan(b(j)))/(tan(a(j))+tan(b(j)));
        end
        if j-nc<=1 && j~=WALL(k) && j~=CL(k)
            a(j)=mu(j)-theta(j);
```

```
            b(j)=0.5*(theta(j-1)+theta(j))+0.5*(mu(j-1)+mu(j));
            z(j)=(r(1)-r(j-1)+z(1)*tan(a(j))+z(j-
1)*tan(b(j)))/(tan(a(j))+tan(b(j)));
            r(j)=r(j-1)+(z(j)-z(j-1))*tan(b(j));
            %r(j)=(r(j-1)*tan(a(j))+r(1)*tan(b(j))+(z(1)-z(j-
1))*tan(a(j))*tan(b(j)))/(tan(a(j))+tan(b(j)));
        end
        if j-nc>1 && j~=WALL(k) && j~=CL(k)
            a(j)=(a(j-nc-2+k)+a(j))/2;
            b(j)=(b(j-1)+b(j))/2;
            z(j)=(r(j-nc-2+k)-r(j-1)+z(j-nc-2+k)*tan(a(j))+z(j-
1)*tan(b(j)))/(tan(a(j))+tan(b(j)));
            r(j)=r(j-1)+(z(j)-z(j-1))*tan(b(j));
            %r(j)=(r(j-1)*tan(a(j))+r(j-(nc+2-k))*tan(b(j))+(z(j-(nc+2-k))-
z(j-1))*tan(a(j))*tan(b(j)))/(tan(a(j))+tan(b(j)));
        end
    end
end

%Evaluate Wall Coordinates
for j=1:nc
    ZW(j)=z(WALL(j));
    RW(j)=r(WALL(j));
end

%Write Data to File
xlswrite('output.xlsx',Im', 'Sheet1', 'B2');
xlswrite('output.xlsx',Ip', 'Sheet1', 'C2');
xlswrite('output.xlsx',w', 'Sheet1', 'D2');
xlswrite('output.xlsx',theta', 'Sheet1', 'E2');
xlswrite('output.xlsx',A', 'Sheet1', 'F2');
xlswrite('output.xlsx',mu', 'Sheet1', 'G2');
xlswrite('output.xlsx',a', 'Sheet1', 'H2');
xlswrite('output.xlsx',b', 'Sheet1', 'I2');
xlswrite('output.xlsx',z', 'Sheet1', 'J2');
xlswrite('output.xlsx',r', 'Sheet1', 'K2');
xlswrite('output.xlsx',ZW', 'Sheet1', 'L3');
xlswrite('output.xlsx',RW', 'Sheet1', 'M3');
end
```

References

[1] M. K. Tikhonravov (ed.), *Works on Rocket Technology by E. K. Tsiolkovsky*, Publishing House of the Defense Ministry, Moscow, 1947; translated from the 1947 Russian text by NASA as NASA TT F-243, 1965.

[2] H. Oberth, *Wege zur Raumschiffahr,* Druck und Verlag von R. Oldenbourg, Munich and Berlin, 1929.

[3] E. Stulinger, "Possibilities of Electrical Space Ship Propulsion," Ber. 5th Intern. Astronaut. Congr., Innsbruck, pp. 100, August 1954.

[4] E. Stulinger, "Electrical Propulsion Systems for Space Ships with Nuclear Power Sources," *J. Astronaut.*, Vol. 2 pp. 149, 1955, Vol. 3 pp.11, 33, 1956.

[5] E. Stulinger, "Flight Path of an Electrically Propelled Space Ship," *Jet Propulsion*, Vol. 27, No. 4, pp. 410, April 1957.

[6] E. Y. Choueiri, "A Critical History of Electric Propulsion: The First Fifty Years (1906 – 1956)," AIAA 2004-3334, *40th AIAA/ASME/SAE/ASEE Joint Propulsion Conference and Exhibit*, Ft. Lauderdale, FL, July 2004.

[7] R. G. Jahn, *Physics of Electric Propulsion*, Dover Publications Inc., New York, 1968.

[8] P. W. Garrison, J. F. Stocky, "Future Spacecraft Propulsion," *Journal of Propulsion and Power*, Vol. 4, pp. 520 – 525, 1988.

[9] M. D. Rayman, P. Varghese, D. H. Lehman and L. L. Livesay, "Results from the Deep Space 1 Technology Validation Mission," *Acta Astronautica*, Vol.47, p.475, 2000.

[10] J. Brophy, C. Garner, B. Nakazono, M. Marcucci, M. Henry and D. Noon, "The Ion Propulsion System For Dawn," AIAA-2003-4542, *39th AIAA/ASME/SAE/ASEE Joint Propulsion Conference and Exhibit*, Huntsville, Alabama, July 20-23, 2003

[11] C.R. Koppel, F. Marchandise, M. Prioul, D. Estublier and F. Darnon, "The SMART-1 Electric Propulsion Subsystem around the Moon: In Flight Experience", AIAA 2005-3671, *42nd AIAA/ASME/SAE/ASEE Joint Propulsion Conference and Exhibit*, Tucson, AZ, July 2005.

[12] D. M. De Cara, D. Estublier, "SMART-1; an analysis of flight data", IAF Paper IAC-04-S.4.02, October 2004.

[13] H. Kuninaka, K. Nishiyama, I. Funaki, T. Yamada, Y. Shimizu, and J. Kawaguchi, "Powered Flight of Electron Cyclotron Resonance Ion Engines on Hayabusa Explorer," *Journal of Propulsion and Power*, Vol. 23, No. 3, May-June 2007.

[14] J. Kawaguchi, A. Fujiwara, T. K. Uesugi, "The ion engines cruise operation and the Earth swingby of Hayabusa (Muses-C)", IAF Paper IAC-04-Q.5.02, October 2004.

[15] E. Stulinger, *Ion Propulsion for Space Flight*, McGraw Hill Book Company, New York, 1964.

[16] A. V. Arefiev, B. N. Breizman, "Collisionless Plasma Expansion into Vacuum: Two New Twists on an Old Problem," *Physics of Plasmas*, Vol. 16, No. 5, 055707, May 2009.

[17] K. Liffman, A. Siora, "Magnetosonic Jet Flow," *Monthly Notices of the Royal Astronomical Society*, Vol. 290, pp. 629-635, 1997.

[18] C. A. Deline, R. D. Bengtson, B. N. Breizman, M. R. Tushentsov, J. E. Jones, D. G. Chavers, C. C. Dobson, B. M. Schuettpelz, "Plume Detachment from a Magnetic Nozzle," *Physics of Plasmas*, Vol. 16, No. 3, 033502, March, 2009.

[19] R. Winglee, T. Ziemba, L. Giersch, J. Prager, J. Carscadden, B. R. Roberson, "Simulation and Laboratory Validation of Magnetic Nozzle Effects for the High Power Helicon Thruster," *Physics of Plasmas*, Vol. 14, No. 6, 063501, June, 2007

[20] R. P. Hoyt, J. T. Scheur, K. F. Schoenberg, R. A. Gerwin, R. W. Moses Jr., I. Henins, "Magnetic Nozzle Design for Coaxial Plasma Accelerators," *IEEE Transactions on Plasma Science*, Vol. 23, No. 3, June, 1995.

[21] L. R. Shepard, A. V. Cleaver, "The Atomic Rocket: Parts 1-4," *Journal of the British Interplanetary Society*, Vol. 7, No. 5 and 6, and Vol. 8, No. 1 and 2, 1947-1948.

[22] C. Bruno, T. A. Lawrence, D. G. Fearn, M. Auweter-Kurtz, H. Kurtz, R. X. Lenard, "IAA Position Paper on Nuclear Power and Propulsion," IAC-06-D2.8/C3.5/C4.701, *57th International Astronautical Conference*, Valencia, Spain, October 2006.

[23] M. I. Yarymovych, F. A. deWies, R. R. John, "Feasibility of Arcjet-Propelled Spacecraft," *Astronautics*, Vol. 7, No. 6, pp. 36-42 June 1962.

[24] C. G. Sauer Jr., R. M. Jones, "Near Earth Electric Propulsion with SP-100," SP-100 Program Technical Information Report, JPL D-2327, April 1985.

[25] W. D. Deininger, R. J. Vondra, "Arcjet Propulsion System for an SP-100 Flight Experiment," *Journal of Spacecraft and Rockets*, Vol. 25, No. 6, Nov.-Dec. 1988.

[26] W. D. Deininger, R. J. Vondra, "Spacecraft and Mission Design for the SP-100 Flight Experiment," *Jornal of Spacecraft and Rockets*, Vol. 26, No. 2 Mar.-Apr. 1989.

[27] W. D. Deininger, R. J. Vondra, "Arcjet Nuclear Electric Propulsion (NEP) System for the SP-100 Reference Mission," Jet Propulsion Laboratory, JPL D-4739, Mar. 1988.

[28] W. D. Deininger, R. J. Vondra, "Spacecraft and Mission Design for the SP-100 Flight Experiment," IEPC 88-013, *Proceedings of the 20th International Electric Propulsion Conference*, DGLR Bericht 88-02, Oct. 1988.

[29] W. D. Deininger, R. J. Vondra, "A Baseline Spacecraft and Mission Design for the SP-100 Flight Experiment," AIAA 89-2594, *25th AIAA/ASME/SAE/ASEE Joint Propulsion Conference and Exhibit*, Monterey, CA, July 1989.

[30] N. F. Shepard, R. A. Birch, T. A. Marotta, "Mission and Design Considerations Affecting the First Flight Experiment for the SP-100," AIAA 87-2379, 1987.

[31] R. J. Vondra, W. D. Deininger, "Options for a 30 kWe SP-100 Flight Demonstration," AIAA 89-2597, *25th AIAA/ASME/SAE/ASEE Joint Propulsion Conference and Exhibit*, July 1989.

[32] W. M. Phillips, "Nuclear Electric Power and Propulsion System for Earth Orbital and Solar System Exploration Applications," AIAA 79-1337, *15th AIAA/ASME/SAE/ASEE Joint Propulsion Conference and Exhibit*, June, 1979.

[33] E. V. Pawlik, W. M. Phillips, "A Nuclear Electric Propulsion Vehicle for Planetary Exploration," AIAA 76-1041, *International Electric Propulsion Conference*, Key Biscayne, FL, November, 1976.

[34] L. K. Rudolph, D. Q. King, "100 kWe Magnetoplasmadynamic Thruster System Design," *Journal of Spacecraft and Rockets*, Vol. 21, No. 6, Nov.-Dec. 1984.

[35] K. L. Atkins, J. C. Beckman, K. T. Nock, "Expedition to Mars," Jet Propulsion Laboratory, February 10, 1983.

[36] E. P. Coomes, D. Q. King, J. M. Cuta, B. J. Webb, "PEGASUS: A Multi-Megawatt Nuclear Electric Propulsion System," AlAA 86-1583, *22nd AIAA/ASME/SAE/ASEE Joint Propulsion Conference and Exhibit*, June 1986.

[37] E. P. Coomes, D. Q. King, J. M. Cuta, B. J. Webb, "The PEGASUS Drive: A Multi-Megawatt Nuclear Electric Propulsion System," AIAA 87-1038, *19th AIAA International Electric Propulsion Conference*, May 1987.

[38] E. P. Coomes, L. A. McCauley, J. L. Christian, M. A. Gomez, W. A. Wong, "Unique Mission Options Available with a Megawatt-Class Nuclear Electric Propulsion System," AIAA 88-2839, *24th AIAA/ASME/SAE/ASEE Joint Propulsion Conference and Exhibit*, July, 1988.

[39] R. J. Cassaday, "An MPD Thruster Driven Cargo Ferry for Support of the Manned Mars Mission," AIAA 88-2896, *24th AIAA/ASME/SAE/ASEE Joint Propulsion Conference and Exhibit*, July, 1988.

[40] R. H. Frisbee, N. J. Hoffman, "Electric Propulsion Options for Mars Cargo Missions," AIAA 96-3173, *32nd AIAA/ASME/SAE/ASEE Joint Propulsion Conference and Exhibit*, Lake Buena Vista, FL, July 1996.

[41] M. L. Tapper, "A Nuclear Powered Pulsed Inductive Plasma Accelerator as a Viable Propulsion Concept for Advanced OTV Space Applications," AIAA 82-1899, *16th AIAA International Electric Propulsion Conference*, November, 1982.

[42] R. J. Beale, "The Conceptual Design of a Nuclear-Electric Power Spacecraft for the Exploration of Jupiter," JPL TR 32-115, Jet Propulsion Laboratory, May 1961.

[43] H. Brown, P. Ortiz, "Mission Engineering Study of Electrically Propelled Manned Planetary Vehicles," GE Contractor Report GE Doc. 6300-214, NASA Contract NAS8-20372, July 1967.

[44] W. C. Estabrook, W. M. Phillips, T. Hsieh, "System Design for a Nuclear Electric Spacecraft Utilizing Out-of-Core Thermionic Conversion," JPL TM-33-791, Jet Propulsion Laboratory, Sept. 1976.

[45] E. V. Pawlik, W. M. Phillips, "A Nuclear Electric Propulsion Vehicle for Planetary Exploration," AIAA 76-1041, *AIAA International Electric Propulsion Conference*, Key Biscayne, FL, November 1976.

[46] W. M. Phillips, "Nuclear Electric Power System for Solar System Exploration," *Journal of Spacecraft and Rockets*, Vol. 17, No. 4, July 1980.

[47] T. H. Silva, D. C. Byers, "Orbital Transfer of Large Space Structures with Nuclear Rockets," AAS 80-083, in Commercial Operations in Space 1980-2000, *18th Goddard Memorial Symposium*, Vol. 51, Science and Technology Series, 1981.

[48] T. H. Silva, D. C. Byers, "Nuclear Electric Propulsion System Utilization for Earth Orbit Transfer of Large Spacecraft Structures," AIAA 80-1223, *16th AIAA/ASME/SAE/ASEE Joint Propulsion Conference and Exhibit*, Hartford, CT, June 1980.

[49] P. W. Garrison, K. T. Nock, "Nuclear Electric Propulsion (NEP) Spacecraft for the Outer Planet Orbiter Missions," AIAA 82-1276 *18th AIAA/ASME/SAE/ASEE Joint Propulsion Conference and Exhibit*, Cleveland, OH, June 1982.

[50] K. T. Nock, "Rendezvous with Saturn's Rings," IAU Colloquium No. 75, Planetary Rings, September 1982 in *Planetary Rings*, A. Brahic (ed.), Cepadues, 1984.

[51] K. T. Nock, P. Garrison, "Nuclear Electric Propulsion Mission to Neptune," AIAA 82-1870, *16th AIAA International Electric Propulsion Conference*, New Orleans, LA, November 1982.

[52] R. M. Jones, C. G. Sauer, "Nuclear Electric Propulsion Missions," *Journal of the British Interplanetary Society*, Vol. 36, pp. 395-400, 1984.

[53] L. Jaffe, et. Al. "Nuclear Reactor Power for an Electrically Powered Orbital Transfer Vehicle," AIAA 87-1102, *19th AIAA International Electric Propulsion Conference*, Colorado Springs, CO, May 1987.

[54] K. T. Nock, "TAU - A Mission to a Thousand Astronomical Units," AIAA 87-1049, *9th AIAA International Electric Propulsion Conference*, Colorado Springs, CO, May 1987.

[55] P.F. Bythrow, B.H. Mauk and N.A.Gatsonis, "Operational Experiments and Thruster Performance Plan for the Nuclear Electric Propulsion Space Test Program NEPSTP)," AIAA-93-1896, *AIAA/SAE/ASME/ASEE 29th Joint Propulsion Conference and Exhibit*, Monterey CA, July, 1993.

[56] G. A. Herbert, M. Day, "NEPSTP Propulsion Module Design and Flight Test Plans," Space Nuclear Power and Propulsion: Eleventh Symposium, *AIP Conference Proceedings*, Volume 301, pp. 253-263, 1994.

[57] S. R. Oleson, F. W. Elliott, T. M. Randolph, N. Dipprey, "The Electric Propulsion Segment of Prometheus 1," AIAA 2005-3888, *41st AIAA/ASME/SAE/ASEE Joint Propulsion Conference & Exhibit*, Tucson, AZ, July, 2005.

[58] H. W. Loeb, G. A. Popov, "A Nuclear-Electric Propulsion Module for Advanced Solar System Exploration Programs," *Acta Astronautica*, Vol. 37, pp. 153-166, 1995.

[59] M. Noca, J. Polk, R. Lenard, "Evolutionary strategy for the use of nuclear electric propulsion in planetary exploration," *Space Technology & Applications International Forum, 18th Symposium on Nuclear Power and Propulsion*, Albuquerque, NM, February 2001.

[60] R. Y. Nakagawa, J. O. Elliott, T. R. Spilker, C. M. Grayson, "Concept for a Shuttle-Tended Reusable Interplanetary Transport Vehicle Using Nuclear Electric Propulsion," JPL TR 02-2753, Jet Propulsion Lab, Pasadena, CA, March 2003.

[61] W. D. Deninger, K. T. Nock, "A Review of Electric Propulsion Spacecraft System Concepts," AIAA 90-2553, *21st AIAA/DGLR/JSASS International Electric Propulsion Conference*, Orlando FL, July 1990.

[62] B. B. Bevard, G. L. Yoder, "Technology Development Program for an Advanced Potassium Rankine Power Conversion System Compatible with Several Space Reactor Designs," *AIP Conference Proceedings*, Vol. 654, pp. 629, 2003.

[63] R. D. Rovang, J. C. Mills, E. B. Baumeister, "Multimegawatt Potassium Rankine Power for Nuclear Electric Power," *AIP Conference Proceedings*, Vol. 217 pp. 373, 1991.

[64] J. A. George, "Multimegawatt Nuclear Power Systems for Nuclear Electric Propulsion," AIAA 1991-3607, *NASA/OAI Conference on Advanced SEI Technologies*, Cleveland , OH, Sept. 1991.

[65] G. L. Yoder, J. J. Carbajo, R. W. Murphy, A. L. Qualls, J. Hojnicki, M. P. Moriarty, F. J. Widman, K. J. Metcalf, M. Nikitkin, "Potassium Rankine Cycle System Design Study for Space Nuclear Electric Propulsion," AIAA 2005-5637, *3rd International Energy Conversion Engineering Conference*, San Francisco, CA August 2005.

[66] L. O. Cropp, D. R. Gallup, A. C. Marshall, "Mass and Performance Estimates for 5 to 1000 kWe Nuclear Reactor Power Systems for Space Applications," SAND90-0312, Sandia National Lab, March 1991.

[67] MALTO, Mission Analysis Low-Thrust Optimization, Software Package, Ver. 5.3.6, California Institute of Technology Jet Propulsion Lab, Pasadena CA, 2008.

[68] T. D. Kowalkowski, E. A. Rinderle, D. F. Landau, "User's Guide for MALTO: Mission Analysis Low-Thrust Optimizer," Jet Propulsion Laboratory, University of California, July 2008.

[69] J. A. Sims, P. A. Finlayson, E. A. Rinderle, M. A. Vavrina, T. D. Kowalkwski, "Implementation of a Low-Thrust Trajectory Optimization Algorithm for Preliminary Design," AIAA 2006-6746, *AAS/AIAA Astrodynamics Specialist Conference*, 2006.

[70] D. White, M. Martinez-Sanchez, L. Daniel, "Mission Analysis for the Design of High Power Electric Propulsion Thrusters," AIAA 2009-5262, *45th AIAA/ASME/SAE/ASEE Joint Propulsion Conference*, Denver, CO, July 2009.

[71] J. A. Angelo Jr., D. Buden, *Space Nuclear Power*, Orbit Book Company Inc., Malabar, FL, 1985.

[72] M. S. El-Genk, "Deployment History and Design Considerations for Space Reactor Power Systems," *Acta Astronautica*, Vol. 64, No. 9-10, May-June, 2009.

[73] D. R. Koenig, "Experience Gained from the Space Nuclear Rocket Program (ROVER)," LA-10062-H, Los Alamos National Laboratory, Los Alamos, NM, May 1986

[74] D. L. Black, S. V. Gunn, "Space Nuclear Propulsion," *Encyclopedia of Physical Science and Technology*, 2004, pp. 555 – 575.

[75] G. L. Bennett, "Space Nuclear Power," *Encyclopedia of Physical Science and Technology*, 2004, pp. 537 – 553.

[76] G. R. Schmidt, D. H. Manzella, H. Kamhawi, T. Kremic, S. R. Oleson, J. W. Kankanich, L. A. Dudzinski, "Radioisotope Electric Propulsion (REP): A Near-Term Approach to Nuclear Propulsion," *Acta Astronautica*, Vol. 66, No. 3-4, Feb. – Mar. 2010.

[77] R. J. Noble, "Radioisotope electric propulsion for robotic science missions to near-interstellar Space," *Journal of British Interplanetary Society* Vol. 49, 1996, pp. 322–328.

[78] N. E. Todreas, M. S. Kazimi, *Nuclear Systems I – Thermal Hydraulic Fundamentals*, Taylor and Francis Group, New York, NY, 1990.

[79] V. Yarygin, et al., "Energy Conversion Options For NASA's Space Nuclear Power Systems Initiative – Underestimated Capability Of Thermionics", *Proc. 2nd International Energy Conversion Engineering Conference*, Providence, RI, Aug. 2004

[80] M. J. Wollman (ed.), M. J. Zika (ed.), "Project Prometheus Reactor Module Final Report," SPP-67110-0008 US DOE Naval Reactors Division, April 2006

[81] J. C. Moyers, J. P. Nichols, "ALKASYS: A Computer Program for Studies of Rankine-Cycle Space Nuclear Power Systems," ORNL TM-10427, Oak Ridge National Laboratory, September 1987.

[82] J. G. Collier, *Convective Boiling and Condensation,* 2nd Ed., McGraw Hill Book Co., New York, NY, 1972.

[83] G. B. Wallis, *One-Dimensional Two-Phase Flow*, McGraw Hill Book Co, New York, NY, 1969.

[84] *SP-100 Gound Engineering System (GES) Baseline System Definition and Characterization Study: Final Report: Volume I, Thermoelectric Power Conversion System*, Document No. 85 DS4268, General Electric Company, August 9, 1985.

[85] G. Samuels, *Fuel Element Design for Boiling Potassium Reactors*, ORNL/TM-1344, Oak Ridge National Laboratory, January 1966.

[86] S. K. Bhattacharyya et. al., *Evaluation of Multi-Megawatt Space Power Plants for Air Force Missions*, ANL SPC-3 Rev. 1, Argonne National Laboratory, April 20, 1984.

[87] W. W. Engle Jr., et al., "Optimization of a Shield for a Heat-Pipe Cooled Fast Reactor Designed as a Nuclear Electric Space Power Plant," ORNL/TM-3449, Oak Ridge National Laboratory, June 15, 1971

[88] R. A. Robinson, et al., "Brayton-Cycle Radioisotope Heat Source Design Study: Phase I (Conceptual Design) Report," ORNL/TM-1691, NASA CR-72090, pp. 90-100, Oak Ridge National Laboratory, December 1966

[89] D. E. Carlson, "A Parameter Study for the SP-100 Radiation Shield," SP TN 101, Los Alamos National Laboratory, 1985

[90] Garrett Corp., *Potassium Turbo Alternator (KTA) Preliminary Design Study, Vol. I – Turbine, Bearing, and Seal Parametric Design*, NASA CR-1498, National Aeronautics and Space Administration, April 1970.

[91] A. P. Fraas et al., *Design Comparison of Cesium and Potassium Vapor Turbine-Generator Units for Space Power Plants*, ORNL/TM-2024, Oak Ridge National Laboratory, February 1969.

[92] Space Power Inc., "Megawatt Class Nuclear Space Power System (MCNSPS), Conceptual Design and Evaluation Report," SP-58-S-84, March 1985.

[93] Westinghouse Electric Corporation, "Space Electric Power Systems Study, Final Report," Vols. 1-4, D-Spec. No. D 709553, National Aeronautics and Space Administration, December 1962.

[94] D. G. Gilmore (Ed.), *Spacecraft Thermal Control Handbook Volume 1: Fundamental Technologies*, 2nd Edition, The Aerospace Press, El Segundo CA, 2002

[95] J. P. Tournier, M. S. El-Genk, "Liquid Metal Loop and Heat Pipe Radiator for Space Reactor Power Systems," Journal of Propulsion and Power, Vol. 22, No. 5, Sept. - Oct. 2006

[96] A. J. Juhasz, G. P. Peterson, "Review of Advanced Radiator Technologies for Spacecraft Power Systems and Space Thermal Control," NASA-TM-4555, NASA Lewis Research Center, June 1994

[97] A. J. Juhasz, R. D. Rovang, "Composite Heat Pipe Development Status: Development of Lightweight Prototype Carbon-Carbon Heat Pipe with Integral Fins and Metal Foil Liner," NASA TM-106909, 9th International Heat Pipe Conference, Albuquerque, NM, May 1995

[98] A. J. Juhasz, "Design Considerations for Lightweight Space Radiators Based on Fabrication and Test Experience with a Carbon-Carbon Composite Prototype Heat Pipe," NASA TP-1998-207427, NASA Glenn Research Center, September, 2002

[99] A. J. Juhasz, "High Conductivity Carbon-Carbon Heat Pipes for Light Weight Space Power System Radiators," AIAA 2008-5784, *6th International Energy Conversion Engineering Conference*, Cleveland, OH, July 2008

[100] NASA JPL Jupiter Icy Moons Orbiter Team, "Jupiter Icy Moons Orbiter Annual Report," NASA 982-R06933; JPL Publication 04-16, October 2004.

[101] Joint Titan Saturn System Mission Science Definition Team, ESA Study Team, NASA Study Team, "Titan Saturn System Mission (TSSM) NASA/ESA Joint Summary Report," JPL D-48442 and ESA-SRE(2008)3, January 2009.

[102] A.E. Lyngvi, M.L. van den Berg, P. Falkne, "Study Overview of the Interstellar Heliopause Probe," ESA Report SCI-A/2006/114/IHP, Issue 3 Rev. 4, April 2007.

[103] P. Liewer, R. Mewaldt, A. Ayon, R. Wallace, "NASA's Interstellar Probe Mission," *Space Technology and Application International Forum*, Albuquerque NM, January 2000.

[104] B. G. Drake, "From the Moon to Mars – The Things we Most Need to Learn at the Moon to Support the Subsequent Human Exploration of Mars: Background of the Design Reference Architecture 5.0," Lunar Exploration Analysis Group (LEAG) Annual Workshop, October 2007. URL: http://www.lpi.usra.edu/meetings/leag2007/presentations/20071001.drake.pdf [cited 6 July 2009].

[105] B. Bienstock, D. Atkinson, S. Atreya, K. Baines, M. Wright, J. Masciarelli, "Neptune Orbiter, Probe, and Triton Lander Mission," in *NASA Space Science Vision Missions*, M. S. Allen (ed.), American Institute of Aeronautics and Astronautics, Reston, VA, 2008.

[106] Gill, P. E., "User's Guide for SNOPT Version 7, A Fortran Package for Large-Scale Nonlinear Programming," December 4, 2004.

[107] H. de la Fuente, J. L. Raboin, G. R. Spexarth, G. D. Valle, "TransHab: NASA's Large-Scale Inflatable Spacecraft," AIAA 2000-1822, *41st AIAA/ASME/ASCE/AHS/ASC Structures, Structural Dynamics, and Materials Conference and Exhibit*, Atlanta, GA, April 2000.

[108] R. Zubrin, "The Use of Practical Nuclear Thermal Rocket Stages to Support the Human Exploration of the Moon and Mars," AIAA-92-3407, 28th AIAA/ASME/SAE/ASEE Joint Propulsion Conference and Exhibit, Nashville, TN, July 1992

[109] M. Martinez-Sanchez, S. A. Miller, "Arcjet Modeling: Status and Prospects," *Journal of Propulsion and Power*, Vol. 12, No. 6, Nov.-Dec. 1996

[110] M. Martinez-Sanchez, A. Sakamoto, "Simplified Analysis of Arcjet Thrusters," AIAA Paper 93-1904, June 1993

[111] M. Auweter-Kurtz, T. Golz, H. Habiger, F. Happer, H. Kurtz, M. Riehle, C. Sleziona, "High-Power Hydrogen Arcjet Thrusters," *Journal of Propulsion and Power*, Vol. 14, No. 5, 1998, pp. 764-773

[112] T. Golz, M. Auweter-Kurtz, H. L. Kurtz, "100 kW Hydrogen Arcjet Thruster Experiments," AIAA 92-3836, July 1992.

[113] T. M. Golz, M. Auweter-Kurtz, H. L. Kurtz, "Development and Testing of a 100 kW Radiation-Cooled Thermal Hydrogen Arcjet Thruster," IEPC-93-221, *Proceedings of the 23rd International Electric Propulsion Conference*, pp. 2079-2088, Seattle, WA, September 1993.

[114] R. W. Boswell, F. F. Chen, "Helicons - The early years." *IEEE Transactions on Plasma Science, 25*(6), 1229-1244 (1997)

[115] F. F. Chen, R. W. Boswell, "Helicons - The past decade." *IEEE Transactions on Plasma Science,* Vol. 25, No. 6, 1245-1257 (1997)

[116] E. A. Bering III, F. R. Chang Díaz, J. P. Squire, T. W. Glover, M. D. Carter, G. E. McCaskill, B. W. Longmier, M. S. Brukardt, W. J. Chancery, V. T. Jacobson, "Observations of single-pass ion cyclotron heating in a trans-sonic flowing plasma," *Physics of Plasmas*, Vol. 17, 043509, 2010.

[117] F. R. Chang Diaz, J. P. Squire, "The Physics and Engineering of the VASIMR Engine," AIAA 200-3756, *36th AIAA/ASME/SAE/ASEE Joint Propulsion Conference*, Huntsville, AL, July 2000

[118] E. A. Bering III, B. W. Longmier, M. Ballenger, C. S. Olsen, J. P. Squire, F. R. Chang Diaz, "Performance Studies of the VASIMR VX-200," AIAA 2011-1071, *49th AIAA Aerospace Sciences Meeting*, Orlando, FL, Jan. 2011

[119] K. Shenai, P. G. Neudeck, "Performance Evaluation of Silicon Carbide Devices in Power Converters," AIAA 2000-2805, *35th Intersociety Energy Conversion Engineering Conference and Exhibit*, Las Vegas, NV, July 2000

[120] G. Schwarze, "Advanced Electrical Materials and Components Development – An Update," AIAA 2005-5717, *3rd International Energy Conversion Engineering Conference*, San Francisco, CA, August 2005.

[121] K. Shenai, R. S. Scott, B. J. Baliga, "Optimum Semiconductors for High-Power Electronics," *IEEE Transactions on Electronic Devices*, Vol. 36, pp. 1811-1823, September 1989.

[122] Z. Luo, T. Chen, A. C. Ahyi, A. K. Sutton, B. M. Haugerud, J. D. Cressler, D. C. Sheridan, J. R. Williams, P. W. Marshall, R. A. Reed, "Proton Radiation Effects in 4H-SiC Diodes and MOS Capacitors," *IEEE Transactions on Nuclear Science*, Vol. 51, No. 6, December 2004.

[123] R. S. Bhatia, "Review of Spacecraft Cryogenic Coolers," *Journal of Spacecraft and Rockets*, Vol. 39, No. 3, May-June 2002.

[124] P. Kittel, "Cryocooler Performance Estimator," *Cryocoolers 14*, Kluwer Academic/Plenum Publishers, New York, 2005, pp. 563-572

[125] H. J. M. ter Brake, G. F. M. Wiegernick, "Low Power Cryocooler Survey," *Cryogenics*, Vol. 42, No. 11, pp. 705-718 November 2002

[126] D. G. Fearn, "The Use of Ion Thrusters for Orbit Raising," *Journal of the British Interplanetary Society*, Vol. 33, pp. 129-137, 1980

[127] R. Walker, C. Bramanti, O. Sutherland, R. Boswell, C. Charles, D. G. Fearn, J. Gonzalez Del Amo, P. E. Frigot, M. Orlandi, "Initial Experiments on a Dual-Stage 4-Grid Ion Thruster for Very High Specific Impulse and Power," AIAA 2006-4669, *42nd AIAA/ASME/SAE/ASEE Joint Propulsion Conference*, Sacramento, CA, July 2006.

[128] J. R. Brophy, I. Katz, J. Polk, J. R. Anderson, "Numerical Simulations of Ion Thruster Accelerator Grid Erosion," *38th AIAA/ASME/SAE/ASEE Joint Propulsion Conference*, Indianapolis, Indiana, July 7-10, 2002.

[129] E. Y. Choueiri, "Fundamental Difference between the Two Variants of Hall Thrusters: SPT and TAL," AIAA-2001-3504, *37th AIAA/ASME/SAE/ASEE Joint Propulsion Conference*, Salt Lake City, UT, July 2001

[130] D. H. Manzella, R. S. Jankovsky, R. R. Hofer, "Laboratory Model 50 kW Hall Thruster," AIAA 2002-3676, *38th AIAA/ASME/SAE/ASEE Joint Propulsion Conference and Exhibit*, Indianapolis, IN, July 2002.

[131] A. I. Bugrova, N. A. Maslennikov, A. I. Morozov, "Similarity Laws for the Global Properties of a Hall Accelerator," *Sov. Phys. Tech. Phys.*, Vol. 36, No. 6, June 1991.

[132] A. I. Bugrova, A. S. Lipatov, A. I. Morozov, D. V. Churbanov, "On a Similarity Criterion for Plasma Accelerators of the Stationary Plasma Thruster Type," *Technical Physics Letters*, Vol. 28, No. 10, pp 821-823, 2002.

[133] V. Khayms, M. Martinez-Sanchez, "Design of a Miniaturized Hall Thruster for Microsatellites," AIAA 96-3291, *32nd AIAA/ASME/SAE/ASEE Joint Propulsion Conference and Exhibit*, Lake Buena Vista, FL, July 1996.

[134] V. Kim, "Main Physical Features and Processes Determining the Performance of Stationary Plasma Thrusters," *Journal of Propulsion and Power*, Vol. 14, No. 5, pp 736-743, 1998.

[135] W. A. Hargus Jr., M. A. Cappelli, "Development of a Linear Hall Thruster," AIAA 98-3336, *34th AIAA/ASME/SAE/ASEE Joint Propulsion Conference and Exhibit*, Cleveland, OH, July 1998.

[136] Y. Daren, D. Yongjie, Z. Zhi, "Improvement on the Scaling Theory of the Stationary Plasma Thruster," *Journal of Propulsion and Power*, Vol. 21, No. 1 pp. 139-143, 2005.

[137] M. Andrenucci, F. Battista, P. Piliero, "Hall Thruster Scaling Methodology," IEPC 2005-187, The 29th International Electric Propulsion Conference, Princeton University, October 2005.

[138] K. Dannenmayer, S. Mazouffre, "Sizing of Hall-Effect Thrusters with Input Power and Thrust Level: An Empirical Approach," *Journal of Technical Physics*, Vol. 49, No. 3-4, 2008.

[139] B. A. Arhipov, L. Z. Krochak, S. S. Kudriavcev, V. M. Murashko, T. Randolph, "Investigation of the Stationary Plasma Thruster (SPT-100) Characteristics and Thermal Maps at the Raised Discharge Power," AIAA-98-3791, *34th AIAA/ASME/SAE/ASEE Joint Propulsion Conference and Exhibit*, Cleveland, OH, July 1998.

[140] P. C. Lozano, *Studies of the Ion-Droplet Mixed Regime in Colloid Thrusters*, Ph. D. Thesis, The Massachusetts Institute of Technology, February 2003.

[141] D. G. Courtney, H. Li, P. Diaz, T. P. Fedkiw, P. Lozano, "On the Validation of Porous Nickel as Substrate Material of Electrospray Ion Propulsion," AIAA 2010-7020, *46th AIAA/ASME/SAE/ASEE Joint Propulsion Conference & Exhibit*, Nashville, TN, July 2010.

[142] J. W. John, T. Sarver-Verhey, D. T. Jacobson, H. Kamhawi, "High Current Cathode Development for 50 kW Class Hall Thrusters," AIAA 2005-4244, *41st AIAA/ASME/SAE/ASEE Joint Propulsion Conference and Exhibit*, Tuscon, AZ, July 2005.

[143] H. Maecker, ''Plasma Jets in Arcs in a Process of Self-induced Magnetic Compression,'' *Zeitschrift fur Physik*, Vol. 141, No. 1, 1955, pp. 198 – 216

[144] D. Q. King, K. E. Clark, R. G. Jahn, "Effect of Choked Flow on Terminal Characteristics of MPD Thrusters," AIAA Paper 81-0686, 1981.

[145] Baksht F. G., Moizhes, B. Ya., and Rybakov, A. B., "Critical Regime of a Plasma Accelerator," *Soviet Physics—Technical Physics*, Vol. 18, No. 12, 1974, pp. 1613-1616.

[146] Shubin, A. P., "Dynamic Nature of Critical Regimes in Steady-State High-Current Plasma Accelerators," *Soviet Journal of Plasma Physics*, Vol. 2, No. 1, 1976, pp. 18-21.

[147] Schrade, H. O., Auweter-Kurtz, M., and Kurtz, H. L., "Stability Problems in Magnetoplasmadynamic Arc Thrusters," *AIAA 18th Fluid Dynamics and Plasmadynamics and Laser Conference*, Cincinnati, OH, 1985.

[148] Martinez-Sanchez, M. and Heimerdinger, D. J., "Analysis of Performance Limiting Factors in MPD Thrusters," *IEEE International Conference on Plasma Science*, Pittsburgh, PA, 1985.

[149] Lawless, J. L. and Subramaniam, V. V., "Theory of Onset in Magnetoplasmadynamic Thrusters," *Journal of Propulsion and Power*, Vol. 3, March-April 1987, pp. 121-127.

[150] Subramaniam, V. V. and Lawless, J. L., "The Electrical Characteristics of Magnetoplasmadynamic Thrusters," *IEEE International Conference on Plasma Science*, Pittsburgh, PA, 1985.

[151] H. Tahara, H. Yasui, Y. Kagaya, T. Yoshikawa, "Thruster Performance and Acceleration Mechanisms of a Quasi-Steady Applied-Field MPD Arcjet," AIAA 87-1001, *19th AIAA/DGLR/JSASS International Electric Propulsion Conference*, Colorado Springs, CO, May 1987.

[152] H. Tahara, Y. Kagaya, T. Yoshikawa, "Hybrid MPD Thruster with Axial and Cusp Magnetic Fields," IEPC 88-058, *20th International Electric Propulsion Conference*, Garmisch-Partenkirchen, Germany, October, 1988.

[153] H. Tahara, Y. Kagaya, T. Yoshikawa, "Quasi-Steady Magnetoplasmadynamic Thruster with Applied Magnetic Field for Near Earth Missions," *Journal of Propulsion and Power*, Vol. 5, No. 6, pp. 713-717, 1989.

[154] H. Tahara, H. Yasui, Y. Kagaya, T. Yoshikawa, "Thruster Performance and Acceleration Mechanisms of a Quasi-Steady Applied-Field MPD Arcjet," AIAA 90-2554, *21st AIAA/DGLR/JSASS International Electric Propulsion Conference*, Orlando, FL, July, 1990.

[155] H. Tahara, Y. Kagaya, T. Yoshikawa, "Effects of Applied Fields on Performance of a Quasi-Steady Magnetoplasmadynamic Arcjet," *Journal of Propulsion and Power*, Vol. 11, No. 2, pp. 337-342, 1995.

[156] H. Tahara, Y. Kagaya, T. Yoshikawa, "Performance and Acceleration Process of Quasi-Steady Magnetoplasmadynamic Arcjets with Applied Magnetic Fields," *Journal of Propulsion and Power*, Vol. 13, No. 5, 1995.

[157] R. L. Burton, P. J. Turchi, "Pulsed Plasma Thruster," *Journal of Propulsion and Power*, Vol. 14, No. 5, 1998

[158] L. Hogberg, K. Vogel, "Experiments with Electrodeless Generation and Acceleration of Plasma Rings," *Nuclear Instruments and Methods*, Vol. 10, pp. 95, 1961

[159] C. W. Matthews, W. F. Cuddihy, "A Single-Coil Induced Electromotive Force Plasma Accelerator," NASA Report No. TN D-639, 1961

[160] C. L. Dailey and R. H. Lovberg, "Large Diameter Inductive Plasma Thrusters," AIAA Paper 79-2093, October 1979

[161] J. H. Poylio, D. Russell, W. Goldstein, B. Jackson, R. H. Lovberg, C. L. Dailey, "Pulsed Inductive Thruster: Flight-Scale Proof of Concept Demonstrator," *40th AIAA/ASME/SAE/ASEE Joint Propulsion Conference and Exhibit*, Ft. Lauderdale, FL, July 2004

[162] A. Sengupta, J. A. Anderson, C. Garner, J. Brophy, K. K. deGroh, B. A. Banks, T. A. Thomas, "Deep Space 1 Flight Spare Ion Thruster 30,000-Hour Life Test," *Journal of Propulsion and Power*, Vol. 25, No. 1, Jan –Feb. 2009.

[163] R. E. Wirz, I. Katz, D. M. Goebel, J. R. Anderson, "Electron Backstreaming Determination for Ion Thrusters," AIAA 2008-4732, *44th AIAA/ASME/SAE/ASEE Joint Propulsion Conference and Exhibit*, Hartford CT, July 2008.

[164] J. Wang, J. Polk, J. Brophy, I. Katz, "Three-Dimensional Particle Simulations of Ion-Optics Plasma Flow and Grid Erosion," *Journal of Propulsion and Power*, Vol. 19, No. 6, pp. 1192-1199, Nov. – Dec. 2003.

[165] J. Anderson, I. Katz, D. Goebel, "Numerical Simulation of Two-Grid Ion Optics Using a 3D Code," AIAA-2004-3782, *40th AIAA/ASME/SAE/ASEE Joint Propulsion Conference and Exhibit*, Fort Lauderdale, Florida, July 2004.

[166] I. Katz, I. Mikellides, R. Wirz, J. Anderson, D. Goebel, "Ion Thruster Life Models," AIAA-2005-4256, *41st AIAA/ASME/SAE/ASEE Joint Propulsion Conference and Exhibit*, Tucson, Arizona, July 10-13, 2005.

[167] D. Gobel, I. Katz, *Fundamentals of Electric Propulsion: Ion and Hall Thrusters*, JPL Space Science and Technology Series, John Wiley & Sons, Inc., Hoboken, NJ, 2008.

[168] M. Knudsen, *Ann. Physik*, Vol. 4, No. 28, pp. 75, 1909

[169] M. v. Smoluchowski, *Ann. Physik*, Vol. 4, No. 33, pp. 1159, 1910

[170] S. Dushman, "Production and Measurement of High Vacuum," p. 32, Schenectady (1922); Int. Crit. Tabl., Vol. 1 pp. 91, New York (1926), J. Franklin Inst. Vol 211, pp. 689 (1931).

[171] P. Clausing, "The Flow of Highly Rarefied Gases through Tubes of Arbitrary Length," *The Journal of Vacuum Science and Technology*, Vol. 8, No. 5, pp. 636 – 646

[172] J. Bohdansky, J. Roth, H. L. Bay, "An Analytical Formula and Important Parameters for Low-Energy Ion Sputtering," *Journal of Applied Physics*, Vol. 51, No. 5, May 1980

[173] E. Hechtl, J. Bohdansky, "Sputtering Behavior of Graphite and Molybdenum at Low Bombarding Energies," *Journal of Nuclear Materials*, Vol. 123, No. 1-3, pp. 1431 – 1436, May 1984

[174] J. Polk, "An Overview of the Nuclear Electric Xenon Ion System (NEXIS) Program," AIAA 2004-4173, *40th AIAA Joint Propulsion Conference and Exhibit*, Ft. Lauderdale, FL, July 2004.

[175] T. Randolph, J. Polk, "An Overview of the Nuclear Electric Xenon Ion System (NEXIS) Activity," AIAA 2004-3450, *40th AIAA Joint Propulsion Conference and Exhibit*, Ft. Lauderdale, FL, July 2004.

[176] I. V. Melikov, "Equilibrium Flow in a Hall-current Plasma Accelerator," *Journal of Technical Physics*, Vol. 44, pp 549-553, 1974 (in Russian).

[177] A. I. Morozov, I. V. Melikov, "The Process of Scaling in the Plasma Accelerator with Closed Electron Drift Under the Condition of Ionization," *Sov. Phys. Tech. Phys.*, Vol. 19, pp 340, 1974.

[178] E. Ahedo, J. M. Gallardo, M. Martinez-Sanchez, "Effects of the Radial Plasma-Wall Interaction on the Hall Thruster Discharge," *Physics of Plasmas*, Vol. 10, No. 8, August 2003.

[179] J. M. Sankovic, J. A. Hamley, T. W. Haag, "Performance Evaluation of the Russian SPT-100 Thruster at NASA LeRC," IEPC 1993-094, *23rd International Electric Propulsion Conference*, Seattle, WA, September 1993.

[180] J. R. Brophy, J. W. Barnett, J. M. Sankovic, D. A. Barnhart, "Performance of the Stationary Plasma Thruster: SPT-100," AIAA-92-3155, *28th AIAA/SAE/ASME/ASEE Joint Propulsion Conference*, Nashville, TN, July 1992.

[181] M. Auweter-Kurtz, B. Glocker, H. L. Kurtz, O. Loesener, H. O. Schrade, N. Tubanos, T. Wegmann, D. Willer, J. E. Polk, "Cathode Phenomena in Plasma Thrusters," *Journal of Propulsion and Power*, Vol. 9, No. 6, pp 882-888, Nov.-Dec. 1993.

[182] H. O. Schrade, M. Auweter-Kurtz, H. L. Kurtz, "Cathode Erosion Studies on MPD Thrusters," *AIAA Journal*, Vol. 25, No. 8, 1987, pp. 1105-1112.

[183] J. E. Polk, T. J. Pivirotto, "Alkali Metal Propellants for MPD Thrusters," AIAA 91-3572, AIAA Conference on Advanced SEI Technologies, Cleveland, OH, 1991.

[184] D. M. Goebel, I. Katz, J. Polk, I. G. Mikellides, K. K. Jameson, T. Liu, R. Dougherty, "Extending Hollow Cathode Life for Electric Propulsion in Long-Term Missions," AIAA 2004-5911, *Space 2004 Conference and Exhibit*, San Diego, CA, September 2004.

[185] D. J. Heimerdinger, M. Martinez-Sanchez, "Two-Dimensional Analysis of an MPD Arcjet," AIAA 85-2040, 18th International Electric Propulsion Conference, Alexandria, VA, 1985.

[186] D. J. Heimerdinger, *Fluid Mechanics in a Magnetoplasmadynamic Thruster*, Ph. D. Dissertation, Massachusetts Institute of Technology, Department of Aeronautics and Astronautics, Cambridge, MA, January 1988.

[187] D. J. Heimerdinger, D. B. Kilfoyle, M. Martinez-Sanchez, "Experimental Characterization of Contoured Magnetoplasmadynamic Thrusters," AIAA 88-3205, *24th AIAA/SAE/ASME/ASEE Joint Propulsion Conference*, Boston, MA, July 1988.

[188] K. Kuriki, H. Suzuki, H., "Quasisteady MPD Arcjet with Anode Gas Injection," AIAA Paper 79-2058, *14th International Electric Propulsion Conference*, Princeton, NJ, Oct.-Nov., 1979.

[189] R. E. Peterkin, Jr., M. H. Frese, C. R. Sovinec, "Transport of Magnetic Flux in an Arbitrary Coordinate ALE Code," *Journal of Computational Physics*, Vol. 140, No. 1, pp. 148-171, February 1998.

[190] R. E. Peterkin, Jr., M. H. Frese, "MACH: A Reference Manual," 2nd Ed., Air Force Research Laboratory: Directed Energy Directorate, Apr. 2000

[191] J. U. Brackbill, "Numerical Magnetohydrodynamics for High-Beta Plasma," *Methods in Computational Physics*, John Killeen, ed., Academic Press, New York, 1976

[192] S. K. Borowski, M. L. McGuire, L. M. Mason, J. H. Gilland, T. J. Packard, "Bimodal NTR Propulsion for Artificial Gravity HOPE Missions to Callisto," 20th Symposium on Space Nuclear Power and Propulsion, *Space Technology and Applications International Forum*, Albuquerque, NM, Feb. 2003

[193] M. L. McGuire, S. K. Borowski, L. M. Mason, J. H. Gilland, "High Power MPD Nuclear Electric Propulsion (NEP) for Artificial Gravity HOPE Missions to Callisto," NASA/TM – 2003-0212349, *Space Technology and Applications International Forum*, Albuquerque, NM, Feb. 2003

[194] P. A. Troutman, K. Bethke, F. Stillwagen, D. L. Caldwell, Jr., R. Manvi, C. Strickland, S. A. Krizan, "Revolutionary Concepts for Human Outer Planet Exploration (HOPE)," *Space Technology and Applications International Forum*, Albuquerque, NM, Feb. 2003

[195] S. Y. Park, H. Seywald, S. A. Krizan, F. H. Stillwagen, "Mission Design for Human Outer Planet Exploration (HOPE) Using a Magnetoplasma Spacecraft," Planetary and Space Science, Vol. 54, No. 8, pp. 737-749, 2006

[196] E. G. Schnitzler, J. L. Jones, J.L., G. F. Chapline, "Fission Fragment Rocket preliminary Feasibility Assessment," Idaho National Engineering Laboratory Contract No. DEACO7-76IDO1570, Lawrence Livermore National Laboratory Contract No. W-7405-ENG-88, 1989.

[197] Forward, R.L, "Radioisotope Sails for Deep Space Propulsion and Electrical Power," AIAA-95-2596, 31st AIAA/ASME/SAE/ASEE Joint Propulsion Conference, San Diego CA, July 10-12, 1995.

[198] R. Clark, R. Sheldon, "Dusty Plasma Based Fission Fragment Nuclear Reactor," AIAA 2005-4460, 41st AIAA/ASME/SAE/ASEE Joint Propulsion Conference and Exhibit, Tuscon, AZ, July 2005.

[199] B. N. Cassenti, "Hybrid Fusion Propulsion," AIAA 1998-3590, 34th AIAA/ASME/SAE/ASEE Joint Propulsion Conference and Exhibit, Cleveland, OH, July 1998.

[200] A. R. Martin, Ed., "Project Daedalus - The Final Report of the BIS Starship Study," *Journal of the British Interplanetary Society – Supplement*, 1978.